

Compact Microwave Dual-band Bandpass Filter Design

Yahui Wu, BEng, MSc

Doctor of Philosophy

University of York

Electronic Engineering

September 2017

Abstract

The modern wireless communication systems require dual-band bandpass filters to support the standards that work at multiple frequency bands. This thesis demonstrates two design approaches for the development of compact microwave dual-band bandpass filters. The first approach is based on synthesising a dual-passband filter response utilising only one resonant frequency of the resonators. The second approach employs dual-band resonators that have tuneable the first and the second resonant frequencies to form the dual-passbands filter response.

The dual-passband response synthesis method synthesises a response with dual passbands that is generated by a frequency transformation that places a finite frequency zero within the single-passband of a filter to split it into dual passbands. The transformed dual-passband response is characterised by the synthesised coupling matrix that consists of the coupling coefficients between coupled resonators. Two filters have been designed and fabricated using microstrip square open-loop and $TE_{01\delta}$ mode quarter cylindrical dielectric resonators. The investigation based on simulation studies and measured results revealed that unloaded quality factor of the resonator is required to be ten times greater than the quality factor of each passband in order to realise the narrow passbands.

The dual-band resonator methods employ multiple resonant modes of the resonator operating at different frequencies to implement the multiple passbands, respectively. Stepped impedance resonators in stripline and coaxial configurations have been presented and analysed for the realisation of dual-band bandpass filters. A second order dual-band bandpass filter formed by coaxial stepped impedance resonators has been designed, fabricated and tested. The measured frequency response agree well with the simulated response. The estimated breakdown power shows that the filter is capable of high power applications. Non-uniform pitch helical resonators are also proposed for the implementation of dual-band bandpass filters. Two non-uniform pitch helical resonator structures have been analytically modelled. The theoretical models of the non-uniform pitch helical resonators have been developed for accurate prediction of its dual-band characteristics. It is also employed in the general design process of the non-uniform pitch helical resonators. Resonator examples have been presented to show the applicability and validity of the analysis and simulation. Three dual-band bandpass filters have been designed and implemented using non-uniform pitch helical resonators. Their measured frequency responses agree reasonably with the ideal responses. Additionally, the simulation shows that the designed dual-band bandpass filters have relatively high power handling capability.

Contents

Abstract	II
List of figures.....	VI
List of Tables	XII
Acknowledgements.....	XIII
Declarations	XIV
Chapter 1: Introduction.....	1
1.1 Research background	1
1.2 Previous research on dual-band bandpass filters.....	3
1.3 Aims and objectives of the research.....	4
1.4 Outline of the Thesis	5
Chapter 2: Concepts, theories and tools for microwave filter design	7
2.1 Introduction	7
2.2 Design process of microwave filter.....	8
2.3 Resonators	9
2.3.1 Q factor	9
2.3.2 Lumped element circuits.....	10
2.3.3 Transmission line resonators.....	12
2.3.4 Dielectric resonator	15
2.3.5 Helical resonator	19
2.4 Coupled resonator circuits.....	28
2.4.1 General coupling theory.....	28
2.4.2 External coupling coefficient and external quality factor	29
2.4.3 Inter-resonator coupling coefficient.....	30
2.5 Simulation and Modelling	41
2.5.1 MATLAB	42

2.5.2	Keysight ADS	42
2.5.3	CST MWS.....	43
2.6	Measurement	44
2.6.1	Unloaded Q measurement.....	44
2.6.2	External quality factor measurement	46
2.6.3	Inter-resonator coupling coefficient measurement	46
2.7	Power handling capability	47
Chapter 3: Dual-passband response synthesis.....		49
3.1	Introduction	49
3.2	Frequency transformation for symmetric dual-passband frequency response	51
3.3	Coupling matrix synthesis.....	53
3.3.1	Transfer function.....	53
3.3.2	Coupling matrix synthesis for symmetric frequency response	58
3.3.3	Coupling matrix synthesis for asymmetric frequency response	61
3.3.4	Coupling matrix reduction	63
3.4	Design process and filter examples	65
3.4.1	An eighth order dual-band BPF	65
3.4.2	A sixth-order dual-band BPF	80
3.5	Limitations and further work	98
3.6	Conclusions	98
Chapter 4: Dual-band resonators		101
4.1	Introduction	101
4.2	Stepped Impedance Resonator (SIR)	103
4.2.1	Resonance characteristics of SIR.....	104
4.2.2	Coaxial SIR.....	107
4.2.3	Dual-band bandpass filter design using Coaxial SIRs.....	110
4.3	Non-uniform pitch helical resonator	121

4.3.1	Analysis of non-uniform pitch helical resonator	121
4.3.2	Design procedure	140
4.3.3	Experimented non-uniform pitch helical resonators.....	144
4.3.4	External coupling and inter-resonator coupling.....	149
4.3.5	Filters using non-uniform pitch helical resonators	158
4.4	Further work and discussion	180
4.4.1	Coaxial SIR filters.....	180
4.4.2	Non-uniform pitch helical resonator filters.....	181
4.5	Conclusions	186
Chapter 5: Conclusions		190
5.1	Achievements	190
5.2	Conclusions and further work	194
Abbreviations		201
References		203

List of figures

1.1 RF front end of a GSM cellular base station.....	1
1.2 Block diagram of a receiver architecture with two single-band bandpass filters in parallel.	2
1.3 Block diagram of a receiver architecture with a wideband BPF and a BSF in series.....	2
1.4 Block diagram of a receiver architecture with a dual-band BPF.	3
2.1 RLC resonant circuits. (a) Parallel RLC circuit. (b) Series RLC circuit.	11
2.2 A general coaxial resonator structure.	12
2.3 General microstrip structure.	13
2.4 TE _{01δ} mode field patterns of an isolated cylindrical DR. (a) E-field in the equatorial plane (b) H-field in the meridian plane.	17
2.5 Practical TE _{01δ} mode DR structure and parameters. (a) 3D. (b) Cross-section.	17
2.6 A typical uniform pitch helical resonator.	20
2.7 Sheath model of helix.	21
2.8 Tape helix model.....	22
2.9 Transmission line model of helix.....	22
2.10 A helical resonator with 6 turns.	27
2.11 Equivalent circuit of the singly loaded resonator circuit.	29
2.12 Equivalent circuit for determining the coupling coefficient of a pair of coupled resonators.	31
2.13 Equivalent circuits of the electric coupling between synchronously tuned resonators. .	34
2.14 Equivalent circuits of the magnetic coupling between synchronously tuned resonators.	35
2.15 Equivalent circuit of the mixed coupling.....	36
2.16 Asynchronously tuned coupled resonator circuit with electric coupling.....	37
2.17 Asynchronously tuned coupled resonator circuits with magnetic coupling. .	39
2.18 Asynchronously tuned resonator circuit with mixed coupling.	40
3.1 Frequency responses in the Ω , Ω' and ω domains.	51
3.2 Two-port linear network.....	53
3.3 Equivalent-circuit of n -loop coupled resonator circuit.	58
3.4 General process of dual-passband response synthesis method for the filter realisation. ..	65
3.5 Frequency response of the four pole Chebyshev prototype in Ω domain.....	66

3.6	Dual-band frequency response after frequency transformation in Ω' domain.....	67
3.7	Canonical coupling topology of the eighth-order filter.....	67
3.8	Equivalent circuit of the eighth order filter in Keysight ADS.	69
3.9	Simulated frequency response of the equivalent circuit with an infinite unloaded Q factor.	70
3.10	Topology of coupled square open-loop resonators. (a) electric coupling. (b) magnetic coupling. (c) and (d) mixed coupling.....	71
3.11	The topology of the eighth order filter.	71
3.12	External quality factor profile of the resonator.	73
3.13	Inter-resonator coupling profile for the (a) type electric coupling.	74
3.14	Inter-resonator coupling profile for the (b) type magnetic coupling.	74
3.15	Inter-resonator coupling profile for the (d) type mixed coupling - electric coupling dominant.	75
3.16	Inter-resonator coupling profile for the (d) type mixed coupling - magnetic coupling dominant.	75
3.17	Filter structure and dimensions.....	76
3.18	EM simulated and measured S_{11} parameters of the eighth order dual-band BPF.	77
3.19	EM simulated and measured S_{21} parameters of the eighth order dual-band BPF.	77
3.20	Simulated S_{11} parameters of the equivalent circuit with a finite unloaded Q of 280.....	78
3.21	Simulated S_{21} parameters of the equivalent circuit with a finite unloaded Q of 280.....	78
3.22	Simulated frequency response of the equivalent circuit with a finite unloaded Q of 400.	79
3.23	Simulated frequency response of the equivalent circuit with a finite unloaded Q of 800.	80
3.24	Asymmetrical frequency response of the three pole Chebyshev prototype in Ω domain.	81
3.25	Dual-band sixth-order frequency response after frequency transformation in Ω' domain.	82
3.26	Equivalent circuit of the sixth order dual-band BPF.....	83
3.27	Simulated frequency response of the equivalent circuit with infinite Q of resonator.	84
3.28	Resonator structures and fields patterns for $TE_{01\delta}$ mode cylindrical DR. (a) full cylindrical type. (b) quarter type.....	85
3.29	Resonator structure and dimensions for filter design.	86

3.30	Fabricated resonator in a cavity.	87
3.31	Simulated frequency response of the equivalent circuit with finite Q of 2100.	87
3.32	External coupling by a probe inserted into the DR.	88
3.33	External coupling structure.	88
3.34	Inter-resonator coupling structure: electric coupling.	89
3.35	Equivalent circuit simulation with unloaded Q of 2200 and $K_{16}=K_{61}=0$	90
3.36	Inter-resonator coupling structure: magnetic coupling type I.	90
3.37	Inter-resonator coupling profile of magnetic type I.	91
3.38	Inter-resonator coupling structure: magnetic coupling type II.	91
3.39	Inter-resonator coupling profile of magnetic type II.	92
3.40	Structure of the sixth order dielectric filter.	93
3.41	Initial EM simulated frequency response of the filter.	93
3.42	Structure and dimensions of the sixth order dielectric filter.	95
3.43	Simulated frequency responses of the sixth order dual-band BPF.	95
3.44	Fabricated sixth-order dielectric filter.	96
3.45	Measured and simulated frequency response with epoxy.	97
4.1	Basic structure of SIR in stripline. (a) Quarter-wavelength type. (b) Half-wavelength type.	104
4.2	Relationship between frequency ratio (f_{s1}/f_0) and impedance ratio (R_z) of dual-section quarter- and half-wavelength type SIRs.	107
4.3	Structure of a coaxial SIR.	108
4.4	Frequency ratio (f_1/f_0) profile of coaxial SIR against diameter ratio (D_1/D_2).	109
4.5	Determined coaxial SIR structure and dimensions for the dual-band BPF design.	110
4.6	Fabricated coaxial SIR.	111
4.7	Tunable external coupling structure for the coaxial SIR.	112
4.8	External coupling profile of the first band.	113
4.9	External coupling profile of the second band.	113
4.10	Field patterns at the first resonance of the coaxial SIR. (a) electric field. (b) magnetic field.	114
4.11	Field patterns at the second resonance of the coaxial SIR. (a) electric field. (b) magnetic field.	115
4.12	Inter-resonator coupling structure.	116
4.13	Inter-resonator coupling profile of the first resonance.	117

4.14	Inter-resonator coupling profile of the second resonance.	118
4.15	Fabricated 2 nd order dual-band bandpass filter.	118
4.16	Wideband frequency responses of the designed 2 nd order filter.	119
4.17	Simulated and measured frequency responses of the filter: the first passband.	119
4.18	Simulated and measured frequency responses of the filter: the second passband.	120
4.19	Typical structures of non-uniform pitch helical resonator. (a) Category I: pitch modified by the number of turns. (b) Category II: pitch modified by the height.	122
4.20	The fundamental resonant frequency of the uniform pitch helical resonator.	124
4.21	The first spurious resonant frequency of the uniform pitch helical resonator.	124
4.22	The second spurious resonant frequency of the uniform pitch helical resonator.	125
4.23	Simulated frequency ratio against the ratio of the number of turns.	126
4.24	Frequency ratio against the ratio of heights ($h_{\text{btm}}/h_{\text{top}}$) from simulation and SIR model.	127
4.25	Equivalent circuit of a uniform pitch helical resonator with an inductive load.	129
4.26	Equivalent circuit of a uniform pitch helical resonator with a capacitive load.	131
4.27	Frequency ratio from simulation results and circuit model prediction.	134
4.28	Frequency ratio against the ratio of heights from simulation and circuit model.	136
4.29	Developed model for Category I resonator with curve fitting residuals.	138
4.30	Developed model for Category II resonator with curve fitting residuals.	140
4.31	Frequency ratio against the ratio of height ($h_{\text{btm}}/h_{\text{top}}$) of the helical resonator when $d=7.0$ mm, $h_{\text{btm}}=18$ mm.	142
4.32	Fundamental resonant frequency and the corresponding unloaded Q against the coil diameter when $h_{\text{top}}=6.38$ mm, $h_{\text{btm}}=18$ mm.	143
4.33	3D printed dual-section formers. (a) Category I. (b) Category II.	144
4.34	Fabricated Category I non-uniform pitch helical resonators. (a) With lids. (b) Without lids.	146
4.35	Fabricated helical resonator in a cylindrical tube [51].	147
4.36	Fabricated Category II non-uniform pitch helical resonators. (a) With lids. (b) Without lids.	148
4.37	Topologies of direct tapping. (a) Right. (b) Left. (c) Front. (d) Back. (e) Bottom.	150
4.38	Parallel plate coupling.	151
4.39	General inter-resonator coupling by aperture.	152
4.40	Field distributions of a non-uniform pitch helical resonator.	152

4.41	Step-width aperture for inter-resonator coupling structure.....	154
4.42	Simulation of the coupling coefficients at the first resonant frequency (f_1).	154
4.43	Simulation of the coupling coefficients at the second resonant frequency (f_2).....	155
4.44	Coupling coefficient (k_1) against lower aperture height (H_1).	156
4.45	Coupling coefficient (k_2) against lower aperture height (H_1).	156
4.46	Inter-resonator coupling topology for non-uniform pitch helical resonators with rotation of 180° and 90° respectively.	157
4.47	Inter-resonator coupling topology with a mirrored helical resonator.	157
4.48	Interdigital type topology of inter-resonator coupling.....	158
4.49	External coupling profile of the 2 nd order dual-band BPF.	159
4.50	Inter-resonator coupling profile at the first band.	160
4.51	Inter-resonator coupling profile at the second band.....	160
4.52	Structure of the designed 2 nd order dual-band BPF.....	161
4.53	The fabricated 2 nd order BPF that $d=7.5$ mm.....	162
4.54	S_{11} parameters of the 2 nd order dual-band BPFs.	162
4.55	Frequency responses of the second order dual-band BPFs over a wide frequency range..	163
4.56	Passband S_{21} parameters of the 2 nd order dual-band BPFs.....	163
4.57	The fabricated 2 nd order filter using insulated copper wire that $d=7.5$ mm.....	165
4.58	Frequency responses of the 2 nd order filters using insulated and uninsulated copper wires.	165
4.59	Direct coupling by probe on the support of helix.	167
4.60	External coupling profile when tapping the support of the helical resonator.	167
4.61	Inter-resonator coupling profile of the first band.....	168
4.62	Inter-resonator coupling profile of the second band.	168
4.63	Initial simulated S-parameters of the 3 rd order BPF.....	169
4.64	Passbands of the initial simulated frequency response of the 3 rd order BPF.	169
4.65	Structure and dimensions of the 3 rd order filter using Category I resonators (Front view).	170
4.66	Structure and dimensions of the 3 rd order filter (Perspective view).	171
4.67	Photographs of the fabricated filter. (a) Front view. (b) Back lid. (c) Back view.	171
4.68	Simulated and measured frequency responses of the 3 rd order dual-band BPF using Category I non-uniform pitch helical resonators.	172

4.69	Passband frequency responses of the 3 rd order dual-band BPF.	172
4.70	External coupling profile of the Category II non-uniform pitch helical resonator.	175
4.71	Inter-resonator coupling with step-width aperture.	175
4.72	Simulated inter-resonator coupling profile of the first band.	176
4.73	Simulated inter-resonator coupling profile of the second band.	176
4.74	Structure and dimensions of the designed 2 nd order filter using Category II resonators.	177
4.75	Photographs of the fabricated filter.	178
4.76	Measured and simulated frequency response of the 2 nd order dual-band bandpass filter using Category II resonators.	178
4.77	Passband frequency responses of the 2 nd order dual-band BPF using Category II resonators.	179
4.78	Resonant frequencies of the Category I non-uniform pitch helical resonator with load.	182
4.79	Frequency ratio of the Category I non-uniform pitch helical resonator with load.	183
4.80	Resonant frequencies of the Category II resonator with load.	183
4.81	Frequency ratio of the Category II resonator with load.	184
4.82	A helical resonator made of metallic printed strip lines on a dielectric load.	185
4.83	Helical resonator realised by multi-layer strip lines via hole.	185

List of Tables

3-I Radii of the DRs of the designed sixth order dual-band BPF.	94
3-II Tuned coupling dimensions of the filter.....	94
4-I Simulated and measured results of the designed coaxial SIR.	111
4-II Preset parameters for the inter-resonator coupling structure.	116
4-III Data of the fabricated Category I resonators.	146
4-IV Data of the fabricated Category II resonators.	148
4-V Data of the filter characteristics.	164
4-VI Data of the 3 rd order dual-band BPF using Category I resonators.	173
4-VII Data of the 2 nd order dual-band BPF using Category II resonators.	179

Acknowledgements

I wish to thank the following people for their help and support over the past four years.

First of all, I wish to thank my supervisors, Dr Ruwan Gajaweera and Prof Jeremy Everard. They have provided encouragement, guidance for the academic research during my entire PhD study.

Secondly, I would like to thank the technicians in Technical Support Service and mechanical workshop, Mr Mark Hough, Mr Brent Wilkinson, Mr Jason Flatt, and Mr Wayne Robinson, for their help and manufacture of cavities, resonators, and filters.

I also wish to thank my thesis advisor, Dr Martin Robinson, who have kindly given me feedback and evaluation for my work in the past four years.

Many thanks are due to my colleges in the EMC group, Dr Pratik Deshpande and Xiaotian Zhang, who provided help for research and had valuable discussions with me. In addition, many thanks to my friends Cheng Chen and Jialu Lun, who have spent the important time with me in life and the study in York for the past five years.

Finally, I thank to my dear parents and my dear girlfriend Xinyuan. They have supported me to overcome the difficulties in this life journey.

Declarations

I declare that this thesis is a presentation of original work and I am the sole author. This work has not previously been presented for an award at this, or any other, University. All sources are acknowledged as References.

Part of the work has been published in the following papers:

Y. Wu, R. Gajaweera, and J. Everard, "Dual-band bandpass filter using helical resonators," in 2016 46th European Microwave Conference (EuMC), 2016, pp. 237-240.

Y. Wu, R. Gajaweera, and J. Everard, "Dual-band bandpass filter using coaxial Stepped Impedance Resonators," in 2016 International Conference for Students on Applied Engineering (ICSAE), 2016, pp. 181-185.

Y. Wu, R. Gajaweera, and J. Everard, "Dual-band bandpass filter using $TE_{01\delta}$ mode quarter cylindrical dielectric resonators," in 2016 Asia-Pacific Microwave Conference (APMC), 2016, pp. 1-4.

Chapter 1: Introduction

This thesis presents the design, development and implementation of compact dual-band bandpass filters working at microwave frequencies.

1.1 Research background

Filters have been a significant component in electrical circuits since the invention of the first telephony system [1]. In RF and microwave applications, such as communications, radar, navigation, radio astronomy, medical instrumentation, which cover a frequency range of 300 kHz up to 300 GHz [2], filters are usually used to primarily separate or select a frequency band from the shared frequency spectrum [3]. Figure 1.1 shows the typical placement of filters in the RF front end of a GSM cellular base station. The transmit (Tx) filter is used to filter the out-of-band intermodulation products and harmonics that generated by the power amplifier to prevent leakage into the receiver as well as transmit the signal to the antenna. Meanwhile, the receiver is protected by a filter with high attenuation in the transmit band to isolate the high power transmission [3]. These filters are passive bandpass filters (BPFs) to select the signals within a frequency band with high power handling capability and are normally required to be low cost [4].

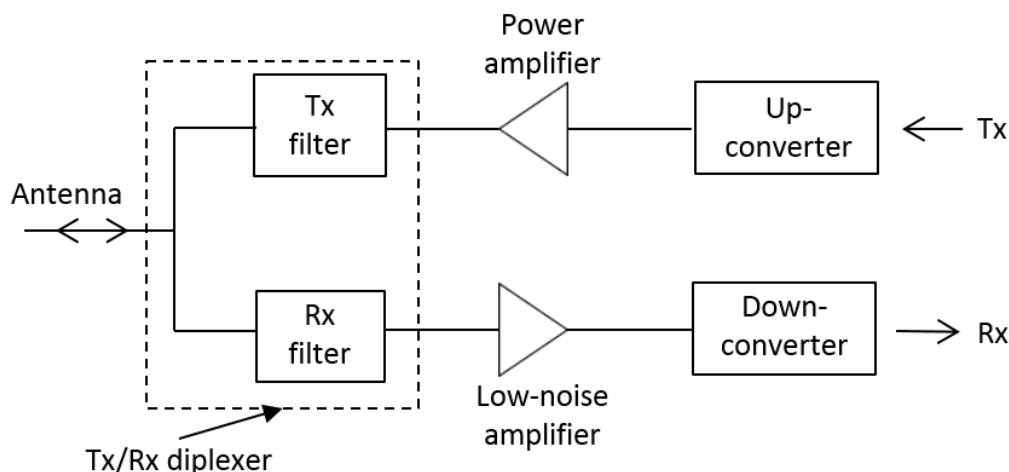


Figure 1.1 RF front end of a GSM cellular base station [3].

A modern wireless communication system simultaneously supports multiple standards that operate at different frequency bands. For example, the Global System for Mobile Communications (GSM) works at 900 MHz and 1800MHz band; the Long Term Evolution (LTE) uses 800 MHz and 2600 MHz band [5]; IEEE 802.11n Wireless Local Area Network

(WLAN) supports 2.4 GHz and 5 GHz band [6]. The recent development in communication standards and applications promoted the design of dual-band wireless systems, which require filters with dual-band capability to extract signals.

One possible way of achieving dual frequency operation of GSM receiver is by replicating the receiving chains for each independent signal path [7], as shown in Figure 1.2. The transceiver chain will have similar arrangement.

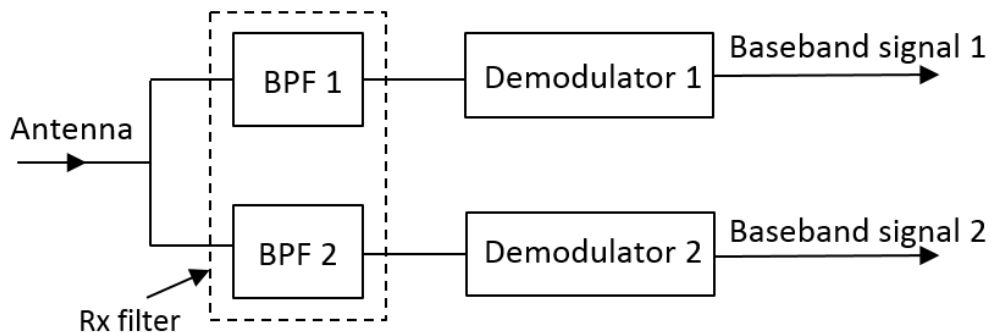


Figure 1.2 Block diagram of a receiver architecture with two single-band bandpass filters in parallel.

Another possibility is to cascade a wideband bandpass filter with a band-stop filter (BSF) to realise the required dual-band signals [8, 9], as illustrated in Figure 1.3.

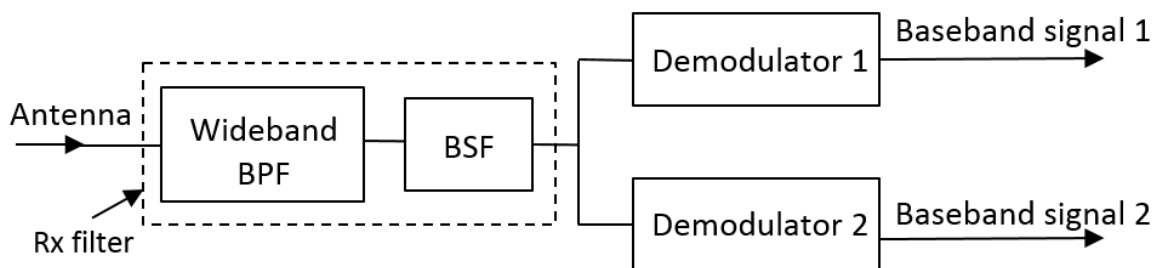


Figure 1.3 Block diagram of a receiver architecture with a wideband BPF and a BSF in series.

The above two approaches increase the component count and hence the physical size of the entire receiver circuit. Additionally, the latter approach suffers from high insertion loss and it is difficult to control the passband and stopband characteristics of the filter simultaneously.

A single filter with dual-band characteristics, known as a dual-band bandpass filter, significantly reduces the size and weight of the filter and the entire system. Figure 1.4 shows a block diagram of a dual-band bandpass filter in a receiver chain, which may save up to 50% of the required size and weight, compared to the above approaches that utilise two filters. Dual-band bandpass filters may also be featured in cognitive radio and military applications where communication channels need to be switched to different frequency bands for tactical purposes.

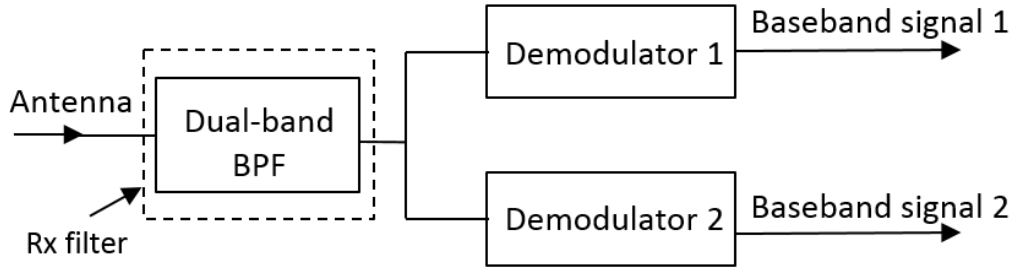


Figure 1.4 Block diagram of a receiver architecture with a dual-band BPF.

Miniaturisation is very important for modern wireless communication systems, especially for the ones with size and weight constraints, such as air-borne communication systems, dual-and multi-band mobile communication systems, and satellite communications systems [1]. The dual-band bandpass filter shown in the above configuration miniaturises the RF filter component and hence the entire wireless communication system.

1.2 Previous research on dual-band bandpass filters

With the advent of modern communication standards in the recent years, there has been a significant research interest in developing components for multi-band multi-mode transceivers, thus an increase research interest in dual-band bandpass filters. The previous research on the realisation of dual-band bandpass filters can be broadly categorised as two approaches: dual-passband response synthesis and dual-band resonators.

The dual-passband response synthesis focuses on the synthesis of filter design process. A frequency transformation is applied to a normalised low pass frequency response to form a dual-passband response [9-11]. The frequency transformation can be viewed as introducing finite frequency transmission zeros within the passband of a single-passband response to split it into a dual-passband response [9]. A coupling matrix for the filter can be generated from the transformed dual-passband response using the synthesis procedures in [12-14]. Then the dual-band bandpass filter can be designed based on the synthesised coupling matrix. This dual-passband response synthesis method has been used to design and implement dual-band bandpass filters in [15-18]. However, the synthesis of coupling matrix in [12-14] has constraints on the filter topology and filter order. In addition, the dual-band bandpass filters in [15-18] are based on microstrip resonators hence suffer from the high insertion loss and low power handling capability. Gajaweera [19] has proposed the Newton-Raphson method to synthesise the coupling matrix that suites the realisation of dual-band bandpass filter with suitable topologies and orders. Nevertheless, there have not been any filter implemented based

on the coupling matrix that is synthesised using Newton-Raphson method.

In the second approach, a resonator with tuneable resonant frequencies is employed to realise more than one passband. In the case of this research, the number of tuneable frequencies is two hence realising two passbands. One such resonator is the stepped-impedance resonators (SIRs). The initial work by Makimoto and Yamashita in the early 1980s [20] showed that the second resonant frequency of a stepped-impedance microstrip resonator can be tuned by changing the impedance ratio of the non-uniform microstrip line while the overall length of the microstrip line determines the fundamental resonant frequency. Most of the dual-band bandpass filter designs to date [21-23] utilising modified microstrip SIRs suffer from high insertion loss and low power handling capability. There have been limited study on non-planar SIR, which is of interest. Dielectric resonators have also been studied and developed for dual-band bandpass filters with low loss and relatively high power handling capability [24, 25], however, there is not a general method available to design dual-band bandpass filters using dielectric resonators. The non-uniform pitch helix was used in dual-band antennas [26, 27], however, there have been few previous research on this structure for resonator and filter use.

1.3 Aims and objectives of the research

The aims of this research program are to develop and characterise resonator structures and synthesis procedures for the realisation of dual-band bandpass filters working at microwave frequencies.

The objectives of the research are shown below:

- 1) Design and implement dual-band bandpass filters based on the synthesised coupling matrices.
- 2) Develop a coaxial SIR for the realisation of dual-band bandpass filters.
- 3) Design and implement dual-band bandpass filters with low loss and high power handling capability using the developed coaxial SIRs.
- 4) Investigate the dual-band characteristics of non-uniform pitch helical resonator.
- 5) Design, develop and implement dual-band bandpass filters using non-uniform pitch helical resonators.

1.4 Outline of the Thesis

The thesis is divided into five chapters. The technical content of the thesis begins with Chapter 2, providing essential background knowledge required for microwave filter design, covering design process, resonators, coupled resonator circuits, simulation and modelling, measurement, and power handling capability. Firstly, this chapter introduces the general design process of microwave filters, starting from specifications to realisation. Secondly, it presents various types of resonators that will be used and modified for dual-band bandpass filter design in later chapters, including lumped element circuits, transmission line resonators, dielectric resonators, and helical resonators. The frequency response of bandpass filters is characterised by the external and inter-resonator couplings. Chapter 2 also describes the theory related to the external and inter-resonator couplings, showing the derivation and extraction of external quality factors and inter-resonator coupling coefficients from coupled circuits. Brief descriptions of the simulation and modelling techniques involved in this research are then given in this chapter. Next, it discusses the measurements associated with microwave filters. The extractions of parameters from the measured frequency response are given. In the last section of Chapter 2, the theoretical approaches of approximating the power handling capability of filters are reviewed.

Chapter 3 demonstrates a synthesis method for dual-band bandpass filter design. A frequency transformation technique [9, 10] that generates a symmetric dual-passband filter response from a normalised low pass prototype response is presented. The synthesis of coupling matrices from the frequency response is then reviewed. The synthesised coupling matrices provide a direct synthesis of narrowband filters. Next, the general design procedures of the dual-passband response synthesis method are described. Chapter 3 reviews the transfer function of a filter and relates it to the network parameters. The synthesis procedures of coupling matrix from the frequency response and network parameters are reviewed for symmetric [12, 13] and asymmetric frequency responses [14]. It is necessary to simplify the coupling matrix resulted from those synthesis procedures for practical filter design. A general coupling matrix reduction method proposed in [14] is provided. However, these synthesis and reduction methods of coupling matrix are applicable to certain filter topologies with limited orders. A coupling matrix reduction technique based on the Newton-Raphson method [19] is then introduced to synthesise coupling matrices for selected filter orders and topologies. The chapter then describes the characterisation of microstrip square open-loop resonator and $TE_{01\delta}$ mode quarter

cylindrical dielectric resonator along with the characterisation of external and inter-resonator coupling for those two resonator types, based on simulation studies and measurements of fabricated components. These two types of resonator were then used for the realisation of dual-band bandpass filters. The simulated and measured frequency responses of the filters are then shown and analysed. The effect of finite unloaded quality factor on filter response is also investigated and given in this chapter. Finally, the limitations of the above mentioned method in realisation of dual-band bandpass filters and the suggestions for further work are given.

Chapter 4 presents two types of dual-band resonator for the implementation of dual-band bandpass filters: stepped impedance resonator and non-uniform pitch helical resonator. The dual-band characteristics of a stripline SIR and a quarter-wavelength coaxial SIR are reviewed. The characterisation of coaxial SIR, the external and inter-resonator couplings are given and used for a second order dual-band bandpass filter. This chapter then presents non-uniform pitch helical resonator structure for dual-band bandpass filter design. Two non-uniform pitch helical resonator structures have been discussed and analysed in this chapter, categorised as Category I and II non-uniform pitch helical resonators, in terms of pitch modification. Category I non-uniform pitch helical resonator has equal number of turns for the top and the bottom sections, therefore, the pitch is modified by the height of each section. Category II non-uniform pitch helical resonator has equal height for the top and the bottom sections, but different number of turns for the top and the bottom sections to modify its pitch. Two models used to analyse non-uniform pitch helical resonators are then described: the SIR model and the circuit model. A set of design curves that can accurately show the frequency ratios of the proposed non-uniform pitch helical resonator structures is produced by developing the theoretical models and simulations. The general design procedures of non-uniform pitch helical resonator is then described. Experimented results are provided in the following section to verify the analysis and simulation of non-uniform pitch helical resonators. In addition, this chapter includes the structures and topologies of external and inter-resonator couplings for filters using non-uniform pitch helical resonators. Three dual-band bandpass filters have been demonstrated to verify the dual-band capability of non-uniform pitch helical resonators on filter design. Finally, this chapter discusses and suggests further research on SIR and non-uniform pitch helical resonator, including the dielectric loaded resonators, possible tri-band applications, advanced fabrication techniques, and modified structures.

The technical content of the thesis ends with Chapter 5, stating the achievements of the research and drawing conclusions of the research presented in the thesis.

Chapter 2: Concepts, theories and tools for microwave filter design

2.1 Introduction

This chapter provides essential background knowledge for microwave filter design. This chapter should enable understanding of the fundamentals of microwave dual-band bandpass filter design. Firstly, it introduces the general design process of microwave filter. Secondly, the definition of Q factors and several basic types of resonators are described. Methods to characterise the external and inter-resonator couplings in coupled resonator circuits are then presented. Next, the simulation and modelling techniques that are employed in the research program are introduced. In addition, the measurements associated with designed microwave filters are discussed. Finally, a method to estimate the power handling capability of filters is reviewed.

The design process is basis for microwave filter design. Section 2.2 introduces a typical design process of microwave filter, which includes four steps: specification, approximation, synthesis, and realisation. Section 2.3 reviews the Q factor of a resonator as a narrowband filter has specific requirements for the unloaded Q factor of the employed resonators. Since resonators work as the key elements in microwave filter design, Section 2.3 also presents various types of resonator that involved in this research, including the lumped element circuits, the transmission line resonators, dielectric resonators, and helical resonators. Their basic structures, advantages and disadvantages, and characteristic design equations are introduced.

The synthesis process of the microwave bandpass filters is based on coupled resonator circuits [2]. Therefore, the external coupling between resonator and input/output, and the coupling between resonators require characterisation for filter design. Section 2.4 describes the general theory of coupling between any coupled elements. The methods to derive the external quality factor and inter-resonator coupling coefficients in the equivalent lumped element circuits are demonstrated in this section.

Computer tools are required for complex mathematical computation of filter parameters and visualisation of analytical filter characteristics. The development of commercial software has also made it possible to synthesise, construct, and analyse the circuits and physical structures of filters. In addition, the simulation tools are able to provide and visualise the analytical

solutions and characteristics of the designed structures. Matrix Laboratory (MATLAB), Keysight Advanced Design System (Keysight ADS) and CST Microwave Studio (CST MW) have been used in this research program, as introduced in Section 2.5.

The designed resonators, couplings and filters require evaluation by measurements. The measured frequency responses provide the evaluation on frequency characteristics, allowing the extractions of the evaluation parameters, such as the resonant frequencies, unloaded Q factors, external Q factors, and inter-resonator coupling coefficients, as described in Section 2.6.

The evaluation of filters also includes power handling capability and temperature stability. However, they are not as significant as the frequency characteristics for the research presented in this thesis. Section 2.7 reviews a method to estimate the peak breakdown power of a microwave filter by analysing the simulated electric fields and group delays of the filter. The estimated breakdown power may not be an accurate approximation, but still help engineers to understand the power handling capability of the designed filter.

2.2 Design process of microwave filter

The general design process of microwave filter starts with a set of specifications and completes with the implementation of a prototype filter [28]. The microwave filter design process can be summarised in four general steps: specification, approximation, synthesis, and realisation. The design specifications of the filter list the requirement that needs to be accomplished. The approximation step generates a mathematical transfer function of the filter that satisfies the design specifications. The synthesis step converts the transfer function into a network that consists of filter elements and elemental interconnections. Many synthesis methods that relate the transfer function to network parameters and element values for filter design have been proposed in the past decades [2, 3, 12-14, 29-31]. During the approximation and synthesis step, there are assumptions made to ease analysis, such as linear lossless elements, infinite unloaded Q factors, and frequency invariant parameters. In practice, however, these assumptions may be less accurate under certain conditions, leading to the limitations of approximation and synthesis. The effect of the limitations on the filter response has to be studied and analysed before realisation. The realisation step of a prototype filter involves the modelling, simulation, fabrication and measurement of the filter. There are decisions to be made in this process, including types of components and packaging, filter dimensions, methods for manufacture, testing and tuning of the filter.

2.3 Resonators

Resonators, also called resonating circuits, are important components in RF and microwave filters, oscillators, amplifiers, and tuners [32]. Fields inside a resonator store energy at the resonant frequency where equal storage of electric and magnetic energies occurs [32]. The input impedance at resonance is purely real since the reactance is cancelled out due to the equally stored electric and magnetic energies [33]. The Q factor is an important figure of merit for a resonator. It relates the electromagnetic energy storage capacity of a resonator with the thermal energy dissipation [3, 32]. The definitions of Q factors are described in Section 2.3.1.

The resonators are generally categorised as lumped elements and distributed elements. The lumped elements are combinations of resistor, inductor and capacitor, which have no physical dimensions related to the wavelength of the operating frequency [3]. Section 2.3.2 introduces the typical lumped element circuits and their characteristics. In the microwave spectrum, the lumped elements suffer from their dimensions which become long compared to the wavelength [3] whereas the distributed elements have one or more dimensions comparable and related to the wavelength of the operating frequency. Consequently, the distributed elements may provide more compact size than the lumped elements at microwave or higher frequencies in interest. The distributed elements have inductance, capacitance, and resistance that cannot be isolated into separate lumped inductors, capacitors, or resistors. They can be categorised by the structure as coaxial lines, strip lines, waveguides, dielectric resonators, and helical resonators. The general structures of coaxial resonator, microstrip resonator, dielectric resonator and helical resonator which are modified and employed in the filter designs in this thesis are presented in Section 2.3.3 – 2.3.5.

2.3.1 Q factor

The unloaded Q factor of a resonator is defined by (2.1), as the ratio of energy stored in the resonator to the energy dissipated per cycle [3, 32].

$$Q_0 = 2\pi \cdot \frac{\text{Maximum energy stored in a cycle of the resonator}}{\text{Energy dissipated per cycle of the resonator}}. \quad (2.1)$$

There is a loss introduced when power is delivered from resonator to external circuit or vice versa, resulting in the external quality factor (Q_e). The external quality factor characterises the ratio of energy stored in the resonator to the energy dissipated in external circuit per cycle [3,

32], introduced in Section 2.3.3. The external circuit is a load to the resonator, resulting in slightly different resonant frequency of the resonator. The loaded quality factor (Q_L) of a resonator has the following relationship with the unloaded Q factor and the external quality factor of the resonator [34]:

$$\frac{1}{Q_L} = \frac{1}{Q_0} + \frac{1}{Q_e}. \quad (2.2)$$

Equation (2.2) shows that the unloaded Q factor is higher than the loaded Q factor of a resonator. There is also an equivalent definition of loaded Q factor, expressed by [3, 32]

$$Q_L = \frac{f}{BW} \quad (2.3)$$

where f and BW represents the resonant frequency and 3-dB bandwidth of the resonator.

The expression (2.3) is used to extract the loaded Q factor from the frequency response of resonator or filter. Therefore, the filter response has a requirement for the unloaded Q factor of resonator. The unloaded Q factor is used to evaluate the capability of resonator in bandpass filter design. In Chapter 3, the unloaded Q factor of resonator and the loaded Q factor extracted from filter response for narrowband bandpass filter design will be discussed.

2.3.2 Lumped element circuits

A lumped element circuit usually refers to the RLC circuit, consisting of inductors represented by L , capacitors represented by C , and resistors represented by R . The resonance of a RLC circuit occurs when the inductive and capacitive reactances are equal in magnitude but cancel each other due to the 180 degrees phase difference [33]. When the circuit is at its resonant frequencies, the combined imaginary component of its impedance is zero, and only the resistive component is observed.

The circuit elements, R , L and C , can be combined in a number of topologies, such as parallel RLC circuit and series RLC circuit, which are shown in Figure 2.1.

For the parallel RLC circuit, the input impedance is [32]

$$Z_{in} = \left(\frac{1}{R} + \frac{1}{j\omega L} + j\omega C \right)^{-1}. \quad (2.4)$$

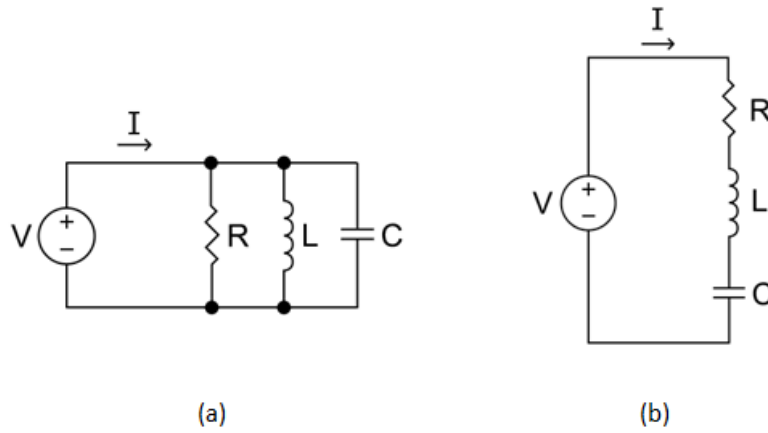


Figure 2.1 RLC resonant circuits. (a) Parallel RLC circuit. (b) Series RLC circuit.

The resonance occurs when the reactance is zero, thus $Z_{in} = R$. The fundamental angular resonant frequency ω_0 is [32]

$$\omega_0 = \frac{1}{\sqrt{LC}}. \quad (2.5)$$

The unloaded Q factor of this parallel resonant circuit is [32]

$$Q_0 = \frac{R}{\omega_0 L} = \omega_0 RC. \quad (2.6)$$

For the series RLC circuit, the input impedance is [32]

$$Z_{in} = R + j\omega L + \frac{1}{j\omega C}. \quad (2.7)$$

The resonance occurs when the reactance is zero, thus $Z_{in} = R$. The fundamental angular resonant frequency ω_0 is [32]

$$\omega_0 = \frac{1}{\sqrt{LC}}. \quad (2.8)$$

The unloaded Q factor of this series resonant circuit is [32]

$$Q_0 = \frac{\omega_0 L}{R} = \frac{1}{\omega_0 RC}. \quad (2.9)$$

Lumped elements are often used for wideband filters because of the limited quality factor [33]. When operating in low frequencies, they have very compact size but relatively low power handling capability, compared to the distributed elements [32]. However, as mentioned earlier, the lumped elements may not be as compact as distributed elements when operating in the microwave spectrum [3]. The lumped element circuit is also used as the equivalent circuit of the distributed elements for design analysis and simulation.

2.3.3 Transmission line resonators

In addition to the lumped element circuit, a section of a transmission line can also function as a resonator. The resonating mode of the transmission line resonators is transverse electromagnetic (TEM) mode or quasi-TEM mode [1]. The inductance and the capacitance of a transmission line are distributed along the length of the line [32]. The transmission line resonators introduced in this section include coaxial and microstrip resonators. They operate over a wide frequency range starting at 100 MHz extending to around 100 GHz, as the most common choice for microwave filters in wireless communication systems [1].

Coaxial resonator

The coaxial resonator is formed by an outer conductor, known as cavity, and an inner conductor. The area between the outer and inner conductors can be filled with a high dielectric constant (ϵ_r) material to reduce the overall size of the coaxial resonator if required. Additionally, the inner conductor can be a metal tube filled with vacuum or air to reduce the weight of the resonator. Figure 2.2 shows a typical structure of a coaxial resonator.

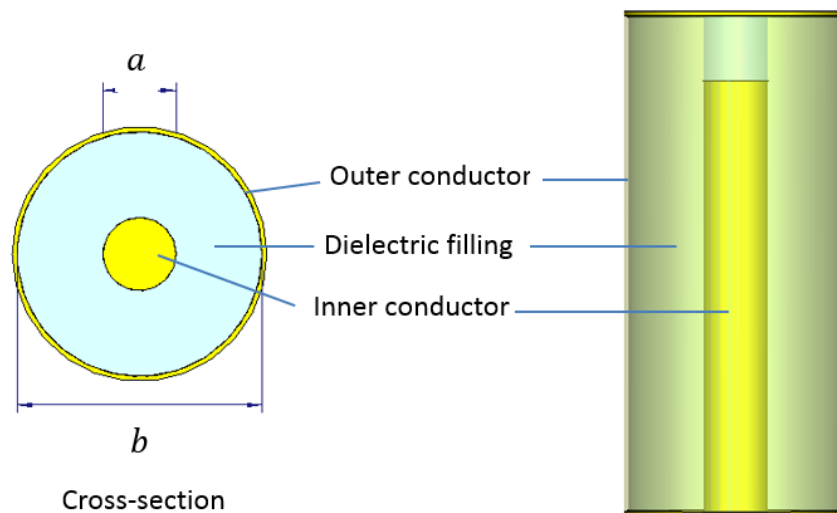


Figure 2.2 A general coaxial resonator structure.

The fundamental resonant mode of an infinite long coaxial resonator is pure TEM since the electric fields and magnetic fields of the resonator have no component in the wave propagation direction. There are two common types of coaxial resonator: quarter-wavelength ($\lambda/4$) type and half-wavelength ($\lambda/2$) type. The $\lambda/4$ type coaxial resonator has one end short-circuited to the cavity while the other end is open-circuited. The $\lambda/2$ type coaxial resonator has both ends open-circuited. The open-circuited ends have fringing effects, causing the resonant modes to not be pure TEM mode. However, neglecting the fringing effects, the dominant mode behaves like TEM mode, called quasi-TEM mode. The discontinuities in coaxial resonator must be taken into consideration in the designs. The empirical results suggest that the resonator length should be designed approximately 6% shorter in order to cancel the discontinuities [1].

A coaxial resonator has a simple 3D structure. Although large in size, the coaxial resonator has higher Q factor and higher power handling capability than planar structures such as microstrip resonators, surface acoustic wave (SAW) resonators and coplanar waveguide (CPW) resonators. Additionally, it has larger size and limited Q factor in comparison to waveguide or dielectric resonators. Since the coaxial resonator offers the lowest cost design among other types of resonator, they are widely employed, particularly in wideband RF/microwave applications [35].

Microstrip resonator

Microstrip is a planar type of transmission lines that has a conducting strip (microstrip line) with a width W and a thickness (t) on the top of the dielectric substrate with a relative dielectric constant (ϵ_r) and a thickness (h) where there is a ground plane (conduction surface) at the bottom, as Figure 2.3 illustrates [2].

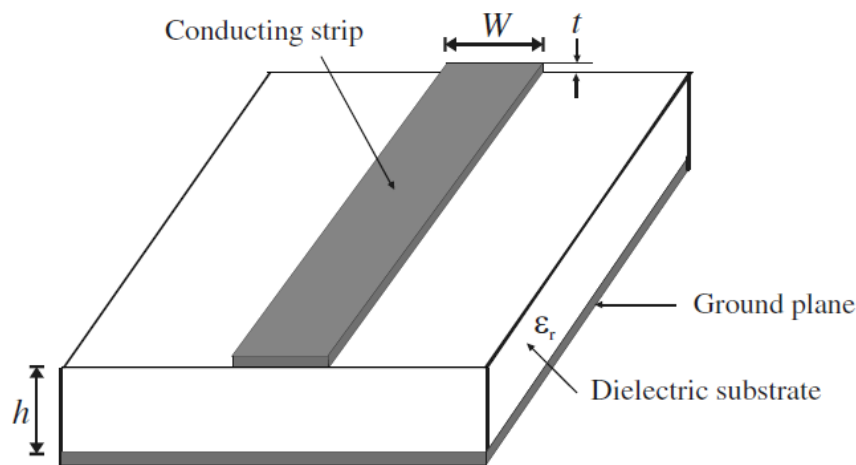


Figure 2.3 General microstrip structure [2].

Microstrip does not support the pure TEM mode due to the inhomogeneity. This is because the fields in the microstrip extend within the air above and dielectric below. At non-zero frequencies, there are longitudinal components besides of the transverse components for both the electric field and magnetic field. However, the longitudinal components are much smaller than the transverse components. Neglecting the longitudinal components, the dominant mode behaves like TEM mode, which refers to the quasi-TEM mode [2, 36].

Hammerstad [37] derived the effective dielectric constant ϵ_{re} and characteristic impedance Z_c for microstrip line with very thin conductors, expressed as follows.

For $W/h \leq 1$:

$$\epsilon_{re} = \frac{\epsilon_r + 1}{2} + \frac{\epsilon_r - 1}{2} \left\{ \left(1 + \frac{12h}{W} \right)^{-0.5} + 0.04 \left(1 - \frac{W}{h} \right)^2 \right\} \quad (2.10)$$

$$Z_c = \frac{\eta}{2\pi\sqrt{\epsilon_{re}}} \ln \left(\frac{8h}{W} + \frac{W}{4h} \right). \quad (2.11)$$

For $W/h \geq 1$:

$$\epsilon_{re} = \frac{\epsilon_r + 1}{2} + \frac{\epsilon_r - 1}{2} \left(1 + \frac{12h}{W} \right)^{-0.5} \quad (2.12)$$

$$Z_c = \frac{\eta}{\sqrt{\epsilon_{re}}} \left\{ \frac{W}{h} + 1.393 + 0.677 \cdot \ln \left(\frac{W}{h} + 1.444 \right) \right\}^{-1} \quad (2.13)$$

where ϵ_r is the dielectric constant of substrate, h is the height of substrate, W is the width of microstrip line, and η is the wave impedance in free space that is $\eta = 120\pi$ Ohms, respectively.

The guided wavelength of the quasi-TEM mode of microstrip is given by [2]

$$\lambda_g = \frac{\lambda_0}{\sqrt{\epsilon_{re}}} \quad (2.14)$$

where λ_0 is the free space wavelength at operating frequency f .

For a given physical length of l , the electrical length θ is defined as [2]

$$\theta = \beta \cdot l \quad (2.15)$$

where β is the propagation constant and $\beta = 2\pi/\lambda_g$.

Most microstrip circuit applications require a metallic enclosure in case of radiation loss and electromagnetic interference [2]. The presence of conducting top and side walls lowers both the effective dielectric constant and the characteristic impedance [38]. Garg et al. [39] gave the formulae to predict the effects of a microstrip shield with a conducting top cover alone. Hong and Lancaster [2] also suggested a rule of thumb to reduce the enclosure effect in filter design which requires the height up to the cover more than eight times the substrate thickness and the distance to side walls at least five times more than the substrate thickness.

Discontinuities exist in all practical distributed circuits. Although the discontinuities in microstrip lead to very small capacitances and inductances, the reactance can become significant at high microwave and millimetre-wave frequencies [38]. When the frequency is below 2 GHz, the effects of discontinuities are often neglected [38]. Microstrip discontinuities in filter design include steps, open-ends, bends, gaps, and junctions. The effects of discontinuities can be modelled and taken into account in the filter designs with full-wave EM simulations [2].

Microstrip resonators have valuable features: a simple structure, a very compact size, and the capability of wide applications. Moreover, they can be easily integrated with other active circuits [1], such as monolithic microwave integrated circuit (MMIC), since they are manufactured of metalized films on dielectric substrate. Microstrip losses include conductor loss, dielectric loss, and radiation loss [36]. These losses affect the performance of microstrip and lead to a lower unloaded Q factor thus high insertion loss when compared to non-planar structures such as coaxial, waveguide, dielectric, and helical resonators. In addition, the power handling capability of microstrip resonators is relatively small. The dielectric resonator has the advantages of compact size, very high unloaded Q factor, high temperature stability, and high power handling capability [40], as demonstrated below.

2.3.4 Dielectric resonator

The dielectric resonator is a dielectric block mounted inside a cavity [32, 35]. The fundamental shape of a dielectric resonator is a short solid cylinder [32], but there are also modified shapes, including tubular [41], spherical, cross-shaped [42], Y-shape [43]. Dielectric resonators (DRs) have been used to replace coaxial and waveguide resonators in RF and microwave circuits since the 1970s when the first low loss, temperature stable, high dielectric constant dielectric material was developed [44]. Since then, many new and improved materials that exhibit a wide range of dielectric constant, extremely low loss, and excellent temperature stability have been

developed. High Q factor dielectric materials with the dielectric constant ranging from 20–90 and a temperature drift ranging from -6 to $+6$ ppm/ $^{\circ}\text{C}$ are now commercially available from various manufacturers [35]. Typical applications for the dielectric resonators include microwave oscillators, filters, and antennas in base stations, satellite communication receivers, and Global Positioning Systems (GPS).

One significant advantage of using dielectric resonator is that the high dielectric material offers size reduction of the component [44] since the guided wavelength (λ_g) is reduced, the square root of the relative dielectric constant (ϵ_r), expressed by

$$\lambda_g = \frac{\lambda_0}{\sqrt{\epsilon_r}} \quad (2.16)$$

where λ_0 is the free space wavelength at the operating frequency f .

The resonant modes of dielectric resonators can be categorised as transverse electric (TE) modes, transverse magnetic (TM) modes, and hybrid electromagnetic (HEM) modes. $\text{TE}_{01\delta}$ is a commonly resonant mode in an isolated cylindrical DR, originally described by Cohn [45]. Although the geometrical form of a DR is simple, the exact solutions of the Maxwell equations are very complex. Consequently, the exact resonant frequency of a mode can only be computed by complicated numerical procedures [32]. With the development of simulation tools in recent years, the resonant frequencies and field patterns of a DR can be easily obtained.

Kajfez and Guillon provide an approximate estimation of the $\text{TE}_{01\delta}$ mode resonant frequency of an isolated DR, shown in (2.17), which is accurate to about 2% in the range $0.5 < a/L < 2$ and $30 < \epsilon_r < 50$ [32].

$$f = \frac{34}{a \sqrt{\epsilon_r}} \left(\frac{a}{L} + 3.45 \right) \quad (2.17)$$

where f is the frequency in gigahertz, a and L are the radius and height of the DR in millimetres, and ϵ_r is the relative dielectric constant, respectively.

Figure 2.4 shows the $\text{TE}_{01\delta}$ mode field patterns of an isolated DR in a cavity. In practice, the $\text{TE}_{01\delta}$ mode DR is held by a supporting structure of low loss, low dielectric constant inside a metallic cavity [3]. Figure 2.5 shows the practical structure and parameters of a $\text{TE}_{01\delta}$ mode cylindrical DR.

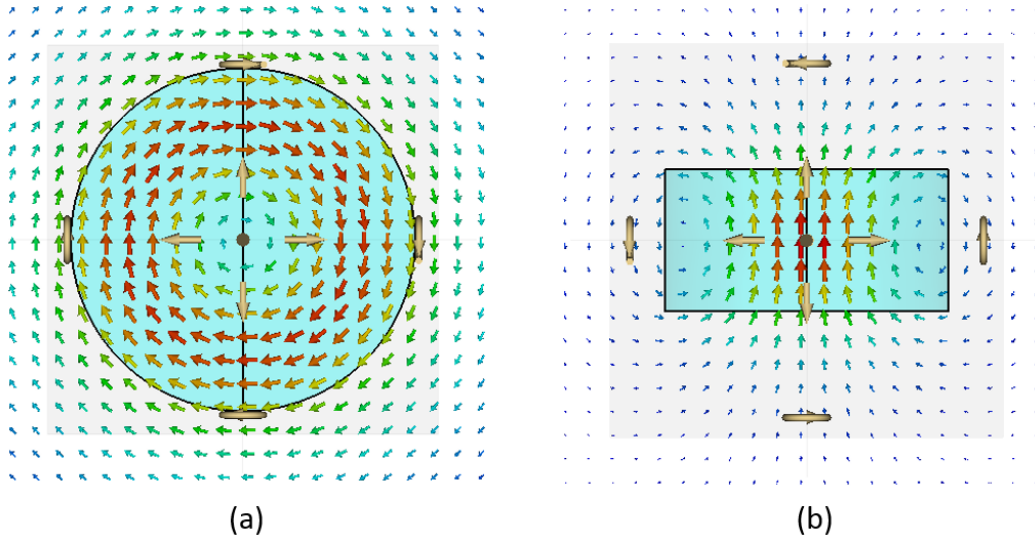


Figure 2.4 TE_{018} mode field patterns of an isolated cylindrical DR. (a) E-field in the equatorial plane (b) H-field in the meridian plane.

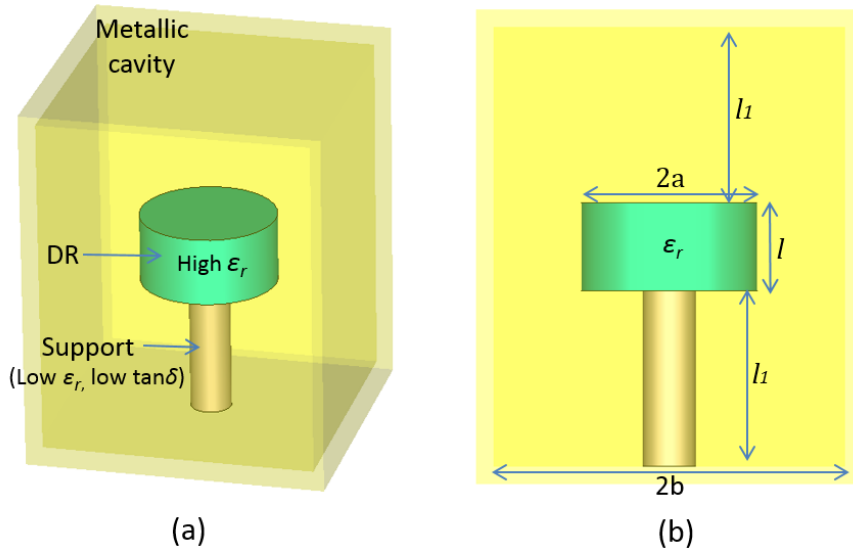


Figure 2.5 Practical TE_{018} mode DR structure and parameters. (a) 3D. (b) Cross-section.

The TE_{018} mode is the fundamental resonant mode of such a DR. Therefore, employing TE_{018} mode of the resonator gives the most compact size in comparison with employing other modes of the DR. Additionally, there is no spurious performance issue at lower frequencies when using TE_{018} mode. The spurious performance of this resonator at higher frequencies is affected by TM modes, HEM modes, and higher order TE modes.

Hunter [3] suggests that introducing a hole in the centre of the DR, forming it into a ring [46], improves the spurious performance. This is because the TE_{018} mode has zero electric field in the centre of the resonator while other modes have finite electric field there. Since the DR stores more electric energy rather than magnetic, removing the regions where the electric field

of a particular mode is strong will increase the resonant frequency of that mode [3]. Hunter has also shown an example that improves the frequency ratio of the fundamental mode and the first spurious mode from 1.303 to 1.508 with a proper diameter of the hole [3]. This method is also applicable to other spurious mode suppressions by introducing slots or holes into the DR [24, 25, 47, 48]. Moraes et al. [48] proposed an alternative efficient way for undesirable mode suppression by analysing the energy density of the DR. For example, if the most of energy stored by the DR is magnetic at the operating mode, removing the area of the DR that has weak magnetic energy density in the operating mode but high magnetic energy density in spurious mode will increase all the resonant frequencies. However, there will be a slight frequency increase of the operating mode but significantly frequency increase of the spurious mode, thus the frequency ratio will be increased, i.e. the spurious performance will be improved.

It is demonstrated that the dielectric filters operating TE_{01} mode are the ideal choice for high power applications [35]. However, not only the resonators themselves, but also the support and adhesive material have significant influence in high power dielectric filter designs. Compared to TE and HEM modes dielectric filters, the ones operating in TM modes have the advantage that the heat generated inside the DRs can be directly transferred to the metallic cavity since no support is required [32]. Additionally, the TM mode DR has the advantage of compact size but lower unloaded Q factor, compared to the TE and HEM mode DR.

DR can be modified so that several resonant modes are merged into one resonant frequency. This type of DR that utilises the degeneracy of modes at one resonant frequency is called a multi-mode DR [49]. It is electrically equivalent to multiple single-mode resonators working at the same frequency. Therefore, the size of filter can be reduced by using multi-mode DRs, in comparison with that using single-mode DRs. Mansour [35] pointed out that dual-mode DR filters offer roughly 30% volume saving in comparison with single-mode dielectric resonator filters.

The high dielectric constant of the material confines most of the electromagnetic energy within the DR, which virtually eliminates radiation losses [3, 44]. Since modern dielectric materials have very low intrinsic losses, the DR could have extremely high unloaded Q factor which reduces power drain and heat build-up while improves the insertion loss, filter selectivity, and spurious performance [44].

Generally, the DRs are not suitable for wideband applications because of their very high unloaded Q factors and their poor spurious performance. Nevertheless, there are configurations

offering a compromise filter design by simultaneously using coaxial resonators and DRs [50]. It offers high Q but smaller size in comparison with the design using only coaxial resonators. Compared to the filter designs using DRs only, this filter is capable realising wide passband with reasonably good Q factor. Moreover, the overall temperature drift of the dielectric filter can be reduced to 1 ppm/°C with the proper choice of dielectric material [35]. DRs are also compatible with microstrips and MMICs because they can easily be mounted on planar substrates [46]. The DRs used to be costly, however, the cost has been decreasing since the 1980s. Since 2000, the increasing demand for DRs has further reduced the cost of them. This has enhanced the advantages of DRs, thus the DRs are expected to have a significant share and growth in resonator market [35].

Compared to microstrip, coaxial, and dielectric resonators, helical resonators provide a balanced solution for resonators that require compact size, relatively high unloaded Q factor, relatively high power handling capability, and low cost. The next section introduces traditional helical resonators.

2.3.5 Helical resonator

Helical resonators are slow-wave structures that have been studied since 1950s and are widely used in RF and microwave components for VHF/UHF applications such as microcell and picocell base stations, vehicular transceivers, and satellite transceivers [51, 52]. Zverev and Blinichikoff [52] gave an example of the spacing save characteristic of helical resonator, stating that a coaxial resonator with an unloaded Q of 550 at 54 MHz would be 1.37 m long by 1.78 cm in diameter, whereas the same quality helical resonator would be just 3.8 cm long (coil height) and 5.1 cm in diameter. The coaxial resonator and dielectric resonator generally have a much higher unloaded Q-factor than helical resonator, however, helical resonator still provides a sufficiently high Q factor (>500) for most narrow-band filters [53]. Compared to the microstrip resonator, helical resonator has the advantages of higher Q factor and higher power handling capability. Overall, helical resonators benefit from compact size, relatively high Q factor, relatively high power handling capability, and low cost [53].

The traditional helical resonator consists of a single-layer uniform pitch coil enclosed in a conductive cavity [52]. Figure 2.6 shows an example of a typical helical resonator with uniform pitch. One end of the coil is short-circuited (connected to the cavity) while the other end is left open. The cavity usually has a circular or square cross-section. The coil and cavity are usually made of good conductive material to reduce losses and maximise the Q factor [53].

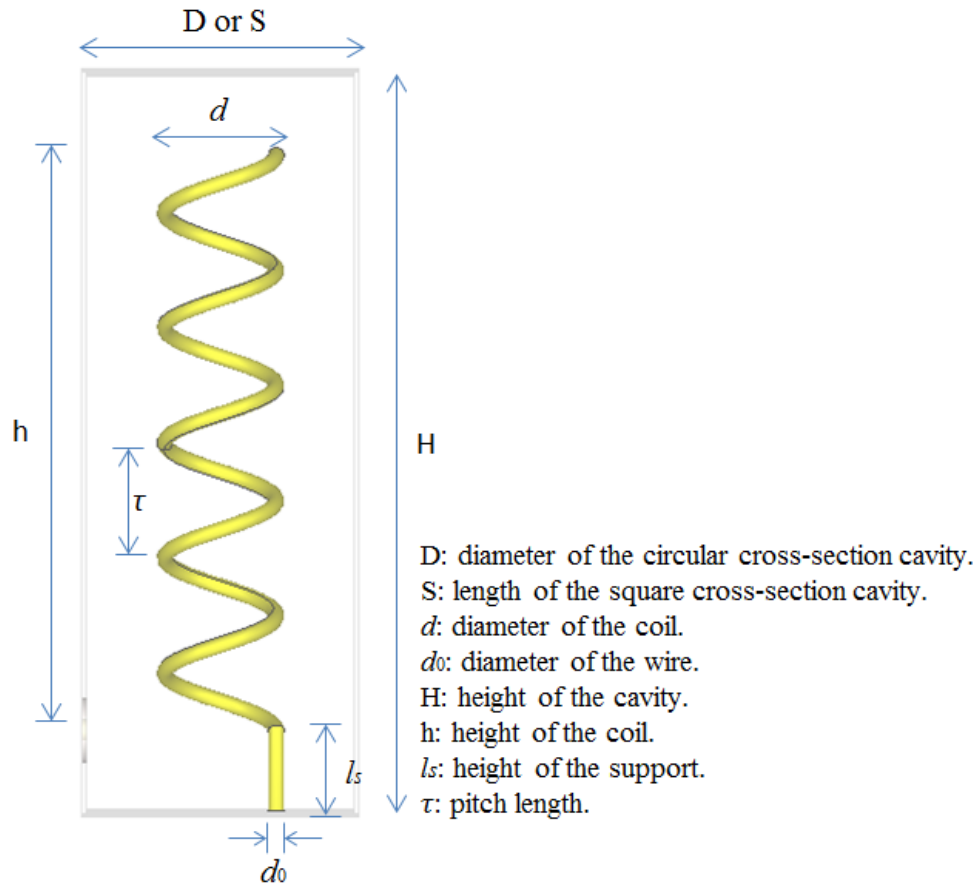


Figure 2.6 A typical uniform pitch helical resonator.

There have been a number of models analysing the fields within a uniform pitch helical resonator. Most of the analytical equations of helical resonator are obtained from the classic models: the sheath helix model, the tape helix model, and the transmission line model. These models are introduced in this section as follows.

Sheath helix model

The sheath helix model consists of an infinitely thin, conducting cylindrical sheath which supports a helical current in a circular cavity [53, 54], shown in Figure 2.7. Miley and Beyer [55] applied the boundary conditions at the sheath and the cavity of a tightly wound coil ($\tau \leq \lambda/2$, where τ is turn space and λ is the wavelength at resonant frequency).

By solving the Maxwell's equations at low frequencies, the field components in the cylindrical coordinate were obtained. The filled dielectric was assumed the same for both inside and outside of the coil. Miley and Beyer assumed that the axial field components are small enough to neglect, implying that the propagation along the helix is a quasi-TEM mode.

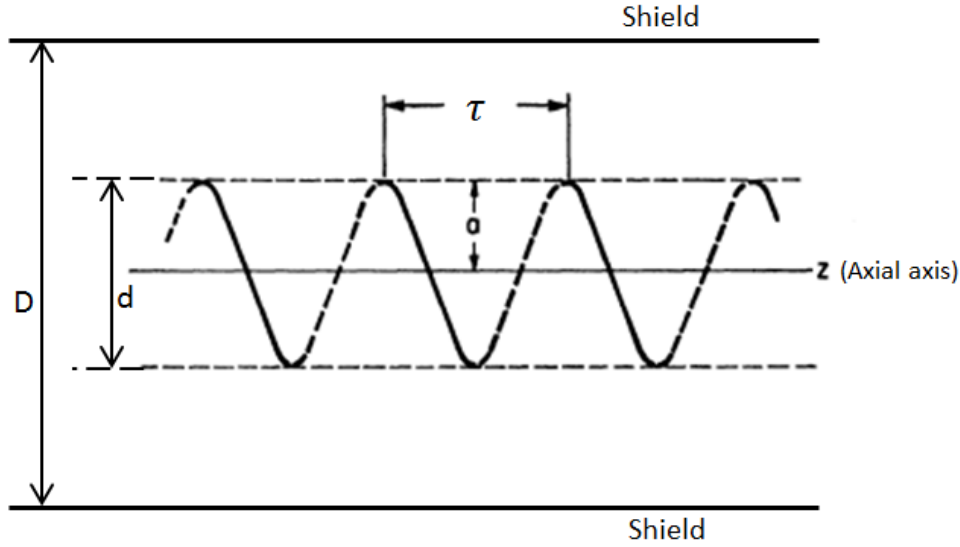


Figure 2.7 Sheath model of helix.

Thus the approximation of characteristic impedance is [55]

$$Z_0 = 201 \frac{\sqrt{\mu_r}}{\sqrt{\epsilon_r}} \cdot n_t d \sqrt{\left(1 - \frac{d^2}{D^2}\right) \cdot \log_{10} \left(\frac{D}{d}\right)} \text{ ohms} \quad (2.18)$$

where μ_r is the relative permeability, ϵ_r is the relative dielectric constant, n_t is the number of turns per centimetre, d is the mean diameter of the coil in centimetres, and D is the inner diameter of the cavity in centimetres.

It is noted that the propagation along the helix is not a TEM mode as the case of $\lambda/4$ type coaxial resonator [53]. The above expression of the characteristic impedance is just an approximation. Additionally, the sheath model is not applicable to helix with large pitch that the axial displacement current is not negligible [53]. Sensiper [54] provides more general forms of using sheath model, considering the range of pitch angles (from 0 degree to 90 degrees). The fields of helix in higher order modes are analytically derived in [56].

Tape helix model

The tape helix is a helix wound of a wire that is assumed as a perfect conductor with finite axial extension only, shown in Figure 2.8 [53, 54]. Applying the necessary boundary conditions at the tape, the Maxwell's equations are solved to obtain the fields. Such analysis and results have been obtained in complex forms [54, 57] involving Bessel functions, which are not convenient for design and analysis purposes.

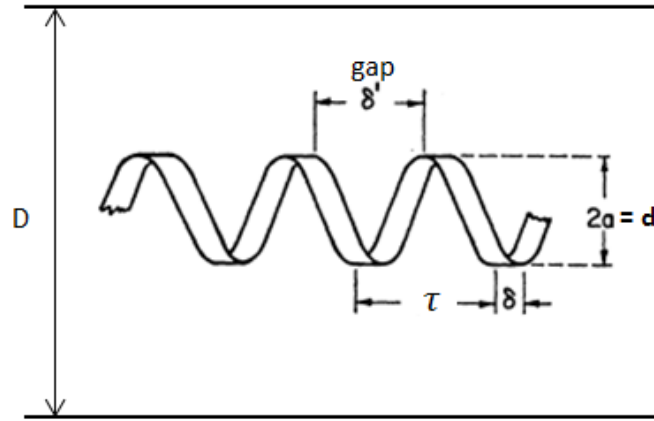


Figure 2.8 Tape helix model.

Transmission line model of helix

Unlike the sheath and tape model of helix, the transmission line model of helix does not supply any accurate field solutions. However, it provides computationally simple equations for practical resonator design. This model assumes that the helix has a uniformly distributed inductance, capacitance and resistance [58]. The resistance is considered to be so low that it does not affect the resonant frequency or the distribution of current and voltage [58].

Figure 2.9 shows the equivalent circuit of the transmission line model of helix. The helix has a length l , $x=0$ end (AD) is the short-circuited end while $x=l$ (BC) is the open end, and CD is the ground plane of the circuit.

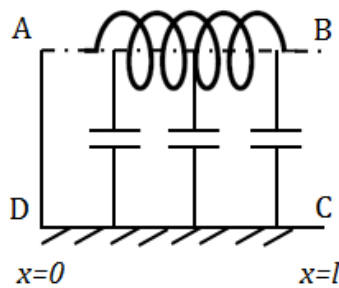


Figure 2.9 Transmission line model of helix.

The reactance of the wires is given as [59]

$$X = -\sqrt{\frac{L}{C}} \cot(\omega\sqrt{LC}) ; L = L_0 \cdot l \text{ and } C = C_0 \cdot l \quad (2.19)$$

where ω is the frequency in radian, L and C are the total inductance and capacitance realised

by these wires, L_0 and C_0 are the inductance and capacitance per unit length, respectively.

The resonance occurs when the reactance equals to zero. Therefore, the resonant frequencies are given by [58]

$$f = \frac{m}{4\sqrt{LC}} ; m = 1, 3, 5, \text{etc.} \quad (2.20)$$

In the case of air filling, the inductance per unit length of the helix is proposed by Macalpine and Schildknecht [60], derived from Nagaoka equation. The expression was modified to consider the cavity and the correction factor is set to unity since the helix is assumed having an infinite length, shown as

$$L_0 = 0.025 n_t^2 d^2 \left[1 - \left(\frac{d}{D} \right)^2 \right] \mu\text{H/axial inch.} \quad (2.21)$$

where d represents the coil diameter in inches, D represents the cavity diameters in inches, and n_t is the number of turns per axial inch, respectively.

The empirical value of capacitance per unit length (C_0) is then obtained from measurement as

$$C_0 = \frac{0.75}{\log_{10} \frac{D}{d}} \text{ pF/axial inch.} \quad (2.22)$$

The characteristic impedance of a helical resonator is expressed by [52, 60]

$$Z_0 = \sqrt{\frac{L_0}{C_0}} = 183 \cdot n_t d \sqrt{\left(1 - \frac{d^2}{D^2} \right) \cdot \log_{10} \left(\frac{D}{d} \right)} \text{ ohms.} \quad (2.23)$$

which gives 10% smaller impedance compared to the value predicted by (2.18).

Substitute (2.21) (2.22) into (2.20), the resonance frequencies of helical resonator are obtained.

$$f = 1826 \frac{m}{l \cdot n_t \cdot d} \sqrt{\frac{\log_{10} \frac{D}{d}}{1 - \left(\frac{d}{D} \right)^2}} \text{ MHz; } m = 1, 3, 5, \text{etc.} \quad (2.24)$$

Equation (2.24) shows that the resonance of a helix is related to four parameters which characterise the resonator: the diameter of the coil d , the diameter of the shield D , the axial

length of the coil l , and the number of turns per axial length n_t .

It is stated that the electrical length of a helix is 5 to 7 percent less than a quarter wavelength [52, 60]. Since the number of turns N equals to $l \cdot n_t$ for a uniform pitch helix, (2.24) can be written as:

$$f = \frac{1720 m}{N \cdot d} \sqrt{\frac{\log_{10} \frac{D}{d}}{1 - \left(\frac{d}{D}\right)^2}} \text{ MHz; } m = 1, 3, 5, \text{ etc.} \quad (2.25)$$

Neglecting the dielectric losses, the unloaded Q of a helical resonator is expressed as

$$Q_u = \frac{2\pi f L_0}{R_c + R_s} \quad (2.26)$$

where R_c is the resistance of the coil due to skin and proximity effect, and R_s is the resistance due to the currents in the shield.

The resistance R_c and R_s are given by [60]

$$R_c = \frac{0.083}{1000} \cdot \frac{\phi}{n_t d_0} \cdot n_t^2 \pi d \sqrt{f} \quad \Omega/\text{axial inch} \quad (2.27)$$

$$R_s = \frac{9.37 n_t^2 l^2 (d/2)^4 \sqrt{1.724 f}}{l \cdot [D^2(l+d)/8]^{4/3}} \cdot \sqrt{\frac{\rho_{\text{cavity}}}{\rho_{\text{coil}}}} \cdot 10^{-4} \quad \Omega/\text{axial inch} \quad (2.28)$$

where f is the resonant frequency in MHz, ϕ is the proximity factor, d_0 is the diameter of wire, ρ_{cavity} is the resistivity of the cavity material and ρ_{coil} is the resistivity of the coil material.

Estimating proximity factor and substituting (2.27) (2.28) into (2.26), two practical formula for a resonator with copper coil and cavity can be given as [60]

$$Q_0 = 220 \frac{\frac{d}{D} - \left(\frac{d}{D}\right)^3}{1.5 + \left(\frac{d}{D}\right)^3} D \sqrt{f} \quad (2.29)$$

$$Q_0 \approx 50 D \sqrt{f} \quad (2.30)$$

where D is the cylindrical cavity diameter in inches, f is the resonant frequency in MHz.

For $0.45 < d/D < 0.6$, $l/D > 1.0$, and $d_0 > 5\delta$ where δ is skin depth, the simplified formulae (2.29) (2.30) provide predictions within 10% difference from the actual value [60]. The Q values resulted from these formulae are 10% lower in comparison with the theoretical values, due to the imperfect surface conditions [60].

The validity of (2.21) - (2.30) has been verified for the following limits [52, 53]:

$$\begin{aligned}
1.0 &< l/d < 4.0 \\
0.45 &< d/D < 0.6 \\
0.4 &< \frac{d_0}{\tau} = d_0 \cdot n_t < 0.6 \quad \text{at} \quad \frac{l}{d} = 1.5 \\
0.5 &< \frac{d_0}{\tau} = d_0 \cdot n_t < 0.7 \quad \text{at} \quad \frac{l}{d} = 4.0 \\
\tau &< d/2 \\
d_0 &> 5\delta .
\end{aligned} \tag{2.31}$$

Although the validity of those equations is not only for the above limits, the accuracy of those equations suffers for the following cases: the pitch length (τ) is so small that the coil becomes more likely a coaxial resonator; or the pitch length is so large that the coil becomes a slightly twisted long wire. The accuracy of the equations has an impact on the design and analysis of helical resonators, especially for the non-uniform pitch helical resonators in Chapter 4.

The equivalence between circular and square cavity is shown as [52]

$$D = k \cdot S \tag{2.32}$$

where D is the diameter of cross-section of circular cavity, S is the cross-sectional length of square cavity, and k is a constant. Zverev and Blinichikoff [52] suggested that $k = 1.2$ while Spencer [53] suggested $k = 1.13$.

Equation (2.33) provides conservative Q values in comparison with those values shown by (2.30), since the values of k and the effect of imperfect fabrication processes are considered.

$$Q_0 \approx 50S\sqrt{f} \tag{2.33}$$

where S is in inches, f is in MHz.

Design equations

Based on the above equations, Macalpine and Schildknecht [60] have developed a set of equations and conditions for helical resonator design in a circular cross-section cavity. Zverev and Blinichikoff [52] provide an alternative set of equations and conditions for square cross-section cavity with the equivalence of cavities shown by (2.32). Using their design equations will lead to densely wound coils (i.e. the pitch lengths are small). Such coils could easily vibrate if the helix does not have a dielectric load as an inner support. Nevertheless, the dielectric load would cause more losses and decrease the resonant frequencies and unloaded Q values. An alternative way is to use thick wire to increase the resistivity against vibration, instead of the dielectric load. This also improves the unloaded Q factors, compared to the helical resonator with dielectric load. Additionally, a large pitch length but a small diameter will further improve the resistance to vibration when there is no dielectric inner support of the coil. However, the design equations for large pitch lengths helical resonators were not previously provided. In this section, a set of design equations are derived from empirical results obtained from CST MW simulation for the condition of large pitch lengths, followed by the procedures in [52, 60].

The design equations are given below:

$$\begin{aligned} S &= 2.4 d \approx \frac{Q_0}{50\sqrt{f}} \\ l_s &\approx 0.7 * d \\ N &\approx \frac{1282}{d \cdot f} - 1 \\ l &\approx 5 * d \\ \frac{N}{l} \cdot d_0 &\approx 0.15 \end{aligned} \tag{2.34}$$

where Q_0 is the expected unloaded Q of the fabricated resonator. S , D , d , l_s and l are in inches, and f is the fundamental resonant frequency in MHz.

It is noted that from (2.25) (2.32) and (2.33), N is derived as $1282/d$, which is 1 turn more than that given in (2.34). In addition, the length of coil is set as $5d$, higher than the range $1.5d - 4d$ in [52, 60]. These differences in the number of turns and lengths show that the coil designed by (2.34) has a larger pitch length than the ones designed in [52, 60]. The set of equations (2.34) gives a good approximation of the dimensions of helical resonators, however it is suggested to

use EM simulation tools (CST MW) to verify and optimise the dimensions to realise the specification of the resonators.

Design 1

A uniform pitch helical resonator that realises an unloaded Q of 860 at 668 MHz is designed. Substituting $Q_u=860$ and $f=668$ into (2.34), we got $S = 0.66$ inch, $d = 0.28$ inch, $l_s = 0.195$ inch, $l = 1.4$ inches, $d_0 = 0.036$ inch, $N = 6$ turns. Converting the length unit from inch to millimetre, $S = 16.8$ mm, $d = 7.0$ mm, $l_s = 5.0$ mm, $l = 36.0$ mm, $d_0 = 0.914$ mm.

A resonator with such dimensions is modelled and simulated in CST MWS. Figure 2.10 shows the resonator model. The Eigenmode solver was used for fast simulation and the results confirmed the unloaded Q and fundamental resonant frequency ($Q_0=862.5$ and $f=668.0$ MHz).

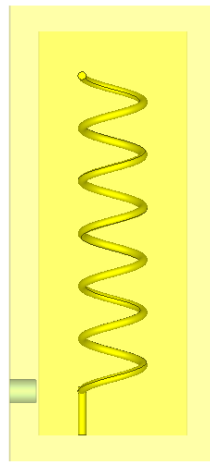


Figure 2.10 A helical resonator with 6 turns.

Design 2

Another example also confirms the validity of (2.34). The resonator is designed to realise an unloaded Q at least 900 at 738 MHz.

From (2.34) and 0.1 mm tolerance of fabrication, we can estimate the dimensions of the resonator as follows: $S = 17.5$ mm, $d = 7.3$ mm, $l_s = 5.0$ mm, $l = 36.0$ mm, $d_0 = 1.0$ mm, $N = 5$ turns. Simulating such a resonator, the results gives $Q_u=960$ at 738 MHz. A resonator was also fabricated and measured. Measured results show that the resonator has an unloaded Q of 660 at 684 MHz. The 10% difference in the resonant frequency was caused by the fabrication process, including coil former fabrication, the coil winding process, and the soldering to fix the coil in cavity. The measured value of unloaded Q factor is about 1/3 lower due to the smaller measured resonant frequency and the imperfect shielding of cavity, since the cavity lid was not

soldered onto the cavity body but attached using copper tape. This type of helical resonators that realised by sparsely wound coils will be used and modified in Chapter 4 to realise controllable dual-band characteristics.

2.4 Coupled resonator circuits

Coupled resonator circuits are significant for design of RF and microwave filters, in particular for the narrowband bandpass filters [2]. There is a general method for designing coupled resonator filters, which can be applied to any type of resonator despite the physical structure [2]. It has been applied to the design of waveguide filters [12], dielectric resonator filters [61], ceramic combline filters [62], microstrip filters [63, 64], superconducting filters [65]. This filter design method is based on the coupling coefficients of coupled resonators and the external quality factors of the input and output resonators [2].

This section describes the theory of coupling in order to establish the relationship between the coupling coefficient and the physical structure of the coupled circuits. Section 2.4.1 demonstrates the general coupling theory between any coupled elements. The general formulation for extracting the external quality factor of the externally loaded resonators and the inter-resonator coupling coefficients are derived in Section 2.4.2 and 2.4.3, respectively.

2.4.1 General coupling theory

The coupling coefficient of coupled elements can be defined on the basis of the ratio of coupled energy to stored energy [66] as the following formula demonstrates [2]

$$k = \frac{\iiint \varepsilon \underline{E}_1 \cdot \underline{E}_2 dv}{\sqrt{\iiint \varepsilon |\underline{E}_1|^2 dv \times \iiint \varepsilon |\underline{E}_2|^2 dv}} + \frac{\iiint \mu \underline{H}_1 \cdot \underline{H}_2 dv}{\sqrt{\iiint \mu |\underline{H}_1|^2 dv \times \iiint \mu |\underline{H}_2|^2 dv}} \quad (2.35)$$

where \underline{E} and \underline{H} represent the electric and magnetic field vectors of the coupled elements, respectively.

It is noted that the coupled elements can be different in structure and resonant frequencies. In addition, all the fields are determined at resonance, and the volume integrals are over all effected regions with permittivity of ε and permeability of μ . The first term on the right-hand side of (2.35) represents the electric coupling whereas the magnetic coupling is represented by the second term. The evaluation of the coupling coefficient from (2.35) requires the field distributions of the space integral. However, deriving the analytical solutions of the fields could

be difficult. It may be much easier to obtain the characteristic frequencies of frequency responses that are related to the coupling from full-wave EM simulation or measurement. The coupling coefficient can then be determined against the physical structure of coupled elements if the relationship between the coupling coefficient and the characteristic frequencies of the frequency responses relationship is established. In the following sections, the formulation of such relationships is derived. Although the following derivations are based on the equivalent circuit model of lumped element circuit, the outcomes are also valid for the coupled distributed elements on a narrow-band basis [2].

2.4.2 External coupling coefficient and external quality factor

The external coupling coefficient (κ) is defined as the ratio of power dissipated in the external circuit to the power dissipated in the resonator [34]. Therefore, it is the ratio of unloaded Q factor to the external Q factor of the resonator, expressed by [34]

$$\kappa = \frac{Q_0}{Q_e} \quad (2.36)$$

where the external quality factor represents the energy that is coupled to the load (resonant circuit) from the external source which is defined as [3]

$$Q_e = 2\pi \cdot \frac{\text{Maximum energy stored in a cycle of the resonator}}{\text{Energy dissipated per cycle of the external circuit}} \quad (2.37)$$

Hong and Lancaster [2] derived a formulation to extract the external quality factor from the S_{11} parameter of a singly loaded resonator. For a lossless LC resonator that is excited by a source i_s with an external conductance G , the equivalent circuit is shown in Figure 2.11.

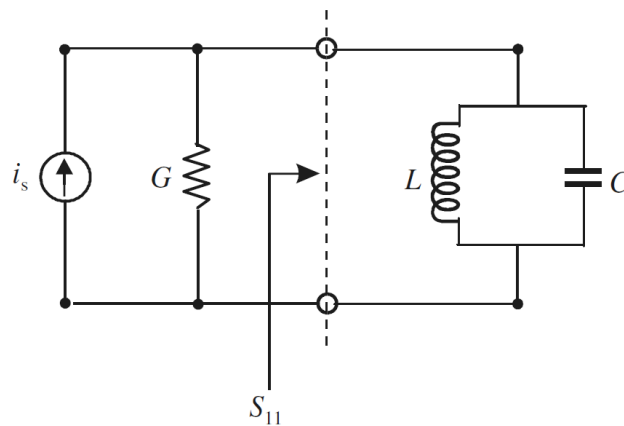


Figure 2.11 Equivalent circuit of the singly loaded resonator circuit [2].

Thus the reflection coefficient S_{11} is given by [2]

$$S_{11} = \frac{G - Y}{G + Y} = \frac{1 - Y/G}{1 + Y/G} \quad (2.38)$$

where

$$Y = j\omega C + \frac{1}{j\omega L} = j\omega_0 C \left(\frac{\omega}{\omega_0} - \frac{\omega_0}{\omega} \right) \quad (2.39)$$

where $\omega_0 = 1/\sqrt{LC}$ is the resonant frequency and Y is the admittance of the resonator.

In the vicinity of resonance, i.e. $\omega = \omega_0 + \Delta\omega$, the admittance Y can be simplified as [2]

$$Y \approx j\omega_0 C \cdot \frac{2\Delta\omega}{\omega_0}. \quad (2.40)$$

Substituting (2.40) and $Q_e = \omega_0 C/G$ into (2.38),

$$S_{11} = \frac{1 - jQ_e \cdot \frac{2\Delta\omega}{\omega_0}}{1 + jQ_e \cdot \frac{2\Delta\omega}{\omega_0}}. \quad (2.41)$$

The magnitude of S_{11} is approximately 1 near the resonant frequency since the resonator is assumed to be lossless, whereas the phase of S_{11} significantly changes against frequency. The external quality factor is extracted by [2]

$$Q_e = \frac{\omega_0}{\Delta\omega_{\pm 90^\circ}} \quad (2.42)$$

where $\Delta\omega_{\pm 90^\circ}$ represents the angular frequency difference when the phase of S_{11} is $\pm 90^\circ$ away from the phase of resonance.

2.4.3 Inter-resonator coupling coefficient

This section demonstrates three methods to derive the inter-resonator coupling coefficient from the coupled resonator circuit, which are the transmission coefficient method, the electric/magnetic wall method, and the impedance calculation method. The transmission coefficient method derives the coupling coefficient from the transmission coefficient which is expressed by the susceptance and conductance of the resonators, and the admittance inverters [1]. The electric/magnetic wall method derives the coupling coefficient between synchronously

tuned resonators (i.e. the coupled resonators are identical) from the characteristic resonant frequencies which are obtained by adding electric and magnetic walls, respectively [2]. The impedance calculation method derives the coupling of asynchronously tuned resonators (i.e. the coupled resonators may be different) from the fact that the impedance of the circuit is resistive at resonance [2].

Transmission coefficient method

Makimoto and Yamashita [1] developed an approximation of the inter-resonator coupling coefficient, assuming that the coupling between two coupled identical resonators is relatively small. Figure 2.12 shows the equivalent circuit of a pair of coupled resonators with source and load. The resonators are expressed by its admittance $Y(\omega)$ while J_0 and J_{12} are the admittance inverters that represent the external coupling and the inter-resonator coupling, respectively.

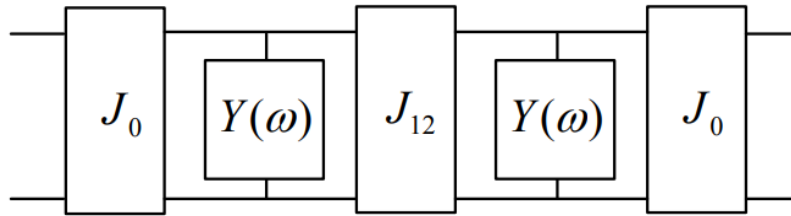


Figure 2.12 Equivalent circuit for determining the coupling coefficient of a pair of coupled resonators.

The admittance $Y(\omega)$ of the resonator is expressed by [1]

$$Y(\omega) = G_0 + jB(\omega) \quad (2.43)$$

where G_0 and $B(\omega)$ are the conductance and susceptance of resonator, respectively.

The transfer matrix $[T]$ of the equivalent circuit is derived as follows [1]:

$$\begin{aligned} [T] &= \begin{bmatrix} 0 & j \\ jJ_0 & 0 \end{bmatrix} \begin{bmatrix} 1 & 0 \\ Y(\omega) & 1 \end{bmatrix} \begin{bmatrix} 0 & j \\ jJ_{12} & 0 \end{bmatrix} \begin{bmatrix} 1 & 0 \\ Y(\omega) & 1 \end{bmatrix} \begin{bmatrix} 0 & j \\ jJ_0 & 0 \end{bmatrix} \\ &= \begin{bmatrix} -jY(\omega)/J_{12} & -\frac{jJ_{12}}{J_0^2} - \frac{jY(\omega)^2}{J_0^2 J_{12}} \\ jJ_0^2/J_{12} & jY(\omega)/J_{12} \end{bmatrix} = \begin{bmatrix} A & B \\ C & D \end{bmatrix} \end{aligned} \quad (2.44)$$

where A , B , C , and D are the matrix elements.

The transmission coefficient of the circuit is expressed by [1]

$$L(\omega) = \frac{|AZ_0 + B + CZ_0 + DZ_0|^2}{4Z_0^2} \quad (2.45)$$

$$= \frac{B(\omega)^4 - 2[J_{12}^2 - (G_0 + Z_0J_0^2)^2]B(\omega)^2 + [J_{12}^2 + (G_0 + Z_0J_0^2)^2]^2}{(2Z_0J_0J_{12})^2}.$$

The transmission coefficient $L(\omega)$ has two peaks when $J_{12}^2 - (G_0 + Z_0J_0^2)^2 > 0$. Under this condition, the following relationship is derived as

$$B(\omega) = \pm \sqrt{J_{12}^2 - (G_0 + Z_0J_0^2)^2}. \quad (2.46)$$

Assuming ω_1 and ω_2 are the two angular frequencies reaching the two peaks, then

$$J_{12} = \sqrt{\frac{(B(\omega_2) - B(\omega_1))^2}{4} + (G_0 + Z_0J_0^2)^2}. \quad (2.47)$$

In addition, the susceptance can be written as follows since it will be cancelled at the resonant frequency:

$$B(\omega) = b_0 \left(\frac{\omega}{\omega_0} - \frac{\omega_0}{\omega} \right) \quad (2.48)$$

where b_0 is the slope parameter of the resonator and ω_0 is the angular resonant frequency.

Thus, we have

$$B(\omega_2) - B(\omega_1) \cong 2b_0 \cdot \frac{\omega_2 - \omega_1}{\omega_0}. \quad (2.49)$$

Also, the following equations exist:

$$J_{12} = b_0 k$$

$$G_0 = b_0 / Q_0 \quad (2.50)$$

$$Q_e = \frac{b_0}{Z_0 J_0^2}.$$

Substitute (2.49) (2.50) into (2.47), the following expression of coupling coefficient can be derived [1].

$$k \cong \sqrt{\left(\frac{\omega_2 - \omega_1}{\omega_0}\right)^2 + \left(\frac{1}{Q_0} + \frac{1}{Q_e}\right)^2} \quad (2.51)$$

Adopting a loose coupling (i.e. $Q_e \gg 1$) and high unloaded Q factor resonators (i.e. $Q_0 \gg 1$), the coupling coefficient between two identical resonators is then obtained as [1]

$$k \cong \frac{\omega_2 - \omega_1}{\omega_0} = \frac{f_2 - f_1}{f_0} \quad (2.52)$$

where f_1 and f_2 are the resonant frequencies near the natural resonance, and f_0 is the natural resonant frequency.

Electric/magnetic wall method

Hong and Lancaster [2] presented a different method to extract the coupling coefficient between coupled identical resonators by adding electric and magnetic walls to the lumped element circuit model. The inter-resonator couplings are categorised in three types: electric coupling, magnetic coupling, and mix coupling. Hong and Lancaster [2] also stated that the derived formulation may be applied to distributed element coupled structures on a narrow-band basis.

Electric coupling

Figure 2.13 shows an equivalent lumped element circuit of the electric coupling between synchronously tuned resonators, which is obtained from the network theory [67]. L and C are the self-inductance and self-capacitance of the lumped element resonator, and C_m represents the mutual capacitance of coupling. The electric coupling is replaced by an admittance inverter that consists of capacitors.

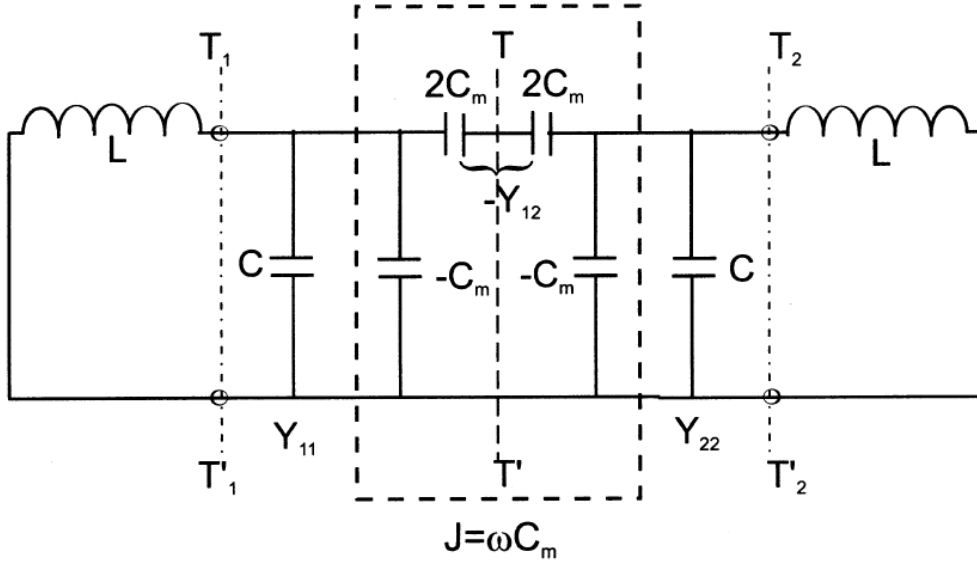


Figure 2.13 Equivalent circuits of the electric coupling between synchronously tuned resonators [2].

Adding an electric wall to the symmetry plane $T - T'$, it is short-circuited at $T - T'$.

The resultant circuit has a resonant frequency [2]

$$f_e = \frac{1}{2\pi\sqrt{L(C + C_m)}}. \quad (2.53)$$

Similarly, adding a magnetic wall instead, it is an open circuit at $T - T'$. The resultant resonant frequency is then [2]

$$f_m = \frac{1}{2\pi\sqrt{L(C - C_m)}}. \quad (2.54)$$

The coupling coefficient k_E is defined by

$$k_E = \frac{C_m}{C}. \quad (2.55)$$

Substitute (2.53) and (2.54) into (2.55), then

$$k_E = \frac{f_m^2 - f_e^2}{f_m^2 + f_e^2}. \quad (2.56)$$

Magnetic coupling

Similar to the electric coupling, an equivalent circuit model of the magnetic coupling is shown in Figure 2.14. The magnetic coupling is represented by an impedance inverter that consists of inductors.

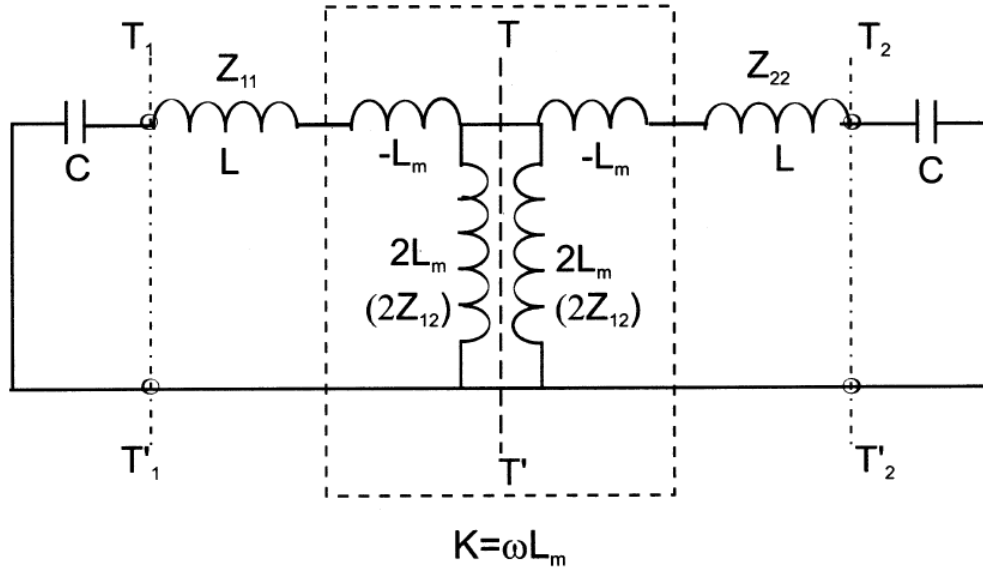


Figure 2.14 Equivalent circuits of the magnetic coupling between synchronously tuned resonators [2].

Replacing the symmetry plane $T - T'$ by an electric wall and a magnetic wall, the resonant frequency will change due to the coupling effect.

The resonant frequencies f_e and f_m are [2]:

$$f_e = \frac{1}{2\pi\sqrt{C(L - L_m)}} \quad (2.57)$$

$$f_m = \frac{1}{2\pi\sqrt{C(L + L_m)}} \quad (2.58)$$

The following expression is derived according to definition of magnetic coupling coefficient.

$$k_M = \frac{L_m}{L} = \frac{f_e^2 - f_m^2}{f_e^2 + f_m^2} \quad (2.59)$$

Mixed coupling

Figure 2.15 shows an equivalent circuit of mixed coupling.

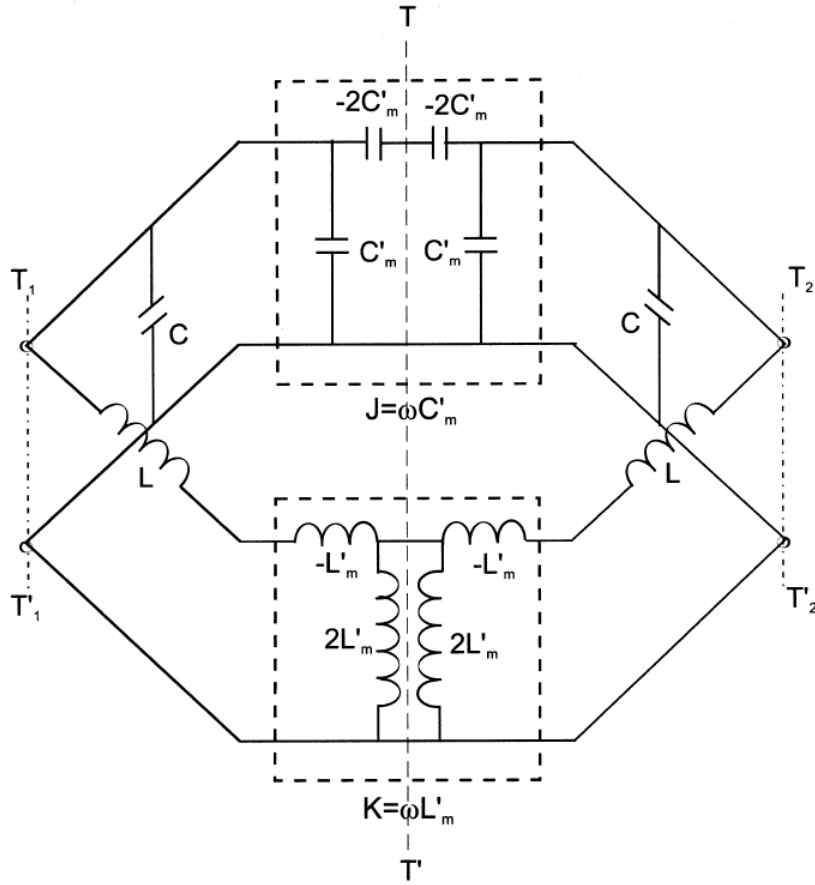


Figure 2.15 Equivalent circuit of the mixed coupling [2].

It combines electric coupling and magnetic coupling using an admittance inverter and an impedance inverter. Adding an electric wall and a magnetic wall into the symmetry plane $T - T'$ respectively, the two characteristic resonant frequencies f_e and f_m will be obtained as [2]

$$f_e = \frac{1}{2\pi\sqrt{(C - C_m')(L - L_m')}} \quad (2.60)$$

$$f_m = \frac{1}{2\pi\sqrt{(C + C_m')(L + L_m')}} \quad (2.61)$$

Therefore, the mixed coupling coefficient k_x is defined by

$$k_x = \frac{f_e^2 - f_m^2}{f_e^2 + f_m^2} = \frac{CL'_m + LC'_m}{LC + L'_m C'_m} \quad (2.62)$$

If the coupling is assumed to be relatively small, i.e. $L'_m C'_m \ll LC$, then (2.62) becomes

$$k_X \approx \frac{L'_m}{L} + \frac{C'_m}{C} = k'_M + k'_E. \quad (2.63)$$

Equation (2.63) shows that the mixed coupling is the superposition of electric coupling and magnetic coupling. It is noted that the electric coupling and magnetic coupling can have opposite signs, which means that they normally cancel each other out in mixed coupling. Hong suggested simulating or measuring the whole coupling structure instead of the half in practice as it is very difficult to implement the electric wall and magnetic wall in most cases [2]. Then the characteristic resonant frequencies f_e and f_m can be obtained by finding the natural resonant frequencies of the two resonant peaks from the frequency responses [63]. Hong and Lancaster [2] also noted that the expressions of coupling (2.56) (2.59) (2.63) are identical to the ratio of the coupled energy to the stored energy of uncoupled single resonator, shown in Section 2.4.1.

Impedance calculation method

This method can be applied to both synchronously tuned and asynchronously tuned coupled-resonator circuits because the impedance of the circuit is resistive or the admittance is conductive (i.e. the reactance is zero) at resonance [2]. Therefore, in the equivalent lossless LC circuit, the impedance or admittance should be zero at resonance.

Electric coupling

The equivalent lumped-element circuit is shown in Figure 2.16.

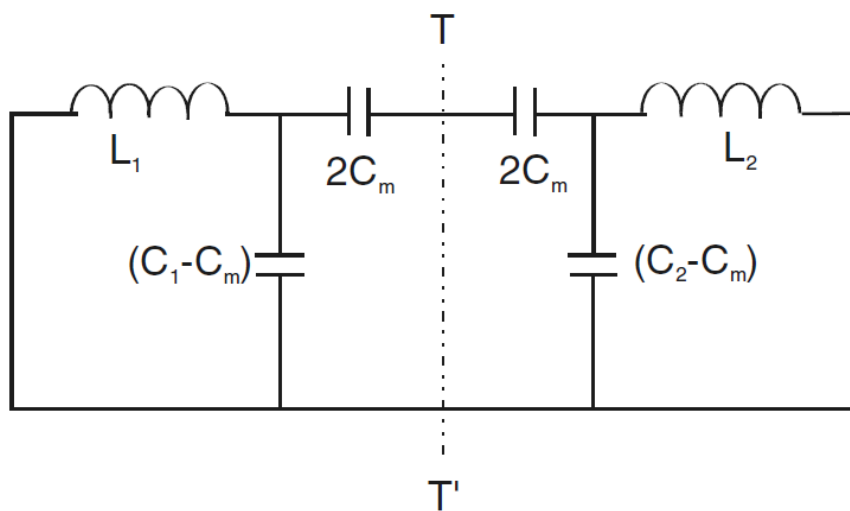


Figure 2.16 Asynchronously tuned coupled resonator circuit with electric coupling [2].

The resonant angular frequencies of the resonators are

$$\omega_{01} = \frac{1}{\sqrt{L_1 C_1}}$$

$$\omega_{02} = \frac{1}{\sqrt{L_2 C_2}}.$$
(2.64)

At resonance, the impedance Z of the circuit is zero. Thus,

$$Z = \frac{1}{\frac{1}{j\omega L_1} + j\omega(C_1 - C_m)} + \frac{1}{j\omega 2C_m} + \frac{1}{j\omega 2C_m} + \frac{1}{\frac{1}{j\omega L_2} + j\omega(C_2 - C_m)} = 0. \quad (2.65)$$

Equation (2.65) has two positive solutions of ω , shown in (2.66), which are measurable.

$$\omega_{1,2} = \sqrt{\frac{(L_1 C_1 + L_2 C_2) \pm \sqrt{(L_1 C_1 - L_2 C_2)^2 + 4L_1 L_2 C_m^2}}{2(L_1 L_2 C_1 C_2 - L_1 L_2 C_m^2)}}. \quad (2.66)$$

Then the following equation could be derived, assuming $\omega_2 > \omega_1$.

$$\left(\frac{\omega_2^2 - \omega_1^2}{\omega_2^2 + \omega_1^2}\right)^2 = \frac{C_m^2}{C_1 C_2} \frac{4}{\left(\frac{\omega_{02}}{\omega_{01}} + \frac{\omega_{01}}{\omega_{02}}\right)^2} + \left(\frac{\omega_{02}^2 - \omega_{01}^2}{\omega_{02}^2 + \omega_{01}^2}\right)^2. \quad (2.67)$$

According to the definition of coupling coefficient in Section 2.4.1, the electric coupling coefficient is then obtained as [2]

$$k_e = \frac{C_m}{\sqrt{C_1 C_2}} = \pm \frac{1}{2} \left(\frac{\omega_{02}}{\omega_{01}} + \frac{\omega_{01}}{\omega_{02}}\right) \sqrt{\left(\frac{\omega_2^2 - \omega_1^2}{\omega_2^2 + \omega_1^2}\right)^2 - \left(\frac{\omega_{02}^2 - \omega_{01}^2}{\omega_{02}^2 + \omega_{01}^2}\right)^2}. \quad (2.68)$$

Magnetic coupling

Figure 2.17 shows the equivalent circuit of the asynchronously tuned coupled resonator circuits with magnetic coupling [2].

The resonators resonate at angular frequencies that $\omega_{01} = \frac{1}{\sqrt{L_1 C_1}}$ and $\omega_{02} = \frac{1}{\sqrt{L_2 C_2}}$. Analysing the whole circuit, at natural resonance, the admittance of the circuit should be zero.

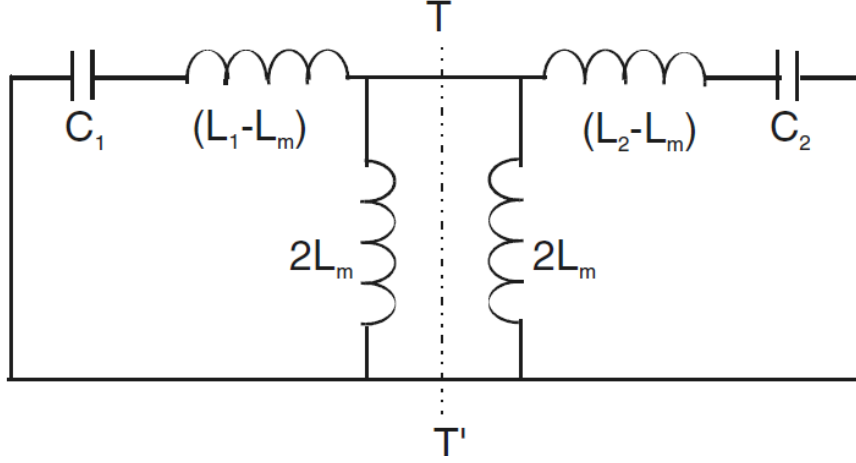


Figure 2.17 Asynchronously tuned coupled resonator circuits with magnetic coupling [2].

Therefore, (2.69) is obtained with two positive solutions given in (2.70).

$$Y = \frac{1}{\frac{1}{j\omega C_1} + j\omega(L_1 - L_m)} + \frac{1}{j\omega 2L_m} + \frac{1}{j\omega 2L_m} + \frac{1}{\frac{1}{j\omega C_2} + j\omega(L_2 - L_m)} = 0 \quad (2.69)$$

$$\omega_{1,2} = \frac{\sqrt{(L_1 C_1 + L_2 C_2) \pm \sqrt{(L_1 C_1 - L_2 C_2)^2 + 4C_1 C_2 L_m^2}}}{2(L_1 L_2 C_1 C_2 - C_1 C_2 L_m^2)}. \quad (2.70)$$

Assuming $\omega_2 > \omega_1$, after some manipulations, (2.71) is derived.

$$\left(\frac{\omega_2^2 - \omega_1^2}{\omega_2^2 + \omega_1^2}\right)^2 = \frac{L_m^2}{L_1 L_2} \frac{4}{\left(\frac{\omega_{02}}{\omega_{01}} + \frac{\omega_{01}}{\omega_{02}}\right)^2} + \left(\frac{\omega_{02}^2 - \omega_{01}^2}{\omega_{02}^2 + \omega_{01}^2}\right)^2 \quad (2.71)$$

Recall the definition of coupling coefficient in Section 2.3.1, the magnetic coupling coefficient is expressed by [2]

$$k_m = \frac{L_m}{\sqrt{L_1 L_2}} = \pm \frac{1}{2} \left(\frac{\omega_{02}}{\omega_{01}} + \frac{\omega_{01}}{\omega_{02}}\right) \sqrt{\left(\frac{\omega_2^2 - \omega_1^2}{\omega_2^2 + \omega_1^2}\right)^2 - \left(\frac{\omega_{02}^2 - \omega_{01}^2}{\omega_{02}^2 + \omega_{01}^2}\right)^2}. \quad (2.72)$$

Mixed coupling

The circuit model of asynchronously tuned coupling structures that both electric and magnetic coupling exist is depicted in Figure 2.18 [2].

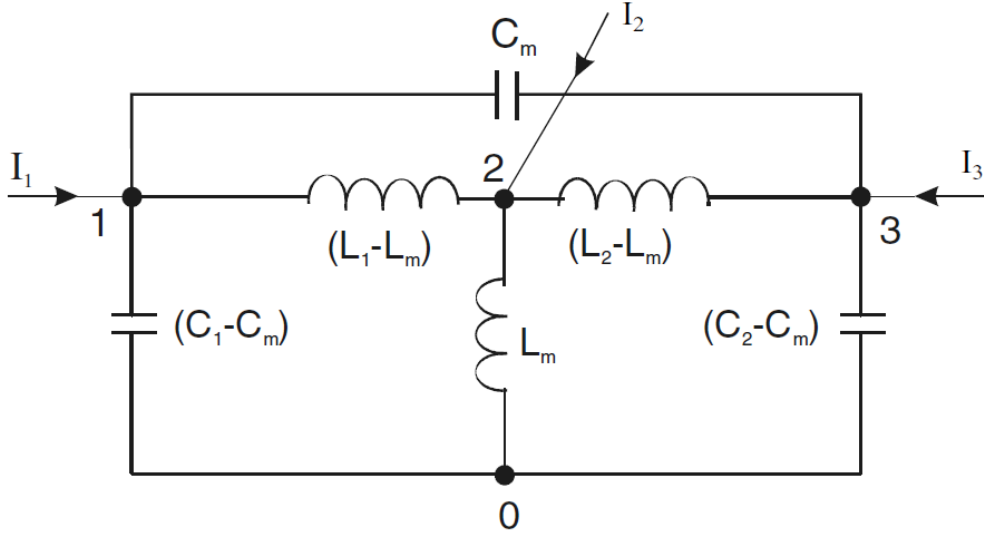


Figure 2.18 Asynchronously tuned resonator circuit with mixed coupling [2].

The external currents flowing into the circuit are represented by I_1 , I_2 and I_3 . With a reference at node “0”, we can derive

$$\begin{bmatrix} I_1 \\ I_2 \\ I_3 \end{bmatrix} = \begin{bmatrix} Y_{11} & Y_{12} & Y_{13} \\ Y_{21} & Y_{22} & Y_{23} \\ Y_{31} & Y_{32} & Y_{33} \end{bmatrix} \cdot \begin{bmatrix} V_1 \\ V_2 \\ V_3 \end{bmatrix} \quad (2.73)$$

where the Y parameters are expressed by

$$Y_{11} = j\omega C_1 + \frac{1}{j\omega(L_1 - L_m)}$$

$$Y_{12} = Y_{21} = -\frac{1}{j\omega(L_1 - L_m)}$$

$$Y_{13} = Y_{31} = -j\omega C_m$$

$$Y_{22} = \frac{1}{j\omega L_m} + \frac{1}{j\omega(L_1 - L_m)} + \frac{1}{j\omega(L_2 - L_m)}$$

$$Y_{23} = Y_{32} = -\frac{1}{j\omega(L_2 - L_m)}$$

$$Y_{33} = j\omega C_2 + \frac{1}{j\omega(L_2 - L_m)}$$

At resonance, $\begin{bmatrix} I_1 \\ I_2 \\ I_3 \end{bmatrix} = 0$ whereas $\begin{bmatrix} V_1 \\ V_2 \\ V_3 \end{bmatrix} \neq 0$. Thus,

$$\begin{vmatrix} Y_{11} & Y_{12} & Y_{13} \\ Y_{21} & Y_{22} & Y_{23} \\ Y_{31} & Y_{32} & Y_{33} \end{vmatrix} = 0. \quad (2.74)$$

The positive solutions of (2.74) are ω_1 and ω_2 where $\omega_2 > \omega_1$.

For narrow-band applications, it is assumed that

$$\begin{aligned} L_m C_m &\ll L_1 C_1 + L_2 C_2 \\ \frac{L_1 C_1 + L_2 C_2}{2\sqrt{L_1 C_1 L_2 C_2}} &\approx 1. \end{aligned} \quad (2.75)$$

With manipulations, we have

$$\left(\frac{\omega_2^2 - \omega_1^2}{\omega_2^2 + \omega_1^2}\right)^2 = \left(\frac{C_m^2}{C_1 C_2} + \frac{L_m^2}{L_1 L_2} - \frac{2L_m C_m}{\sqrt{L_1 C_1 L_2 C_2}}\right) \frac{4}{\left(\frac{\omega_{02}}{\omega_{01}} + \frac{\omega_{01}}{\omega_{02}}\right)^2} + \left(\frac{\omega_{02}^2 - \omega_{01}^2}{\omega_{02}^2 + \omega_{01}^2}\right)^2. \quad (2.76)$$

Therefore, the mixed coupling coefficient is derived as [2]

$$\begin{aligned} k_x &= \sqrt{\frac{C_m^2}{C_1 C_2} + \frac{L_m^2}{L_1 L_2} - \frac{2L_m C_m}{\sqrt{L_1 C_1 L_2 C_2}}} \\ &= \pm \frac{1}{2} \left(\frac{\omega_{02}}{\omega_{01}} + \frac{\omega_{01}}{\omega_{02}}\right) \sqrt{\left(\frac{\omega_2^2 - \omega_1^2}{\omega_2^2 + \omega_1^2}\right)^2 - \left(\frac{\omega_{02}^2 - \omega_{01}^2}{\omega_{02}^2 + \omega_{01}^2}\right)^2} \end{aligned} \quad (2.77)$$

where ω_{01} and ω_{02} are the self-resonant angular frequencies of the coupled resonators, the angular frequencies ω_1 and ω_2 corresponds to the two peaks of the measured or simulated frequency response, respectively.

Equation (2.77) also indicates that the mixed coupling is actually the superposition of electric coupling and magnetic coupling since $k_x = k_e - k_m$ [2]. Obviously, (2.77) is applicable to any asynchronously tuned coupled resonator circuit. It is noted that this method is also applicable to a synchronously tuned coupled resonator circuit.

2.5 Simulation and Modelling

With the power of computing and modelling in the recent decades, commercial software for EM applications have been implemented and developed to assist engineers and scientists on

technical and research problems. During the research presented in the thesis, there were three software products employed for computational problems, circuit analysis, CAD modelling, EM simulation in filter designs: Matrix Laboratory (MATLAB), Keysight Advanced Design System (ADS) and CST Microwave Studio (CST MW).

2.5.1 MATLAB

The MATLAB platform is optimized for solving engineering and scientific problems in areas including machine learning, signal processing, image processing, communications, robotics, and much more [68]. It provides high-performance environment for computational mathematics. The prebuilt toolboxes also implemented relevant functions for data process, analysis and visualisation [68]. Although the executing time of MATLAB might be high comparing to C/C++ or FORTRAN, it is much easier to debug the program and visualise the results.

In the filter designs shown in this thesis, MATLAB is generally used for the data processing, coupling matrix derivation, S-parameters plotting, coupling profiles plotting, curve fitting, and calculation of parameters that include coupling coefficients, external Q factors, unloaded Q factors, and bandwidths.

2.5.2 Keysight ADS

Keysight ADS is an electronic design automation software for RF, microwave, and high speed digital applications, produced by Keysight Technologies [69]. It supports schematic capture, layout, design rule checking, frequency domain and time domain circuit simulation, and electromagnetic simulation for components, circuits, and systems [69, 70]. This circuit-system-EM co-simulation capability allows the engineers to fully characterise, optimise and analyse RF and microwave designs in an integrated platform [69].

The built-in linear simulator is a frequency domain simulator that analyses RF and microwave circuits under linear conditions [71], delivering frequency response (S-parameters). It is often employed in equivalent circuit simulation of filter designs. Keysight ADS provides two 3D EM simulators that are useful for filter designs, providing S-parameters. These simulators are developed based on Method of Moments (MoM) and Finite Element Method (FEM). MoM is a 3D planar EM simulator for RF and microwave passive circuit analysis based on boundary element method by solving partial differential equations [72]. FEM is able to perform EM

simulation of arbitrary 3D structures. It enables seamless co-simulation of the circuit, system components and 3D interconnects and packaging [73]. These EM simulators are widely used in filter designs, especially when EM co-simulation with other circuit components or system is required.

In this thesis, Keysight ADS is used for equivalent circuit simulations of filters to obtain and analyse the frequency responses. The tuning function of Keysight ADS also provides guidance for physical filter tuning process.

2.5.3 CST MWS

CST MWS, one of the leading edge tools for the fast and accurate 3D simulation of high frequency devices [74]. There are several solvers available in the latest educational version supporting different EM designs and analysis, including Transient Solver, Frequency Domain Solver, Eigenmode Solver, and Integral Equation Solver. The Transient Solver of CST MW is a general purpose time domain simulator that studies the field propagating through components or alone the traces of components [75]. It is also capable of delivering broadband frequency domain results like S-parameters. A huge range of EM applications employs the Transient Solver, such as antennas, signal integrity (SI) and electromagnetic compatibility (EMC) simulations. The Frequency Domain Solver of CST MW is a general purpose tool that analyses and delivers the EM near field and farfield as well as the S-parameters [6]. It is the better choice for electrically small structures or high Q structures, such as filters, couplers, and oscillators. Eigenmode Solver is dedicated to the simulation of closed resonant structures, providing the field distribution of the modes, the eigen frequencies of the structures [72]. CST's proprietary perfect boundary approximation is applied to obtain fast convergence in short time. The typical application areas of Eigenmode Solver are the determination of the poles of resonant structures, Q-value (unloaded and external) calculation, and the design of slow wave structures [72]. Integral Equation Solver is a specialised solver that uses MoM with a surface integral formulation of electric and magnetic field [5]. It is efficient for electrically large structures simulations that are beyond feasibility of volume methods.

The research demonstrated in this thesis employed the Frequency Domain Solver and the Eigenmode Solver for the design of dual-band bandpass filters. The Frequency Domain Solver is used to obtain the S-parameters, from which the resonant frequencies, Q factors (unloaded and external), coupling coefficients can be obtained [76]. As mentioned earlier, the Eigenmode Solver does not provide S-parameters but delivers the resonant frequencies, Q factors, coupling

coefficients, as well as field patterns and energy distribution of each resonant mode. Additionally, the Eigenmode solver also delivers the degenerate modes. The post processing function of CST MWS is extremely useful as it provides the ability to process and manipulate simulation results by the user, with which the results that not directly provided by CST MWS can be obtained. For example, the power handling capability of filters can be obtained by the post processing of E-fields and group delays [77].

2.6 Measurement

The evaluation of RF and microwave filters includes the frequency response, power handling capability, and temperature stability. The power handling capability and temperature stability provide additional information of the filter characteristics. However, they are not critically important in the design procedure of filters in this thesis. The measurement involved in the thesis mainly focuses on the frequency response (S-parameters) since the research aims to design, develop and implement compact bandpass filters with dual-band characteristics. As the key components and structures, the resonators and couplings of the filter are also evaluated from the measured frequency responses. The formulae and procedures extracting the measured unloaded Q factor, external quality factor and inter-resonator coupling coefficient are demonstrated in Section 2.6.1 – 2.6.3, respectively.

2.6.1 Unloaded Q measurement

The measurement of the unloaded Q can be realised by transmission-type or reflection-type measurement, in terms of the required port(s) [34]. The transmission-type measurement requires a two-port network to measure the S_{21} parameter, from which the unloaded Q factor is obtained. The external coupling of transmission-type measurement can be realised by two ways, either loosely coupled or symmetrical coupled, discussed in detail below.

Loose external coupling measurement

The S_{21} parameter is measured when loose coupling is applied to both input and output [2, 78]. Loose coupling, also called over-critical coupling, means that more power is dissipated in the external circuit than in the resonator [34]. The overall external coupling coefficient (κ) is the sum of those from each port [34], i.e. the inverse ratio of the overall external quality factor (Q_e) is the sum of the inverse ratio of the external quality factor from each port. The external coupling condition in this case is $\kappa \rightarrow 0$, i.e. $Q_e \rightarrow \infty$. Applying this condition to the unloaded

Q expression in (2.2), the unloaded Q is approximately equal to the loaded quality factor (Q_L) of the resonator. The loaded quality factor (Q_L) is obtained from S_{21} parameter as the inverse ratio of 3-dB fractional bandwidth (FBW), i.e. the ratio of resonant frequency (f) to the 3-dB bandwidth (BW), shown in (2.78).

$$Q_0 \approx Q_L = \frac{f_0}{\text{BW}} = \frac{1}{\text{FBW}} \quad (2.78)$$

In practice, the external quality factor (Q_e) can be assumed as infinite when the insertion loss at resonance is more than 30 dB.

Symmetrical external coupling measurement

Alternatively, the unloaded Q factor can be obtained from a symmetrical external coupled measurement [34]. The magnitude of S_{21} parameter at the resonant frequency can be expressed by

$$|S_{21}(f_0)| = \frac{2\sqrt{\kappa_1\kappa_2}}{1 + \kappa_1 + \kappa_2} \quad (2.79)$$

where κ_1 and κ_2 represents the external coupling coefficient from input and output, respectively.

For symmetrical external coupling, i.e. $\kappa_1 = \kappa_2$, the overall external coupling coefficient κ is

$$\kappa = \frac{|S_{21}(f_0)|}{1 - |S_{21}(f_0)|} \quad (2.80)$$

Thus, the expression of external quality factor (Q_e) is derived from (2.36) (2.80).

$$Q_e = \frac{1 - |S_{21}(f_0)|}{|S_{21}(f_0)|} Q_0 \quad (2.81)$$

When this is substituted into (2.2), the unloaded Q factor can be computed as [34, 79]

$$Q_0 = \frac{Q_L}{1 - |S_{21}(f_0)|} \quad (2.82)$$

where the loaded quality factor (Q_L) is obtained from the measured S_{21} parameter as the inverse ratio of 3-dB fractional bandwidth (FBW). The magnitude of S_{21} parameter at resonant

frequency $|S_{21}(f_0)|$ is a linear value obtained from its decibel form, the insertion loss (α).

Compared to the loosely external coupling measurement, the symmetrical external coupling measurement quantifies the effect of external coupling in the calculation of external Q factor. However, it has very high requirement on fabrication quality to ensure the symmetrical external coupling structure [34]. For asymmetrical resonators, it may not be possible to realise symmetrical external coupling. Additionally, the accuracy is significantly reduced when $|S_{21}(f_0)|$ approaches unity that the external coupling is strong. This is indicated by (2.82) that a small error in the denominator will cause a large error in Q_0 even though the Q_L is measured accurately [34].

2.6.2 External quality factor measurement

The measured external quality factor (Q_e) is obtained from the measured S_{11} parameter of a one-port network. The external quality factor is extracted from a transformation of (2.42) using frequencies obtained from measured S_{11} parameter instead of angular frequencies [2], as

$$Q_e = \frac{f_0}{\Delta f_{\pm 90^\circ}} \quad (2.83)$$

where $\Delta f_{\pm 90^\circ}$ represents the frequency difference when the phase of S_{11} parameter is $\pm 90^\circ$ away from the phase of the resonant frequency.

2.6.3 Inter-resonator coupling coefficient measurement

The measured inter-resonator coupling coefficient is obtained from the measured S_{21} parameter of a loosely external coupled two-port network. Section 2.4.3 has demonstrated three methods to derive the inter-resonator coupling coefficients from the equivalent circuits. The type of coupling is always mixed coupling since the electric coupling and magnetic coupling coexist and cancel each other in practice [2, 51]. Considering the fact that the coupled resonators are not always identical (synchronously tuned), the asynchronously tuned coupling equation (2.77) provides a general equation to extract the inter-resonator coupling coefficients, which can be rewritten in frequencies as

$$k = \pm \frac{1}{2} \left(\frac{f_{02}}{f_{01}} + \frac{f_{01}}{f_{02}} \right) \sqrt{\left(\frac{f_2^2 - f_1^2}{f_2^2 + f_1^2} \right)^2 - \left(\frac{f_{02}^2 - f_{01}^2}{f_{02}^2 + f_{01}^2} \right)^2} \quad (2.84)$$

where f_{01} and f_{02} are the measured self-resonant frequencies of the resonators, f_1 and f_2 corresponds to the frequencies of the two peaks of the measured S_{21} parameter, respectively.

By assuming synchronously tuned (electrically identical) coupled resonators, (2.52) (2.62) (2.84) are all applicable to extract the measured coupling coefficients. In this case, (2.84) can be degenerates to [2]

$$k = \frac{f_2^2 - f_1^2}{f_2^2 + f_1^2} \quad (2.85)$$

where f_1 and f_2 are the resonant frequencies of the peaks of the measured S_{21} parameter.

The natural resonant frequency of the coupled resonator circuit f_0 in (2.52) cannot be obtained directly from the frequency response. Hong and Lancaster noted that f_1 and f_2 in (2.85) correspond to either f_e or f_m in (2.62). Therefore, this universal formulation (2.85) is employed to extract the measured inter-resonator coupling coefficient.

2.7 Power handling capability

When designing RF and microwave filters, the power handling capability needs to be estimated, especially for space-bound and some ground-based components [80]. There are two general limitations of power handling: the average power causes hardware failure due to thermal effects; the peak power that causes hardware problem through break down effects [81].

The average power limited by thermal effects, the heat due to average input power and the heat transferred to a heat sink. The analysis of thermal effects is a complex subject with many impact factors, such as input signal power, material temperature stability, thermal conductivity, structure topology, and cooling equipment. There is not any analytical method available for fast estimation on averaging power handling capability. In practice, the average power handling capability is estimated from measurement. As a result, it is not covered in the thesis.

Yu [80] has stated the peak power breakdown effects that has to be considered when designing filters for high power applications, which are multipaction, ionization, and passive intermodulation (PIM) interferences. Multipaction is a RF vacuum breakdown mechanism that there is resonant growth of free electron space charge between surfaces [80] [75]. In RF and microwave applications, multipaction causes loss and distortion of the signal. It can also damage components or subsystems when the reflected or dissipated power exceeds the limitation [81]. Ionization breakdown is a RF gas breakdown phenomenon where an initially

low electron density increases and turns the isolating gas into conducting plasma [80, 82]. Multipaction and ionization are the main RF failure that have been analysed for decades. They are extremely complicated phenomena to analyse since there are many factors influencing them, such as input RF signal and environmental factors that include temperature, pressure, and humidity [80]. In practice, it is extremely difficult and costly to measure the RF breakdown. Yu [80] summarised and developed the theories and processes in [44, 83] to analyse the breakdown by analysing the field strength. The analysis of the electrical field in a filter involves analysis by EM simulation tools because the analytical solution of field is difficult to derive and not always available.

The peak input power is expressed by [80]

$$P_{peak} = \left(\frac{E_{break}}{E_{em}} \right)^2 \cdot \frac{1}{W} \quad (2.86)$$

where E_{break} is the breakdown electric field strength for the filled material in the filter, which is approximately 3.3 MV/m for air [77]; E_{em} is the normalised maximum electric field strength obtained from EM simulation; and W is the stored energy in the filter.

E_{em} can be obtained by normalising the maximum electric field strength in CST MW to 1 nJ [80], while the stored energy W can be obtained as the product of 1W input (CST MWS simulation setup) and the group delay (τ) [84]. A transformed equation of (2.86) is more convenient to obtain the peak power, shown as follows [51, 77]

$$P_{peak} = \left(\frac{E_{break}}{E_{max} \cdot \sqrt{1 \cdot 10^{-9}}} \right)^2 \cdot \frac{1}{\tau} \text{ Watt} \quad (2.87)$$

where E_{max} is the maximum electric field strength directly obtained from CST MWS Eigenmode solver, and τ is the numerical value of the group delay in nanosecond (ns).

Chapter 3: Dual-passband response synthesis

3.1 Introduction

One of the design approaches focuses on the synthesis procedures for the realisation of dual-band bandpass filters, called dual-passband response synthesis, has been studied and developed with filter examples in [10, 11, 15-18, 40]. The basic idea of this method is using frequency transformation techniques [9-11, 18, 85, 86] to place finite frequency transmission zeros within the passband of a single-band bandpass filter to split it into dual passbands [9].

The purpose of this chapter is to demonstrate the dual-passband response synthesis for the realisation of dual-band bandpass filters. A frequency transformation technique that generates a symmetric dual-passband filter response from a normalised low pass prototype response is presented. The synthesis of coupling matrices from the transformed frequency responses is then reviewed as the synthesised coupling matrices provide a direct synthesis of narrowband filters. Finally, the general design procedures of the dual-passband response synthesis method are described with two filter designs.

The frequency transformation described in [85] is only applicable to the synthesis of symmetrical dual-passband filter responses. There is another frequency transformation method presented in [86] that realises asymmetrical dual-passband responses. However, it generates transmission zeros at one location in the stopband, which limits the attenuation when a wide stopband is required. Lee and Sarabandi [10, 11] proposed a frequency transformation technique that can be used in generation of symmetrical and asymmetrical dual- and tri-passband filter responses. The transmission and reflection zeros of a normalised low pass frequency response are transformed into new locations in an intermediate frequency domain. Additional pairs of frequency zeros are generated during the frequency transformation process, which split the original single-passband into multiple ones [10, 15]. Section 3.2 illustrates the frequency transformation technique proposed by Lee and Sarabandi [9, 10] for synthesis of symmetric dual-passband frequency responses.

A narrowband bandpass filter can be directly synthesised according to the coupling coefficients. The couplings between resonators are most easily represented and manipulated in matrix form. The elements in the matrix depicting the intensity of coupling are called coupling coefficients.

The synthesis procedures of coupling matrix were firstly proposed by Atia and Williams [12, 13] for symmetrical filter responses in 1970s and then revised by Cameron [14] for asymmetrical filter responses in 1999. The synthesis procedures of coupling matrix have also been studied and developed in [2, 9, 29]. It has been shown that the coupling matrix can be synthesised for a given filter response represented by S-parameters. Matrix similarity transformation has been applied to reduce the coupling matrix to a realisable form [14, 29]. However, the synthesis methods based on similarity transformation are limited to certain filter topologies and limited filter orders. Gajaweera and Lind [30, 31] provided a method to extract and simplify the coupling matrix from given frequency zeros by solving a set of non-linear equations using the Newton-Raphson procedure. It is said that this method can be extended to any filter topology of any order as long as the filter network has a sufficient number of non-zero couplings [19]. The synthesis procedures of coupling matrices are demonstrated in Section 3.3. The transfer function is reviewed and related to the network parameters of a lossless time-invariant two-port network. Next, the synthesis procedures of coupling matrix from the frequency response and network parameters are reviewed for symmetric [12, 13] and asymmetric frequency responses [14]. In practice, the coupling matrix has to be transformed to a convenient form for filter implementation. The coupling matrix reduction methods are then discussed.

Section 3.4 demonstrates the general design process of dual-passband response synthesis for dual-band BPF design. Two dual-band BPFs have been designed and implemented, shown in Section 3.4.1 and 3.4.2. The eighth order dual-passband response is synthesised from a symmetrical four-pole generalised Chebyshev response, followed by the synthesis of the coupling matrix. The eighth order dual-band BPF is then designed and implemented utilising microstrip square open-loop resonators. However, the frequency responses of the filter is not reasonable due to the low unloaded Q factor of resonators. The effect of finite unloaded Q on resonators for the realisation of narrow dual-band bandpass filters have been investigated and shown. High Q $TE_{01\delta}$ mode quarter-cylindrical dielectric resonators have been used for the realisation of the sixth order dual-band BPF. The measured frequency response is not to a satisfactory level, mainly because of the epoxy losses and the imperfect $TE_{01\delta}$ mode.

Section 3.5 discusses the limitation of the synthesis method for the realisation of dual-band bandpass filters. It also suggests the further reasearch on this subject. Finally, this chapter is summarised by Section 3.6.

3.2 Frequency transformation for symmetric dual-passband frequency response

The frequency transformation for dual-band bandpass filter synthesis has been proposed by Macchiarella and Tamiazzo [85, 86], Guan et al. [18], Lee and Sarabandi [9, 10]. As mentioned, frequency transformation techniques proposed by Lee and Sarabandi [10, 11] can be used in generation of symmetrical and asymmetrical, dual- and tri-passband filter responses. Their frequency transformation method maps the reflection and transmission zeros of a normalised transfer function in the Ω domain to the locations in the intermediate Ω' domain. In this section, their frequency transformation procedure for dual-band symmetric frequency response is demonstrated. Figure 3.1 shows the frequency responses in the Ω , Ω' and ω domains, respectively.

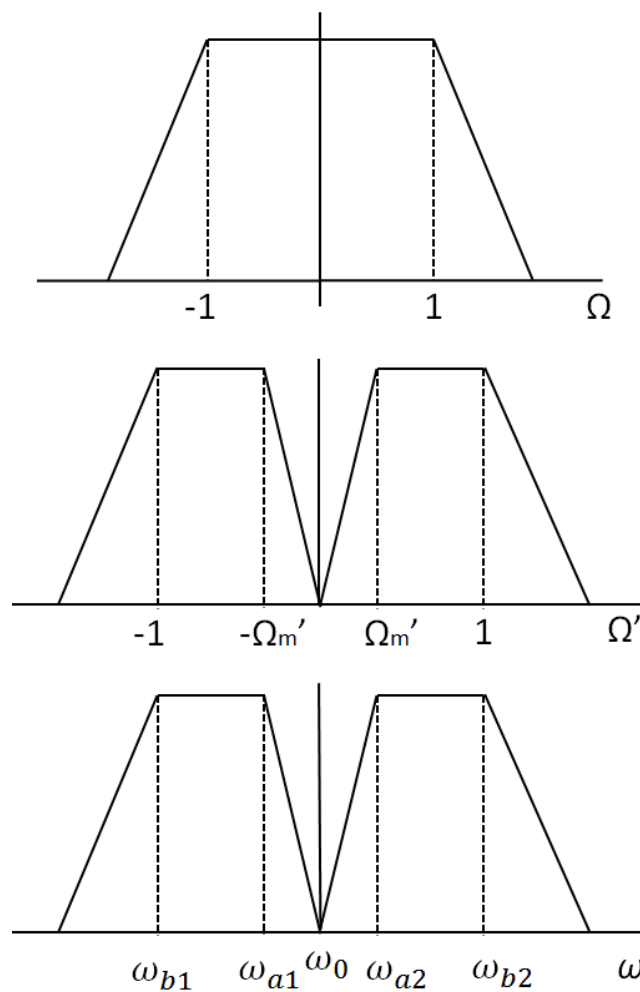


Figure 3.1 Frequency responses in the Ω , Ω' and ω domains.

The Ω domain is the normalised frequency domain for the single-band frequency response. It is actually a normalised low pass prototype response with the negative frequencies. The Ω' domain is the transformed normalised frequency domain for the dual-passband response. The coupling matrix of the dual-band bandpass filter is obtained from the transformed dual-band frequency response in the Ω' domain. The ω domain is the actual frequency domain where the filter operates in practice. The frequency response in the ω domain can be obtained by applying two frequency transformations consecutively to the prototype single-passband frequency response in the Ω domain. The coupling matrix of the dual-passband filter is obtained from the transfer function of the filter in the Ω' domain.

The frequency variable S in the Ω domain of the transfer function is transformed to that in the Ω' domain as [10]

$$\begin{aligned} S &= \frac{S'}{c_1} + \frac{c_2}{S'} \quad \text{for } \Omega' > 0 \\ S &= -\left(\frac{S'}{c_1} + \frac{c_2}{S'}\right) \quad \text{for } \Omega' < 0 \end{aligned} \tag{3.1}$$

where $S = j\Omega$ and $S' = j\Omega'$. Since 1 and -1 in the Ω domain are transformed to 1 and Ω'_m in the Ω' domain for $\Omega' > 0$, respectively; and 1 and -1 in the Ω domain are transformed to -1 and $-\Omega'_m$ in the Ω' domain for $\Omega' < 0$, respectively, we have

$$\begin{aligned} 1 &= \frac{c_1}{2} \left(1 + \sqrt{1 + 4 \frac{c_2}{c_1}} \right) \\ \Omega'_m &= \frac{c_1}{2} \left(-1 + \sqrt{1 + 4 \frac{c_2}{c_1}} \right) c_2. \end{aligned} \tag{3.2}$$

Therefore, the constants c_1 and c_2 in (3.1) are expressed as

$$\begin{aligned} c_1 &= 1 - \Omega'_m \\ c_2 &= \frac{\Omega'_m}{1 - \Omega'_m} \end{aligned} \tag{3.3}$$

where Ω'_m is the band edge frequency in the Ω' domain.

Similarly, the frequency transformation from the Ω' domain to the ω domain is expressed by

$$S' = \frac{s}{d_1} + \frac{d_2}{s} \quad \text{for } \Omega' > 0 \quad (3.4)$$

where $s = j \omega$ and the constants d_1 and d_2 are expressed by the band edge frequencies as

$$\begin{aligned} d_1 &= \omega_{b2} - \omega_{b1} \\ d_2 &= \frac{\omega_{b2} \cdot \omega_{b1}}{\omega_{b2} - \omega_{b1}}. \end{aligned} \quad (3.5)$$

In addition, the band edge frequency Ω'_m in the Ω' domain is derived by

$$\Omega'_m = \frac{\omega_{a2} - \omega_{a1}}{\omega_{b2} - \omega_{b1}}. \quad (3.6)$$

3.3 Coupling matrix synthesis

The coupling matrix M is an $n \times n$ reciprocal matrix (i.e. $M_{ij} = M_{ji}$) which theoretically includes all the couplings between all resonators in a circuit [2]. The coupling matrix and the external quality factor can be obtained from a given filter frequency response represented by S-parameters for filter synthesis. The methods to generate coupling matrices from the given S-parameters have been studied and developed in [2, 9, 13, 14, 19]. This section shows a general coupling matrix synthesis method derived from a symmetric network.

3.3.1 Transfer function

Figure 3.2 gives an equivalent circuit of a linear doubly terminated network, with source voltage V_0 , source resistance R_1 , load resistance R_2 , and load voltage V_2 .

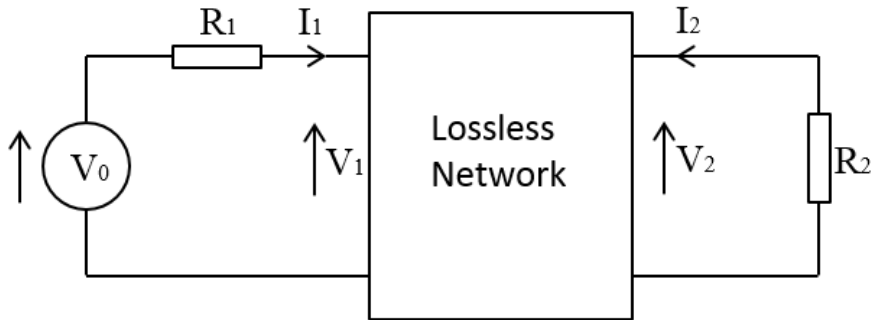


Figure 3.2 Two-port linear network.

The admittance matrix Y , whose elements are the y -parameters, of the two-port network is defined as [3, 78]

$$\begin{bmatrix} I_1 \\ I_2 \end{bmatrix} = [Y] \cdot \begin{bmatrix} V_1 \\ V_2 \end{bmatrix} = \begin{bmatrix} y_{11} & y_{12} \\ y_{21} & y_{22} \end{bmatrix} \cdot \begin{bmatrix} V_1 \\ V_2 \end{bmatrix}. \quad (3.7)$$

The impedance matrix Z of a two-port network, whose elements are the z -parameters, is defined as [3, 78]

$$\begin{bmatrix} V_1 \\ V_2 \end{bmatrix} = [Z] \cdot \begin{bmatrix} I_1 \\ I_2 \end{bmatrix} = \begin{bmatrix} z_{11} & z_{12} \\ z_{21} & z_{22} \end{bmatrix} \cdot \begin{bmatrix} I_1 \\ I_2 \end{bmatrix}. \quad (3.8)$$

The z -parameters are also known as open-circuit parameters and the y -parameters are known as short-circuit parameters.

Equation (3.7) and (3.8) also show that the impedance matrix is the inverse matrix of the admittance matrix for a linear network:

$$[Z] = [Y]^{-1}. \quad (3.9)$$

The transfer matrix T , formed by ABCD parameters, is often used to define a two-port network [3, 78]. The voltage at load and source can be expressed by the transfer matrix according to the circuit theory as [3, 87]

$$\begin{bmatrix} V_1 \\ I_1 \end{bmatrix} = [T] \begin{bmatrix} V_2 \\ -I_2 \end{bmatrix} = \begin{bmatrix} A & B \\ C & D \end{bmatrix} \begin{bmatrix} V_2 \\ -I_2 \end{bmatrix}. \quad (3.10)$$

The power that the source supplies to the rest of circuit reaches maximum when [78]

$$V_1 = \frac{V_0}{2}. \quad (3.11)$$

Thus, the maximum supplied power P_m from the source and the power delivered to the load P_2 are [78]

$$P_m = \frac{|V_0|^2}{4R_1} \quad (3.12)$$

$$P_2 = \frac{|V_2|^2}{R_2}.$$

Therefore, the power transfer function is given as [78]

$$\frac{P_2}{P_m} = \left| 2 \sqrt{\frac{R_1}{R_2}} \cdot \frac{V_2}{V_0} \right|^2 = |t(s)|^2 \quad (3.13)$$

where $t(s)$ represents the transfer function of the linear network, s represents the frequency variable that $s = j\omega$. The magnitude squared transfer function can be represented by the characteristic function $K(s)$ which determines the response shape as [87]

$$|t(s)|^2 = \frac{1}{1 + \varepsilon^2 |K(s)|^2} \quad (3.14)$$

where ε is the ripple constant.

For the two-port network shown in Figure 3.2, the transfer function $t(s)$ can be represented by the one of the scattering parameters as [78]

$$|t(s)| = |S_{21}| \quad (3.15)$$

where S_{21} is the transmission coefficient of the network.

Since the voltages in Figure 3.2 are frequency dependent, the transmission coefficient is a function of frequency. From (3.13) (3.15), the transmission coefficient is expressed by [78, 88]

$$S_{21}(s) = 2 \sqrt{\frac{R_1}{R_2}} \cdot \frac{V_2(s)}{V_0(s)}. \quad (3.16)$$

Thus, the transmission coefficient S_{21} and the reflection coefficient S_{11} can be written as functions of ABCD parameters [3, 78, 89], respectively.

$$S_{21}(s) = \frac{2}{\sqrt{\frac{R_2}{R_1}} A + \frac{B}{\sqrt{R_1 R_2}} + \sqrt{R_1 R_2} C + \sqrt{\frac{R_1}{R_2}} D} \quad (3.17)$$

$$S_{11}(s) = \frac{\sqrt{\frac{R_2}{R_1}} A + \frac{B}{\sqrt{R_1 R_2}} - \sqrt{R_1 R_2} C - \sqrt{\frac{R_1}{R_2}} D}{\sqrt{\frac{R_2}{R_1}} A + \frac{B}{\sqrt{R_1 R_2}} + \sqrt{R_1 R_2} C + \sqrt{\frac{R_1}{R_2}} D} \quad (3.18)$$

The transmission coefficient, reflection coefficient and characteristic function of a linear, time-

invariant network may be defined as a ratio of two polynomials as [3, 78, 89]

$$S_{21}(s) = \frac{p(s)}{e(s)} \quad (3.19)$$

$$S_{11}(s) = \pm \frac{f(s)}{e(s)} \quad (3.20)$$

$$K(s) = \frac{f(s)}{p(s)} \quad (3.21)$$

where the polynomials $p(s)$ and $f(s)$ can be written as [9]

$$p(s) = \prod_{i=1}^m (s - s_{ti}) \quad (3.22)$$

$$f(s) = \prod_{i=1}^n (s - s_{ri})$$

where s_t and s_r represent transmission zeros and reflection zeros of the filter, respectively.

The following relationship exists for such a lossless network.

$$|S_{21}(s)|^2 + |S_{11}(s)|^2 = S_{21}(s)S_{21}(-s) + S_{11}(s)S_{11}(-s) = 1 \quad (3.23)$$

Alternatively, (3.23) can be written as

$$e(s)e(-s) = f(s)f(-s) + p(s)p(-s) \quad (3.24)$$

In addition, function $e(s)$ and $f(s)$ can be expressed in terms of ABCD parameters and $p(s)$ according to (3.17) - (3.21).

$$e(s) = \frac{p(s)}{2} \left(\sqrt{\frac{R_2}{R_1}} A + \frac{B}{\sqrt{R_1 R_2}} + \sqrt{R_1 R_2} C + \sqrt{\frac{R_1}{R_2}} D \right) \quad (3.25)$$

$$f(s) = \frac{p(s)}{2} \left(\sqrt{\frac{R_2}{R_1}} A + \frac{B}{\sqrt{R_1 R_2}} - \sqrt{R_1 R_2} C - \sqrt{\frac{R_1}{R_2}} D \right)$$

Parameter A, B, C and D can be derived from (3.24) (3.25) as functions of $p(s)$, $e(s)$ and $f(s)$. Parameter A and D are even while B and C are odd functions of the frequency variable for a reactive (lossless) network [3, 87]. Thus, the even and odd parts of $e(s)$ and $f(s)$ can be obtained for even and odd $p(s)$, i.e. the ABCD parameters (transfer matrix) can be derived for even, odd or mixed $p(s)$ in terms of even and odd parts of $e(s)$ and $f(s)$.

With the ABCD parameters, the admittance matrix Y of the two-port network can be derived as [3, 78]

$$[Y] = \begin{bmatrix} y_{11} & y_{12} \\ y_{21} & y_{22} \end{bmatrix} = \begin{bmatrix} \frac{D}{B} & \frac{BC - AD}{B} \\ -\frac{1}{B} & \frac{A}{B} \end{bmatrix}. \quad (3.26)$$

When $p(s)$ is an even function of s ,

$$[Y(s)] = \begin{bmatrix} \frac{1}{R_1} \frac{e_e - f_e}{e_o + f_o} & -\frac{1}{\sqrt{R_1 R_2}} \frac{p(s)}{e_o + f_o} \\ -\frac{1}{\sqrt{R_1 R_2}} \frac{p(s)}{e_o + f_o} & \frac{1}{R_2} \frac{e_e + f_e}{e_o + f_o} \end{bmatrix}. \quad (3.27)$$

When $p(s)$ is an odd function of s ,

$$[Y(s)] = \begin{bmatrix} \frac{1}{R_1} \frac{e_o - f_o}{e_e + f_e} & -\frac{1}{\sqrt{R_1 R_2}} \frac{p(s)}{e_e + f_e} \\ -\frac{1}{\sqrt{R_1 R_2}} \frac{p(s)}{e_e + f_e} & \frac{1}{R_2} \frac{e_o + f_o}{e_e + f_e} \end{bmatrix}. \quad (3.28)$$

When $p(s)$ is neither even nor odd function of s ,

$$[Y(s)] = \begin{bmatrix} \frac{1}{R_1} \frac{p_e(e_e - f_e) + p_o f_o}{p_e(e_o + f_o) - p_o(e_e + f_e)} & \frac{1}{\sqrt{R_1 R_2}} \frac{(p_e - p_o)(p_e + p_o)}{p_o(e_e + f_e) - p_e(e_o + f_o)} \\ \frac{1}{\sqrt{R_1 R_2}} \frac{(p_e - p_o)(p_e + p_o)}{p_o(e_e + f_e) - p_e(e_o + f_o)} & \frac{1}{R_2} \frac{p_e(e_e + f_e) - p_o(e_o + f_o)}{p_e(e_o + f_o) - p_o(e_e + f_e)} \end{bmatrix} \quad (3.29)$$

where the subscript ‘ o ’ corresponds to the odd part of the functions and the subscript ‘ e ’ corresponds to the even part of the functions.

3.3.2 Coupling matrix synthesis for symmetric frequency response

This section shows the synthesis procedure of coupling matrix proposed by Atia and Williams [12, 13] for symmetrical filter responses. Figure 3.3 shows the equivalent circuit of n -loop coupled resonator circuit. The resonators are identical, are all assumed tuned to the normalised centre frequency $\omega_0 = 1$, and to have normalised characteristic impedance $z_0 = 1$ [13].

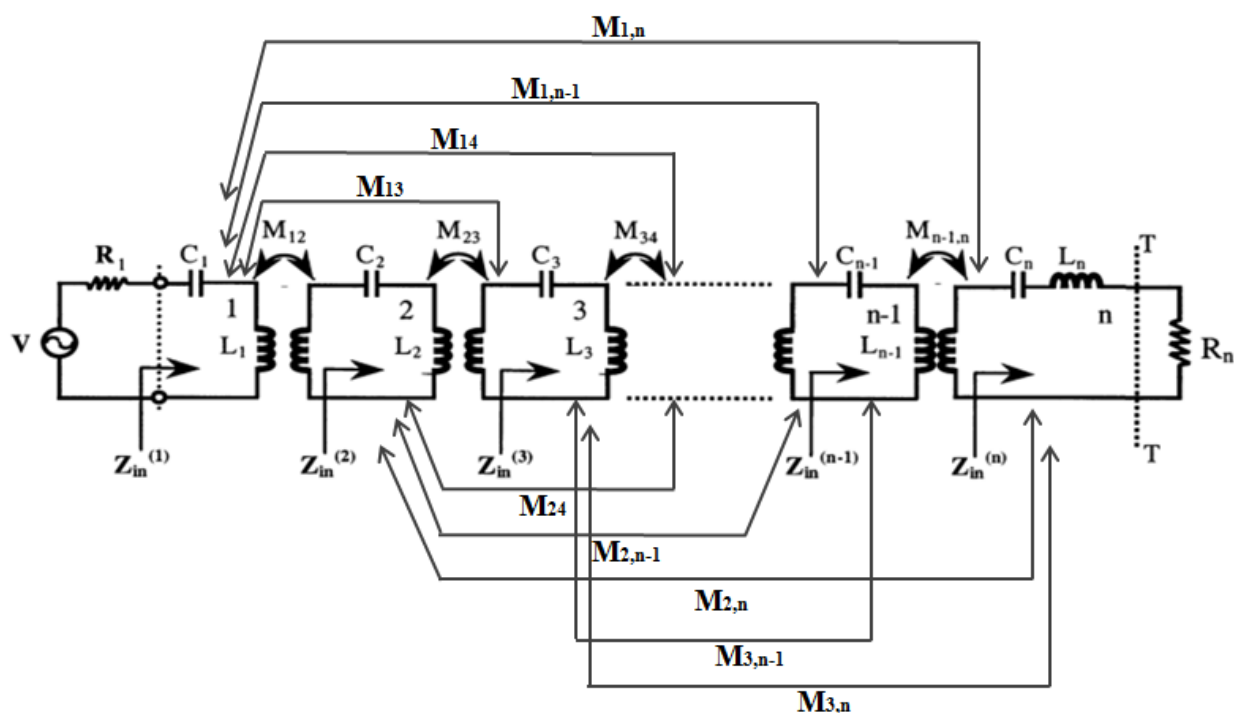


Figure 3.3 Equivalent-circuit of n -loop coupled resonator circuit.

By assuming the coupling matrix M is purely real and frequency independent for frequencies near resonance ω_0 , which implies a narrow-band approximation, the impedance matrix of the n -loop coupled resonator circuit can be written as [13]

$$Z_{loop}(P) = P I_n + jM \quad (3.30)$$

where P is a bandpass frequency variable that $P = -j(s + s^{-1})$, I_n is an identity matrix of order n , M is the $n \times n$ symmetric coupling matrix.

The coupling matrix M of the circuit is a symmetric matrix that can be diagonalised to its (real) eigenvalues by a real orthogonal matrix T as [13]

$$M = -T\Lambda T^t \quad (3.31)$$

where $TT^t = I$, $\Lambda = \text{diag}[\lambda_1, \dots, \lambda_n]$; $\lambda_1, \dots, \lambda_n$ are the eigenvalues of M , and n is the order of the matrices.

Thus the admittance matrix is [13]

$$Y_{loop}(P) = (P I_n + jM)^{-1} = T \text{diag} \left[\frac{1}{P - j\lambda_1}, \dots, \frac{1}{P - j\lambda_n} \right] T^t = \sum_{k=1}^n \frac{K^{(k)}}{P - P_k}. \quad (3.32)$$

The residues $K^{(k)}$ and poles P_k can be calculated if y-parameters are known, which results in the residues series $K^{(k)}$, $K^{(k)'}$ and $K^{(k)''}$ shown in (3.33) - (3.35) [13].

$$y_{11}(P) = \sum_{k=1}^n \frac{K^{(k)}}{P - P_k} = \sum_{k=1}^n \frac{T_{1k}^2}{P - P_k} \quad (3.33)$$

$$y_{21}(P) = y_{12}(P) = \sum_{k=1}^n \frac{K^{(k)'}}{P - P_k} = - \sum_{k=1}^n \frac{T_{1k}T_{nk}}{P - P_k} \quad (3.34)$$

$$y_{22}(P) = \sum_{k=1}^n \frac{K^{(k)''}}{P - P_k} = \sum_{k=1}^n \frac{T_{nk}^2}{P - P_k} \quad (3.35)$$

These y-parameters can be obtained from the (3.36) - (3.38), by using bandpass frequency variable P instead of frequency variable s in the admittance matrices (3.27) - (3.29).

When $p(P)$ is an even function of P ,

$$[Y(P)] = \begin{bmatrix} \frac{1}{R_1} \frac{e_o - f_o}{e_e + f_e} & - \frac{j}{\sqrt{R_1 R_2}} \frac{p(P)}{e_e + f_e} \\ - \frac{j}{\sqrt{R_1 R_2}} \frac{p(P)}{e_e + f_e} & \frac{1}{R_2} \frac{e_o + f_o}{e_e + f_e} \end{bmatrix}. \quad (3.36)$$

When $p(P)$ is an odd function of P ,

$$[Y(P)] = \begin{bmatrix} \frac{1}{R_1} \frac{e_e - f_e}{e_o + f_o} & -\frac{j}{\sqrt{R_1 R_2}} \frac{p(P)}{e_o + f_o} \\ -\frac{j}{\sqrt{R_1 R_2}} \frac{p(P)}{e_o + f_o} & \frac{1}{R_2} \frac{e_e + f_e}{e_o + f_o} \end{bmatrix}. \quad (3.37)$$

When $p(P)$ is neither even nor odd function of P ,

$$[Y(P)] = \begin{bmatrix} \frac{1}{R_1} \frac{p_e(e_e - f_e) + p_o f_o}{p_e(e_o + f_o) - p_o(e_e + f_e)} & \frac{j}{\sqrt{R_1 R_2}} \frac{(p_e - p_o)(p_e + p_o)}{p_o(e_e + f_e) - p_e(e_o + f_o)} \\ \frac{j}{\sqrt{R_1 R_2}} \frac{(p_e - p_o)(p_e + p_o)}{p_o(e_e + f_e) - p_e(e_o + f_o)} & \frac{1}{R_2} \frac{p_e(e_e + f_e) - p_o(e_o + f_o)}{p_e(e_o + f_o) - p_o(e_e + f_e)} \end{bmatrix} \quad (3.38)$$

where the subscript ‘ o ’ corresponds to the odd part of the functions and the subscript ‘ e ’ corresponds to the even part of the functions.

With the y -parameters obtained from the admittance matrices (3.36) - (3.38), the residues $K^{(k)}$ and poles P_k can be obtained by applying (3.32) - (3.35).

Then, the first and last rows of the orthogonal matrix T can be obtained as [13]

$$\begin{aligned} T_{1k} &= \sqrt{K^{(k)}} \\ -T_{1k} T_{nk} &= K^{(k)'} \end{aligned} \quad (3.39)$$

Atia and Williams showed that the other rows of the orthogonal matrix T are constructed by applying Gram-Schmidt procedure [13]. Once the poles P_k are known, the elements λ_k of the diagonal matrix Λ can be obtained. After that, the coupling matrix M can be obtained by applying (3.31).

However, the derived coupling matrix M is a normalised matrix so that it should be denormalised to realise a realistic coupling matrix by

$$M' = M \cdot \text{FBW} \quad (3.40)$$

where M' represents the denormalised coupling matrix and FBW is the fractional bandwidth.

The sum of the normalised source and load resistances are equal and are related to $e(s)$ indicated in (3.23) [13].

$$R_1 + R_2 = \text{Coefficient of the 2nd highest order of } e(s). \quad (3.41)$$

If $e(s)$ and the ratio R_1/R_2 are known, these resistances can be determined.

From the filter characteristics, not only the coupling matrix, but also the external quality-factor can be derived. The external couplings from source and from the load are identical for most of cases. The denormalised external coupling coefficient Q_e is derived by [13]

$$Q_e = \frac{1}{R \cdot \text{FBW}} \quad (3.42)$$

where R is the normalised source and load resistances. For most microwave filters, the load resistance equals to the source resistance, i.e. $R_1 = R_2 = R$, and the values of resistance are normalised to 50 Ω .

3.3.3 Coupling matrix synthesis for asymmetric frequency response

Cameron [14] provided a method to synthesis the coupling matrix for asymmetric frequency responses based on the driving point impedance. In the two-port network shown in Figure 3.2, the following network equations exist.

$$V_1 = I_1 \left(z_{11} - \frac{z_{12}z_{21}}{z_{22} + R_2} \right) \quad (3.43)$$

where z_{11} , z_{12} , z_{21} , z_{22} are the z -parameters in the impedance matrix Z .

The driving point impedance Z_{in} at port 1 is given by [14]

$$Z_{in}(s) = \frac{V_1(s)}{I_1(s)} = z_{11} - \frac{z_{12}z_{21}}{z_{22} + R_2} = \frac{z_{11} \cdot \left[\left(z_{22} - \frac{z_{12}z_{21}}{z_{11}} \right) + R_2 \right]}{z_{22} + R_2} \quad (3.44)$$

Meanwhile, using ABCD parameters and y -parameter,

$$\left(z_{22} - \frac{z_{12}z_{21}}{z_{11}} \right) = \frac{B}{A} = \frac{1}{y_{22}}. \quad (3.45)$$

Substitute (3.45) into (3.44),

$$Z_{in}(s) = \frac{z_{11} \cdot \left[\frac{1}{y_{22}} + R_2 \right]}{z_{22} + R_2}. \quad (3.46)$$

The driving point impedance Z_{in} at port 1 is also given by reflection coefficient $S_{11}(s)$ [14]

$$Z_{in}(s) = \frac{1 - S_{11}(s)}{1 + S_{11}(s)} R_1 = \frac{e(s) \pm f(s)}{e(s) \mp f(s)} R_1 = \frac{m_1 + n_1}{m_2 + n_2} R_1 \quad (3.47)$$

where m_1 , m_2 , n_1 , and n_2 are complex-even and complex-odd polynomials of frequency variable s , respectively.

If $R_1=R_2=1 \Omega$, for even order case of m_1 , m_2 , n_1 , and n_2 , (3.47) yields [14]

$$Z_{in}(s) = \frac{n_1 \left(\frac{m_1}{n_1} + 1 \right)}{m_2 + n_2}. \quad (3.48)$$

From (3.46) (3.48), y_{22} can be obtained as [14]

$$y_{22} = \frac{n_1}{m_1} \quad (3.49)$$

Since the denominator of y_{21} is the same as that of y_{22} and the numerator of y_{21} has the same transmission zeros as $S_{11}(s)$, y_{21} can be written as [14]

$$y_{21} = \frac{p(s)}{m_1}. \quad (3.50)$$

Similarly, for the odd order case of m_1 , m_2 , n_1 , and n_2 , [14]

$$y_{22} = \frac{m_1}{n_1} \quad (3.51)$$

$$y_{21} = \frac{p(s)}{n_1}.$$

The complex-even and complex-odd polynomials m_1 and n_1 can then be obtained from $e(s)$ and $f(s)$ as [14]

$$\begin{aligned}
m_1 &= \text{Re}(e_0 + f_0) + \text{Im}(e_1 + f_1)s + \text{Re}(e_2 + f_2)s^2 + \dots \\
n_1 &= \text{Im}(e_0 + f_0) + \text{Re}(e_1 + f_1)s + \text{Im}(e_2 + f_2)s^2 + \dots
\end{aligned} \tag{3.52}$$

where e_i and f_i are the i^{th} complex coefficients of $e(s)$ and $f(s)$, and $i=0,1,2,\dots, N$.

With the known y -parameters, the eigenvalues and residues of the coupling matrix M can be derived according to (3.32) - (3.35). Then, applying (3.39), the first and last rows (T_{1k} and T_{nk}) are obtained. Therefore, the coupling matrix M can be obtained by applying Gram-Schmidt procedure proposed in [13].

The source and load resistances may be found by [14]

$$R_1 = \sum_{k=1}^n T_{1k}^2 \quad \text{and} \quad R_2 = \sum_{k=1}^n T_{nk}^2. \tag{3.53}$$

These resistances will then be used to extract the external Q factor according to (3.42).

3.3.4 Coupling matrix reduction

The derived coupling matrix M in the previous sections includes the couplings among all resonators, i.e. it has the maximum number of possible couplings. However, it is not always possible to consider all couplings in practice as a number of the couplings may tend to zero due to the filter topology and coupling structures. Consequently, a method that annihilates some of the couplings without upsetting the filter performance is required.

Cameron [14] gives a method to annihilate elements in a coupling matrix. When annihilating the element M_{kj} (and simultaneously the element M_{jk}), a number i is selected which leads to that the elements in row and column of i may change as well as those in rows and columns of j and k ($i, j \neq 1$ or n ; $i \neq j$; $k \neq i, j$). The transformed matrix M' is calculated according to the following formula:

$$M' = R \cdot M \cdot R^t \tag{3.54}$$

where R is an $n \times n$ rotation matrix and R^t is the transpose of R .

The rotation matrix R has a principal diagonal of 1 except R_{ii} and R_{jj} . All other elements apart from R_{ii} and R_{jj} are zeros. The elements R_{ii} and R_{jj} are calculated by [14]

$$R_{ii} = R_{jj} = \cos\theta, \quad R_{ji} = -R_{ij} = \sin\theta \quad (3.55)$$

where $\theta = -\tan^{-1} \left(\frac{M_{jk}}{M_{ik}} \right)$ and $i, j \neq 1 \text{ or } n; i \neq j; k \neq i, j$.

The transformed coupling matrix has the same eigenvalues as the original coupling matrix [14]. The coupling matrix is transformed until a convenient form for practical design is realised, including a folded form [90] and right-column-justified form [91]. The coupling matrix reduction procedure can be realised by computer programs to iteratively annihilate the elements, according to the filter topology and necessary couplings.

It is noted that when annihilating more than one element of the original coupling matrix, the above transformation procedures must be repeated to annihilate the elements one by one. Also the transformations must be in a certain order to ensure the annihilated element is not regenerated by any subsequent transform in the sequence [14]. The annihilation normally follows from right to left along rows and top to bottom along columns. For example, firstly, elements in the first row are annihilated one by one from right to left. Secondly, elements in the last (n^{th}) column are annihilated one by one from top to bottom. Then, elements in the second row are annihilated following by elements in the $(n-1)^{\text{th}}$ column.

However, the above coupling matrix generation and reduction based on similarity transformation is time consuming and limited to certain filter topologies and selected filter orders. Gajaweera and Lind [19, 30, 31] stated a method to describe the physically realisable coupling matrix generation by a system of non-linear equations which can be solved by applying the Newton-Raphson procedure that converges rapidly near a solution. It is noted that the method also uses the coupling synthesis presented in Section 3.3.3 to obtain the first and last rows of the orthogonal matrix. However, the rest of rows are obtained by solving the system of non-linear equations using Newton-Raphson method. This method not only improves the computation time compared to Gram-Schmidt procedure proposed in [13], but also directly generates the reduced and physically realisable coupling matrix. Additionally, Gajaweera [19] showed that the Newton-Raphson method can be extended to any filter topology of any order as long as there is sufficient number of non-zero couplings. Gajaweera has provided a MATLAB program that generates reduced coupling matrices using the Newton-Raphson method through private communication. It was used to generate the coupling matrices for dual-band bandpass filter designs in Section 3.4.

3.4 Design process and filter examples

The design procedure of dual-passband response synthesis for filter realisation is shown in Figure 3.4. Firstly, a normalised single-passband response in the Ω domain is selected. The pure imaginary transmission and reflection zeros of the response in the Ω domain can then be analytically obtained. Secondly, the transmission and reflection zeros in the Ω domain are transformed into the Ω' domain using the frequency transformation technique expressed by (3.1) and (3.3). With the transformed transmission and reflection zeros, the polynomials to form the transfer function are obtained using the Ω' domain expression of (3.22). Then, the transfer function in the Ω' domain can be analytically obtained, from which the normalised coupling matrix of filter is synthesised. The coupling matrix is synthesised using theories and methods in Section 3.3. Some elements of the coupling matrix are preferably annihilated based on the coupling topology of the filter. Finally, the dual-band bandpass filter can be physically realised with the general design process of single-band bandpass filter.

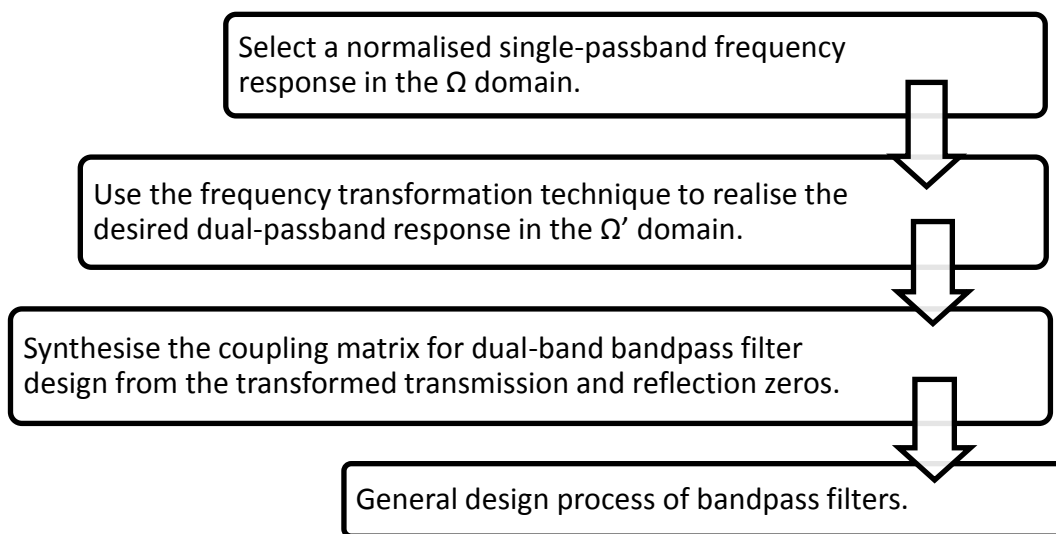


Figure 3.4 General process of dual-passband response synthesis method for the filter realisation.

3.4.1 An eighth order dual-band BPF

A dual-band bandpass filter is designed to demonstrate the synthesis theory. An eighth-order dual-band symmetrical frequency response with a minimum passband return loss of 20 dB and a minimum stopband attenuation of 30 dB is required. The passbands are selected as 3.90-3.95 and 4.05-4.10 GHz for satellite communication.

Coupling matrix generation and equivalent circuit simulation

A symmetrical four-pole generalised Chebyshev response with transmission zeros at $S=\pm j2.1$, $\pm j\infty$ in the Ω domain is used as the normalised low pass response, shown in Figure 3.5.

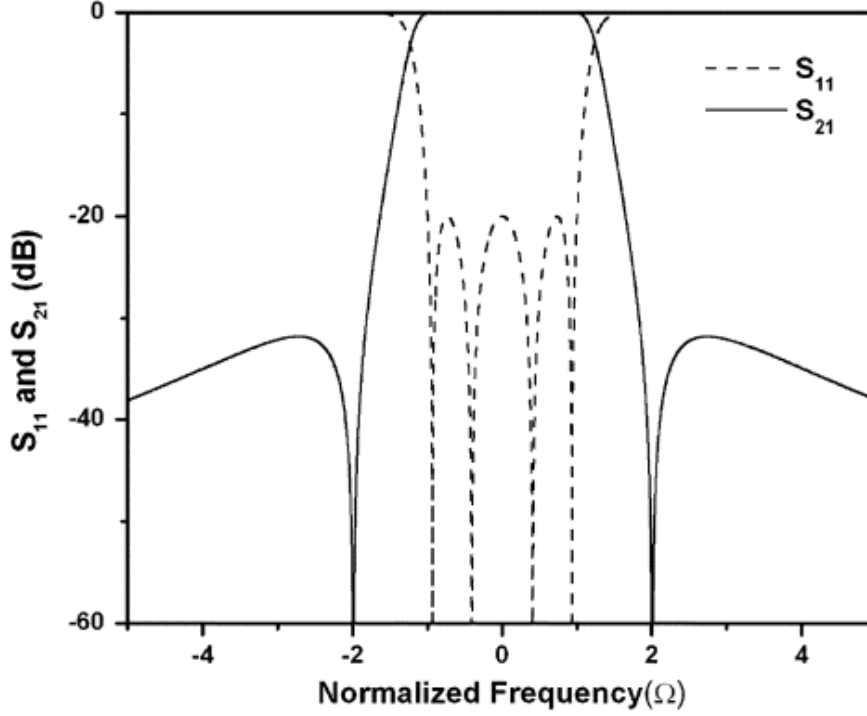


Figure 3.5 Frequency response of the four-pole Chebyshev prototype in Ω domain.

The band edge frequencies of the dual-passband filter are determined from the filter specification, which are $\omega_{b1}=3.90$ GHz, $\omega_{b2}=4.10$ GHz, $\omega_{a1}=3.95$ GHz, $\omega_{a2}=4.05$ GHz. Thus, from (3.6), the band edge frequency in the Ω' domain is $\Omega'_m=0.5$.

The reflection zeros can be found for a given set of transmission zeros, since the characteristic function of the generalised Chebyshev response is known. Using the frequency transformation expressed by (3.1) in Section 3.2, the transmission and reflection zeros of the symmetrical response in the Ω' domains are:

Transmission zeros: $\pm j1.4057, \pm j0.3557, \pm j0, \pm j\infty$;

Reflection zeros: $\pm j0.9776, \pm j0.8152, \pm j0.6134, \pm j0.5115$.

Using the Ω' domain expression of (3.22) and the transfer function expressed by (3.19), the transformed frequency response in the Ω' domain can be obtained.

Figure 3.6 shows the transformed frequency response in the Ω' domain.

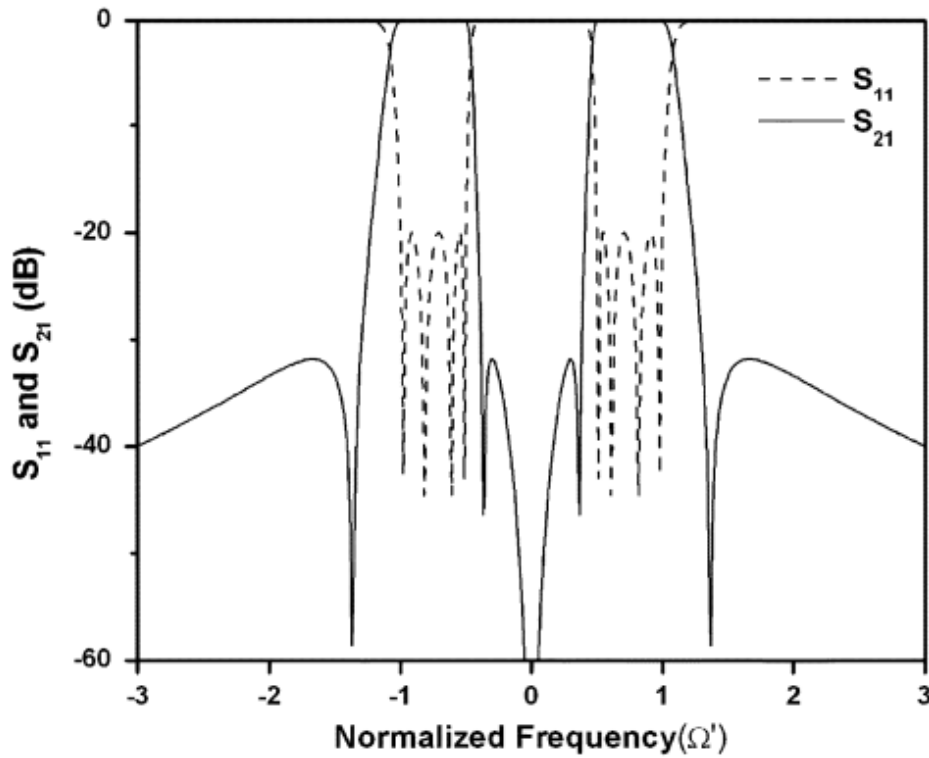


Figure 3.6 Dual-band frequency response after frequency transformation in Ω' domain.

Figure 3.7 shows a canonical coupling topology of the eighth order filter.

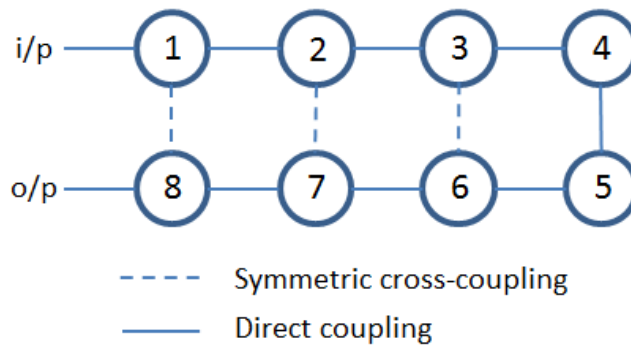


Figure 3.7 Canonical coupling topology of the eighth-order filter.

The non-adjacent couplings and diagonal cross couplings are neglected i.e. the elements representing non-adjacent couplings and diagonal couplings in the coupling matrix are set as zeros. The coupling matrix is then synthesised using the MATLAB program provided by Gajaweera.

The synthesised coupling matrix and the normalised terminal resistance are given as

$$M = \begin{bmatrix} 0 & 0.8317 & 0 & 0 & 0 & 0 & 0 & -0.0761 \\ 0.8317 & 0 & -0.4093 & 0 & 0 & 0 & 0.1053 & 0 \\ 0 & -0.4093 & 0 & 0.4974 & 0 & 0.5020 & 0 & 0 \\ 0 & 0 & 0.4974 & 0 & -0.2273 & 0 & 0 & 0 \\ 0 & 0 & 0 & -0.2273 & 0 & 0.4974 & 0 & 0 \\ 0 & 0 & 0.5020 & 0 & 0.4974 & 0 & -0.4093 & 0 \\ 0 & 0.1053 & 0 & 0 & 0 & -0.4093 & 0 & 0.8317 \\ -0.0761 & 0 & 0 & 0 & 0 & 0 & 0.8317 & 0 \end{bmatrix} \quad (3.56)$$

$$R = 0.5251 \text{ Ohm.} \quad (3.57)$$

Therefore, applying (3.40) (3.42), the denormalised coupling matrix and the external quality factor are obtained, respectively.

$$K = \begin{bmatrix} 0 & 0.0416 & 0 & 0 & 0 & 0 & 0 & -0.0038 \\ 0.0416 & 0 & -0.0205 & 0 & 0 & 0 & 0.0053 & 0 \\ 0 & -0.0205 & 0 & 0.0249 & 0 & 0.0251 & 0 & 0 \\ 0 & 0 & 0.0249 & 0 & -0.0114 & 0 & 0 & 0 \\ 0 & 0 & 0 & -0.0114 & 0 & 0.0249 & 0 & 0 \\ 0 & 0 & 0.0251 & 0 & 0.0249 & 0 & -0.0205 & 0 \\ 0 & 0.0053 & 0 & 0 & 0 & -0.0205 & 0 & 0.0416 \\ -0.0038 & 0 & 0 & 0 & 0 & 0 & 0.0416 & 0 \end{bmatrix} \quad (3.58)$$

$$Q_e = \frac{1}{R \cdot \text{FBW}} = 38.1 \quad (3.59)$$

An equivalent circuit of the filter has been created and simulated in Keysight ADS, using LC elements and admittance inverters to represent the resonators and couplings, respectively. Figure 3.8 shows the equivalent circuit of the eighth order filter in Keysight ADS.

The relevant parameters of the circuit are calculated by [78].

$$J_{01} = \sqrt{\frac{R}{50}}, J_{ij} = M_{ij} \text{ for } i \text{ and } j \neq 0, \quad (3.60)$$

$$L = \frac{\text{FBW}}{2\pi f} \text{ and } C = \frac{1}{2\pi \cdot \text{BW}}$$

where J_{01} and J_{ij} represents the J-values of the admittance inverters for external coupling and the inter-resonator coupling; R is the terminal resistance; M_{ij} is the element obtained from normalised coupling matrix M ; L and C represent the equivalent inductance and capacitance of the LC resonator; BW and FBW represent the overall bandwidth and fractional bandwidth of the transformed dual-band response, respectively.

According to the design passbands, $f=4.0$ GHz, $\text{BW}=200$ MHz, and $\text{FBW}=0.05$.

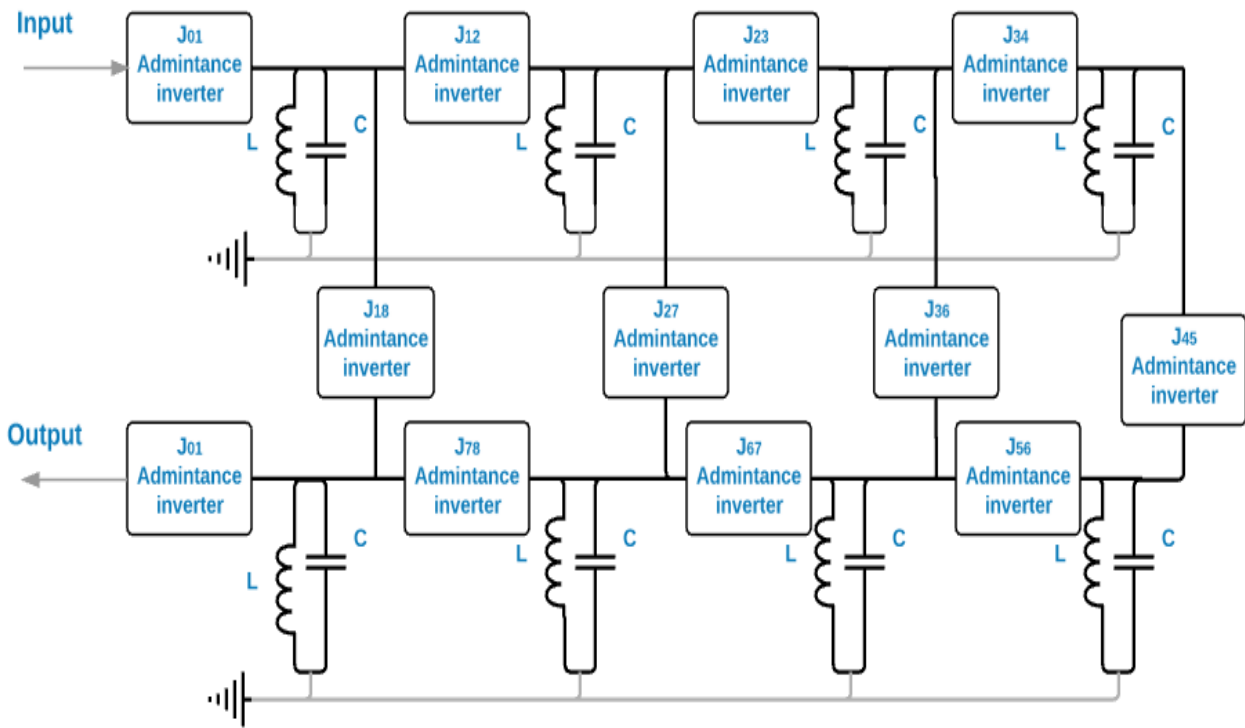


Figure 3.8 Equivalent circuit of the eighth order filter in Keysight ADS.

Figure 3.9 shows the simulated frequency response with infinite unloaded Q factor of the LC resonators, which has similar shape of response of the normalised dual-band frequency response in Figure 3.6. It shows that the passbands at 3.893 - 3.953 GHz and 4.055 - 4.118 GHz. There is very slight difference (less than 1% for both bandwidths and centre frequencies) of passbands in comparison with the filter specification and synthesised dual-band response, generated by the rapid convergent solutions in coupling matrix synthesis.

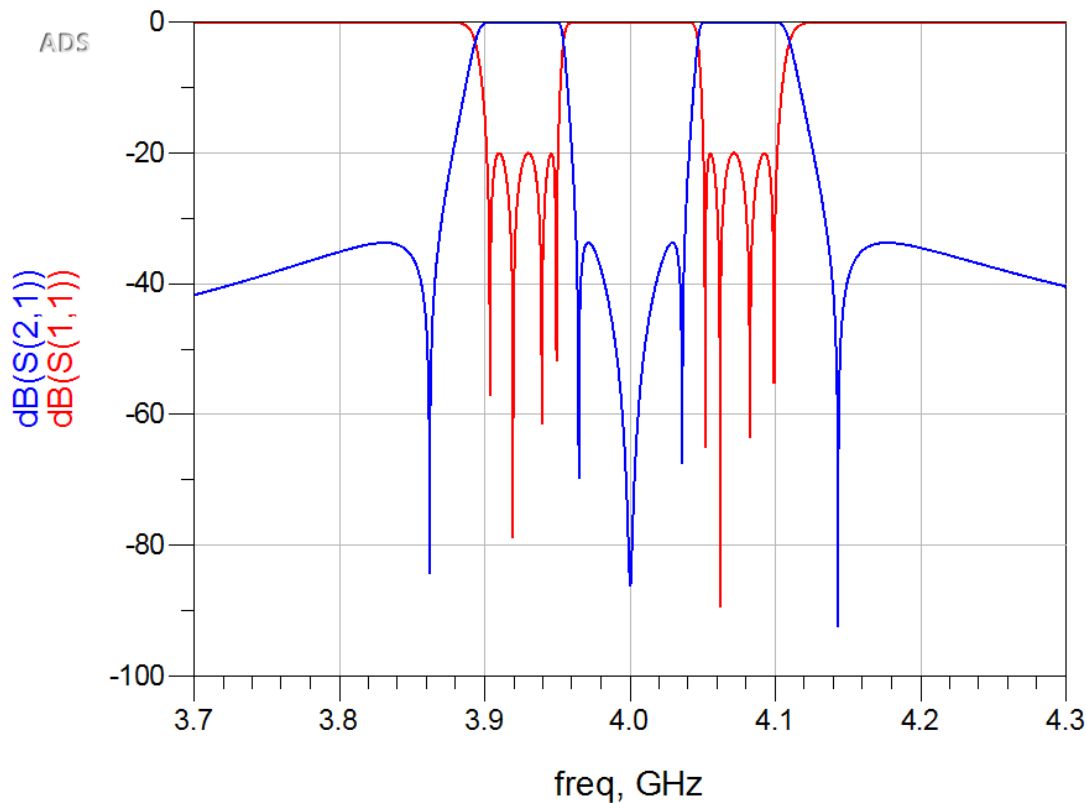


Figure 3.9 Simulated frequency response of the equivalent circuit with an infinite unloaded Q factor.

Resonator and filter topology characterisation

Microstrip square open-loop resonators have been used in [2, 10, 63, 92, 93] for filter design. It is a folded half-wavelength resonator on microstrip substrate, which has the advantages in size, weight, and cost. Most importantly, the coupled microstrip square open-loop resonators could be separated by a spacing s but with different orientations, which realise different types of coupling. Figure 3.10 shows four typical coupling orientations that realise electric coupling, magnetic coupling, and mixed coupling.

These resonators have the maximum electric field density at the gap side and the maximum magnetic field density on the opposite side [2, 63]. Therefore, for the topology in Figure 3.10(a), the electric coupling is strong whereas the magnetic coupling is negligible. For Figure 3.10(b), the magnetic coupling is strong whereas the electric coupling is negligible. However, for the topologies in Figure 3.10(c) and (d), the magnetic coupling and electric coupling coexist and are comparable. Hong and Lancaster [2] stated that the electric coupling is dominant in a certain distance while the magnetic coupling is dominant beyond that distance for the (d) type mixed coupling, because the electric coupling fades faster than the magnetic coupling with the

increase of distance between resonators.

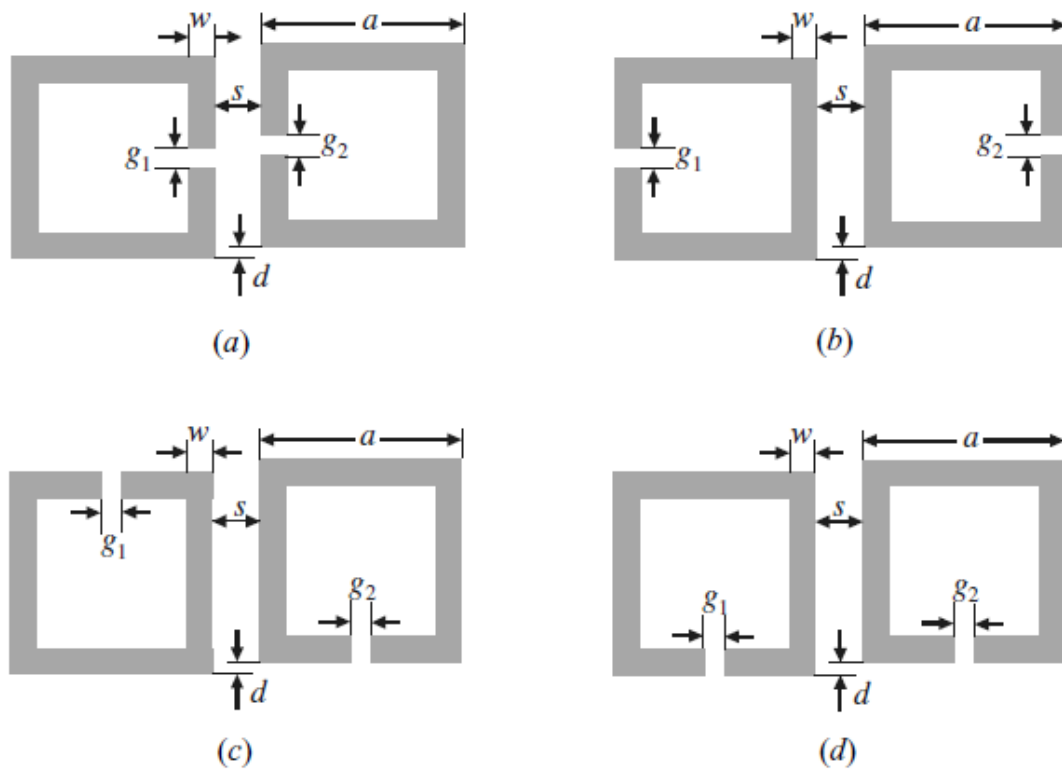


Figure 3.10 Topology of coupled square open-loop resonators [2]. (a) electric coupling. (b) magnetic coupling. (c) and (d) mixed coupling.

It is possible to realise the filter employing (a) (b) and (d) type of inter-resonator coupling structure as Figure 3.11 shows, if assuming that the positive elements in the coupling matrix M' represent electric coupling and the negative ones represent magnetic coupling.

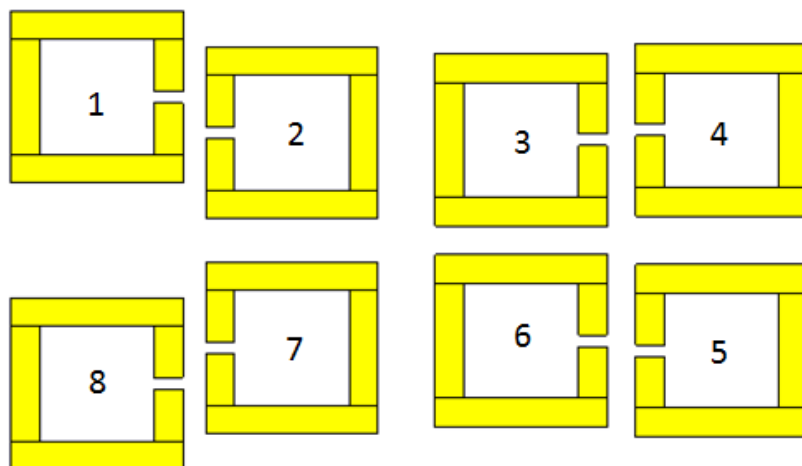


Figure 3.11 The topology of the eighth order filter.

Microstrip square open-loop resonators were used to implement this dual-band BPF. The microstrip substrate was a 1.27 mm thick RO 3006 laminate from Rogers Corporation. The substrate RO 3006 has a dielectric constant of 6.5 so that the resonator and filter can be made relatively small. The circumference of the resonator is about half of the guided wavelength. The width of the strip line forming the square loop was chosen as 1.0 mm, considering the 0.1 mm fabrication tolerance. The gap distance (g) and one-sided strip line length (a) were determined from EM simulation by CST MW. In order to realise a resonance at 4.0 GHz and considering the 0.1 mm fabrication tolerance, we determined that $g = 0.4$ mm and $a = 5.9$ mm, respectively. The unloaded Q factor of the resonator was also obtained from EM simulation in CST MW, which is about 280. As this was the one of the first designs produced by the author, the microstrip square open-loop resonator was not fabricated and tested at that time.

External coupling structure

The external coupling structure for microstrip resonator is usually realised by a direct tapped microstrip line [2, 10, 63, 64, 92, 93] or a parallel coupled microstrip line [94-97]. When using parallel-coupled microstrip line to achieve strong external coupling, the distance between the parallel-coupled line and resonator would be very small so that it may not be practically realisable considering the fabrication tolerance. Considering the 0.1 mm fabrication tolerance for microstrip line and distance, we selected to use direct tapping for this filter design. The external coupling was realised by a 50 Ohm tapped microstrip line on the square open-loop resonator. Figure 3.12 shows the external coupling structure and profile of the external Q factor. The tapping distance (t) controls the intensity of external coupling. The external quality factor Q_e was obtained from the simulated S_{11} parameter by applying (2.42).

Inter-resonator coupling structure

The inter-resonator coupling profiles were required to determine the coupling dimensions. Two coupled resonators were simulated in CST MW with loose coupling from the external source/load. Hong and Lancaster [2] stated that the shift distance (d) between the resonators has small effects on the coupling coefficient. Therefore, the simulation did not involve the shift distance. The distance (s) between coupled resonators was the only parameter that controls the coupling. As the coupling structures are symmetric, (2.62) was used to compute the coupling coefficient. The simulation result showed two peaks of S_{21} parameters near the 4.0 GHz resonant frequency, which represents the characteristic frequencies f_e and f_m in (2.62).

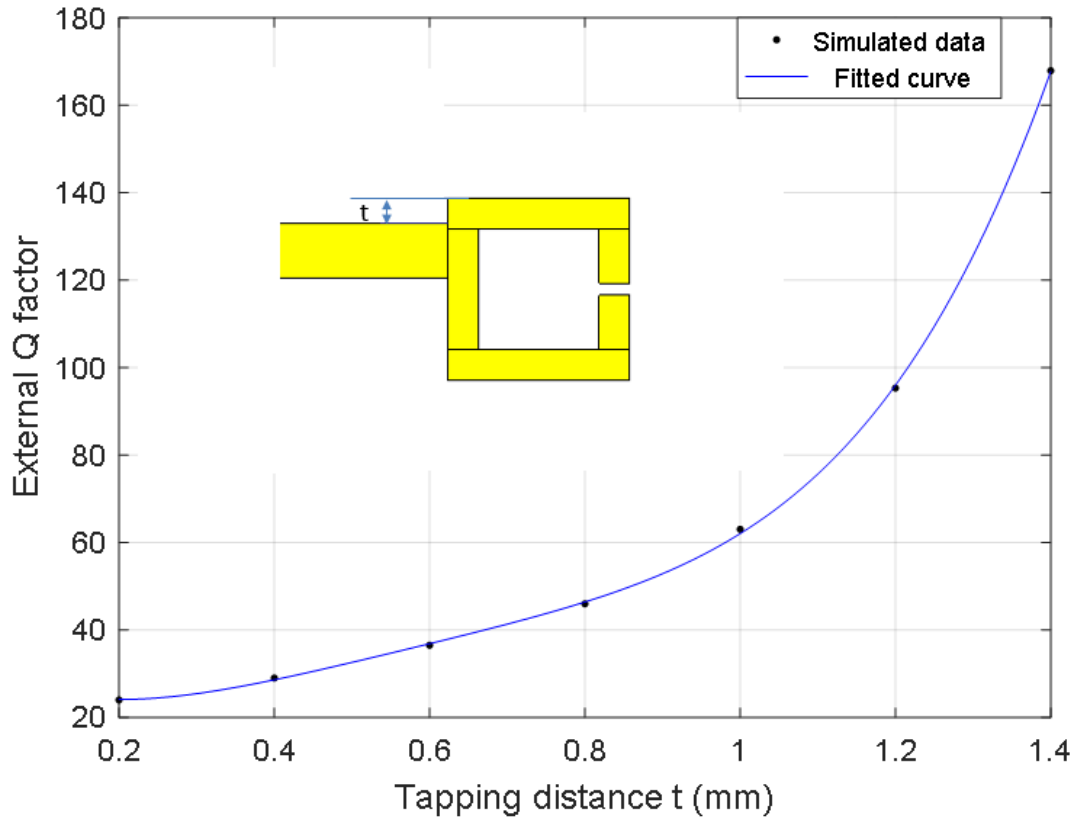


Figure 3.12 External quality factor profile of the resonator.

Figure 3.13 - Figure 3.16 shows the coupling profiles of electric coupling, magnetic coupling and mixed coupling, respectively. It is noted that the coupling coefficients in Figure 3.13 - Figure 3.16 are the absolute values.

The fitted curves in Figure 3.13 and Figure 3.14 show that the electric and magnetic coupling decays exponentially against the distance between resonators because of exponential decay of the field density, respectively. These coupling profiles have good agreement with [2, 63, 92].

Figure 3.15 and Figure 3.16 shows that the electric coupling is dominant for the small coupling spacing ($s < 1.8$ mm) whereas the magnetic coupling becomes dominant when the spacing is larger ($s > 1.8$ mm). The magnetic coupling and the electric coupling cancel each other out in (d) type mixed coupling. When the coupling spacing is within a range of 1.8 – 2.2 mm, the magnetic coupling becomes dominant. The electric coupling is comparably smaller than the magnetic coupling but fades faster than the magnetic coupling. This causes the mixed coupling coefficient increases against the coupling distance (s) within the range $1.8 \text{ mm} \leq s \leq 2.2 \text{ mm}$. Beyond 2.2 mm, the electric coupling is no longer comparable to the magnetic coupling so that the mixed coupling coefficient decays exponentially against the coupling distance. The profiles of the mixed coupling also agree with the observation of the profiles in [2, 63, 92].

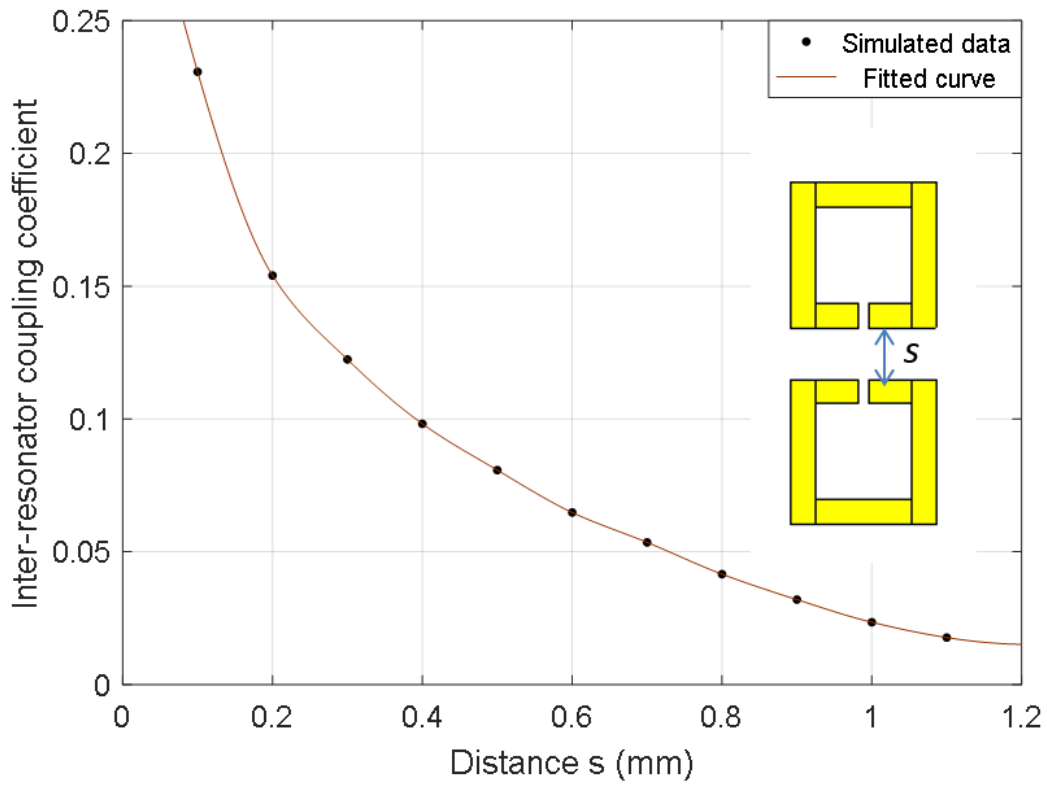


Figure 3.13 Inter-resonator coupling profile for the (a) type electric coupling.

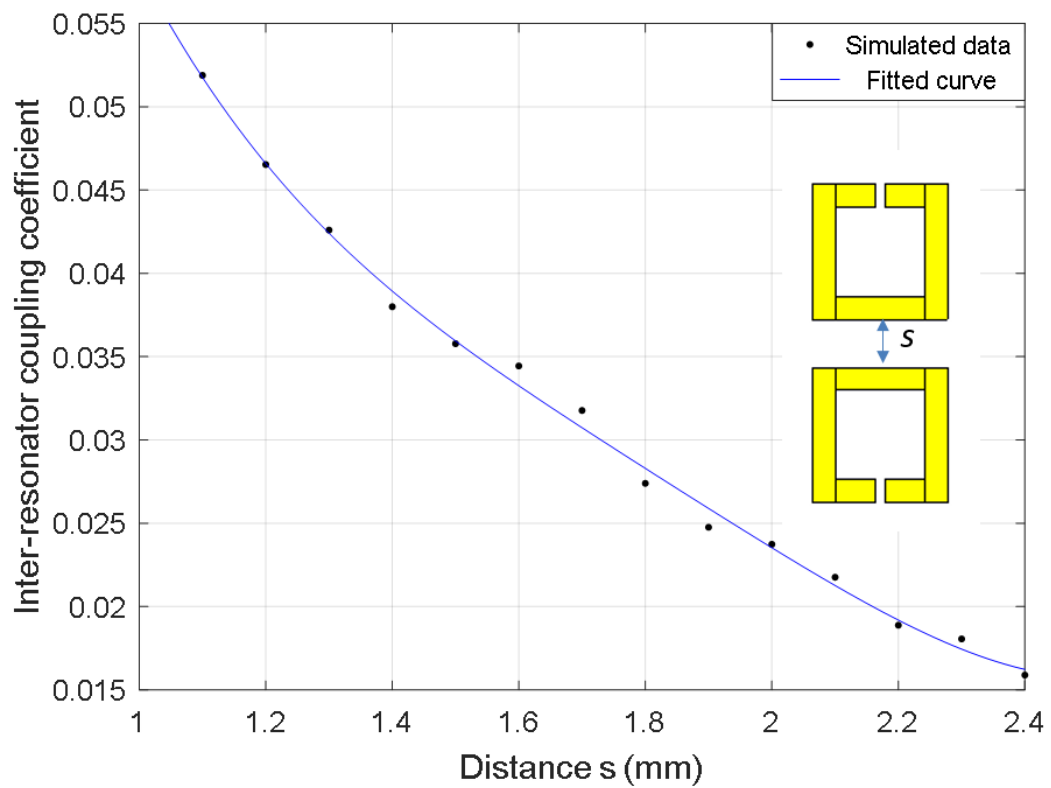


Figure 3.14 Inter-resonator coupling profile for the (b) type magnetic coupling.

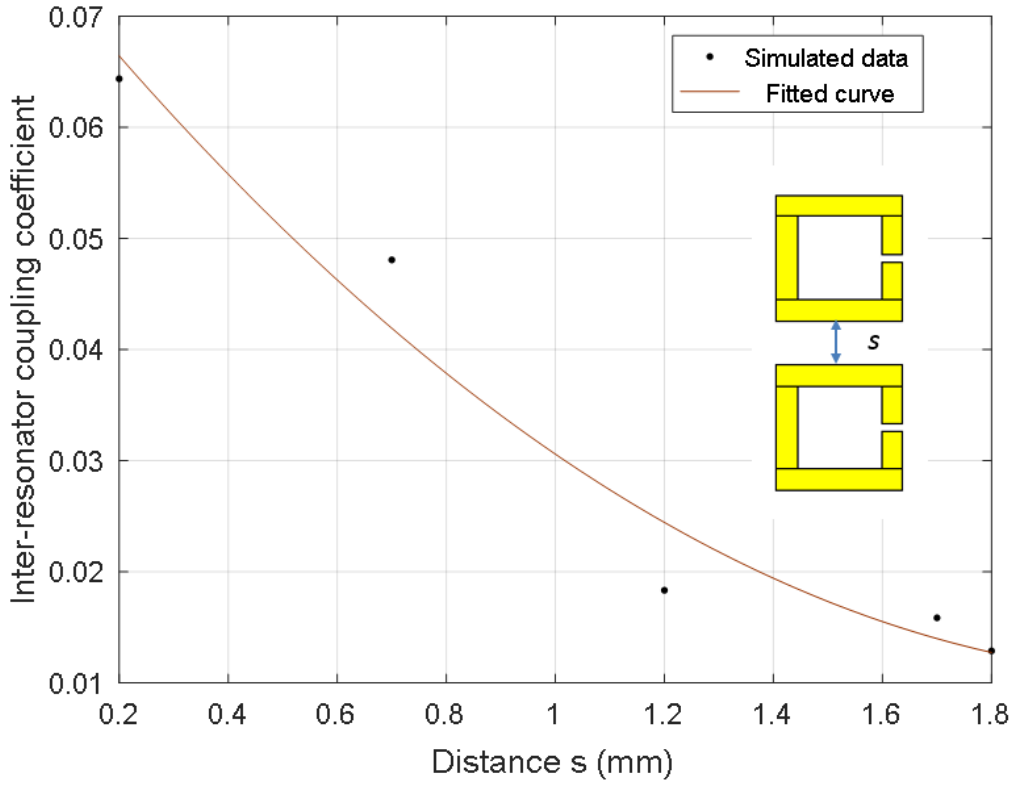


Figure 3.15 Inter-resonator coupling profile for the (d) type mixed coupling - electric coupling dominant.

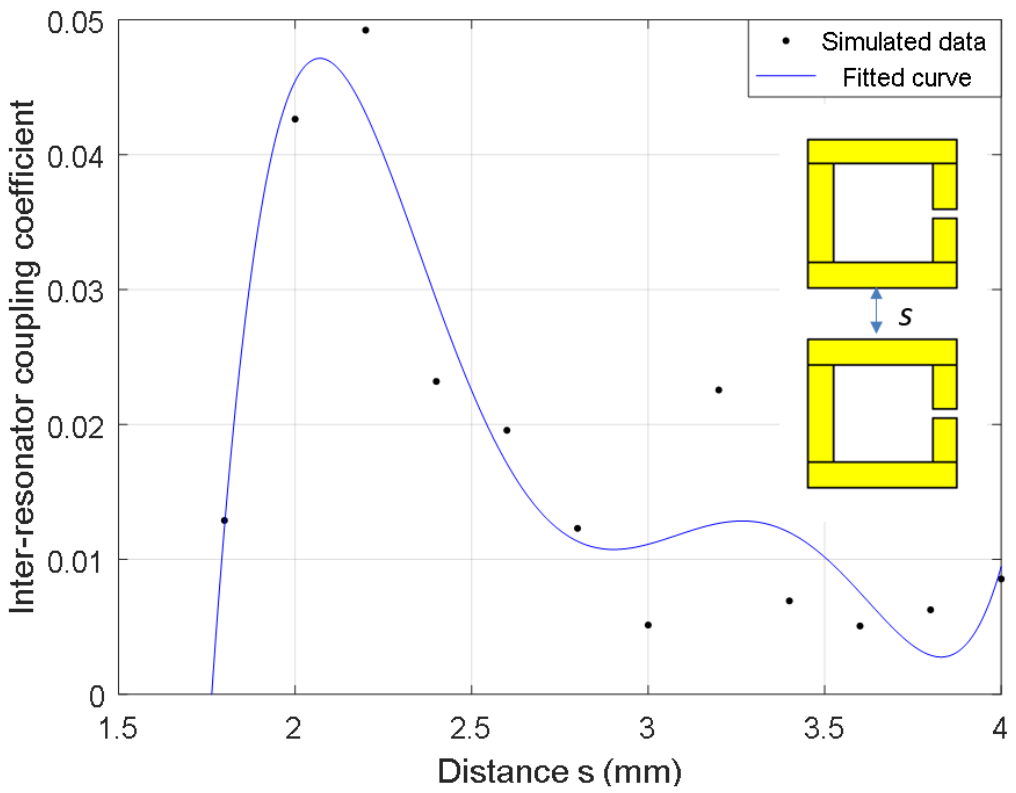


Figure 3.16 Inter-resonator coupling profile for the (d) type mixed coupling - magnetic coupling dominant.

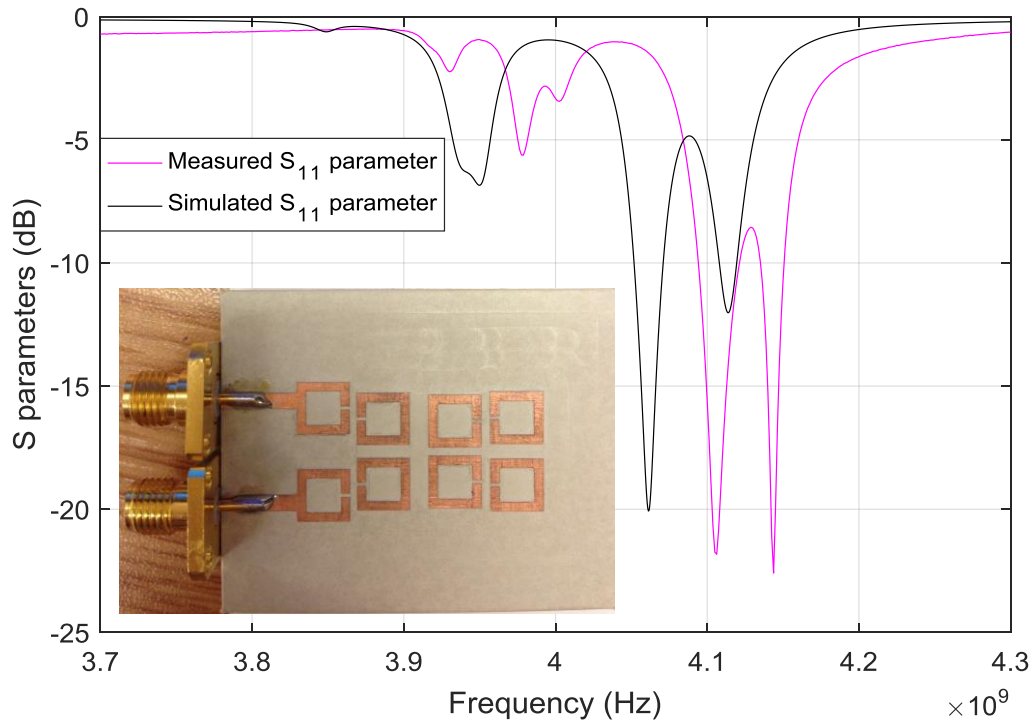


Figure 3.18 EM simulated and measured S_{11} parameters of the eighth order dual-band BPF.

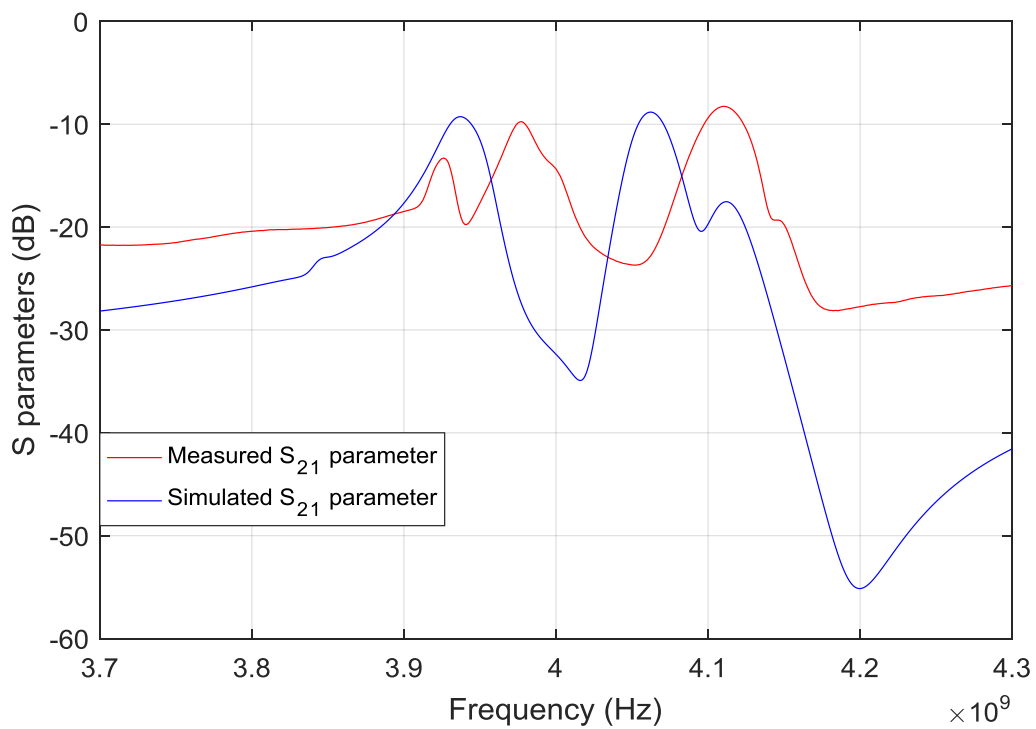


Figure 3.19 EM simulated and measured S_{21} parameters of the eighth order dual-band BPF.

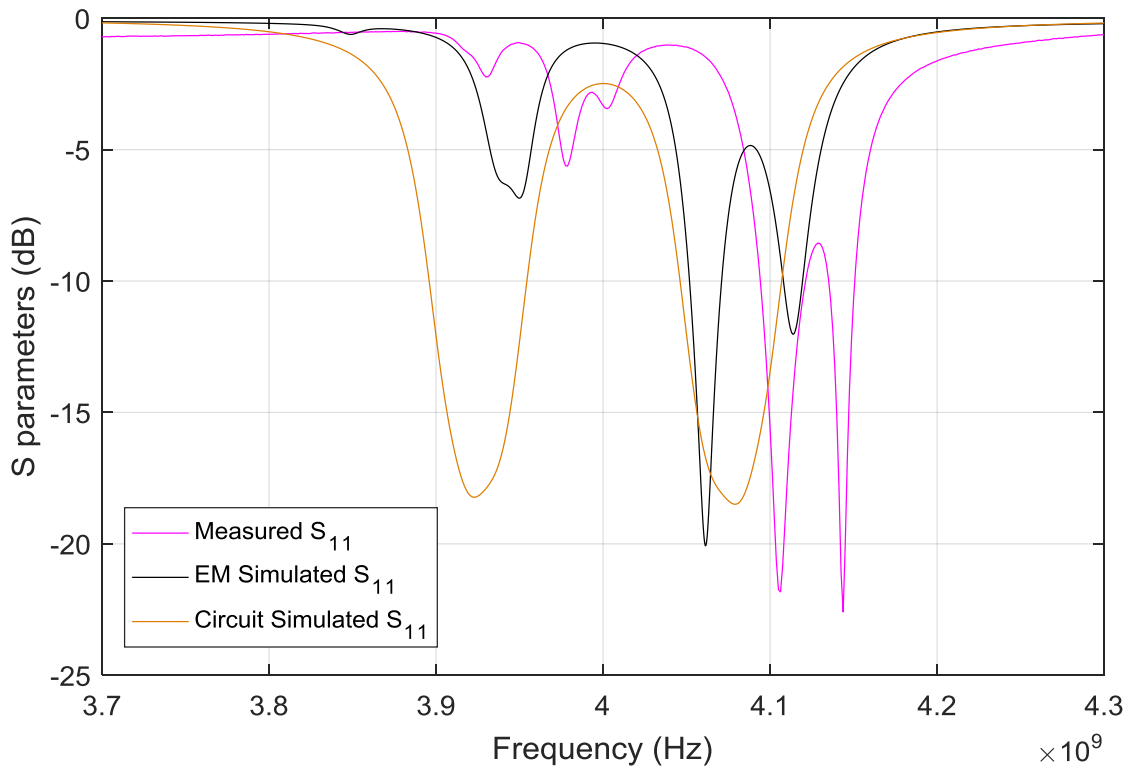


Figure 3.20 Simulated S_{11} parameters of the equivalent circuit with a finite unloaded Q of 280.

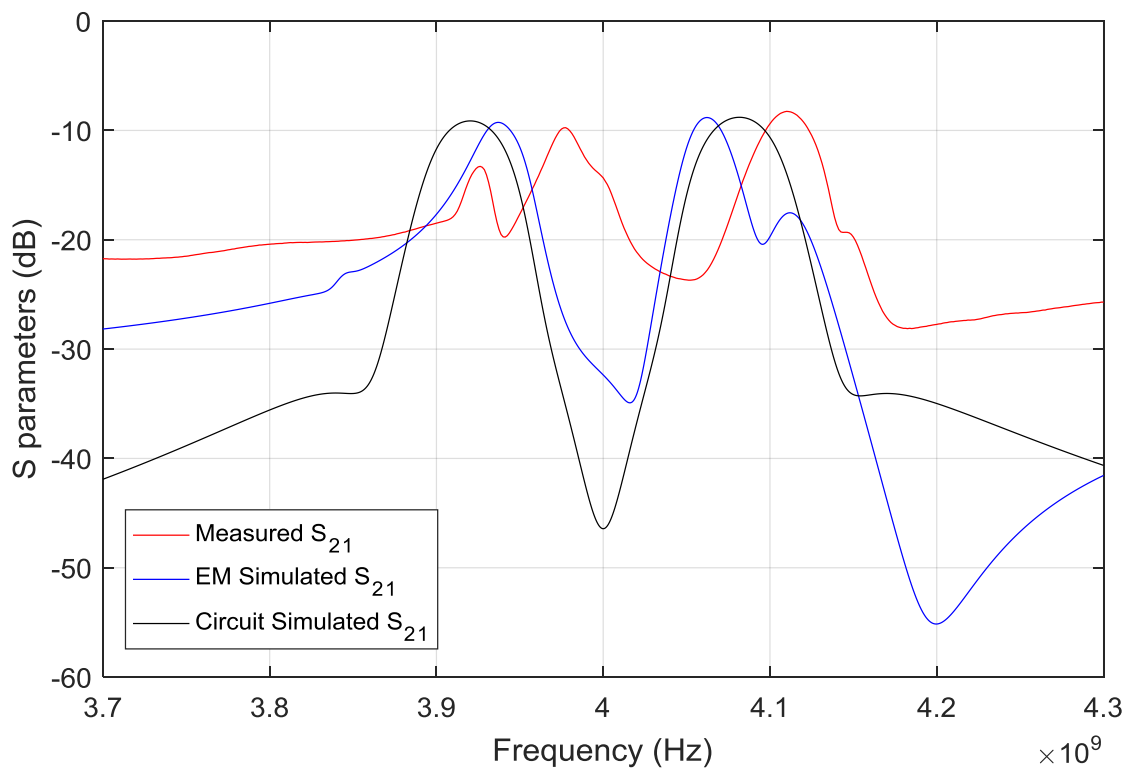


Figure 3.21 Simulated S_{21} parameters of the equivalent circuit with a finite unloaded Q of 280.

The simulated response of the equivalent circuit looks similar to the frequency response of EM simulation. The passbands appear as humps below -8 dB of the S_{21} parameter, forming the unreasonable responses. The narrower passbands and ripples of the EM simulated response may be caused by the loading effect and imperfect couplings.

The passband specification implies that the loaded Q factor is approximately 80 for each band. Thus, the unloaded Q of microstrip open-loop resonator is only about 3.5 times the loaded Q for each passband, which is too low to realise a reasonable narrow dual-passband filter response. Then, we further simulated the equivalent circuit with a series of finite unloaded Q factors to find out the required unloaded Q of the resonator.

Figure 3.22 and Figure 3.23 present the simulated frequency responses of the equivalent circuit with finite unloaded Q of 400 and 800, respectively.

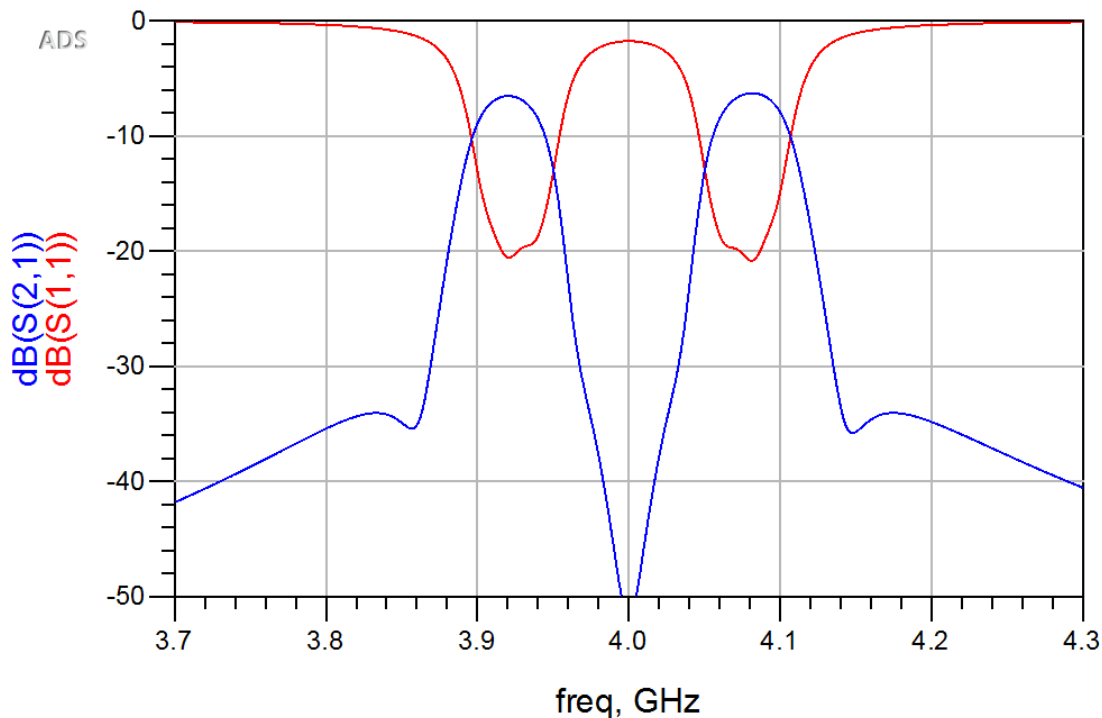


Figure 3.22 Simulated frequency response of the equivalent circuit with a finite unloaded Q of 400.

When the unloaded Q is 400, the insertion losses of passbands are reduced to 6.5 dB in comparison with those when unloaded Q of 280. However, the shape of the frequency response is still not as ideal for a bandpass filter.

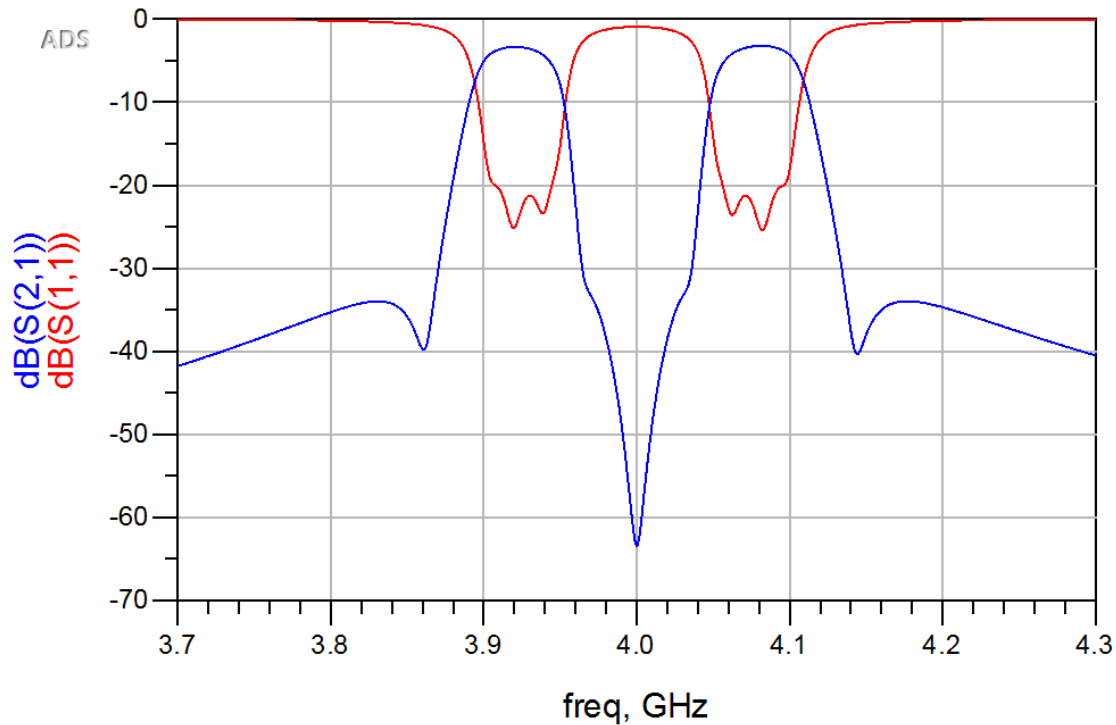


Figure 3.23 Simulated frequency response of the equivalent circuit with a finite unloaded Q of 800.

When the unloaded Q is 800, the frequency response has a reasonable passband with insertion losses of 3.3 dB. This frequency response becomes an acceptable low loss dual-passband response for a BPF.

The above simulation showed that the designed eighth order narrow dual-band BPF has a requirement for unloaded Q factor. The above study on the finite unloaded Q factor indicates that the value of unloaded Q factor of the resonator needs to be at least 10 times of the loaded Q factor, in order to realise a reasonable filter response shape with low insertion losses. Since microstrip resonators have typical unloaded Q factors of 100~300, it is impossible to use microstrip resonators to generate the desired low loss narrow dual-passband filter response.

Consequently, high Q resonators should be used when designing dual-band bandpass filter by the dual-passband response synthesis method. In the next design example, an sixth order dual-band bandpass filter is designed and realised by high Q dielectric resonators.

3.4.2 A sixth-order dual-band BPF

A filter working at LTE band is designed and implemented using high Q resonators to verify the dual-passband response synthesis method. A sixth-order dual-band response with a minimum passband return loss of 20 dB and a minimum stopband attenuation of 20 dB is

desired. The centre frequencies of passbands are 2.565 GHz and 2.635 GHz, both with 30 MHz bandwidth. This designed filter should have relatively high power handling capability, thus suitable for micro/pico LTE base stations.

Coupling matrix generation and equivalent circuit simulation

An asymmetrical three-pole generalised Chebyshev response with transmission zeros at $S=j2.0$, $\pm j\infty$ is used as the single-passband response, shown in Figure 3.24.

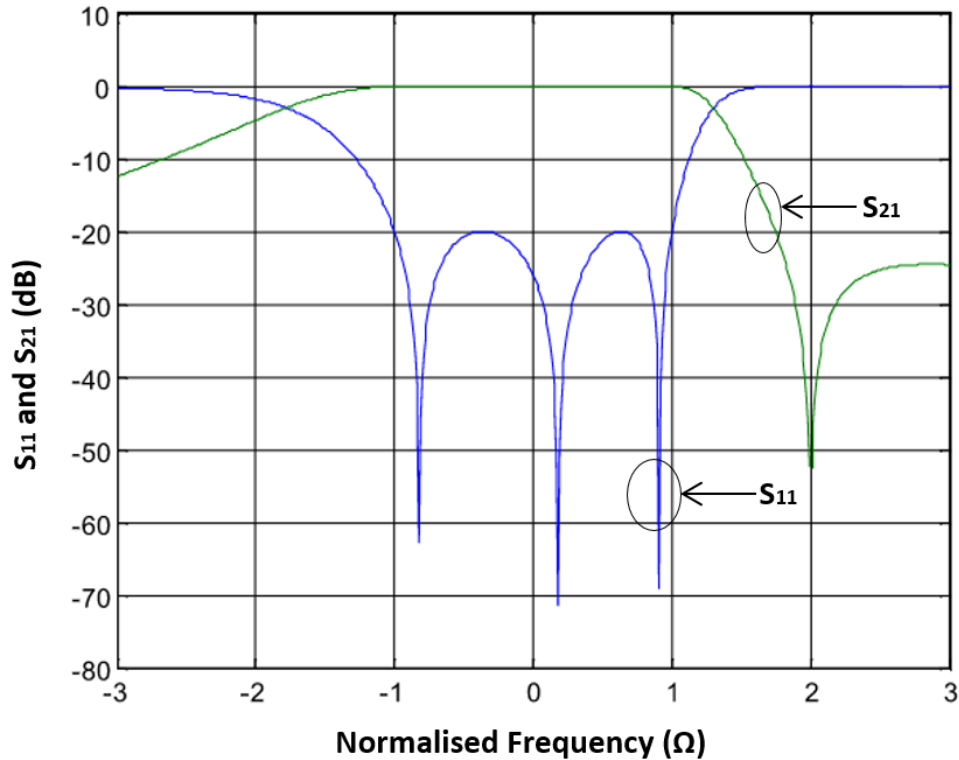


Figure 3.24 Asymmetrical frequency response of the three pole Chebyshev prototype in Ω domain.

The reflection zeros can be found from the given transmission zeros, since the characteristic function of the generalised Chebyshev response is known. Using the frequency transformation expressed by (3.1) in Section 3.2, the transmission and reflection zeros of the symmetrical response in the Ω' domains are:

Transmission zeros: $\pm j1.366, \pm j0.1$;

Reflection zeros: $\pm j0.9704, \pm j0.7533, \pm j0.5309$.

Using the Ω' domain expression of (3.22) and the transfer function expressed by (3.19), the transformed frequency response in the Ω' domain was obtained as Figure 3.25 shows.

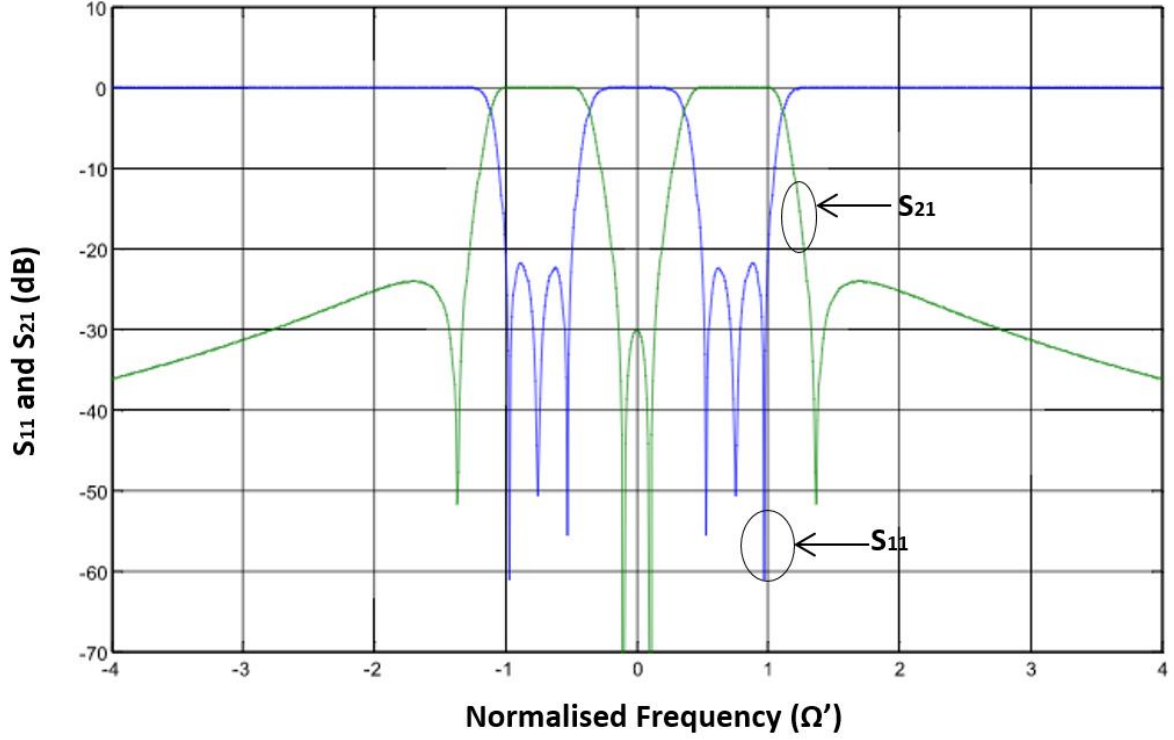


Figure 3.25 Dual-band sixth-order frequency response after frequency transformation in Ω' domain.

The non-adjacent coupling and diagonal cross-couplings are annihilated based on a sixth order canonical coupling topology. The coupling matrix and the normalised terminal resistance are then synthesised using the MATLAB program provided by Gajaweera.

$$M = \begin{bmatrix} 0 & -0.8255 & 0 & 0 & 0 & -0.2009 \\ -0.8255 & 0 & 0.4174 & 0 & -0.3245 & 0 \\ 0 & 0.4174 & 0 & 0.5667 & 0 & 0 \\ 0 & 0 & 0.5667 & 0 & -0.4174 & 0 \\ 0 & 0.0125 & 0 & -0.4174 & 0 & 0.8255 \\ -0.2009 & 0 & 0 & 0 & 0.8255 & 0 \end{bmatrix} \quad (3.61)$$

The terminal resistance is

$$R = 0.6224 \text{ Ohm}. \quad (3.62)$$

To reduce the structure complexity, the canonical structure is chosen to have the direct couplings with the same type of coupling. Therefore, the sub-diagonal of the coupling matrix M should be the same sign. Rhodes and Zabawahwi have given the method to derive a coupling matrix that has a sub-diagonal with the same coupling type [98]: if the sub-diagonal is $M_{i-1,i}$ ($i=2, 3, \dots, N$), then scale the i^{th} row and i^{th} column of the coupling matrix in an ascending manner by the sign of $M_{i-1,i}$. Therefore, (3.61) is transformed as follows.

$$M' = \begin{bmatrix} 0 & 0.8255 & 0 & 0 & 0 & -0.2009 \\ 0.8255 & 0 & 0.4174 & 0 & 0.3245 & 0 \\ 0 & 0.4174 & 0 & 0.5667 & 0 & 0 \\ 0 & 0 & 0.5667 & 0 & 0.4174 & 0 \\ 0 & 0.0125 & 0 & 0.4174 & 0 & 0.8255 \\ -0.2009 & 0 & 0 & 0 & 0.8255 & 0 \end{bmatrix} \quad (3.63)$$

Denormalise the above coupling matrix, we obtain

$$K = \begin{bmatrix} 0 & 0.03175 & 0 & 0 & 0 & -0.008 \\ 0.03175 & 0 & 0.0161 & 0 & 0.0125 & 0 \\ 0 & 0.0161 & 0 & 0.0218 & 0 & 0 \\ 0 & 0 & 0.0218 & 0 & 0.0161 & 0 \\ 0 & 0.0125 & 0 & 0.0161 & 0 & 0.03175 \\ -0.008 & 0 & 0 & 0 & 0.03175 & 0 \end{bmatrix} \quad (3.64)$$

and the external Q factor is shown below.

$$Q_e = \frac{1}{R \cdot \text{FBW}} = 41.7 \quad (3.65)$$

Figure 3.26 shows the equivalent circuit of the sixth order dual-band BPF. The relevant parameters of the circuit are calculated by (3.29) where $f=2.6$ GHz and $\text{BW}=100$ MHz. Figure 3.27 shows the simulated frequency response with infinite Q of resonator. The frequency response looks extremely close to the synthesised dual-passband response in Figure 3.25.

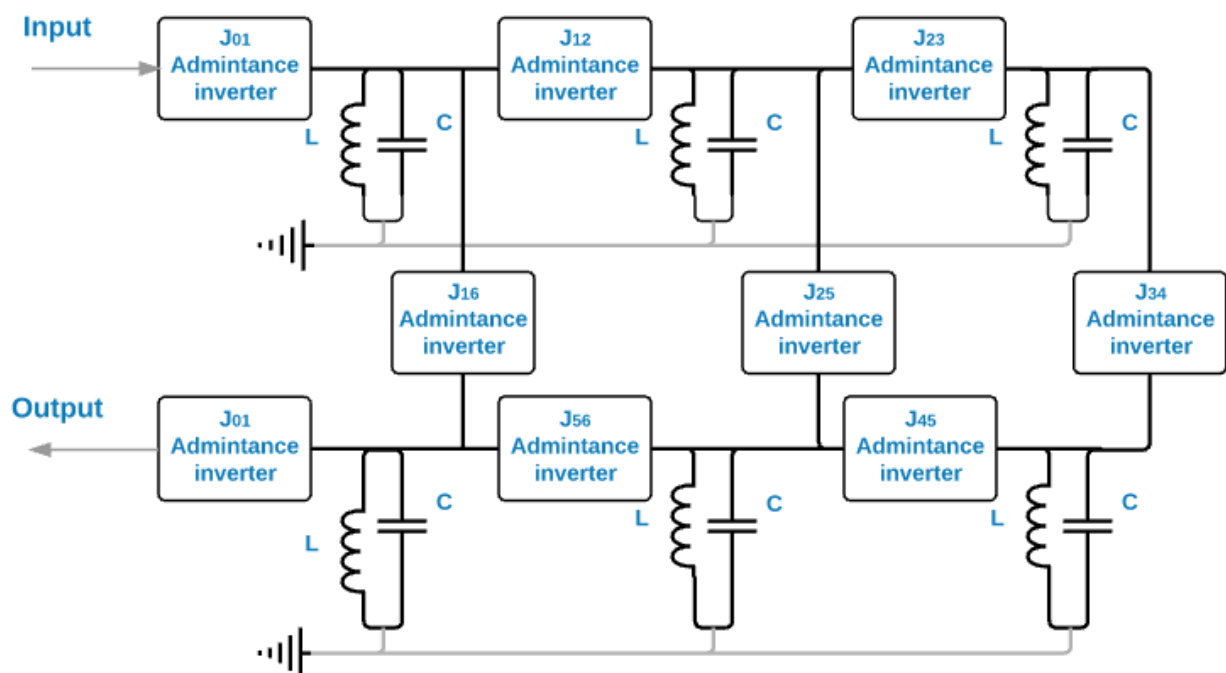


Figure 3.26 Equivalent circuit of the sixth order dual-band BPF.

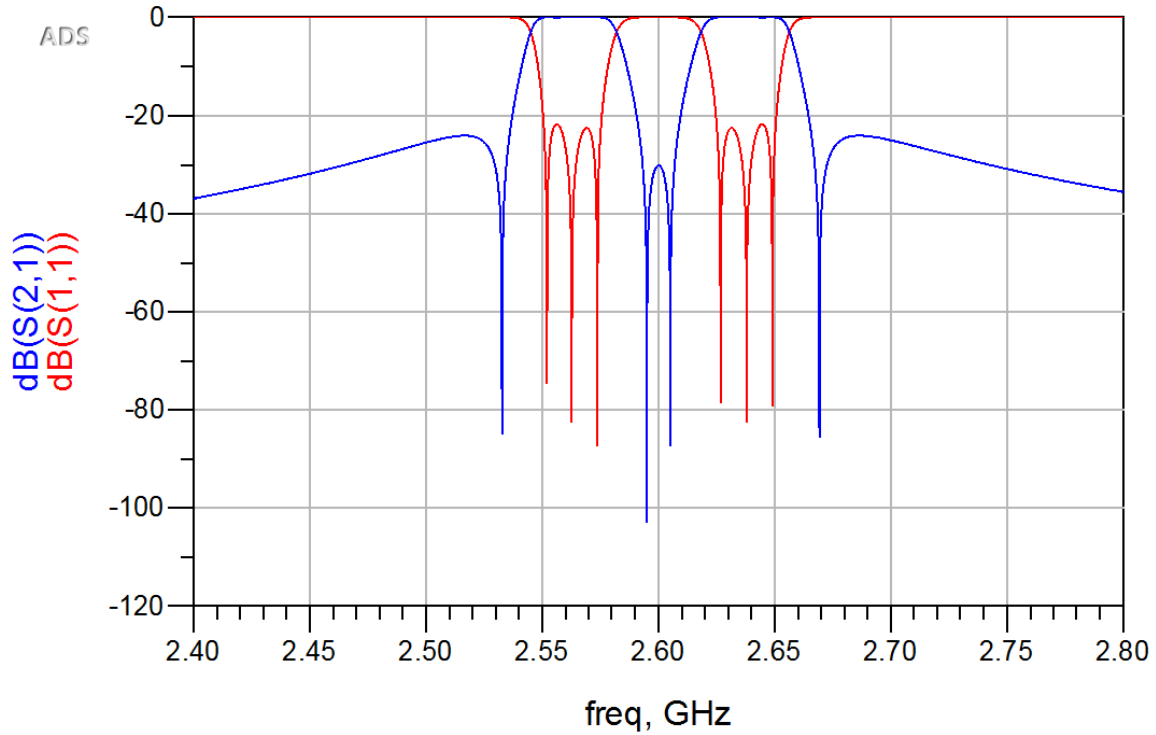


Figure 3.27 Simulated frequency response of the equivalent circuit with infinite Q of resonator.

Resonator characterisation

Dielectric resonators (DRs) were used in this filter design because of their advantages in size, unloaded quality-factor (Q), temperature stability, and power handling capability [35]. As introduced in Section 2.2.4, the $TE_{01\delta}$ mode is the fundamental resonant mode for an isolated cylindrical DR in a metallic cavity [3]. The physical size of $TE_{01\delta}$ mode cylindrical DR can be further reduced, as well as the cost. $TE_{01\delta}$ mode quarter cylindrical DR was proposed as a solution of significant size and cost reduction [99, 100]. The resonator and cavity size can be reduced to about a quarter, compared to conventional design of $TE_{01\delta}$ mode cylindrical DR. In addition, the $TE_{01\delta}$ mode quarter cylindrical DR has 2 surfaces directly contacting the cavity, enabling well heat removal in high power designs [100].

It is demonstrated that introducing an infinite Perfect Electric Conductor (PEC) at symmetry plane does not disturb the original field distribution when the electric fields are orthogonal to the plane [32, 40, 100]. Therefore, for $TE_{01\delta}$ mode, two infinite PEC planes to which the electric fields are orthogonal can be inserted with an arbitrary angle [100]. However, infinite PEC planes do not exist. Therefore, conducting planes are used in practice. Considering the ease of fabrication for both cavity and DR, the angle between the two conducting planes is usually chosen as 90 degrees for ease of fabrication and fitting.

Figure 3.28 shows the structures and field patterns of a TE_{018} mode cylindrical hollow DR and a TE_{018} mode quarter cylindrical DR.

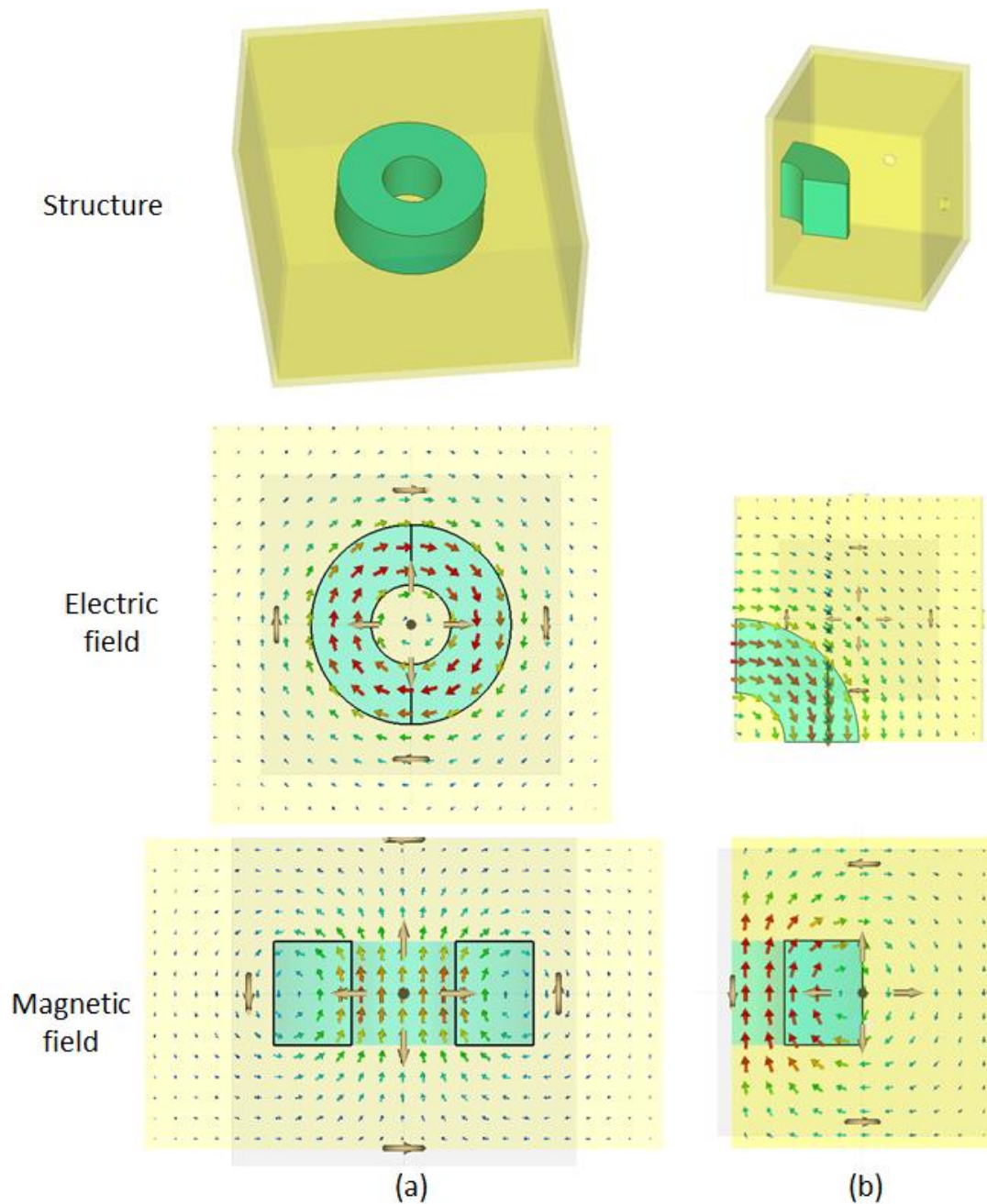


Figure 3.28 Resonator structures and fields patterns for TE_{018} mode cylindrical DR. (a) Full cylindrical type. (b) Quarter type.

The latter DR is a quarter of the full cylindrical DR in a quarter cavity. It can be seen that the field distribution inside or around the quarter cylindrical resonator is the same as that of the full cylindrical resonator. In addition, the fundamental (TE_{018} mode) resonant frequencies for these two structures are almost the same. However, due to the loss of conductor, the unloaded Q factor of the quarter cylindrical DR is smaller than that of the full cylindrical DR.

The resonators are desired to have a fundamental $TE_{01\delta}$ mode resonance at 2.6 GHz. The dielectric material is selected as Calcium titanate - neodymium aluminate (dielectric constant $\epsilon_r=45$, loss $\tan\delta=0.00006$ at 2.7 GHz) to realise very compact resonator and filter. The resonant frequency and unloaded Q of a $TE_{01\delta}$ mode quarter cylindrical DR

The dimensions of the resonator and cavity were determined from CST MW simulation. Figure 3.29 shows the resonator structure and dimension to realise a $TE_{01\delta}$ mode resonance at 2.6 GHz. The simulation also indicates that the unloaded Q factor of the resonator has been reduced to 2200 due to the conductor losses and small cavity.

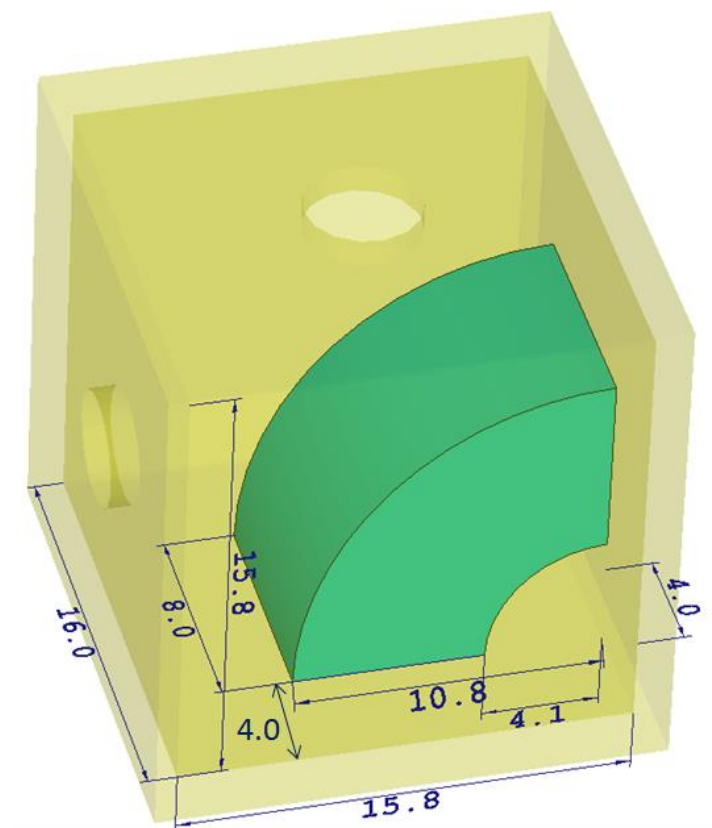


Figure 3.29 Resonator structure and dimensions for filter design.

The resonator was also fabricated and tested. Figure 3.30 shows the resonator in the cavity for test. Nylon support was used to realise perfect contact between the DR and cavity. The measured resonant frequency is 2.838 GHz with an unloaded Q of 2120. Although nylon support was used, there still may be unobservable gaps between the DR and cavity, upsetting the $TE_{01\delta}$ mode. The gaps may cause a higher measured resonant frequency, compared to the simulated one.

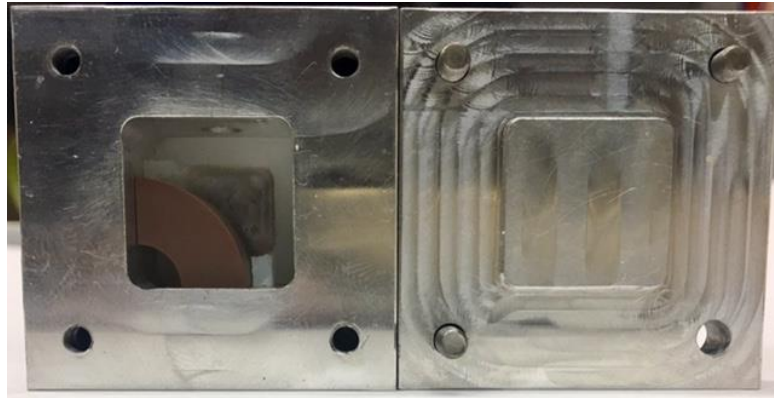


Figure 3.30 Fabricated resonator in a cavity.

The unloaded Q factor of the designed $TE_{01\delta}$ mode quarter cylindrical DR is about 2100, much higher than the required Q which is 10 times of the passband loaded Q. The equivalent circuit has been simulated with unloaded Q factor of 2100 for verification of the finite Q effect.

Figure 3.31 shows the simulated frequency response.

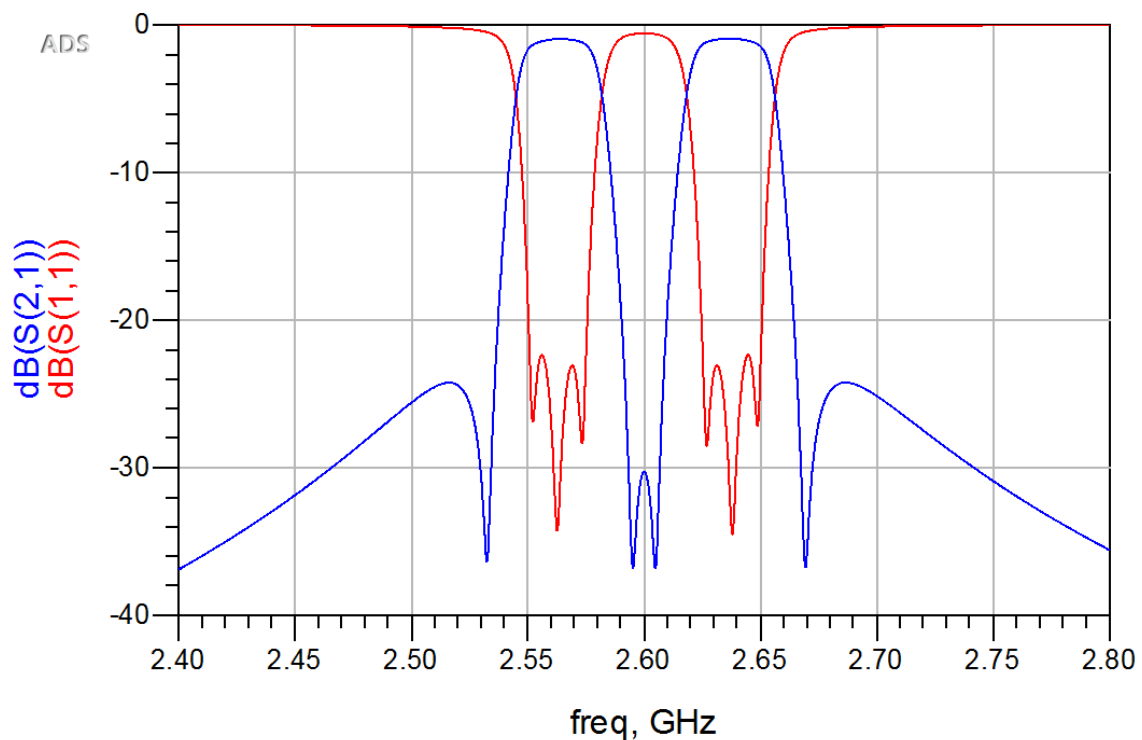


Figure 3.31 Simulated frequency response of the equivalent circuit with finite Q of 2100.

Compared to the one with infinite unloaded Q, the losses of the stopband transmission zeros have been reduced whereas the insertion losses of passband have been increased. However, the insertion losses are still low, less than 1.0 dB, and the frequency response still satisfies the design specification.

This designed resonator was also used to obtain the external coupling profile and inter-resonator coupling profiles from CST MW simulation.

External coupling structures

The external coupling structure for a TE_{018} mode quarter cylindrical DR can be realised by a probe inserted into the resonator, shown in Figure 3.32. It realises electric type external coupling. However, drilling a hole in the DR could break the DR. Besides, the hole would influence the resonant frequency and unloaded Q factor of the resonator.

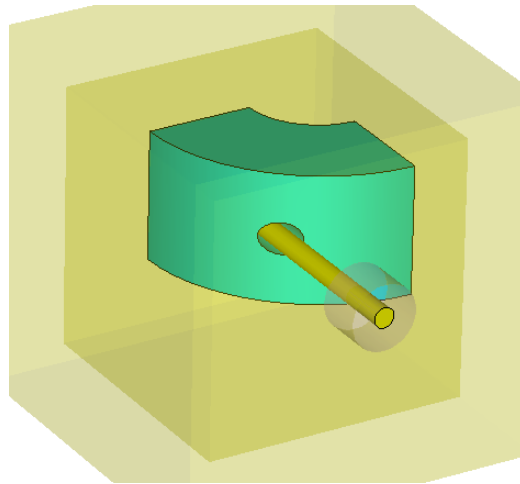


Figure 3.32 External coupling by a probe inserted into the DR.

Alternatively, the external coupling can be realised by using a probe around the DR [40]. Figure 3.33 shows the external coupling structure by a curved probe standing beside the DR. It is a type of magnetic coupling used in this filter design.

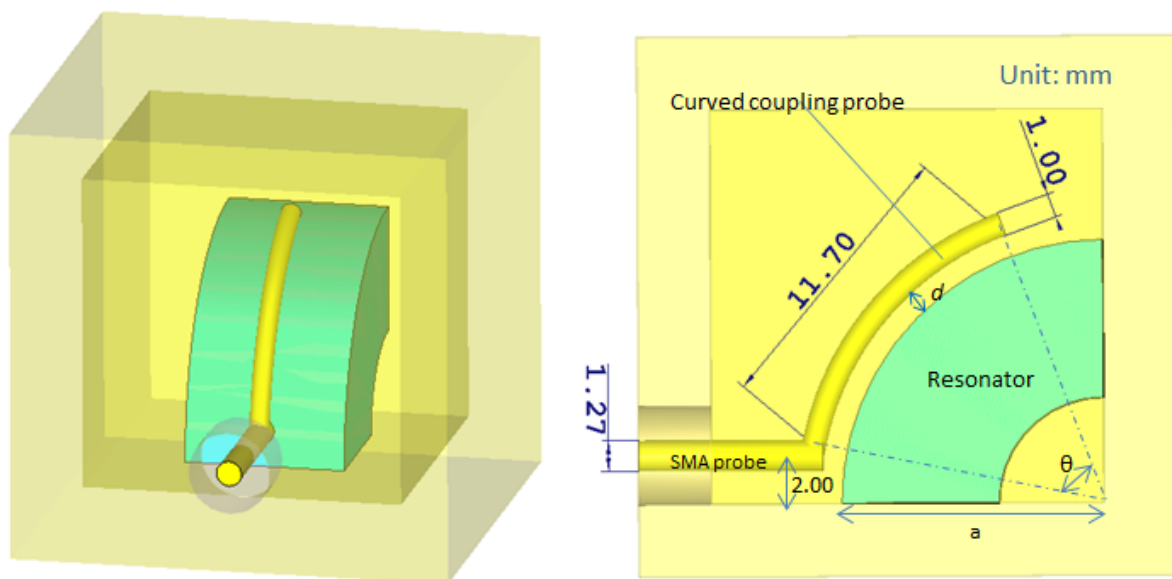


Figure 3.33 External coupling structure.

The curved coupling probe stands in parallel with the outer surface of the resonator with one end connected to the probe of SMA connector. The external Q is controlled by the curving angle of the probe (θ), and the distance (d) between the probe and the resonator. When $\theta=60^\circ$ and $d=1.0$ mm, the structure realises the external Q of 41.

Inter-resonator coupling structures

It is assumed that the positive elements in the coupling matrix represent magnetic coupling whereas the negative elements represent electric coupling. Figure 3.34 shows a structure for electric coupling.

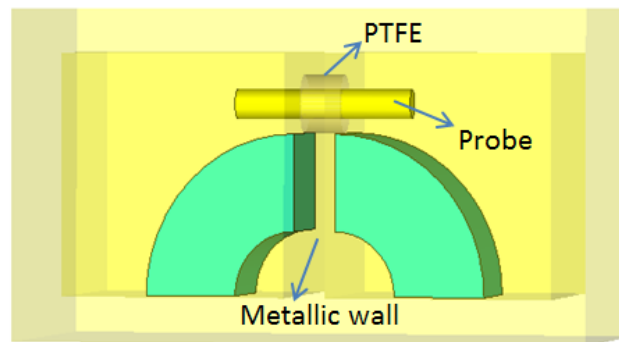


Figure 3.34 Inter-resonator coupling structure: electric coupling.

A probe is used along the cavity to couple the DRs to realise the electric coupling. The dimensions and location of the probe are used to control the coupling intensity. However, the required electric coupling coefficients K_{16} and K_{61} in the denormalised coupling matrix are so small that it is difficult to be realised using this electric coupling structure. The effect of setting K_{16} and K_{61} as zeros has been studied from the simulation of equivalent circuit.

Figure 3.35 shows the simulated frequency response with $K_{16}=K_{61}=0$. Compared to Figure 3.31, the passband insertion losses in Figure 3.35 has been increased to 1.44 dB. In addition, two stopband transmission zeros, which are generated by the coupling between the first and last resonator, have disappeared. This reduces the selectivity of the filter. Nevertheless, this frequency response is reasonable and the design requirements are still satisfied.

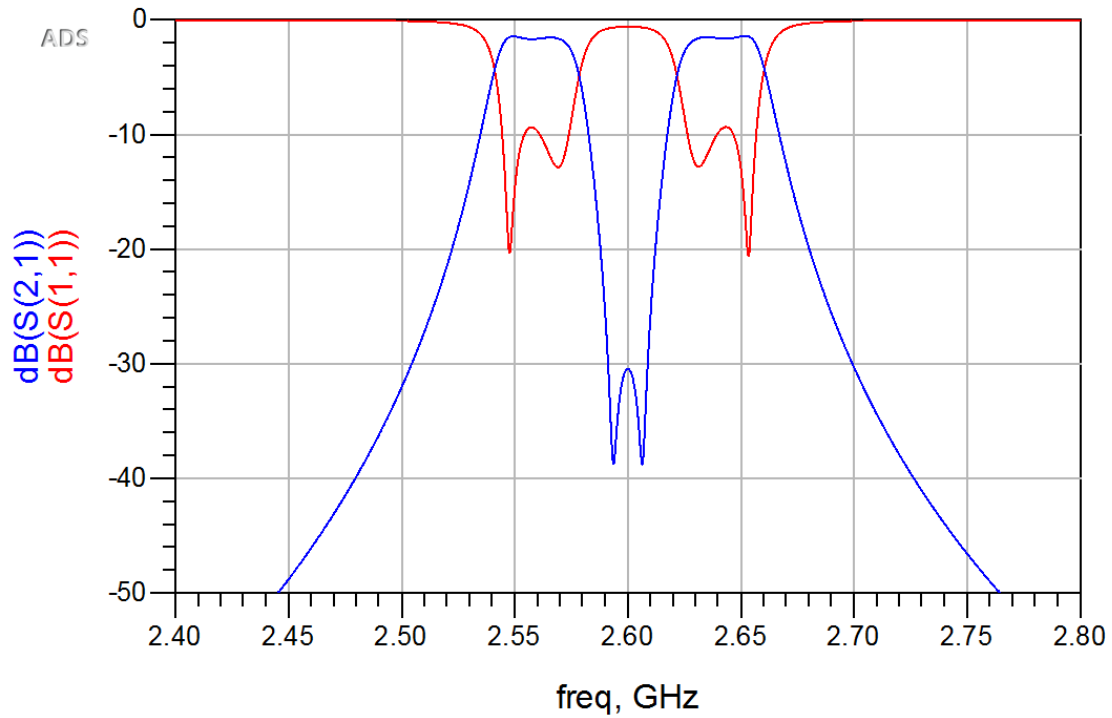


Figure 3.35 Equivalent circuit simulation with unloaded Q of 2200 and $K_{16} = K_{61} = 0$.

The magnetic coupling between DRs is usually realised by apertures. However, the aperture location to realise magnetic coupling between the $TE_{01\delta}$ mode quarter cylindrical DRs must be very carefully chosen because the $TE_{01\delta}$ mode resonance requires conductor to contact its rectangular surfaces. Considering the canonical filter topology and the resonator structure, two types of aperture were selected in realisation of the dual-band BPF [40]. One type is for the couplings between resonator 1 and 2, 2 and 3, 4 and 5, 5 and 6, shown in Figure 3.36.

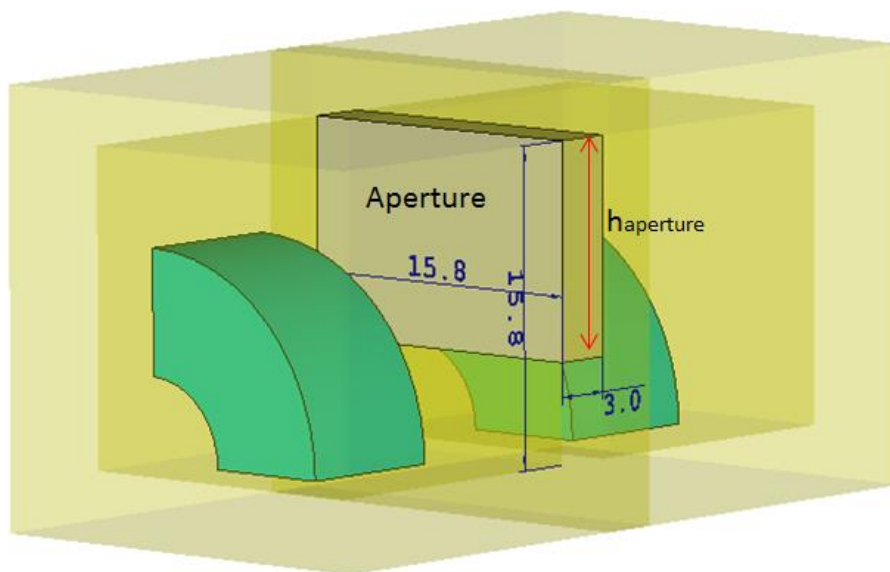


Figure 3.36 Inter-resonator coupling structure: magnetic coupling type I.

For this type of magnetic coupling, the aperture has the same length with the inner length of the sectional cavity. The width of the aperture is 3.0 mm, the thickness of metal walls inside the cavity. The height of aperture (h_{aperture}) controls the coupling, with the profile shown in Figure 3.37.

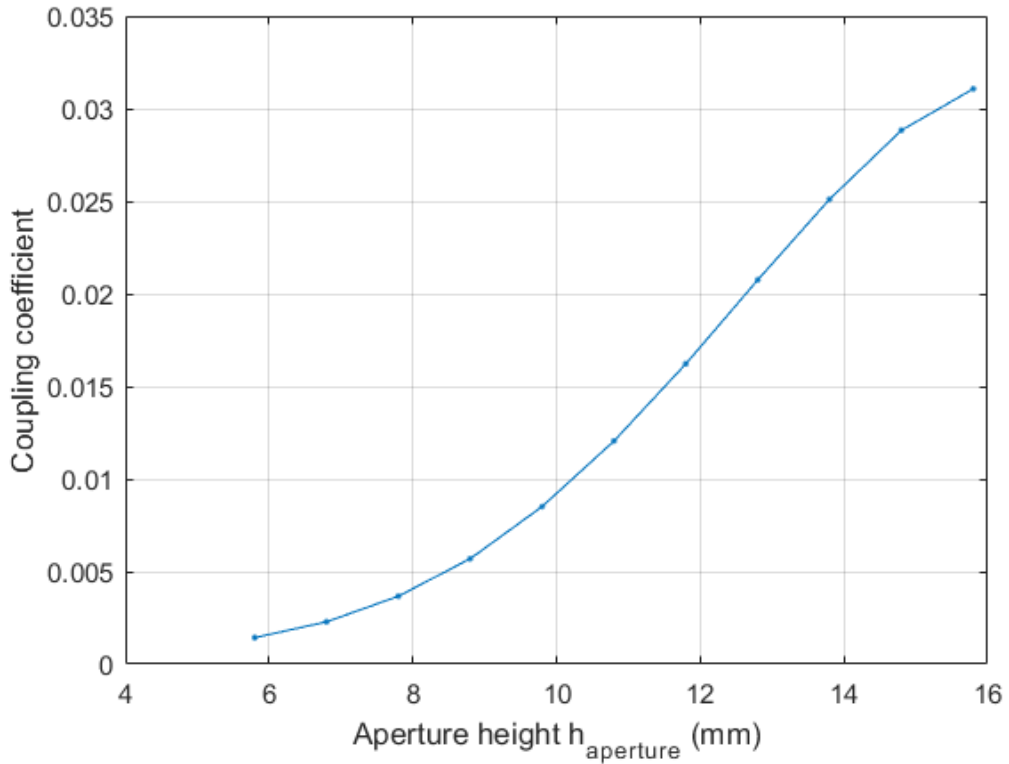


Figure 3.37 Inter-resonator coupling profile of magnetic type I.

The other type is for the couplings between resonator 2 and 5, 3 and 4, shown in Figure 3.38.

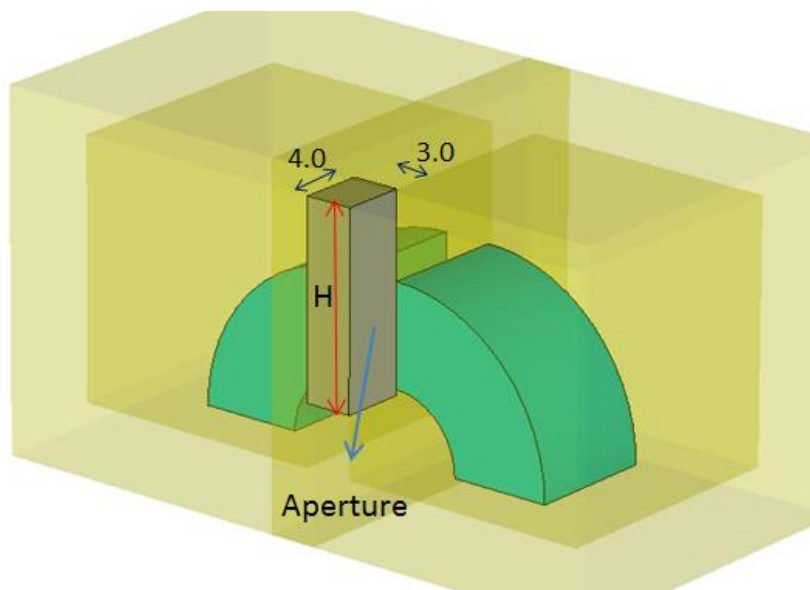


Figure 3.38 Inter-resonator coupling structure: magnetic coupling type II.

For this type of magnetic coupling, the aperture can only be placed beside the resonator rectangular surface in order not to disturb the $TE_{01\delta}$ mode. Therefore, the length of the aperture was selected as 4.0 mm. The width of aperture was also 3.0 mm, the thickness of metal wall. Aperture height (H) is the only parameter used to control the coupling coefficient, with the profile shown in Figure 3.39.

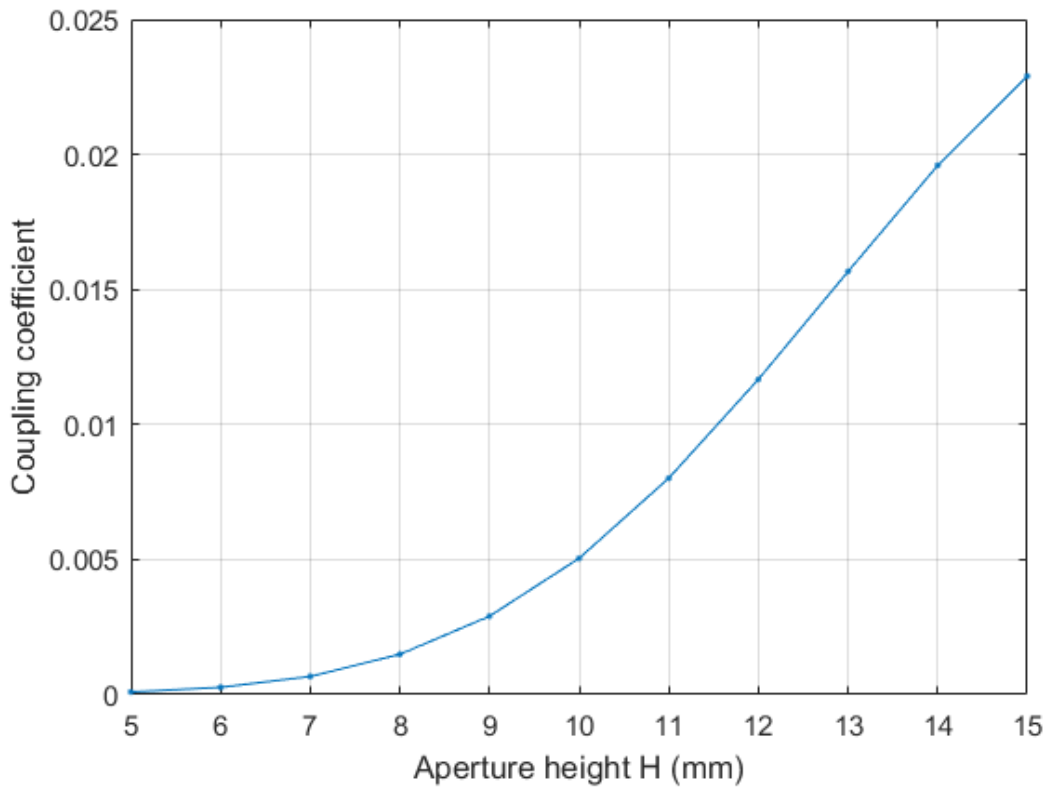


Figure 3.39 Inter-resonator coupling profile of magnetic type II.

Filter characterisation

Figure 3.40 shows the topology and structure of the sixth order dual-band bandpass filter. The initial dimensions of the DRs were kept exactly the same as the one in Figure 3.29. In addition, the initial dimensions of coupling structures were directly obtained from the above profiles. Therefore, all six resonators are identical with outer radius of 10.8 mm and inner radius of 4.32 mm. The height of aperture (h_{aperture}) between DR 1 and 2, 5 and 6 is $h_{12}=h_{56}=15.8$ mm. The height of aperture between DR 2 and 3, 4 and 5 is $h_{23}=h_{45}=11.6$ mm. The height of aperture (H) between DR 2 and 5 is $H_{25}=12.3$ mm while the height of aperture between DR 3 and 4 is $H_{34}=14.4$ mm. Figure 3.41 shows the EM simulated frequency response of the filter with initial dimensions.

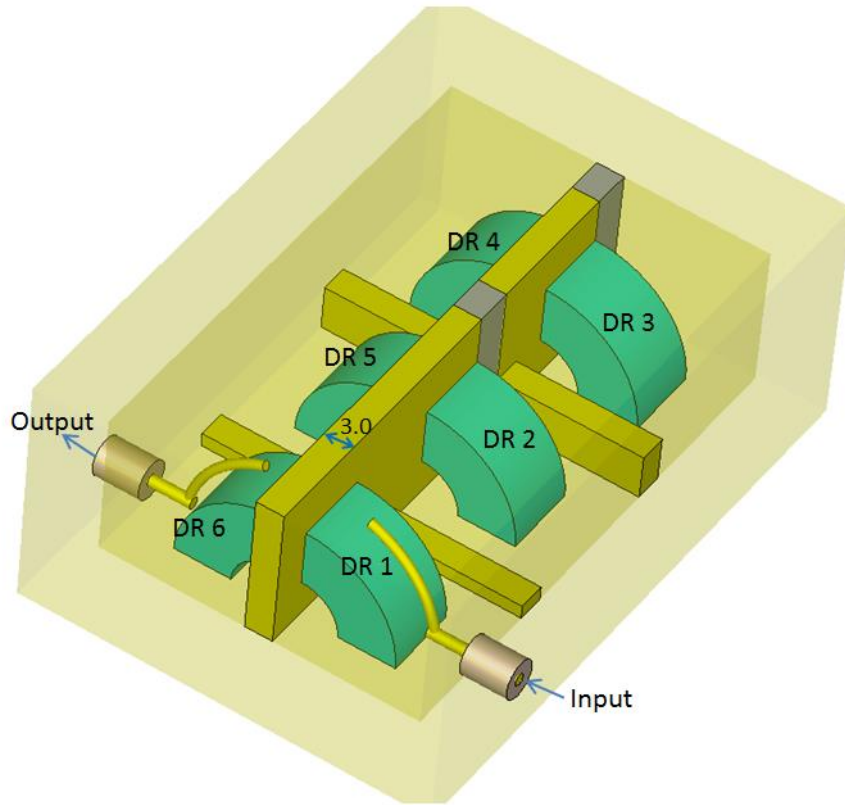


Figure 3.40 Structure of the sixth order dielectric filter.

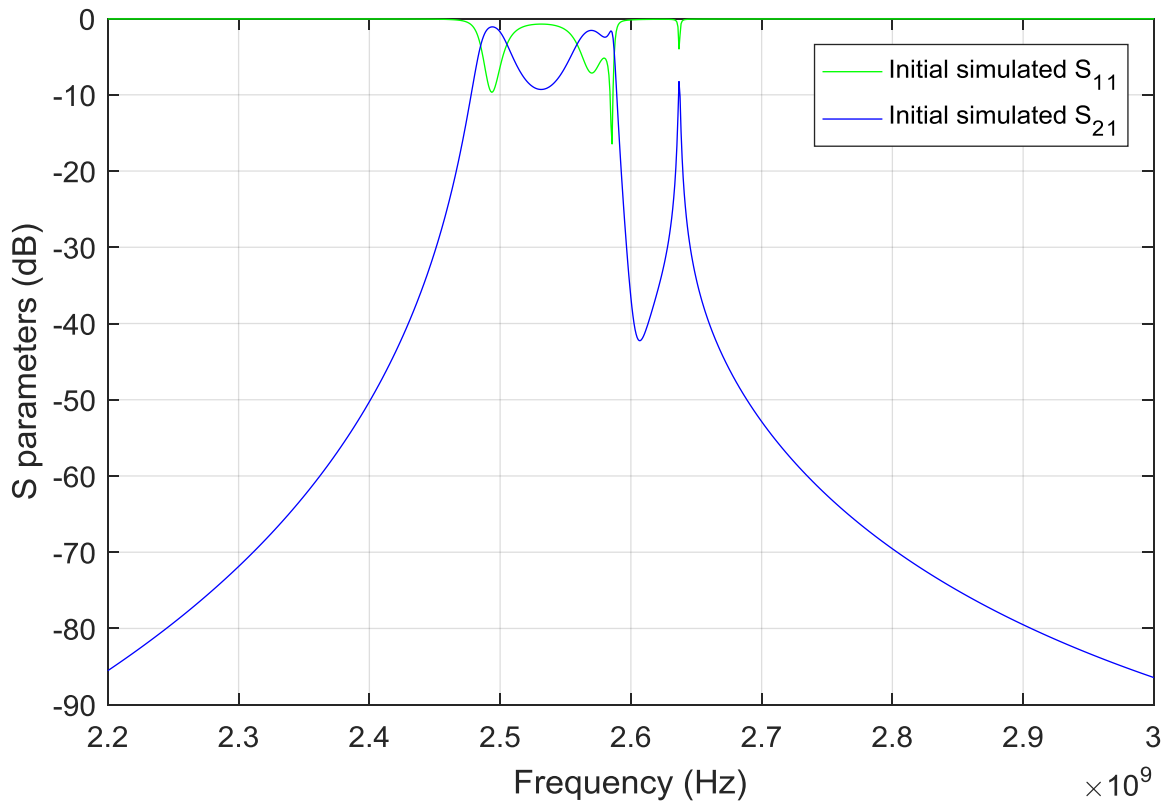


Figure 3.41 Initial EM simulated frequency response of the filter.

This initial simulated frequency response is not reasonable. It was found that the reflection zeros are not placed correctly. By analysing the resonant modes from EM simulation, it was found that DR 1, 2, 5, and 6 are resonating at lower frequencies than expected. It is caused by the loading effect from external source/load.

From the aperture dimensions we can tell that the aperture between DR 1 and 2, and the aperture between DR 2 and 3 are close to completely open aperture. Therefore, the external coupling structure has loading effect on all the DRs. The intensity of external loading effect depends on the coupling intensity between the external source/load and the DR. Therefore, the external source/load has strong loading effect on DR 1 and 6, medium loading effect on DR 2 and 5, and weak loading effect on the DR 3 and 4. In addition, the inter-resonator loading effect mainly influences the resonant frequencies of DR 2 and 5, rather than the DRs at the ends of cavity. Overall, the loading effect on DR 1, 2, 5, and 6 are relatively significant, compared to that on DR 3 and 4. In order to compensate for the loading effect on resonant frequencies of the DRs, the radii of DRs have been tuned. The tuned radii are shown in Table 3-I. Additionally, the height of the apertures were tuned to maintain the required coupling coefficients. These tuned dimensions are shown in Table 3-II.

Table 3-I Radii of the DRs of the designed sixth order dual-band BPF.

Resonator	Outer radius (mm)	Inner radius (mm)
Original characterised DR	$a=10.8$	$b=0.4*a=4.32$
DR 1 and 6	$a_1=a_6=10.45$	$b_1=b_6=4.2$
DR 2 and 5	$a_2=a_5=10.45$	$b_2=b_5=4.2$
DR 3 and 4	$a_3=a_4=10.9$	$b_3=b_4=4.4$

Table 3-II Tuned coupling dimensions of the filter.

Height of aperture	Outer radius (mm)
$h_{12}=h_{56}$	14.3
$h_{23}=h_{45}$	10.8
H_{25}	12.3
H_{34}	13.0

The EM simulation gives two passbands at 2.565 GHz and 2.630 GHz, with 3-dB bandwidth of 28 MHz and 35 MHz, respectively. The insertion losses are 0.98 dB and 0.58 dB, respectively, which are even smaller than those of circuit simulation. Two transmission zeros are introduced between the passbands, achieving good selectivity. The frequency shift between EM simulation and circuit simulation is mainly caused by the parameter tolerance, and the tuned radii of the resonators.

The designed filter is very compact, saving more than 75% volume when compared with a filter using coaxial resonators or traditional cylindrical dielectric resonators. Moreover, it has good thermal resistance since the heat of the DRs can be directly transferred to the Aluminium cavity. The power handling capability of the filter was estimated from EM simulation using (2.87) in Section 2.7. The break down power is approximately 95 Watt, showing that the designed filter has relatively high power handling capability in comparison with planar filters.

The filter was then fabricated. The dielectric resonators were fixed onto the Aluminium surfaces by epoxy to avoid any gap that may upset the $TE_{01\delta}$ mode. Resonator tuning was achieved by sand paper polishing. Figure 3.44 shows the fabricated filter.

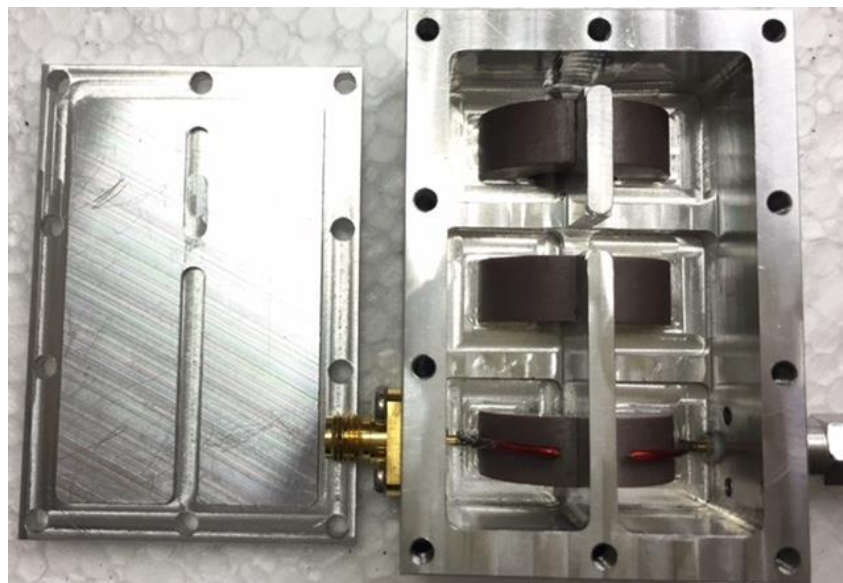


Figure 3.44 Fabricated sixth-order dielectric filter.

The measured frequency response is shown in Figure 3.45, which is not a reasonable frequency response for a dual-band bandpass filter in comparison with the previous EM simulation. Possible reasons include the epoxy losses, the imperfect $TE_{01\delta}$ mode, the soldering losses of the external coupling probes, the imperfect tuning process of the DRs, and the tolerances of fabrication.

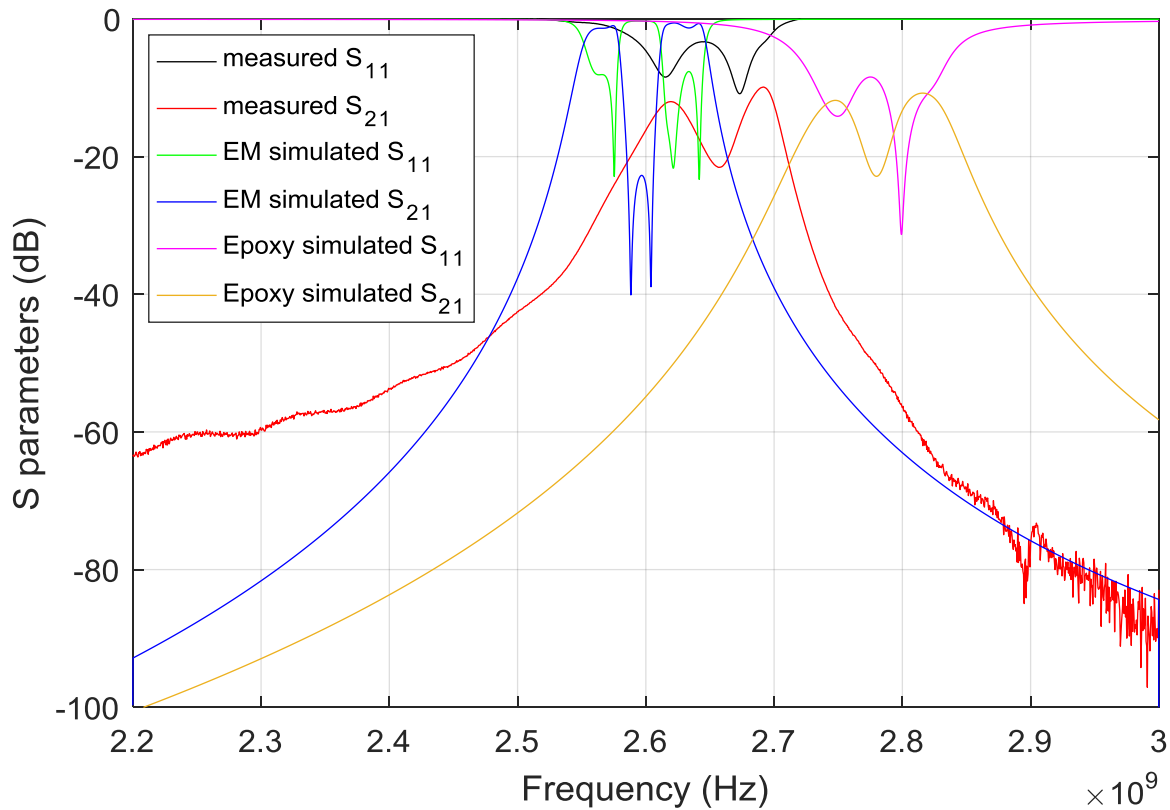


Figure 3.45 Measured and simulated frequency response with epoxy.

The filter was further investigated by simulation in CST MW with a 0.1 mm thick epoxy on the rectangular surfaces of the DRs for fixture. The epoxy has a dielectric constant $\epsilon_r=4.0$ and loss constant $\tan \delta=0.06$ [101]. Figure 3.45 also includes the simulated frequency response with epoxy.

We can see that the measured frequency response is very close to the simulated response with epoxy, apart from the frequency discrepancies. It shows that the epoxy losses and the imperfect $TE_{01\delta}$ mode may be the main factor causing the significant discrepancies between the simulated and measured frequency responses.

There were only six resonators obtained from the dielectric supplier ‘Filtronic’. Thus, the further improvement on resonators and fabrication techniques could not be achieved at this step. However, some advice on further designs are provided by analysing the above results, including using silver-plated DRs, fabricating the DRs in suitable moulds, using a one-piece external coupling probe, and using tuning screws.

3.5 Limitations and further work

The synthesis process and filter designs in the previous sections have shown that the limitation of dual-passband response synthesis method for dual-band bandpass filter design. Firstly, it is only applicable for realisation of narrow dual-band BPFs because the couplings were assumed frequency independent. Secondly, the unloaded Q factor of resonator was assumed infinite when synthesising the dual-passband response. However, it is finite in practice and does cause significant losses and attenuation of filter response. High Q resonators are required when implementing dual-band BPFs. Thirdly, the resonators were assumed electrically and physically identical during the synthesis [102]. However, the loading effect has significant influence on the dual-passband response synthesis. The tuning and optimisation for resonators and couplings might be necessary hence the complexity of filter implementation is increased. Finally yet importantly, the resonator must be designed carefully so that the spurious band do not interfere or overlap with the desired second passband. This is especially important for the resonator that the spurious resonant frequencies are very close to the employed resonant frequency.

Further improvement on the dual-passband response synthesis method could focus on eliminating the limitations to extend the method capability and reduce the implementation consideration and process. Other further work is to improve the fabricated sixth order dual-band BPF to realise desired frequency response. The improvement includes using silver-plated DRs, DRs fabricated in suitable moulds, one-piece external coupling probes, tuning screws for resonators and coupling, and smaller fabrication tolerance.

3.6 Conclusions

In conclusion, the synthesis procedures for the realisation of dual-band bandpass filters have been demonstrated in this chapter.

The frequency transformation technique that generates a symmetrical dual-passband frequency response from a normalised low pass prototype response has been presented. A coupling matrix can be generated from the transformed dual-passband response and then used for the direct synthesis of a dual-band bandpass filter.

Section 3.3 has described synthesis procedures of coupling matrix, derived from the transfer function of the filter. The admittance matrix or impedance matrix can be derived from the known filter transfer function of a linear two-port network. A real orthogonal matrix and a

diagonal matrix are utilised to form the coupling matrix. The orthogonal matrix and the diagonal matrix can be extracted from the admittance matrix of the network which is derived from the transfer function of the network. In practice, the coupling matrix has to be transformed to a convenient form for the filter implementation, based on the filter topology. A physically realisable coupling matrix can be generated by solving a set of non-linear equations using Newton-Raphson procedure. A program provided by Gajaweera generates coupling matrices using Newton-Raphson method. It has been used to synthesise the coupling matrices for filter designs in the research.

Section 3.4 has described the general process of dual-band bandpass filter design using dual-passband response synthesis method. An eighth order dual-band bandpass filter was designed and implemented using microstrip square open-loop resonators. The dual-passband was synthesised from a symmetrical four-pole generalised Chebyshev response, from which the coupling matrix for filter implementation was generated. The resonator, the external and inter-resonator couplings were characterised for filter design. However, the simulation and measurement of the designed filter did not show reasonable frequency responses, due to the low unloaded Q factor of the employed resonators. The passbands are narrow and high selective due to the assumptions made in the synthesis procedures, thus the desired filter requires high Q resonators. The simulation studies on finite Q suggested that the resonator for implementation of narrow dual-band bandpass filters must have an unloaded Q factor at least ten times the loaded Q from the filter response. As this filter was designed at the early stage of the research program, the key effect of finite Q on resonator was not fully considered. Therefore, high Q resonators were used for the design of a sixth order dual-band bandpass filter.

The sixth order dual-band bandpass filter was designed and implemented using $TE_{01\delta}$ mode quarter cylindrical dielectric resonators that provide high Q factor of 2120 with a very compact size. The dual-passband was synthesised from an asymmetrical three-pole generalised Chebyshev response. The coupling matrix for filter implementation was synthesised from the transformed dual-passband response using Newton-Raphson method. The resonator structure, suitable external and inter-resonator coupling structures have been investigated and characterised for the filter design. A curved probe was proposed for the realisation of magnetic type external coupling structure. Two types of aperture were utilised to realise the magnetic inter-resonator couplings. The EM simulation showed two passbands at 2.565 GHz and 2.630 GHz, with 3-dB bandwidth of 28 MHz and 35 MHz, agreeing closely with the simulation of equivalent circuit, the synthesised response, and the design specifications. This designed filter

is very compact, saving more than 75% volume when compared with a filter using coaxial resonators or traditional cylindrical dielectric resonators. Moreover, it has good thermal resistance since the heat of the DRs can be directly transferred to the Aluminium cavity. The breakdown power of the filter was estimated from EM simulation, approximately 95 Watt. It showed a relatively high power handling capability in comparison with planar filters. However, the measured frequency response of the filter was hardly a reasonable bandpass filter response. The study on EM simulation showed that the epoxy losses and the imperfect $TE_{01\delta}$ resonant mode might cause the discrepancies between simulation and measurement. The filter could be further improved by using silver-plated DRs, DRs fabricated in appropriate moulds, one-piece external coupling probes, tuning screws for resonators and inter-resonator couplings, and smaller fabrication tolerance.

The dual-passband response synthesis has limitations and requirements when designing dual-band bandpass filters. The couplings were assumed frequency invariant, implying narrowband approximation. The narrowband filter has a requirement for the unloaded Q factor of resonators. High Q resonators are suggested when designing narrow dual-band bandpass filters. In addition, the external loading effect has been neglected in the synthesis procedures. Therefore, the tuning and optimisation process for resonators are required in filter implementation. Since only the fundamental resonant frequency of the resonators is employed to realise the dual-passband response, the resonator must be designed carefully to avoid any possible interference or overlap with its spurious resonance. The further work includes developing the dual-passband response synthesis method with the consideration of the above limitation and requirement, and improving the designed sixth order dual-band bandpass filter with silver plated DRs.

Chapter 4: Dual-band resonators

4.1 Introduction

This chapter presents dual-band resonators for the realisation of dual-band bandpass filters. Dual resonant modes of the resonator operating at different frequencies are utilised simultaneously to form the passbands of the filter. The resonant modes and resonator structures have been studied to control the resonant frequencies for realisation of dual-band bandpass filters. This chapter shows two types of dual-band resonator structures for the implementation of dual-band bandpass filters: stepped impedance resonator (SIR) and non-uniform pitch helical resonator.

The previous research in [1, 20] proposed a stepped impedance resonator, which is composed of two or more transmission lines with different characteristic impedance, to realise controllable resonant frequencies. Dual-band [22, 23, 103] and tri-band [21, 104, 105] bandpass filters have been designed using dual- and tri-section microstrip SIRs, respectively. Coaxial SIRs have also been studied in [106, 107] to realise dual-band bandpass filters. In Section 4.2.1, the dual-band characteristics of a dual-section SIR in stripline configuration are analysed, showing the relationship between the ratios of resonant frequencies and the impedance ratio of a dual-section quarter-wavelength microstrip SIR. Section 4.2.2 analysed the dual-band characteristics of the quarter-wavelength dual-section SIR in coaxial line configuration. The quarter-wavelength coaxial SIR is then characterised for filter design, as well the external and inter-resonator coupling structures, shown in Section 4.2.3. A second order dual-band bandpass filter has been designed and implemented. There is a good agreement between the measured and simulated frequency responses.

Dual-band antenna has been developed for mobile phones working at GSM (900 MHz) and DCS (1800 MHz) frequency bands based on a non-uniform helix structure [26, 27]. This structure is also applicable to resonator, resulting in a non-uniform pitch helical resonator with dual-band capability [51]. It has been shown by the author that the ratio between the fundamental resonant frequency and the first spurious resonant frequency of a uniform pitch helical resonator can be altered by modifying its pitch [51]. Since then, Chu and Zhang [108] also studied non-uniform pitch helical resonator and used it for dual-band bandpass filter design. Section 4.3 demonstrates the research on the newly proposed and developed dual-section non-

uniform pitch helical resonator structure for dual-band bandpass filter design. Two non-uniform pitch helical resonator structures are discussed and analysed, categorised as Category I and II non-uniform pitch helical resonators, in terms of pitch modification. Category I non-uniform pitch helical resonator has equal number of turns for the top and the bottom sections, therefore, the pitch is modified by the height of each section. Category II non-uniform pitch helical resonator has equal height for the top and the bottom sections, but different number of turns for the top and the bottom sections to modify its pitch.

In Section 4.3.1, two theoretical models are introduced to analyse the dual-band characteristics of the proposed non-uniform pitch helical resonator structures: the SIR model and the circuit model. The analytical study in Section 4.3.1 shows that the non-uniform pitch helical resonator can be modelled as a SIR since the pitch difference causes different impedance [51]. Therefore, the study on the dual-band characteristics of the SIR in Section 4.2 can be applied to the proposed non-uniform pitch helical resonator structures for analysis. The impedance ratio of the dual sections of a Category I non-uniform pitch helical resonator can be estimated as the ratio of the number of turns between the dual sections ($N_{\text{top}}/N_{\text{btm}}$) whereas the impedance ratio of a Category II non-uniform pitch helical resonator can be approximate as the ratio of height between the top and the bottom sections ($h_{\text{btm}}/h_{\text{top}}$). The relationship between frequency ratio and impedance ratio of Category I non-uniform pitch helical resonator can only be obtained from EM simulation since it is formed by two sections with different electrical length. However, there is an analytical equation available to express the frequency ratio of a Category II non-uniform pitch helical resonator, as it can be approximate as two sections with the same effective electrical length. The circuit model analyses the dual-section non-uniform pitch helical resonator as a uniform pitch helical resonator with either a capacitive or inductive load. There are analytical equations derived for Category I and II non-uniform pitch helical resonators, expressing the frequency ratio (f_2/f_1) against the number of turns ($N_{\text{top}}/N_{\text{btm}}$) or the ratio of height ($h_{\text{btm}}/h_{\text{top}}$), respectively. Section 4.3.1 also shows a new model for the proposed dual-section non-uniform pitch helical resonator, based on the above theoretical models and simulation studies. This new model provides fast and accurate prediction of the frequency ratios for each category resonators, and can be used to extract the geometry of resonator structures from the design specifications.

The general design procedure of non-uniform pitch helical resonator was then presented with a resonator design example in Section 4.3.2. Section 4.3.3 presents the experimented results of

fabricated Category I and II non-uniform pitch helical resonators to verify the above analysis and simulation. The external and inter-resonator coupling structures required characterisation for dual-band bandpass filter design using non-uniform pitch helical resonators. Section 4.3.4 illustrates the structures and topologies of the external and inter-resonator couplings. Direct tapping and parallel plate coupling are proposed for the external coupling. The inter-resonator coupling structure can be realised by a uniform-width aperture or a step-width aperture. The step-width aperture has an extra degree of freedom on the width, independently realising the inter-resonator coupling coefficient of each frequency band. Section 4.3.5 presents the implementation of dual-band bandpass filters using non-uniform pitch helical resonators. A second order dual-band BPF and a third order dual-band BPF were designed, simulated, fabricated and tested, using Category I non-uniform pitch helical resonators. Category II non-uniform pitch helical resonators were also utilised for the design of a second order dual-band BPF. The design process, simulation and measurement results of the dual-band bandpass filters are shown in this section.

Section 4.4 discusses and suggests further research on SIR and non-uniform pitch helical resonator. Finally, Section 4.5 summarises the contents of this chapter.

4.2 Stepped Impedance Resonator (SIR)

The concept of SIR was proposed by Makimoto and Yamashita [20] in 1980s. They showed that the second resonant frequency of a stepped impedance resonator varies against the impedance ratio of the non-uniform microstrip line while the overall length of the microstrip line determines the fundamental resonant frequency. The impedance ratio of a stripline SIR is related to the width ratio of the strip lines [22] while the impedance ratio of a coaxial SIR is related to the diameter ratio of the coaxial lines [106, 109]. Therefore, the spurious resonant frequency of a stripline SIR or a coaxial SIR can be controlled by the width ratio or diameter ratio, respectively. The dual-section SIR has been modified and used for dual-band bandpass filters [22, 23, 103, 106, 107]. Tri-section SIR has also been developed and utilised in tri-band bandpass filter design [21, 104, 105].

This section demonstrates the SIR as a dual-band resonator for the design of dual-band bandpass filters. Firstly, it presents the stripline configurations of a SIR and its resonance characteristics. Secondly, the dual-band characteristic of a coaxial SIR is analysed. Thirdly, this section shows a second order dual-band bandpass filter design using characterised coaxial SIRs.

4.2.1 Resonance characteristics of SIR

The SIR is a TEM or quasi-TEM mode resonator which consists of more than two TEM/ quasi-TEM mode transmission lines with different characteristic impedance [1]. Figure 4.1 shows the dual-section structure of the quarter- ($\lambda/4$) and half-wavelength ($\lambda/2$) type SIR in the stripline configuration for analysis.

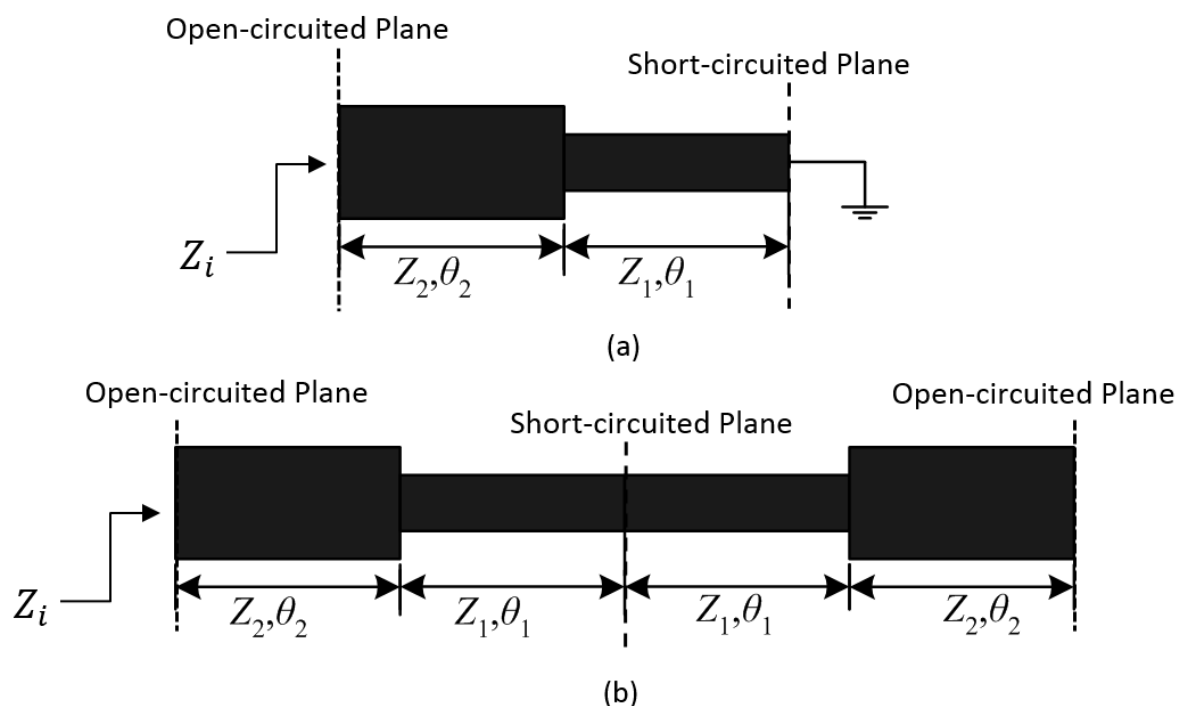


Figure 4.1 Basic structure of SIR in stripline. (a) Quarter-wavelength type. (b) Half-wavelength type.

The characteristic impedance and electrical length of the transmission lines between the open-circuited and the short-circuited ends in Figure 4.1 are defined as Z_1 and Z_2 , θ_1 and θ_2 , respectively. Neglecting the step discontinuity and edge capacitance, the input impedance of the $\lambda/4$ and $\lambda/2$ type SIRs can both be expressed as [1, 109]

$$Z_i = jZ_2 \frac{Z_1 \tan \theta_1 + Z_2 \tan \theta_2}{Z_2 - Z_1 \tan \theta_1 \tan \theta_2}. \quad (4.1)$$

The resonance condition of the SIR is [1, 109]

$$Z_i = \infty. \quad (4.2)$$

From (4.2), we have the resonance condition as

$$Z_1 \tan \theta_1 + Z_2 \tan \theta_2 = \infty \quad (4.3)$$

or

$$Z_2 - Z_1 \tan \theta_1 \tan \theta_2 = 0. \quad (4.4)$$

Equation (4.3) and (4.4) can be written as

$$\tan \theta_1 + R_z \tan \theta_2 = \infty \quad (4.5)$$

$$\tan \theta_1 \tan \theta_2 = R_z \quad (4.6)$$

where R_z represents the impedance ratio that $R_z = Z_2/Z_1$.

It is preferably to select equal-length-stripline for analysis, which means $\theta_1 = \theta_2 = \theta$. Next, we consider the resonance conditions for the $\lambda/4$ and $\lambda/2$ type SIRs respectively.

Quarter-wavelength type SIR

The resonance conditions of the quarter-wavelength type SIR only depend on (4.6), which can be further represented as [1, 109]

$$\tan^2 \theta = R_z \quad (4.7)$$

whose solutions are expressed by

$$\theta = \pm \tan^{-1} \sqrt{R_z} + n \cdot \pi \quad (4.8)$$

where n is an integer.

Let $\theta_0, \theta_{s1}, \theta_{s2}, \dots, \theta_{sn}$ represent the electrical length of the fundamental and the spurious resonances, then

$$\begin{aligned} \theta_0 &= \tan^{-1} \sqrt{R_z} \\ \theta_{s1} &= -\tan^{-1} \sqrt{R_z} = \pi - \theta_0 \\ \theta_{s2} &= \tan^{-1} \sqrt{R_z} + \pi = \pi + \theta_0 \\ \theta_{s3} &= -\tan^{-1} \sqrt{R_z} + \pi = 2\pi - \theta_0 \end{aligned} \quad (4.9)$$

and so on.

Thus the frequency ratios of the $\lambda/4$ type SIR are [110]

$$\frac{f_{s1}}{f_0} = \frac{\theta_{s1}}{\theta_0} = \frac{\pi - \theta_0}{\theta_0} = \frac{\pi}{\tan^{-1}\sqrt{R_z}} - 1 \quad (4.10)$$

$$\frac{f_{s2}}{f_0} = \frac{\theta_{s2}}{\theta_0} = \frac{\pi + \theta_0}{\theta_0} = \frac{\pi}{\tan^{-1}\sqrt{R_z}} + 1 \quad (4.11)$$

where f_0 , f_{s1} and f_{s2} represent the fundamental, the first and the second spurious resonant frequency, respectively.

Half-wavelength type SIR

Equation (4.5) and (4.6) express the resonance conditions for the half-wavelength type SIR, respectively. Since $\theta_1 = \theta_2 = \theta$, the solutions of (4.5) and (4.6) are

$$\theta = \pi/2 + n \cdot \pi \quad (4.12)$$

and
$$\theta = \pm \tan^{-1}\sqrt{R_z} + n \cdot \pi \quad (4.13)$$

where n is an integer.

Thus

$$\begin{aligned} \theta_0 &= \tan^{-1}\sqrt{R_z} \\ \theta_{s1} &= \pi/2 \end{aligned} \quad (4.14)$$

$$\theta_{s2} = -\tan^{-1}\sqrt{R_z} = \pi - \theta_0$$

where θ_0 , θ_{s1} , θ_{s2} corresponds to the electrical length of the fundamental, the first and second spurious resonances, respectively.

The frequency ratios for the $\lambda/2$ type SIR is expressed as [1]

$$\frac{f_{s1}}{f_0} = \frac{\theta_{s1}}{\theta_0} = \frac{\pi/2}{\theta_0} = \frac{\pi}{2 \tan^{-1}\sqrt{R_z}} \quad (4.15)$$

$$\frac{f_{s2}}{f_0} = \frac{\theta_{s2}}{\theta_0} = \frac{\pi - \theta_0}{\theta_0} = \frac{\pi}{\tan^{-1}\sqrt{R_z}} - 1 \quad (4.16)$$

where f_0 , f_{s1} and f_{s2} represent the fundamental, the first and the second spurious resonant frequency, respectively.

Figure 4.2 shows the frequency ratio (f_{s1}/f_0) for quarter- and half-wavelength type SIRs, showing that the frequency ratio is controllable with the impedance ratio.

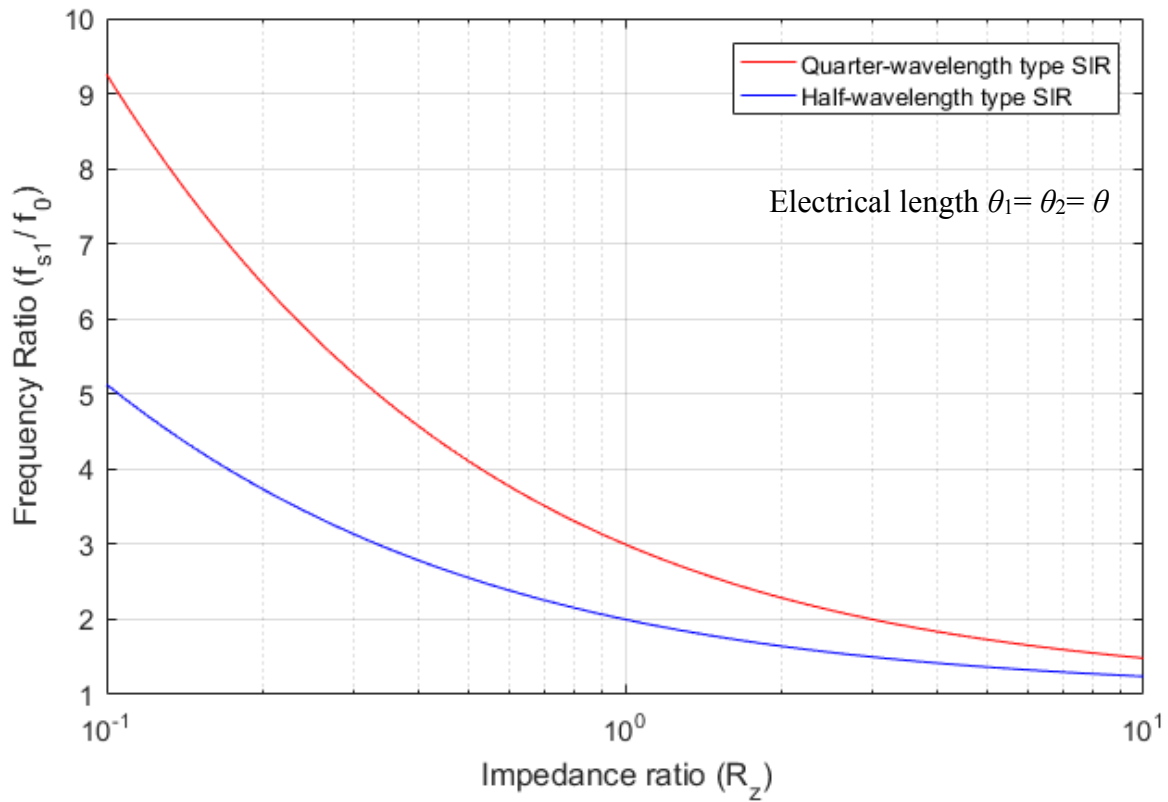


Figure 4.2 Relationship between frequency ratio (f_{s1}/f_0) and impedance ratio (R_z) of dual-section quarter- and half-wavelength type SIRs.

The above derivation also shows that the electrical length θ of an equal-length SIR is independent of the frequency ratios. Therefore, the fundamental resonant frequency and the frequency ratios can be controlled independently by the electrical length and impedance ratio of the SIR, respectively.

4.2.2 Coaxial SIR

The above derivation and analysis of stripline SIR is also applicable to the coaxial SIR. Figure 4.3 shows a typical $\lambda/4$ type coaxial SIR structure that composes of two inner conductors in a cavity. Square cross-section cavity is used for ease of aperture realisation.

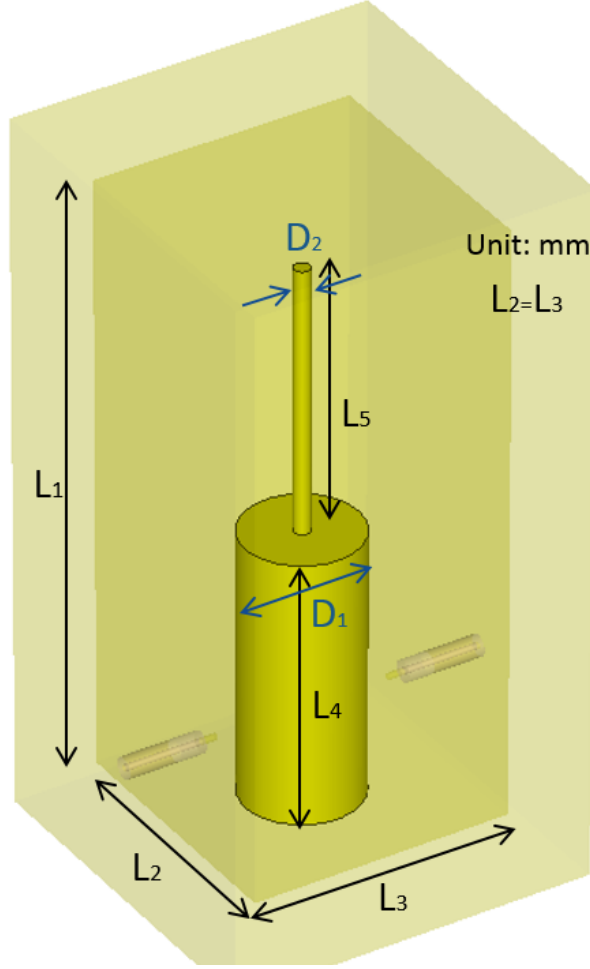


Figure 4.3 Structure of a coaxial SIR.

The characteristic impedance of a cylindrical coaxial resonator is expressed by [109]

$$Z_0 = \frac{60}{\sqrt{\epsilon_r}} \cdot \ln\left(\frac{b}{a}\right) \quad (4.17)$$

where ϵ_r is the dielectric constant of filled material, a and b are the diameters of inner conductor and outer cylindrical cavity, respectively.

Chen et al. [106] suggested that (4.17) is also a good estimation of the characteristic impedance of a coaxial line in a square cavity. Therefore, for the coaxial SIR structure shown in Figure 4.3, the impedance ratio is approximately expressed as

$$R_z = \frac{Z_2}{Z_1} = \frac{\ln \frac{L_2}{D_2}}{\ln \frac{L_2}{D_1}} \quad (4.18)$$

where L_2 is the cross-section length of the square cavity and $L_2=L_3$, D_1 and D_2 are the diameters

of lower and upper coaxial lines, respectively.

Substitute (4.18) into (4.10), the relationship between frequency ratio (f_1/f_0) and diameters of the quarter-wavelength type coaxial SIR is obtained as

$$\frac{f_1}{f_0} = \frac{\pi}{\tan^{-1} \sqrt{\frac{\ln \frac{L_2}{D_2}}{\ln \frac{L_2}{D_1}}}} - 1 \quad (4.19)$$

where f_0 and f_1 are the fundamental and first spurious resonant frequencies.

The coaxial SIR has been simulated in CST MW with the parameters: $L_1=115$, $L_2=L_3=50$, $L_4=L_5=50$, $D_2=3.175$ (Unit: mm). Figure 4.4 shows the simulated and theoretically calculated frequency ratios (f_1/f_0) against the diameter ratio (D_1/D_2), respectively. The simulated result shows good agreement with the theoretical result calculated by (4.19). The difference between simulated and theoretical results when the diameter ratio is large are likely caused by the accuracy of (4.17) which was used to estimate the characteristic impedance of a coaxial line in a square cavity.

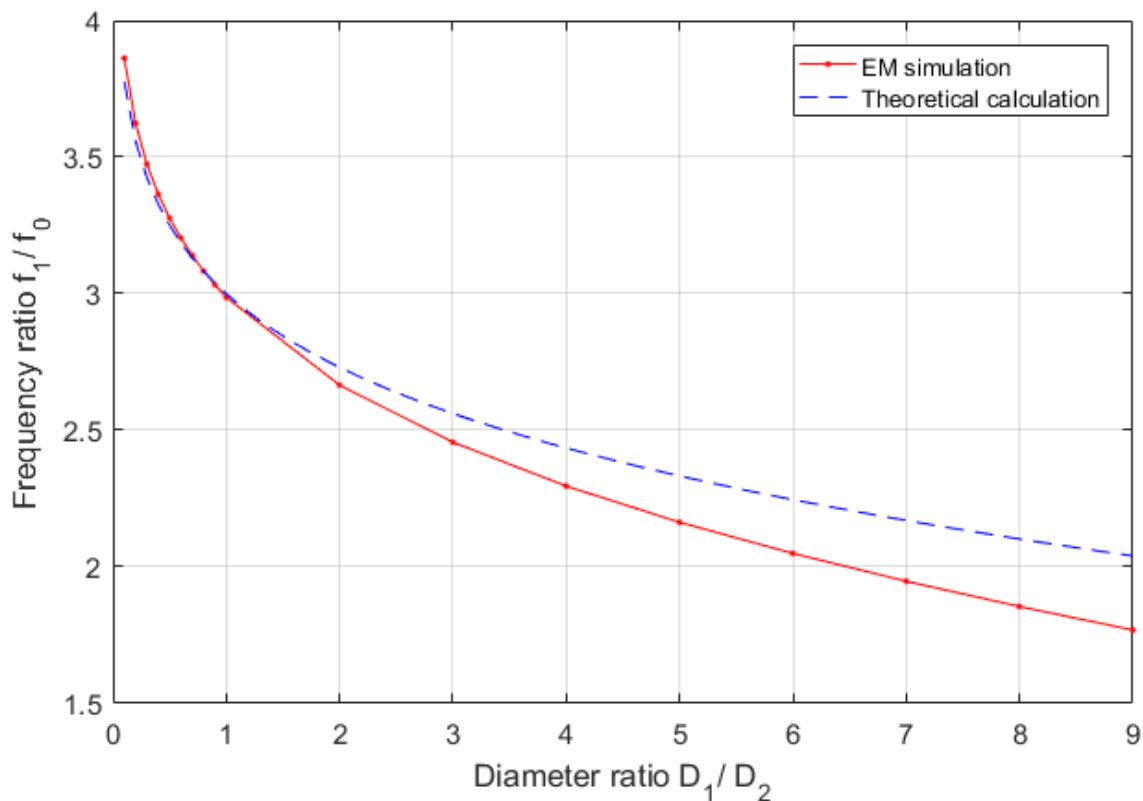


Figure 4.4 Frequency ratio (f_1/f_0) profile of coaxial SIR against diameter ratio (D_1/D_2).

4.2.3 Dual-band bandpass filter design using Coaxial SIRs

A second dual-band bandpass filters working at GSM bands (900/1750 MHz) was designed. The desired frequency response is Chebyshev response with 0.1 dB ripple and the desired 3-dB fractional bandwidths (FBWs) are 1.11% and 1.14% for 900 and 1750 MHz passbands, respectively.

Resonator characterisation

Figure 4.4 shows that the diameter ratio of a $\lambda/4$ type coaxial SIR is approximate 7.0, in order to realise the frequency ratio of the desired dual-band bandpass filter. Thus, the diameter of the bottom post is determined as 22.225 mm. The next step is to determine the lengths of the top and the bottom posts (L_4 and L_5), in order to realise the fundamental resonant frequency at 900 MHz. They were then determined as 51.5 mm, according to the EM simulation.

Figure 4.5 shows the dimensions of the quarter-wavelength type coaxial SIR.

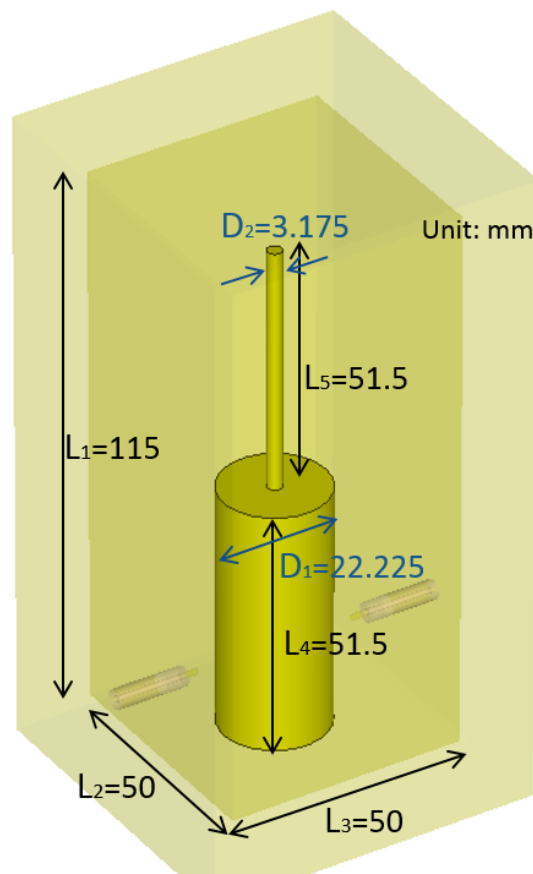


Figure 4.5 Determined coaxial SIR structure and dimensions for the dual-band BPF design.

Figure 4.6 shows the fabricated resonator. The top slim copper post is screwed into the bottom copper post which is screwed into the base of the Aluminium cavity.

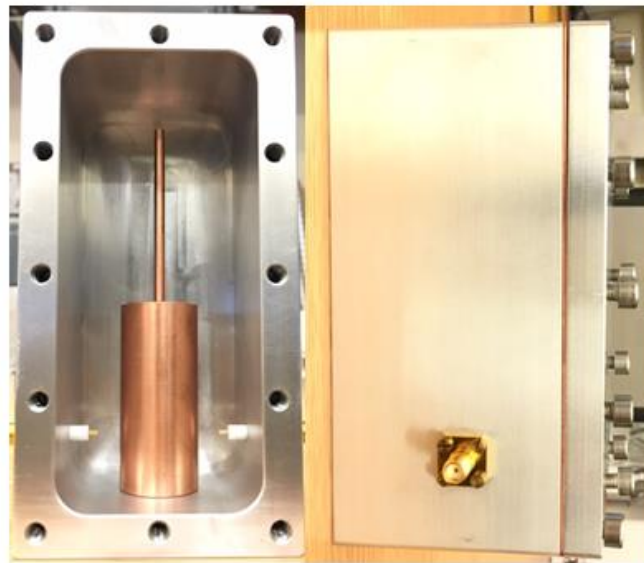


Figure 4.6 Fabricated coaxial SIR.

The simulated and measured results are shown in Table 4-I for comparison. The measured resonant frequencies are about 1% higher than the corresponding simulated frequencies. Additionally, the measured frequency ratio (f_1/f_0) is extremely close to the simulated frequency ratio. However, the measured unloaded Q factors are about 30% smaller than the corresponding unloaded Q factors from simulation. This is probably caused by the losses of aluminum cavity and screw sections used for the fixture of copper posts. In addition, the imperfect shielding would also cause lower unloaded Q factors than expected.

Table 4-I Simulated and measured results of the designed coaxial SIR.

Parameter	Simulated value	Measured value
Fundamental resonant frequency f_0 (MHz)	897	906
Unloaded Q at f_0	3700	2540
Second resonant frequency f_1 (MHz)	1745	1758
Unloaded Q at f_1	4300	2730
The third resonant frequency f_2 (MHz)	2850	2880
Frequency ratio f_1/f_0	1.945	1.940

External coupling structure characterisation

The external coupling structure used for this filter design is shown in Figure 4.7.

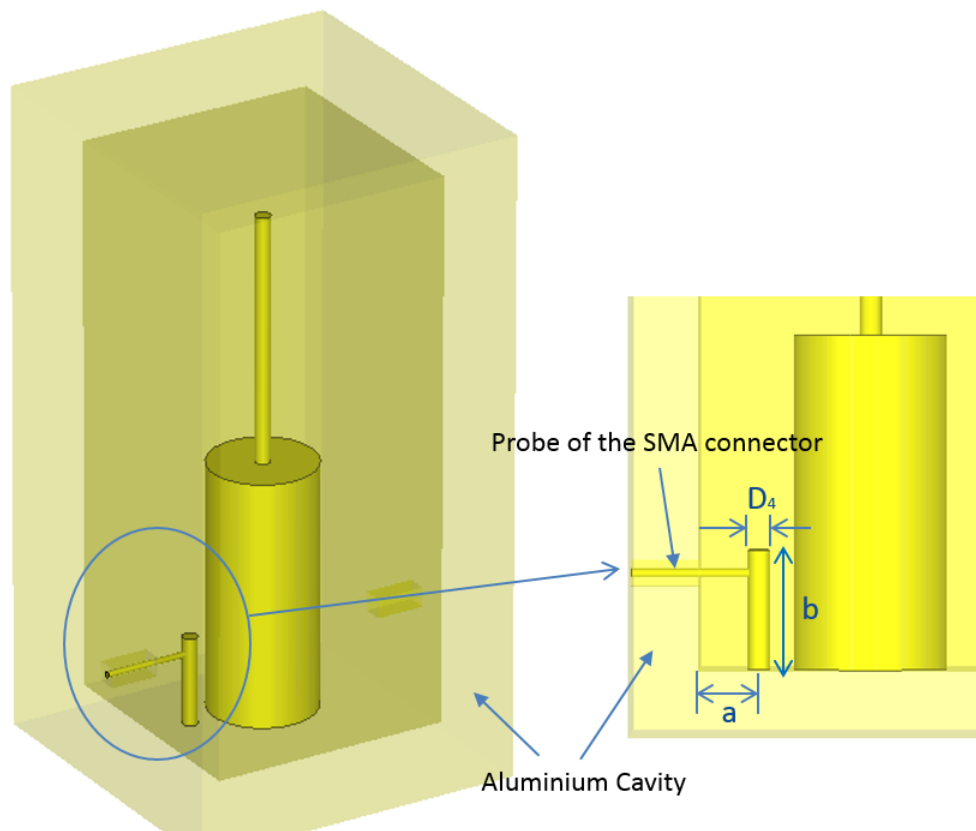


Figure 4.7 Tuneable external coupling structure for the coaxial SIR.

The probe of SMA connector taps into a copper post which is vertically movable. Therefore, there are three parameters affecting the external Q s of the wanted bands: diameter of the post (D_4), distance from the post centre to cavity wall (a), and the post height (b). In practice, the copper post was partly screwed into the cavity base to realise the ability of tuning. Compared to the helical feeding structure in [106], this structure provides ability to tune the external Q factors by vertically moving the copper post.

The post diameter (D_4) was set as 3.175 mm, a standard post diameter that was also used for the upper coaxial line of the SIR. The external coupling profile was obtained by sweeping the parameters a and b . Figure 4.8 and Figure 4.9 shows the external coupling profiles of the first band and the second band, respectively. We can see that the external Q factor of the first band is only affected by the distance from the post centre to cavity wall (a). However, the external Q factor of the second band is controlled by the distance from the post centre to cavity wall (a), and the post height (b). Therefore, we can control the external Q factors of the first and the second bands by simultaneously changing the parameter a and b .

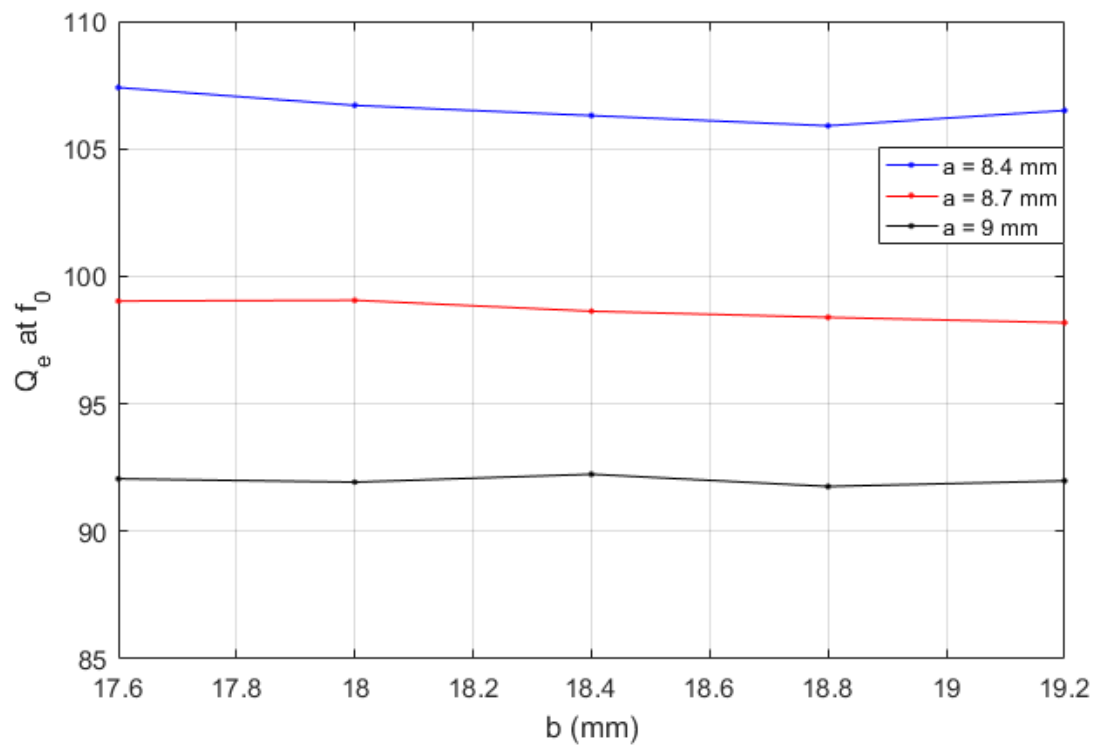


Figure 4.8 External coupling profile of the first band.

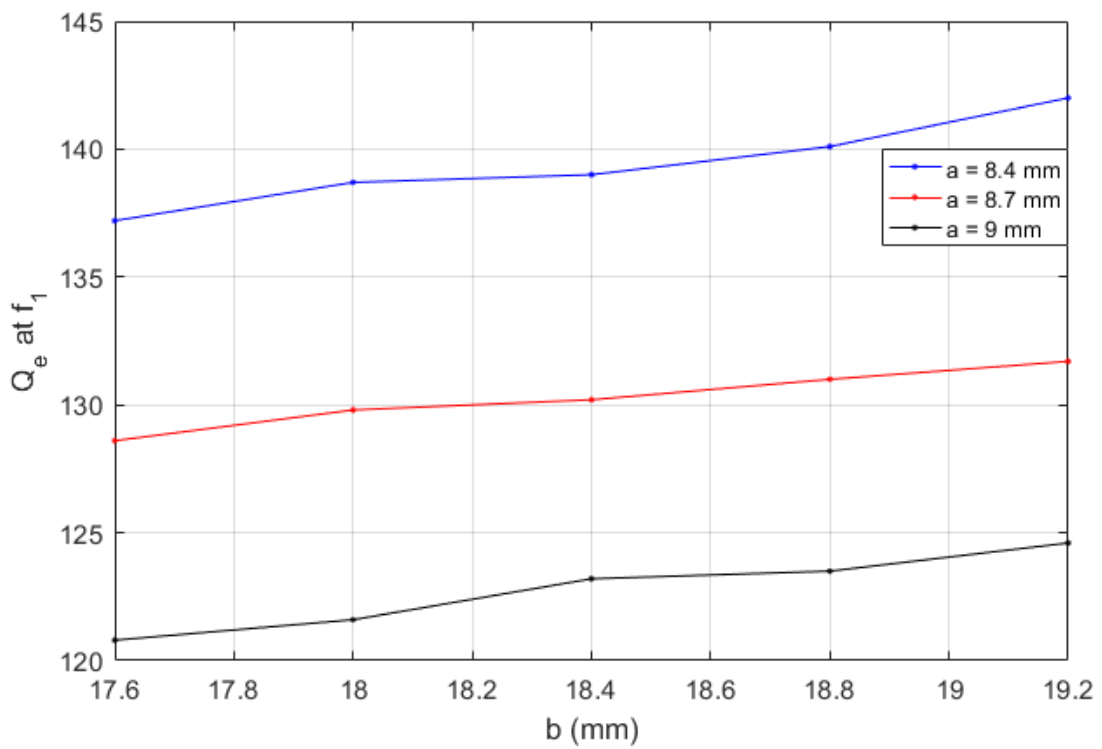


Figure 4.9 External coupling profile of the second band.

Inter-resonator coupling structure characterisation

The field patterns of the coaxial resonator were studied in order to design a structure that relatively independently controls inter-resonator coupling at the first and the second resonances, respectively. The field patterns at the first resonance of the coaxial SIR are shown in Figure 4.10.

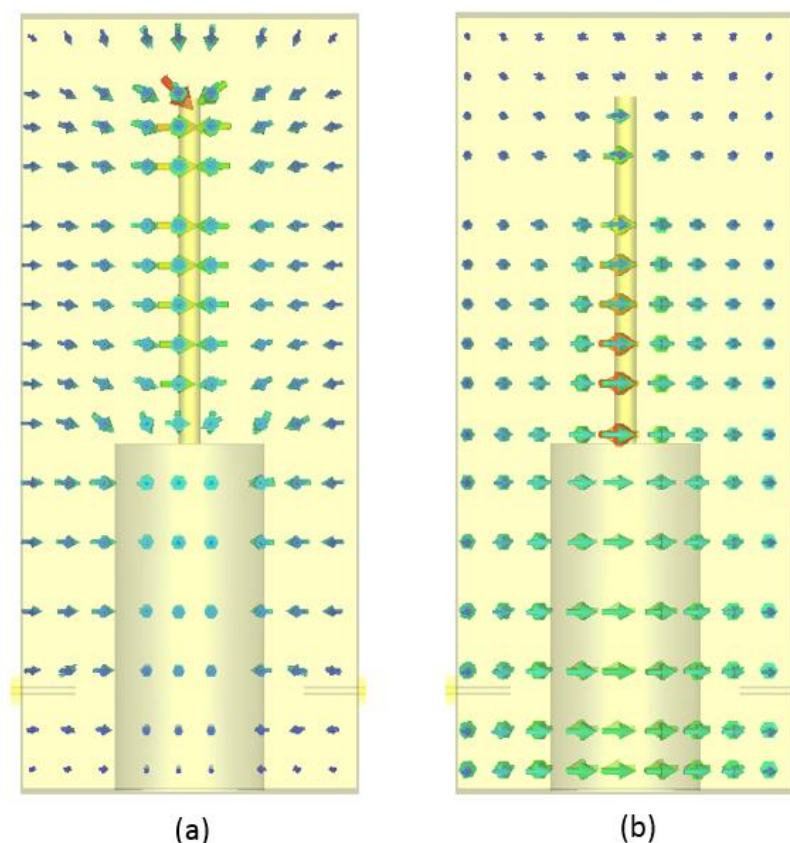


Figure 4.10 Field patterns at the first resonance of the coaxial SIR. (a) electric field. (b) magnetic field.

The electric field reaches maximum at the top of the upper post, reaches minimum at the bottom of the lower post. The peak of the magnetic field appears at the bottom of upper resonator whereas the magnetic field reaches minimum at the top of the upper resonator.

Figure 4.11 shows the field patterns at the second resonance of the coaxial SIR. The scale of the field intensity in Figure 4.10 and Figure 4.11 have been set to the same. Comparing the field patterns at the first and the second resonances, we can see that the maximum and minimum electric and magnetic fields appear at the same area of the coaxial SIR, respectively. However, the electric field of the first resonance is higher than that of the second resonance at the middle and the bottom of upper post. At the middle and the top of the lower post, the magnetic field strength of the first resonance is higher than that of the second resonance.

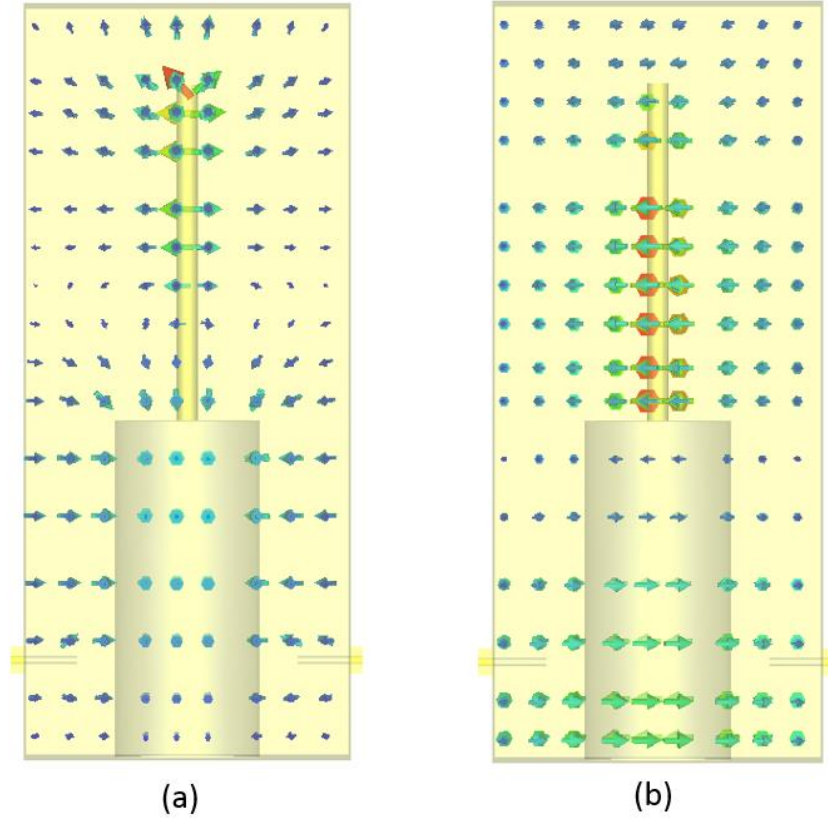


Figure 4.11 Field patterns at the second resonance of the coaxial SIR. (a) electric field. (b) magnetic field.

The electric and magnetic coupling coexist and cancel out when coupling the coaxial SIRs by aperture [107]. We proposed an inter-resonator coupling structure for coaxial SIRs, shown in Figure 4.12. Aperture dimensions (W_1 , W_2 and L_8) coupling screw dimensions (D_3 and L_7) are utilized to control the inter-resonator couplings. When the coaxial SIRs are coupled by a complete open aperture, the magnetic coupling is dominant for both the first and second resonances. By analysing the magnetic fields of the first and the second resonances, the magnetic coupling reduces when reducing the L_8 and W_1 . However, reducing W_1 and L_8 would cause more magnetic coupling reduction of the second resonance, compared to the first resonance. With proper dimensions of L_6 (or L_8), the dominant inter-resonator coupling type of the first and the second resonances may be different. We set the parameters shown in Table 4-II to maintain the coupling coefficients in a certain range. When $L_7=0$, the magnetic coupling is dominant at the first resonance whereas the electric coupling is dominant at the second resonance. From the electric field patterns in Figure 4.10 and Figure 4.11, we can see that a long coupling screw may have more impact on the electric coupling of the second resonance than that of the first resonance. Therefore, the length of the coupling screw can be used to mainly control the coupling of the second resonance.

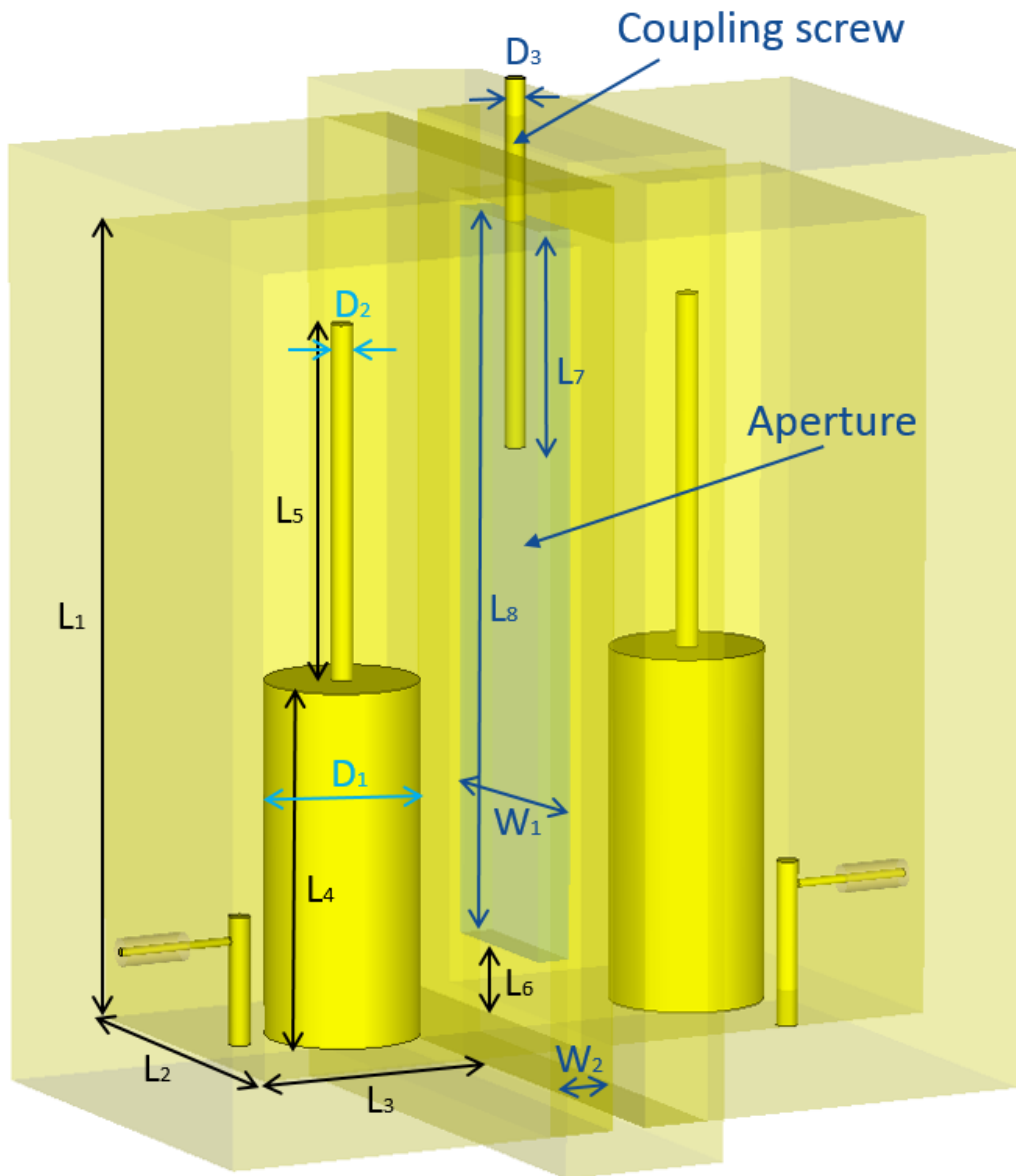


Figure 4.12 Inter-resonator coupling structure.

Table 4-II Pre-set parameters for the inter-resonator coupling structure.

Parameter Name	Value (mm)
D_3	3.0
L_8	105.0
W_1	24.0
W_2	5.0

The profiles of inter-resonator couplings are obtained by varying the screw length (L_7) in both EM simulation and measurement with two resonators both loosely external coupled. The measured inter-resonator coupling coefficient was obtained from the measured S_{21} parameter. Simulated and measured coupling coefficients of the first resonance are shown in Figure 4.13.

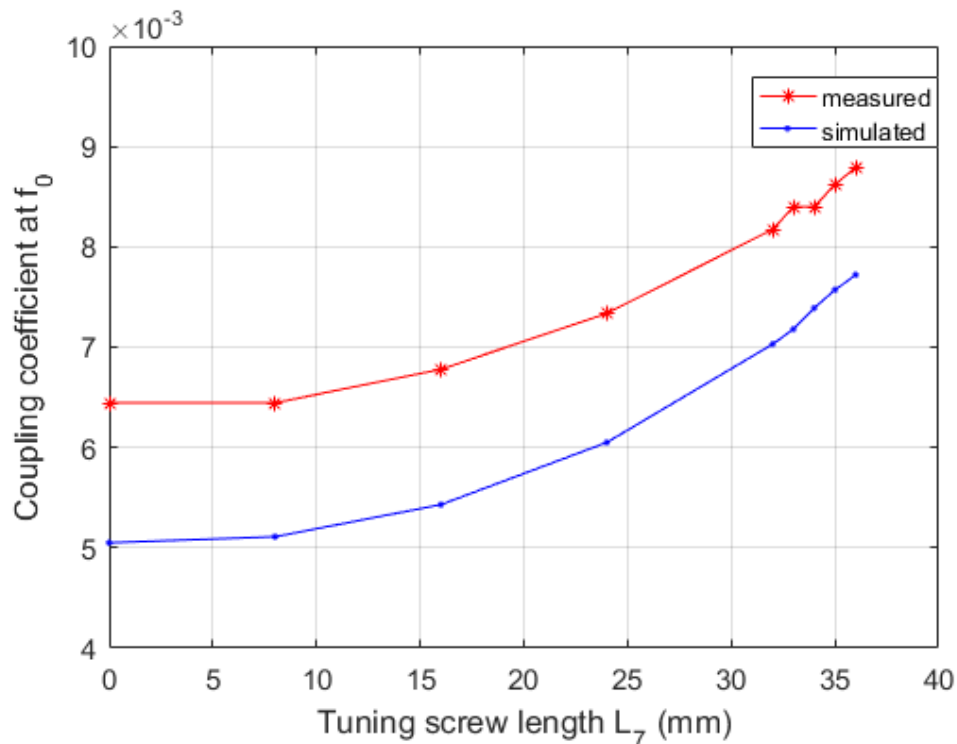


Figure 4.13 Inter-resonator coupling profile of the first resonance.

The trend of the simulated curve agrees with that of the measured curve. As mentioned, the dominant coupling in the mixed coupling is magnetic coupling. Therefore, the coupling screw reduces the electric coupling, resulting in increased coupling coefficients. However, the measured coupling coefficients are larger than the simulated. It may be caused by the screw thread of the fabricated coupling screw and the imperfect shielding of the inter-resonator coupling structure.

Figure 4.14 shows the coupling coefficient of the second resonance. It shows that the dominant coupling changed from electric type to magnetic type when increasing the length of coupling screw. The electric coupling is dominant when $L_7 < 16$ mm, but the overall mixed coupling coefficient is quite small. When $L_7 > 16$ mm, the magnetic coupling becomes dominant, and the mixed coupling coefficient can be adjusted in a wide range.

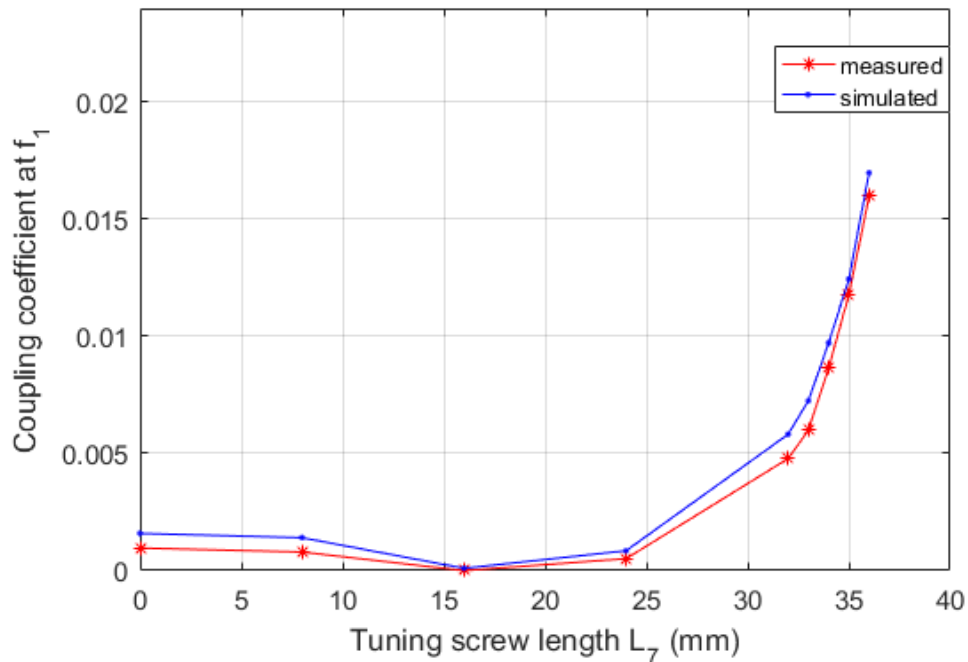


Figure 4.14 Inter-resonator coupling profile of the second resonance.

Filter characterisation

Figure 4.12 also shows the model of the designed second order filter. It was also used for the EM simulation with the dimensions obtained from simulated coupling profiles. Figure 4.15 shows the fabricated filter. Two coaxial SIRs are fabricated and connected through an inter-resonator coupling section. The coupling part dimensions are obtained from measured coupling profiles, which are $a=8.7$, $b=18.4$, $D_3=3$, $L_8=105$, $W_1=24$, $W_2=5$ (Unit: mm). Figure 4.16 shows the simulated and measured S-parameters over a wideband frequency range 0.5 – 3 GHz.

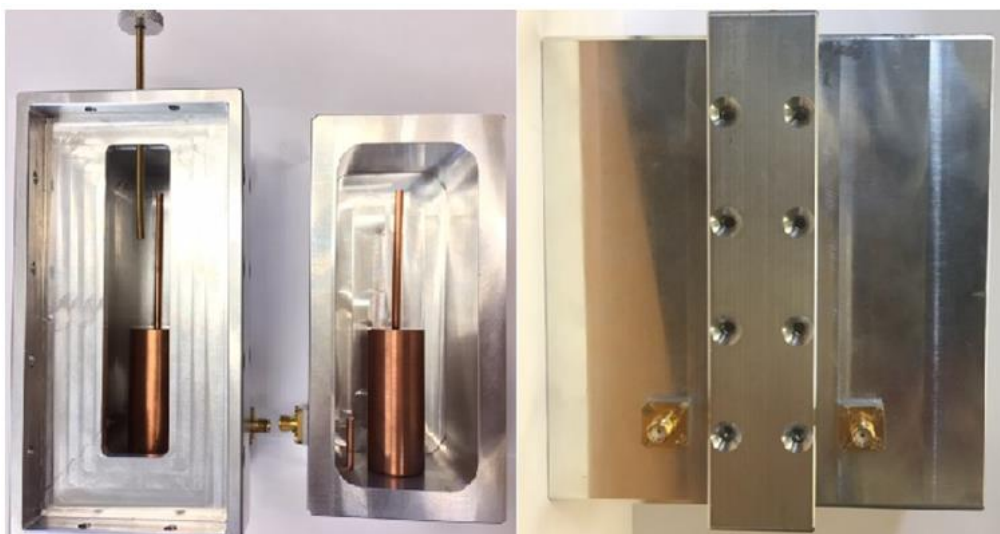


Figure 4.15 The fabricated second order dual-band bandpass filter.

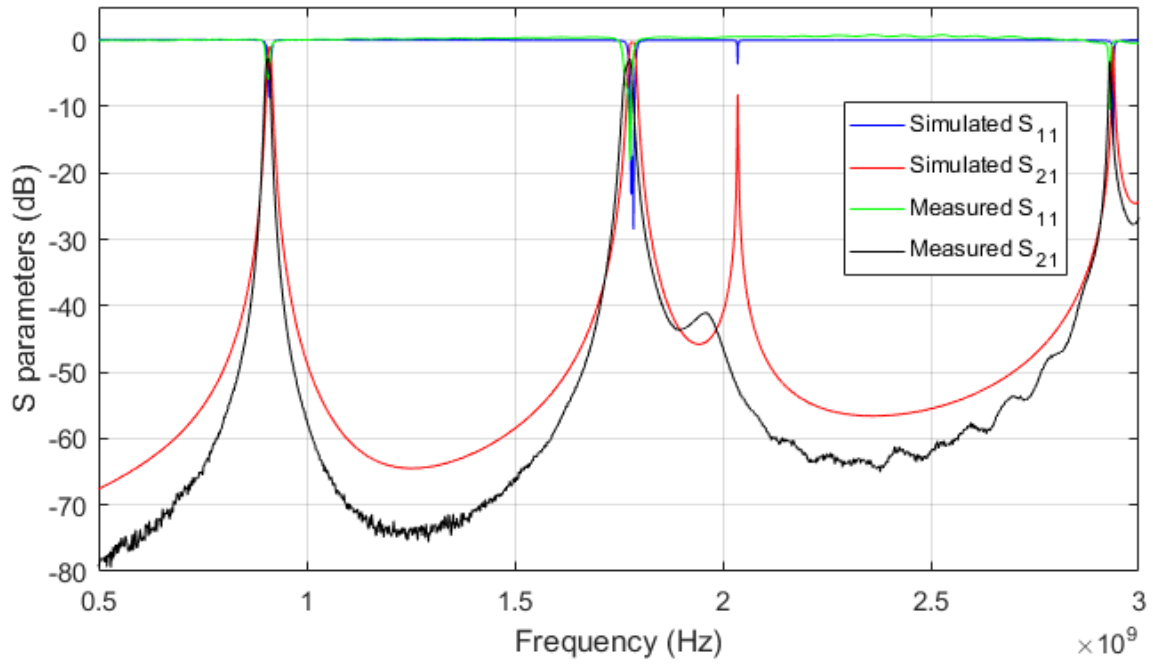


Figure 4.16 Wideband frequency responses of the designed second order filter.

Figure 4.17 and Figure 4.18 shows the detailed frequency responses of the first and the second passbands, respectively.

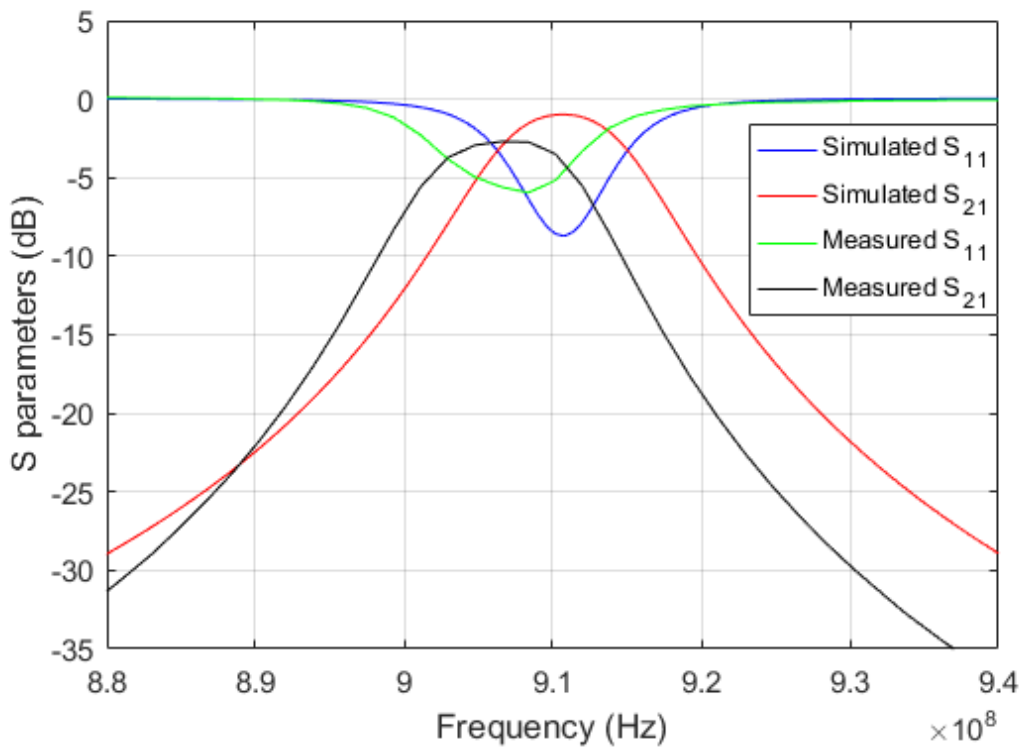


Figure 4.17 Simulated and measured frequency responses of the filter: the first passband.

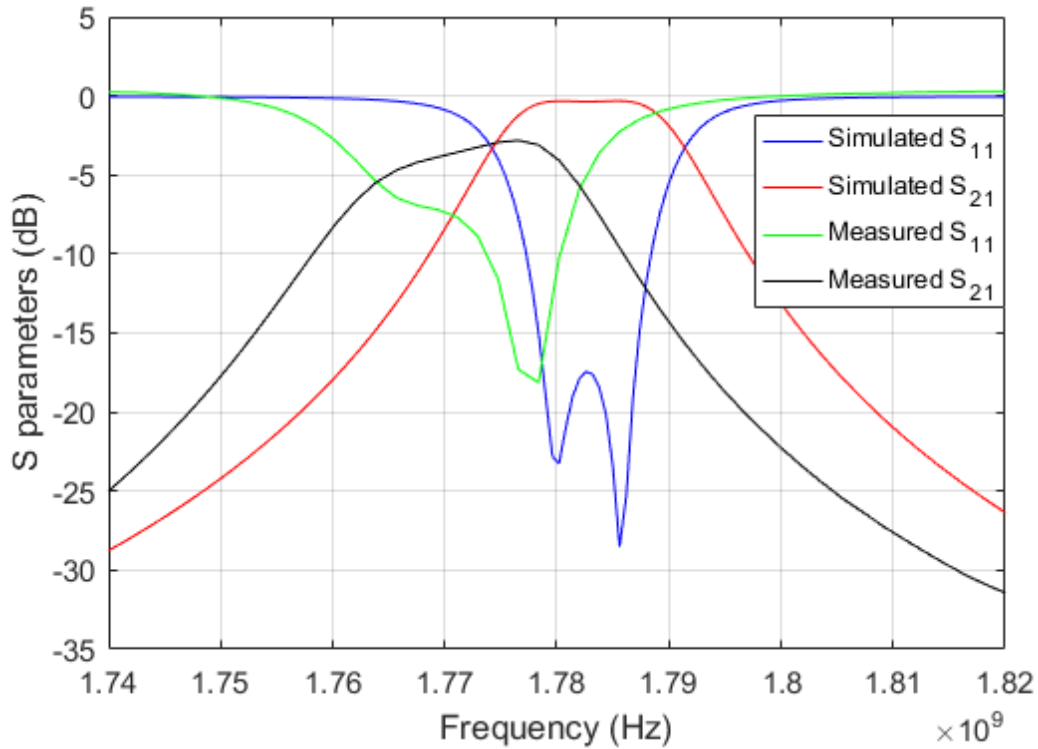


Figure 4.18 Simulated and measured frequency responses of the filter: the second passband.

The breakdown power of the filter is estimated from simulation using (2.87) in Section 2.7, which is approximately 1077.9 Watt. This filter is therefore capable of high power applications.

The fabricated filter realizes 1.23% and 1.07% FBW at 906.5 MHz and 1772.5 MHz, respectively. The insertion losses for these two bands are 2.7 dB and 2.8 dB, respectively. There is a spurious band generated around 2.1 GHz, caused by the coupling screw. The next spurious band, the natural second harmonic frequency of the used coaxial SIR, is at 2.8 GHz.

It can be seen that the measured response agrees reasonably well with simulation results. However, the fixture screws of coaxial SIR, rough inner surfaces of aluminium cavity, and fabrication tolerances, may cause the slight frequency discrepancies and increased insertion losses. The measured insertion losses could be reduced by improving the mechanical design and fabrication process, such as using a one-piece aluminium cavity or a silver plated cavity. The frequency discrepancies could be reduced by tuning screws or reducing the length of coaxial lines.

4.3 Non-uniform pitch helical resonator

The advantages of helical resonators include compact size, relatively high Q factor, relatively high power handling capability, and low cost [51]. The transmission line model of helical resonator has been introduced in Section 2.3.5, which shows that the second resonant frequency of a uniform pitch helical resonator is three times that of its fundamental resonant frequency. In practice, the frequency ratio (f_2/f_1) is approximately 3, usually ranging from 2.9 to 3.1 due to the effect caused by the short-circuited end support and the open-circuited end.

Zhou [26] developed a dual-band antenna for 2G (GSM 900/1800 MHz) mobile phones using non-uniform pitch helix, showing that the second resonant frequency of a traditional uniform pitch helix can be altered by modifying its pitches. However, the background and theory to do so has not been demonstrated and such helical structure has not been used in resonators or filters.

It is the purpose of this section to present research on the newly proposed and developed dual-section non-uniform pitch helical resonators. Firstly, this section describes the theoretical and developed models of the non-uniform pitch helical resonator. Secondly, it shows the general design procedure of the non-uniform pitch helical resonator. Thirdly, the experimented frequency characteristics of the non-uniform pitch helical resonator are shown. Then, the structures and topologies of the external and inter-resonator coupling for filter design are discussed. Finally, it shows the design and implementation of three dual-band bandpass filters using non-uniform pitch helical resonators.

4.3.1 Analysis of non-uniform pitch helical resonator

Two typical structures of the dual-section non-uniform pitch helical resonator are shown in Figure 4.19. The dual-section non-uniform pitch helices compose three parts: the top part, the bottom part, and the support. The pitches of the top and the bottom parts are different and the support is a straight wire connected to the cavity.

The top and the bottom parts of a Category I non-uniform pitch helical resonator are equally high. Thus, the pitch is modified by the numbers of turns for the top and the bottom parts. A Category II non-uniform pitch resonator has an equal number of turns for the top and the bottom parts. Thus, its pitch is modified by the height of the top and the bottom parts.

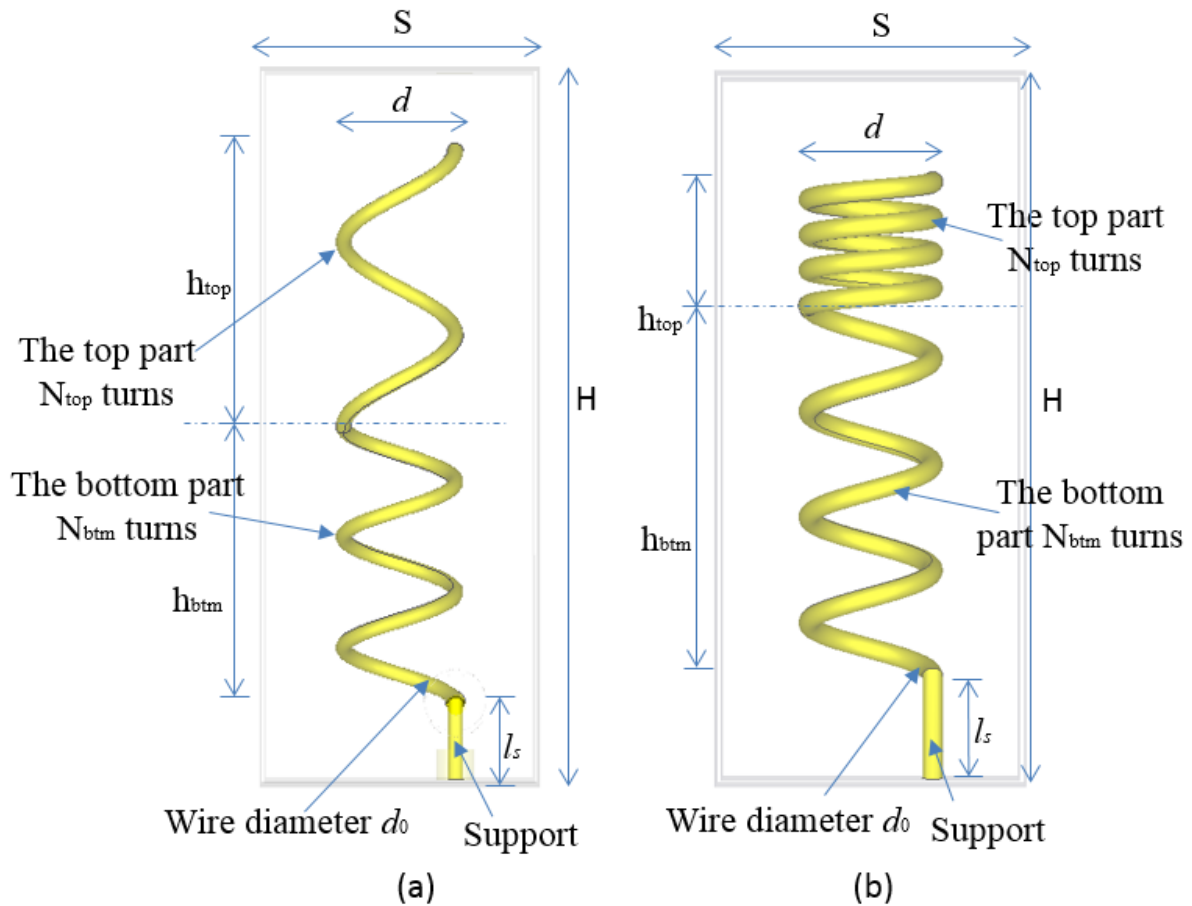


Figure 4.19 Typical structures of non-uniform pitch helical resonator. (a) Category I: pitch modified by the number of turns. (b) Category II: pitch modified by the height.

There are two models analysing the non-uniform pitch helical resonator: the SIR model and the circuit model. These models are presented below to analyse the Category I and II non-uniform pitch helical resonators.

SIR model

The SIR has been introduced and discussed in Section 4.1. The frequency ratio of a dual-section SIR can be altered against its impedance ratio, while the length of the SIR controls the fundamental resonant frequency.

In Section 4.1, the dual-section microstrip and coaxial SIRs are formed by two sections with the same electrical length. The electrical length of a microstrip or a coaxial resonator is proportional to its physical length. Therefore, the physical length of microstrip or coaxial SIR is used to alter the fundamental resonant frequency. However, an extra degree of freedom can be created as the electrical length of the microstrip lines to realise controllable frequency ratios [21, 111], which may extend the range of frequency ratios [22]. The theory of SIR has been

proven applicable to transmission line type resonators for dual-band BPF designs, including microstrip SIRs [23] and coaxial SIRs [106, 107].

The non-uniform pitch helical resonator can be modelled as a SIR since it consists of two sections with an impedance step. Applying the empirical characteristic impedance equation of uniform pitch helical resonators (2.23), the impedance ratio between the top part and the bottom part of the non-uniform pitch helical structures in Figure 4.19 is obtained as follows:

$$R_z = \frac{Z_{top}}{Z_{btm}} = \frac{n_{t_top}}{n_{t_btm}} = \frac{N_{top}/h_{top}}{N_{btm}/h_{btm}} \quad (4.20)$$

where R_z is the impedance ratio, Z_{top} and Z_{btm} are the impedance of top and bottom part, n_{t_top} and n_{t_btm} are the number of turns per inch of top and bottom part, respectively.

However, because of the complexity of helical structure, the electrical length of a uniform pitch helical resonator is not just related to the height of the helical resonator. The electrical length of a uniform pitch helical resonator is then investigated by analysing the resonant frequencies of a uniform pitch helical resonator.

Equation (2.25) shows that the resonant frequencies of a uniform pitch helical resonator are related to three physical parameters: N , d , and D . Therefore, for constant values of coil diameter (d) and cavity diameter (D), the number of turns (N) becomes the only parameter to control the resonant frequencies. This inference has been investigated by simulation since (2.25) is derived from an empirical equation. The simulation is based on a uniform pitch helical resonator that has the following dimensions: $S = 2.4 \cdot d$, $d = 6.0$, $l_s = 2.0$, $d_0 = 1.0$ (Unit: mm). The support length (l_s) is kept as short as 2 mm to reduce the effect on resonance caused by the support. The number of turns (N) is swept from 2.5 to 4.5 with 1 turn step width, while the height of coil (h) was swept from 6 to 27 mm with step width of 3 mm.

Figure 4.20 shows the simulated fundamental resonant frequencies against the height of the uniform pitch helical resonator for different turns, respectively. When $N=2.5$, the fundamental resonant frequency changes within $\pm 8\%$ of the average frequency of simulation for a wide range of the height of helix (6 mm to 27 mm). When $N=3.5$ and 4.5, the simulated fundamental resonant frequency changes within $\pm 5\%$ of its median or average value for the simulated wide range of helix height. However, for the same height of helix, the 1 turn difference leads to a significant difference (20% - 50%) in resonant frequencies.

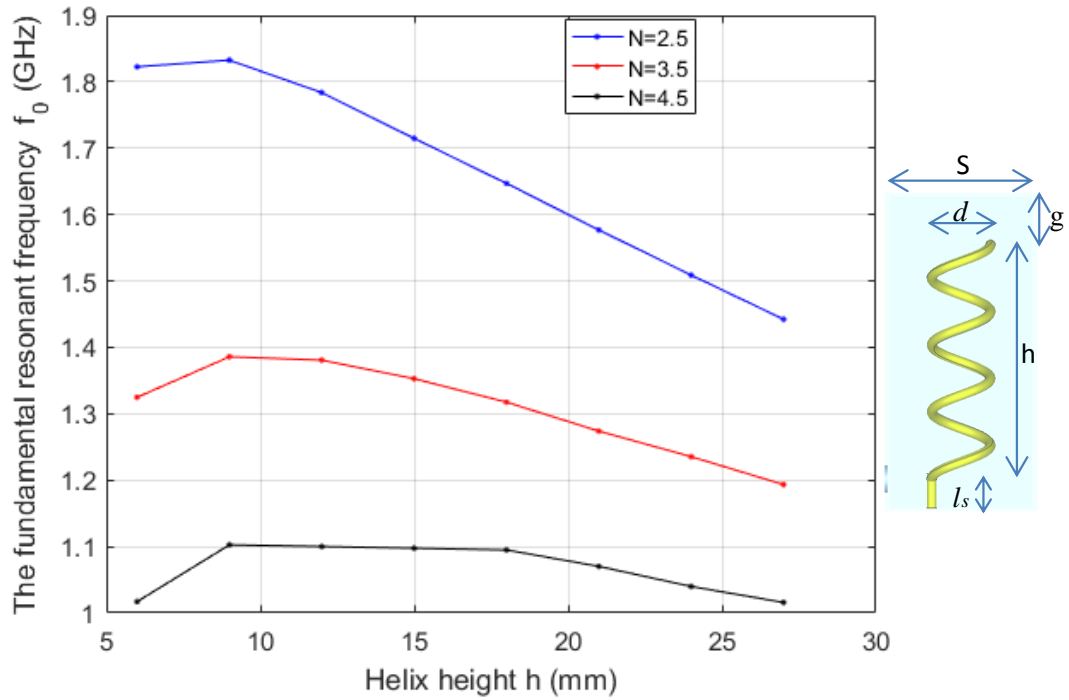


Figure 4.20 The fundamental resonant frequency of the uniform pitch helical resonator.

Figure 4.21 and Figure 4.22 shows the first and the second spurious resonant frequencies of the uniform pitch helical resonator against the height of the uniform pitch helical resonator for different turns, respectively.

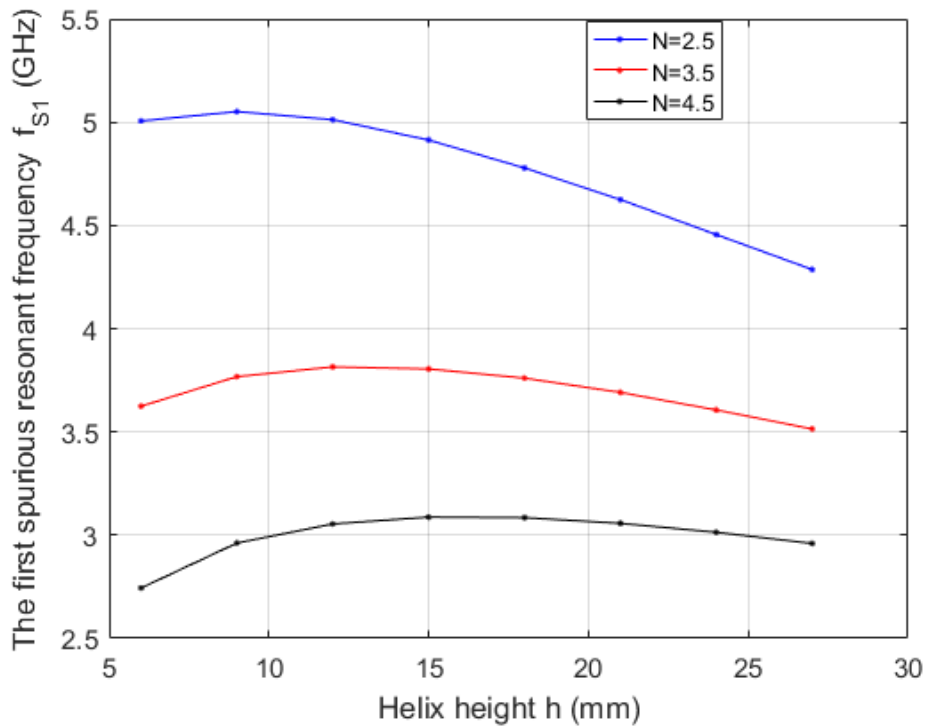


Figure 4.21 The first spurious resonant frequency of the uniform pitch helical resonator.

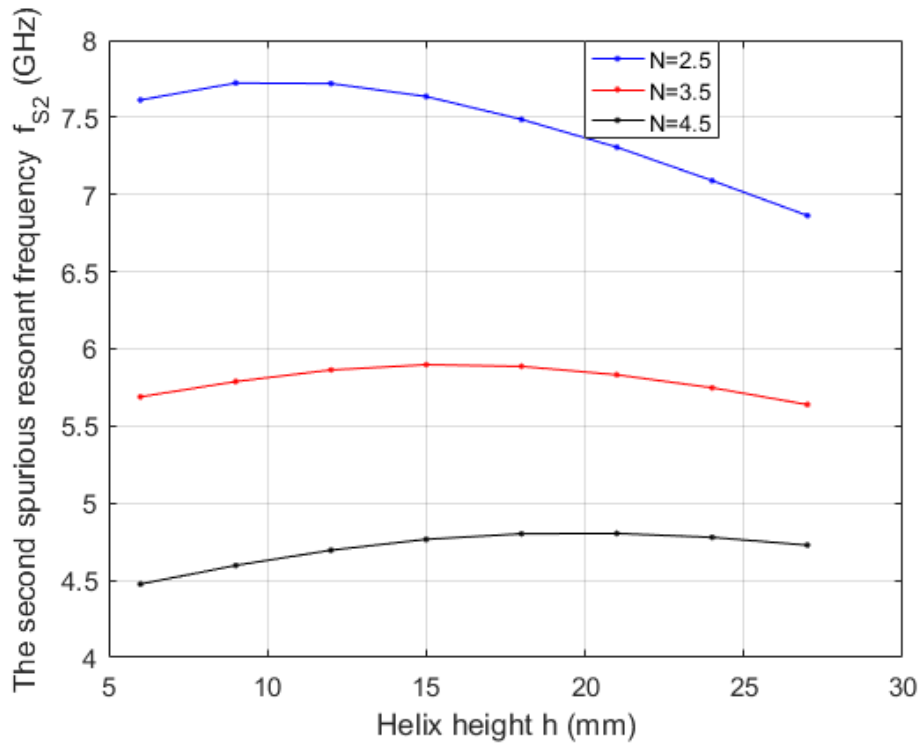


Figure 4.22 The second spurious resonant frequency of the uniform pitch helical resonator.

The first and second spurious resonant frequencies both vary within 10% of the average value. Therefore, the height of helix (h) is relatively independent of the resonant frequencies, compared to the number of turns (N). In other words, the effective electrical lengths of the helical resonators are approximately the same for the same parameters N , d , and D .

Category I non-uniform pitch helical resonator: pitch modified by the number of turns

The top part and the bottom part of the Category I non-uniform pitch helical resonator are equally high, i.e. $h_{\text{top}}=h_{\text{btm}}=h$. Thus, the impedance ratio of the resonator that expressed in (4.20) can be further simplified as

$$R_z = \frac{N_{\text{top}}}{N_{\text{btm}}} . \quad (4.21)$$

The resonant frequencies and electrical lengths of the top and the bottom part are different if the top and the bottom part have different number of turns ($N_{\text{top}} \neq N_{\text{btm}}$). Consequently, there is not any analytical equation available from the SIR model to predict the frequency ratio (f_2/f_1) since (4.10) is not applicable any more. The exact relationship between the frequency ratio (f_2/f_1) and impedance ratio (R_z) must be obtained from simulation or measurement.

A helical resonator structure with the following dimensions were created in CST MW: $S = 17.5$

mm, $d = 7.3$ mm, $l_s = 5.0$ mm, $h_{top} = h_{btm} = h$, $N_{btm}=2.5$, $d_0 = 1.0$ mm. It was then simulated with the three sets of parameter: $N_{btm}=2.5$, $h=18$ mm; $N=4.5$, $h=18$ mm; and $N=2.5$, $h=9$ mm.

Figure 4.23 shows the relationship between the frequency ratio (f_2/f_1) and the ratio of the number of turns (N_{top}/N_{btm}). The simulation results in Figure 4.23 show that the frequency ratio (f_2/f_1) can be realised in a range from 2.5 to 3.2.

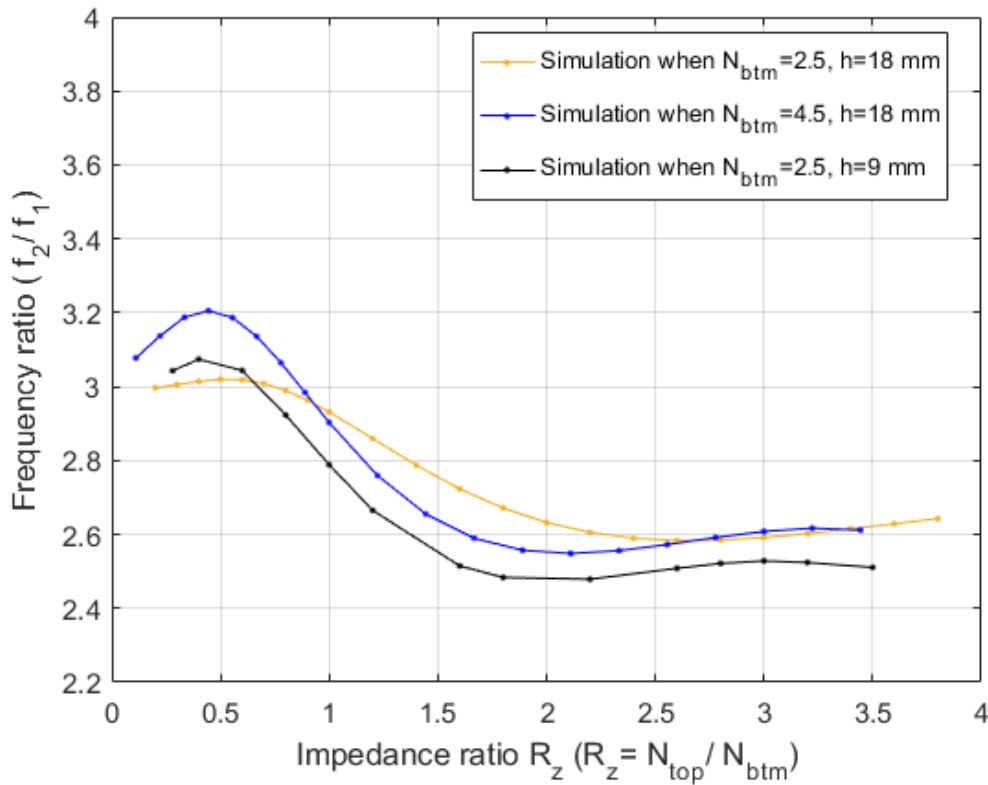


Figure 4.23 Simulated frequency ratio against the ratio of the number of turns.

Category II non-uniform pitch helical resonator: pitch modified by the height

When the top part and the bottom part of the Category II non-uniform pitch helical resonator have the same number of turns (N), i.e. $N_{top}=N_{btm}=N$, they can be approximately considered having the same resonant frequency and effective electrical length. Thus, (4.20) can be written as:

$$R_z = \frac{h_{btm}}{h_{top}}. \quad (4.22)$$

The resonant frequency expression of a uniform pitch helical resonator in (2.20) suggests that a uniform pitch helical resonator can be modelled as a quarter-wavelength quasi-TEM mode resonator.

The frequency ratio of the Category II non-uniform pitch helical resonator is obtained by substituting (4.22) into the frequency ratio expression of the quarter-wavelength type SIR (4.10). The frequency ratio is expressed by

$$\frac{f_2}{f_1} = \frac{\pi}{\tan^{-1} \sqrt{\frac{h_{\text{btm}}}{h_{\text{top}}}}} - 1. \quad (4.23)$$

A helical resonator structure with the following dimensions has been simulated in CST MW: $S = 16.8$ mm, $d = 7.0$ mm, $l_s = 5.0$ mm, $d_0 = 1.0$ mm, $N_{\text{top}}=N_{\text{btm}}=N$ turns. Sufficient simulation has been run for series of the height of the bottom coil (h_{btm}) and the number of turns (N). The simulated frequency ratios of different cases are shown in Figure 4.24, along with the theoretically predicted results by (4.23).

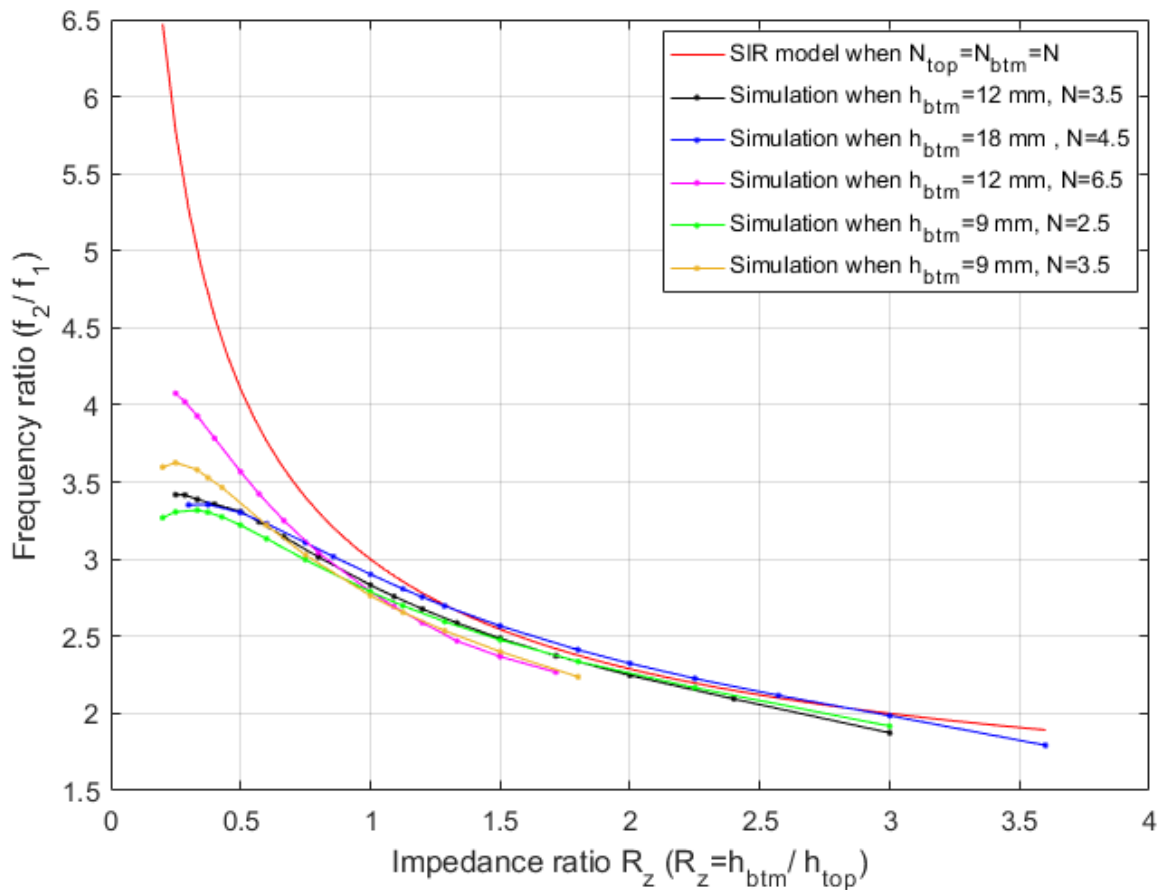


Figure 4.24 Frequency ratio against the ratio of heights ($h_{\text{btm}}/h_{\text{top}}$) from simulation and SIR model.

It shows that the frequency ratio (f_2/f_1) of a non-uniform pitch helical resonator can be tuned in a wide range, from 1.7 to 4.1. It is also shown that when $0.8 \leq R_z \leq 3.6$, the theoretical prediction

has very good agreement (within 10% difference) with the simulation results; when $0.5 \leq R_z \leq 0.8$, the difference between analytical calculation and the simulation results is within 20%; whereas when $R_z \leq 0.5$, the theoretical predicted values are significantly different from the simulation results that the theoretical equation does not provide useful predictions.

The differences are mainly caused by the applied equation (2.23), which was used to obtain the impedance ratio. As mentioned earlier, there is a validity limitation for (2.23). Beyond those valid limits, the accuracy of (2.23) decreases so that (4.23) may not be applicable to predict the frequency ratio of the non-uniform pitch helical resonator. The top coil is sparsely wound in comparison with the bottom coil when $R_z \leq 0.5$. In this case, (2.23) does not provide an accurate expression for the characteristic impedance of the top coil, thus the impedance ratio. Additionally, the supporting part also affects the simulated frequency ratios. It was neglected in the SIR model but it exists in practice.

Considering the practical structural limitation of the coil parameters, the impedance ratio R_z has a valid range for each case of h_{btm} and N , i.e. the impedance ratio R_z is not physically realisable for very small or very large values. The cases that either R_z is very small or large cannot be simulated because of the overlap of structure and meshes. Therefore, these cases are not shown in Figure 4.24. However, they can be analysed in the view of physical structure. When R_z is extremely small, the top coil is more likely a slightly twisted long wire, the whole resonator can be considered as either a solid line with a small inductive load (the previous bottom coil) at the short-circuited end or a uniform pitch helical resonator with a significant capacitive load (the previous top coil) at the open end. They both give an approximate frequency ratio of 3. When R_z is extremely large, the top part becomes a very short coaxial resonator. Thus the whole resonator can be analysed as either a coaxial resonator with an inductive load (the previous bottom coil) at the short-circuited end or a uniform pitch helical resonator with a coaxial load at the open end, whichever case gives the approximate frequency ratio of 3. In summary, the frequency ratio (f_2/f_1) is approximately three for the extreme values of the impedance ratio ($R_z \rightarrow 0$ or $+\infty$).

Comparing the Category I with Category II non-uniform pitch helical resonator, we can see that the frequency ratio of Category I resonator alters in a smaller range than that of Category II resonator. Compared to the microstrip and coaxial SIRs, utilising electrical length as an extra degree of freedom would not extend but shrink the range of the frequency ratio (f_2/f_1).

Circuit model

Generally, a non-uniform pitch helical resonator can be modelled as a uniform pitch helical resonator with a loading coil, neglecting the support of the helix. The small-pitch coils are usually inductive; however, there are cases that the loading coil become more capacitive rather than inductive [58]. For example, when the pitch of the coil approaches zero or infinite, the coil is more like a coaxial line or a slight bended long bar. In these cases, the loading coil is a capacitive load to the resonating part.

Miller [58] has analysed and derived expressions for similar cases that a helical antenna with inductive loading coil at the short-circuited end or capacitor at open end. The derivation is also applicable to helical resonators. Figure 4.25 shows the equivalent circuit that consists of the loading coil with inductance L_{load} , and a coil with the equivalent lumped resistance R_e , inductance L_e and capacitance C_e in the circuit.

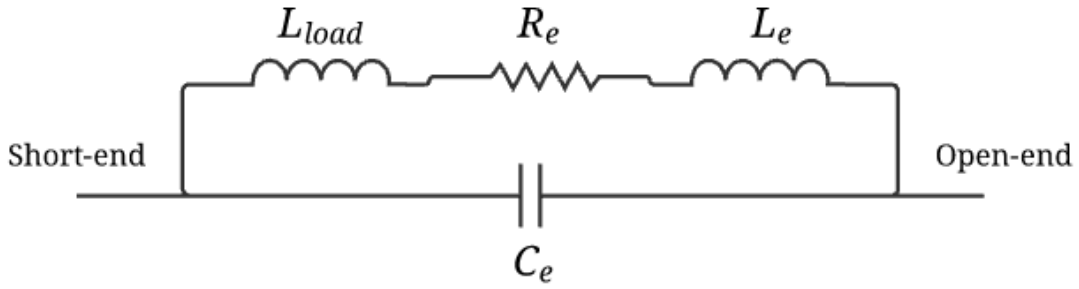


Figure 4.25 Equivalent circuit of a uniform pitch helical resonator with an inductive load.

The resonant frequency of this lumped circuit is given by [58]

$$f = \frac{1}{2\pi\sqrt{(L_{load} + L_e)C_e}} \quad (4.24)$$

where

$$R_e = \frac{R}{2} \left[\frac{1}{\sin^2(\omega\sqrt{LC})} - \frac{\cot(\omega\sqrt{LC})}{\omega\sqrt{LC}} \right]$$

$$L_e = \frac{L}{2} \left[\frac{1}{\sin^2(\omega\sqrt{LC})} - \frac{\cot(\omega\sqrt{LC})}{\omega\sqrt{LC}} \right] \quad (4.25)$$

$$C_e = \frac{C}{\left[\frac{\omega\sqrt{LC} \cot(\omega\sqrt{LC})}{2} - \frac{\omega^2 LC}{2 \sin^2(\omega\sqrt{LC})} \right]}$$

where R , L , C are the static resistance, inductance, and capacitance of the corresponding coil (top part) that can be computed using empirical equations (2.21) (2.22) (2.27) (2.28) from the transmission line model of helical resonators in Section 2.3.5.

The resonant frequencies of a helical resonator can be converted into angular frequencies as

$$\omega\sqrt{LC} = m \cdot \frac{\pi}{2}. \quad (4.26)$$

At the fundamental resonant frequency where $m=1$, substitute (4.26) into (4.25), the values of the equivalent elements (R_e , L_e , and C_e) are obtained as

$$\begin{aligned} R_e &= \frac{R}{2} \\ L_e &= \frac{L}{2} \\ C_e &= \frac{8}{\pi^2} C. \end{aligned} \quad (4.27)$$

From (4.24) (4.27), the fundamental resonant frequency of the inductive loaded helical resonator is

$$f_1 = \frac{1}{2\pi \sqrt{\left(L_{load} + \frac{L}{2}\right) \frac{8}{\pi^2} C}}. \quad (4.28)$$

At the second resonant (the first spurious) frequency where $m=3$, the values of the equivalent elements (R_e , L_e , and C_e) are obtained by substituting (4.26) into (4.25).

$$\begin{aligned} R_e &= \left(\sqrt{2} + \frac{1}{3\pi}\right) R \approx 1.5203 R \\ L_e &= \left(\sqrt{2} + \frac{1}{3\pi}\right) L \approx 1.5203 L \\ C_e &= \frac{4}{9\pi^2 - 3\pi} C \approx 0.0504 C. \end{aligned} \quad (4.29)$$

Hence the second resonant (the first spurious) frequency is

$$f_2 = \frac{1}{2\pi\sqrt{(L_{load} + 1.5203 L) \cdot 0.0504 C}}. \quad (4.30)$$

Figure 4.26 shows the equivalent circuit of a coil with a capacitive load in parallel [58].

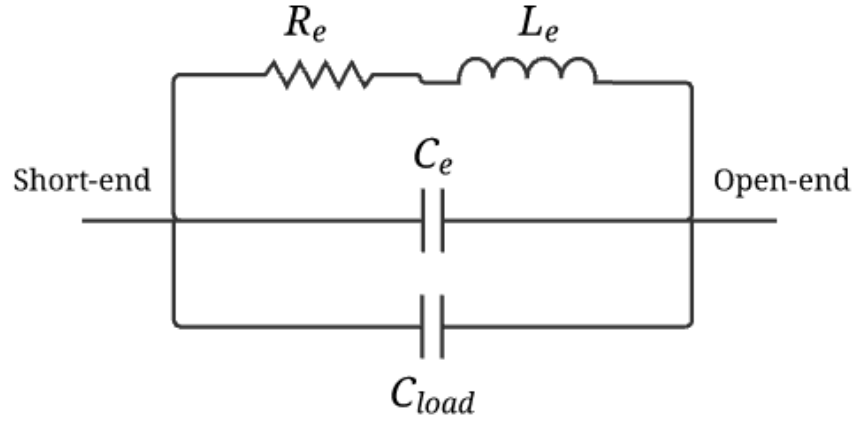


Figure 4.26 Equivalent circuit of a uniform pitch helical resonator with a capacitive load.

The resonant frequency of the circuit is given by [58]

$$f = \frac{1}{2\pi\sqrt{L_e(C_{load} + C_e)}} \quad (4.31)$$

where

$$R_e = \frac{R}{2} \left[\frac{1}{\sin^2(\omega\sqrt{LC})} - \frac{\cot(\omega\sqrt{LC})}{\omega\sqrt{LC}} \right]$$

$$L_e = \frac{L}{\left[\frac{\omega\sqrt{LC} \cot(\omega\sqrt{LC})}{2} - \frac{\omega^2 LC}{2 \sin^2(\omega\sqrt{LC})} \right]} \quad (4.32)$$

$$C_e = \frac{C}{2} \left[\frac{1}{\sin^2(\omega\sqrt{LC})} - \frac{\cot(\omega\sqrt{LC})}{\omega\sqrt{LC}} \right].$$

Similarly, we can derive the values of L_e and C_e at each resonant frequency. At the fundamental resonant frequency where $m=1$, we have

$$\begin{aligned}
R_e &= \frac{R}{2} \\
L_e &= \frac{8}{\pi^2} L \\
C_e &= \frac{C}{2}
\end{aligned} \tag{4.33}$$

Thus, the fundamental resonant frequency (f_1) is expressed as

$$f_1 = \frac{1}{2\pi \sqrt{\frac{8}{\pi^2} L \left(C_{load} + \frac{C}{2} \right)}} . \tag{4.34}$$

At the second resonant frequency (the first spurious) where $m=3$,

$$\begin{aligned}
R_e &= \left(\sqrt{2} + \frac{1}{3\pi} \right) R \approx 1.5203 R \\
L_e &= \frac{4}{9\pi^2 - 3\pi} L \approx 0.0504 L \\
C_e &= \left(\sqrt{2} + \frac{1}{3\pi} \right) C \approx 1.5203 C
\end{aligned} \tag{4.35}$$

hence
$$f_2 = \frac{1}{2\pi \sqrt{0.0504 L \cdot (C_{load} + 1.5203 C)}} . \tag{4.36}$$

The Category I and II non-uniform pitch helical resonators are now discussed respectively.

Category I non-uniform pitch helical resonator: pitch modified by the number of turns

For the general range of the ratio of the number of turns (N_{top}/N_{btm}), the non-uniform pitch helical resonator behaves like a uniform pitch helical resonator (the top part) with a small inductive load (the bottom part) at the short-circuited end.

The values of L_{load} , L , and C can be computed by the expressions of inductance and capacitance per unit length of the transmission line model of the uniform pitch helical resonator in (2.21) and (2.22).

$$\begin{aligned}
L_{load} &= 0.025 \left(\frac{N_{btm}}{h_{btm}} \right)^2 d^2 \left[1 - \left(\frac{d}{D} \right)^2 \right] h_{btm} \\
L &= 0.025 \left(\frac{N_{top}}{h_{top}} \right)^2 d^2 \left[1 - \left(\frac{d}{D} \right)^2 \right] h_{top} \\
C &= \frac{0.75}{\log_{10} \frac{D}{d}} h_{top}
\end{aligned} \tag{4.37}$$

The frequency ratio (f_2/f_1) is obtained by substituting the values of L_{load} , L , and C from (4.37) into (4.28) and (4.30).

$$\frac{f_2}{f_1} = 4.01 \sqrt{\frac{1 + 0.5 \left(\frac{N_{top}}{N_{btm}} \right)^2}{1 + 1.5203 \left(\frac{N_{top}}{N_{btm}} \right)^2}}. \tag{4.38}$$

For the extreme values of the ratio of the number of turns (N_{top}/N_{btm}) that it approaches zero or infinite, the loading part is capacitive since it is either a coaxial line or a slightly bended bar. It is noted that either part could be the capacitive load depending on the values of N_{btm} , N_{top} and N_{top}/N_{btm} . Therefore, the subscripts “btm” and “top” are replaced by “resonator” and “load”.

The values of L , C , and C_{load} can be computed using (2.21) and (2.22) as

$$\begin{aligned}
L &= 0.025 \left(\frac{N_{resonator}}{h_{resonator}} \right)^2 d^2 \left[1 - \left(\frac{d}{D} \right)^2 \right] h_{resonator} \\
C &= \frac{0.75}{\log_{10} \frac{D}{d}} h_{resonator} \\
C_{load} &= \frac{0.75}{\log_{10} \frac{D}{d}} h_{load}.
\end{aligned} \tag{4.39}$$

Since $h_{load} = h_{resonator}$, the frequency ratio (f_2/f_1) is obtained from (4.34) (4.36) (4.39) as

$$\frac{f_2}{f_1} = 3.094. \tag{4.40}$$

Figure 4.27 shows the circuit model results of frequency ratio that is obtained by (4.38), as well as a few simulated results. The theoretical results have good agreement ($\pm 10\%$) with the simulation results in the range of $0.8 \leq N_{\text{top}}/N_{\text{btm}} \leq 3.6$. The circuit model still provides useful predictions (within 20% difference) when $0.5 \leq N_{\text{top}}/N_{\text{btm}} \leq 0.8$.

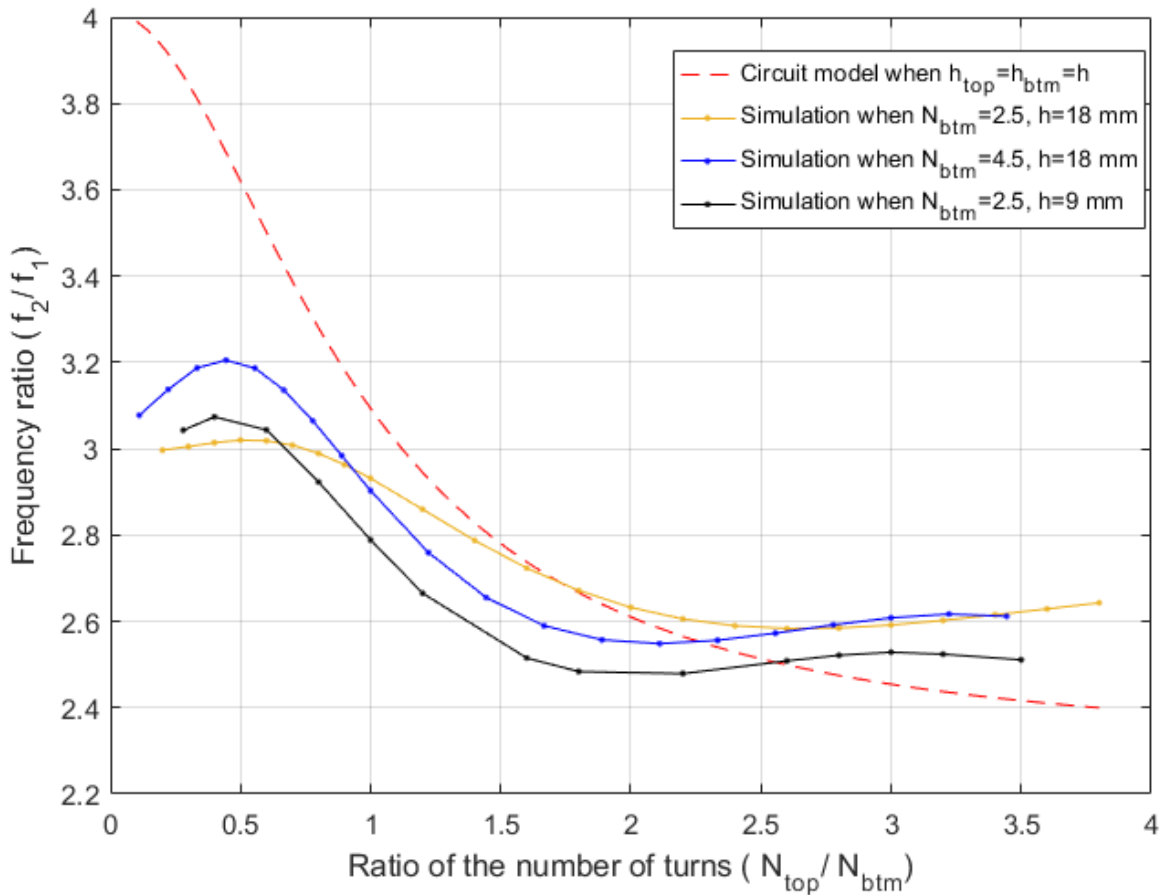


Figure 4.27 Frequency ratio from simulation results and circuit model prediction.

From Figure 4.27, there is a decrease of simulated frequency ratios towards 3.0 when the ratio of the number of turns ($N_{\text{top}}/N_{\text{btm}}$) approaches zero, which agrees with the predicted value 3.094 by (4.40). In addition, the simulated frequency ratios approach to 2.5 when the ratio of the number of turns ($N_{\text{top}}/N_{\text{btm}}$) becomes larger than 2. This does not agree with the extreme case when the ratio of the number of turns ($N_{\text{top}}/N_{\text{btm}}$) approaches infinity, predicted as 3.094 by (4.40).

Category II non-uniform pitch helical resonator: pitch modified by the height

For the general range of the ratio of heights ($h_{\text{btm}}/h_{\text{top}}$), the completely non-uniform pitch helical resonator can be considered as a traditional uniform pitch helical resonator (the top part)

with a small inductive load (the bottom part) at the short-circuited end.

The frequency ratio (f_2/f_1) is then obtained from (4.28), (4.30) and (4.37) as

$$\frac{f_2}{f_1} = 4.01 \sqrt{\frac{1 + 0.5 \frac{h_{\text{btm}}}{h_{\text{top}}}}{1 + 1.5203 \frac{h_{\text{btm}}}{h_{\text{top}}}}} \quad (4.41)$$

When the ratio of heights ($h_{\text{btm}}/h_{\text{top}}$) approaches zero or infinity, the non-uniform pitch helical resonator becomes a uniform pitch helical resonator connected with a capacitive load.

The values of L , C , and C_{load} can be computed using (2.21) and (2.22) as

$$L = 0.025 \left(\frac{N_{\text{resonator}}}{h_{\text{resonator}}} \right)^2 d^2 \left[1 - \left(\frac{d}{D} \right)^2 \right] h_{\text{resonator}}$$

$$C = \frac{0.75}{\log_{10} \frac{D}{d}} h_{\text{resonator}} \quad (4.42)$$

$$C_{\text{load}} = \frac{0.75}{\log_{10} \frac{D}{d}} h_{\text{load}} \cdot$$

where the subscripts “btm” and “top” are replaced by “resonator” and “load” for a generalized case.

The frequency ratio (f_2/f_1) is obtained from (4.34) (4.36) and (4.42).

$$\frac{f_2}{f_1} = 4.01 \sqrt{\frac{1 + 0.5 \frac{h_{\text{resonator}}}{h_{\text{load}}}}{1 + 1.5203 \frac{h_{\text{resonator}}}{h_{\text{load}}}}} \quad (4.43)$$

Since the ratio of heights is zero or infinity, we then have

$$\frac{f_2}{f_1} = 4.01 \quad \text{or} \quad 2.30 \quad (4.44)$$

for the extreme cases, respectively,.

The frequency ratio (f_2/f_1) predicted by (4.41) is shown in Figure 4.28, with a few simulation

results and the prediction from SIR model by (4.23).

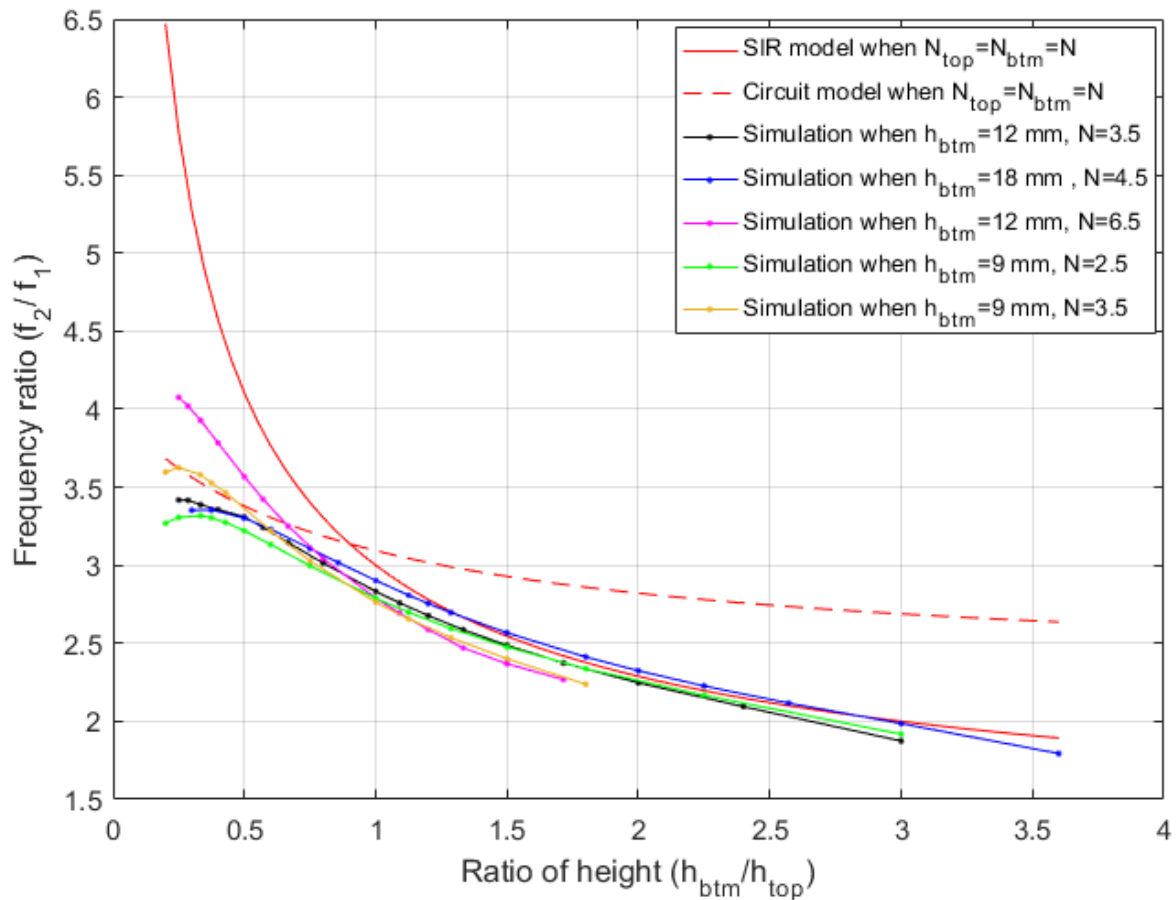


Figure 4.28 Frequency ratio against the ratio of heights from simulation and circuit model.

The difference between circuit model and simulation results is within 10% when $0.2 \leq h_{btm}/h_{top} \leq 1.3$, in which range that the circuit model provides accurate prediction; the difference is within 20% when $1.3 \leq h_{btm}/h_{top} \leq 2.0$; the difference is higher than 20% when $2.0 \leq h_{btm}/h_{top} \leq 3.6$, showing that the circuit model cannot provide useful predictions. The simulation results when the ratio of heights (h_{btm}/h_{top}) approaches zero agrees reasonably with the predicted value 4.01 by (4.44). However, when the ratio of heights (h_{btm}/h_{top}) approaches infinity, the simulated frequency ratios does not agree with the predicted value 2.3 by (4.44). The difference between circuit model prediction in (4.41) and simulation results may be caused by the validity of (2.21) and (2.22), the neglected inductance of loading coil, and the neglected support part at the short-circuited end of the helix.

Developed model

The above models have analysed and derived analytical equations of the frequency ratios (f_2/f_1)

of non-uniform pitch helical resonators. However, the accuracy of the above models is limited by many factors, including the validity and accuracy of the applied equations, the effect of supporting part, and structural limitations. A new model has been developed according to the above theoretical models and simulation studies. The developed model provides accurate predictions on the frequency ratios (f_2/f_1) of non-uniform pitch helical resonators. It can also be used for the design of non-uniform pitch helical resonators.

Category I non-uniform pitch helical resonator: pitch modified by the number of turns

The SIR model does not give any analytical equation for this category non-uniform pitch helical resonator. However, the circuit model provides analytical solutions shown in (4.40) and (4.38). Figure 4.27 shows that the theoretical results have good agreement ($\pm 10\%$) with the simulation results in the range of $0.8 \leq N_{\text{top}}/N_{\text{btm}} \leq 3.6$. Equation (4.38) also shows that frequency ratio (f_2/f_1) is approximate 3.1 when $N_{\text{top}}/N_{\text{btm}} \approx 1$ or 0. These predictions agree with the simulation results that the frequency ratio (f_2/f_1) is about 3 when $N_{\text{top}}/N_{\text{btm}} \leq 1$. In addition, the simulation results showed that the frequency ratio (f_2/f_1) has a peak value ($\pm 10\%$ from 3) when $N_{\text{top}}/N_{\text{btm}} \approx 0.5$. Therefore, the frequency ratio (f_2/f_1) can be assumed as an approximate constant value when $N_{\text{top}}/N_{\text{btm}} \leq 1$.

A developed model can be summarised as a curve with several segments as follows. Considering the continuity of curve, the constant value of the frequency ratio is assumed to be 3.1 when $N_{\text{top}}/N_{\text{btm}} \leq 1$.

$$\frac{f_2}{f_1} = 4.01 \sqrt{\frac{1 + 0.5 \left(\frac{N_{\text{top}}}{N_{\text{btm}}}\right)^2}{1 + 1.5203 \left(\frac{N_{\text{top}}}{N_{\text{btm}}}\right)^2}} \quad \text{for } 1.0 \leq \frac{N_{\text{top}}}{N_{\text{btm}}} \leq 3.6 \quad (4.45)$$

$$\frac{f_2}{f_1} \approx 3.1 \quad \text{for } \frac{N_{\text{top}}}{N_{\text{btm}}} \leq 1.0 \quad (4.46)$$

$$\frac{f_2}{f_1} \approx 2.3 \quad \text{for } \frac{N_{\text{top}}}{N_{\text{btm}}} \rightarrow \infty \quad (4.47)$$

Figure 4.29 shows the developed model along with the simulation results. The developed model has a good agreement with the simulation results in the shown range. However, beyond the shown range, the simulated frequency ratios approach to 2.5, agreeing close to (4.47).

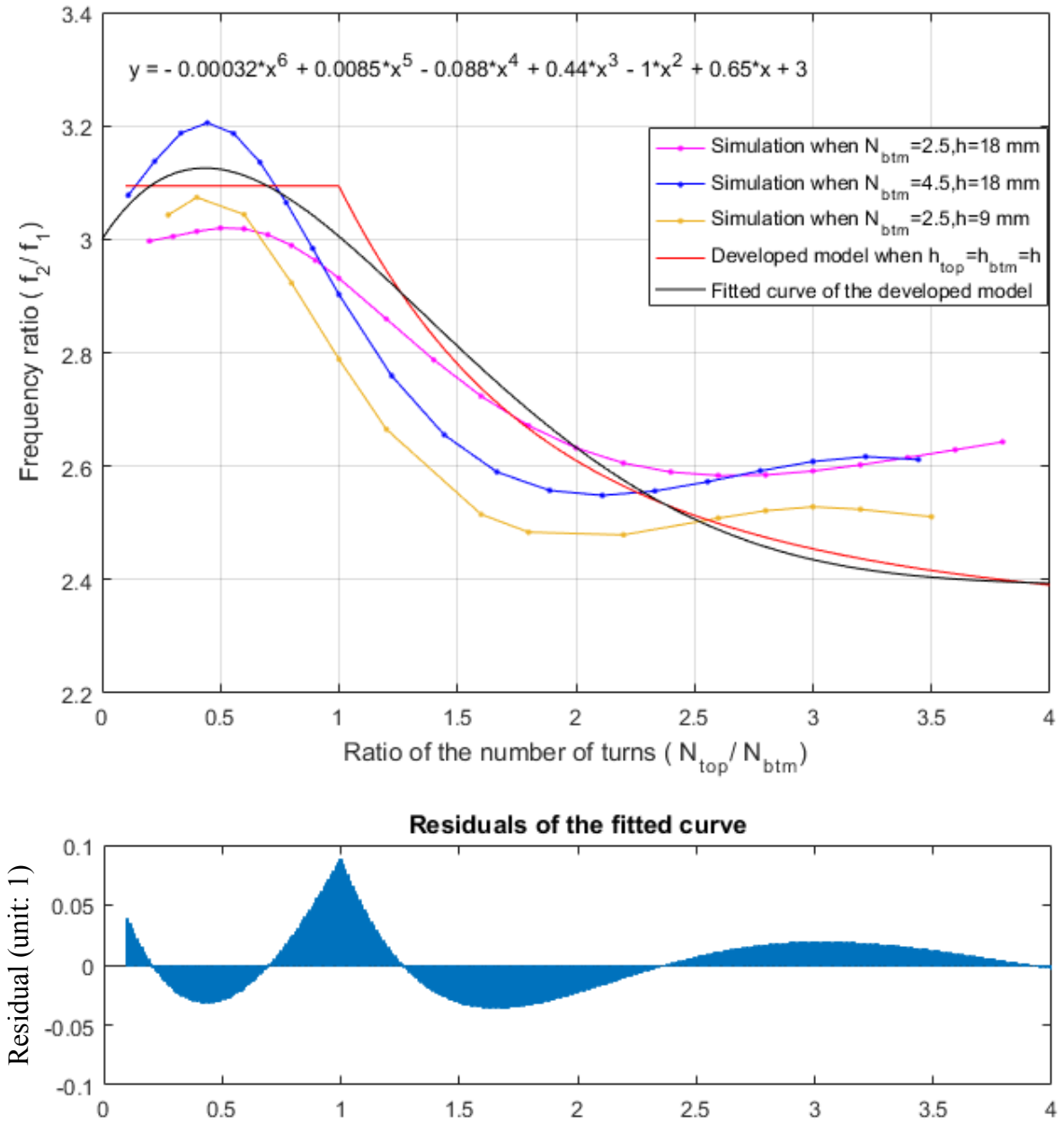


Figure 4.29 Developed model for Category I resonator with curve fitting residuals.

A curve with expression shown in (4.48) was generated to fit the developed model. Compared to the developed model, the fitted curve shows the trends and continuity for the range of $N_{top}/N_{btm} \leq 1$, with residuals less than 0.1.

$$\frac{f_2}{f_1} = -0.00032(R_z)^6 + 0.0085(R_z)^5 - 0.088(R_z)^4 + 0.44(R_z)^3 - (R_z)^2 + 0.65R_z + 3 \quad (4.48)$$

where R_z represents the ratio of heights that $R_z = N_{\text{top}}/N_{\text{btm}}$ and $0 \leq R_z \leq 4$.

Category II non-uniform pitch helical resonator: pitch modified by the height

Comparing the simulation results shown in Figure 4.28 with the curves of the SIR model and the circuit model, we can see that the circuit model has better accuracy of prediction (within 10% difference) in the range of $0.2 \leq h_{\text{btm}}/h_{\text{top}} \leq 0.9$, whereas the SIR model predicts frequency ratios more accurate (within 10% difference) in the range of $0.9 \leq h_{\text{btm}}/h_{\text{top}} \leq 3.6$. Meanwhile, the SIR model and the circuit model have a cross point when $h_{\text{btm}}/h_{\text{top}} = 0.9$.

Therefore, a model can be developed by combining the circuit model and the SIR model according to their accuracy against the range of the ratio of height ($h_{\text{btm}}/h_{\text{top}}$). The circuit model and the SIR model showed that when the ratio of height approaches zero or infinite (i.e. $h_{\text{btm}}/h_{\text{top}} \rightarrow 0$ or ∞), the frequency ratio is approximately 4.01 or 1.0, respectively. The new model is summarised as segments according to the simulation results, shown below.

$$\frac{f_2}{f_1} = 4.01 \sqrt{\frac{1 + 0.5 \frac{h_{\text{btm}}}{h_{\text{top}}}}{1 + 1.5203 \frac{h_{\text{btm}}}{h_{\text{top}}}}} \quad \text{for } 0.2 \leq \frac{h_{\text{btm}}}{h_{\text{top}}} \leq 0.9 \quad (4.49)$$

$$\frac{f_2}{f_1} = \frac{\pi}{\tan^{-1} \sqrt{\frac{h_{\text{btm}}}{h_{\text{top}}}}} - 1 \quad \text{for } 0.9 < \frac{h_{\text{btm}}}{h_{\text{top}}} \leq 3.6 \quad (4.50)$$

$$\frac{f_2}{f_1} \approx 4.01 \text{ or } 1.0 \quad \text{for } \frac{h_{\text{btm}}}{h_{\text{top}}} \rightarrow 0 \text{ or } \infty \quad (4.51)$$

Figure 4.30 shows the simulation results, developed model and a fitted curve.

The fitted curve is a 5th degree polynomial with residuals less than 0.08, expressed as

$$\frac{f_2}{f_1} = 0.014(R_z)^5 - 0.17(R_z)^4 + 0.72(R_z)^3 - 1.2(R_z)^2 - 0.12R_z + 3.7 \quad (4.52)$$

where R_z represents the ratio of heights that $R_z = h_{\text{btm}}/h_{\text{top}}$ and $0 \leq R_z \leq 4$.

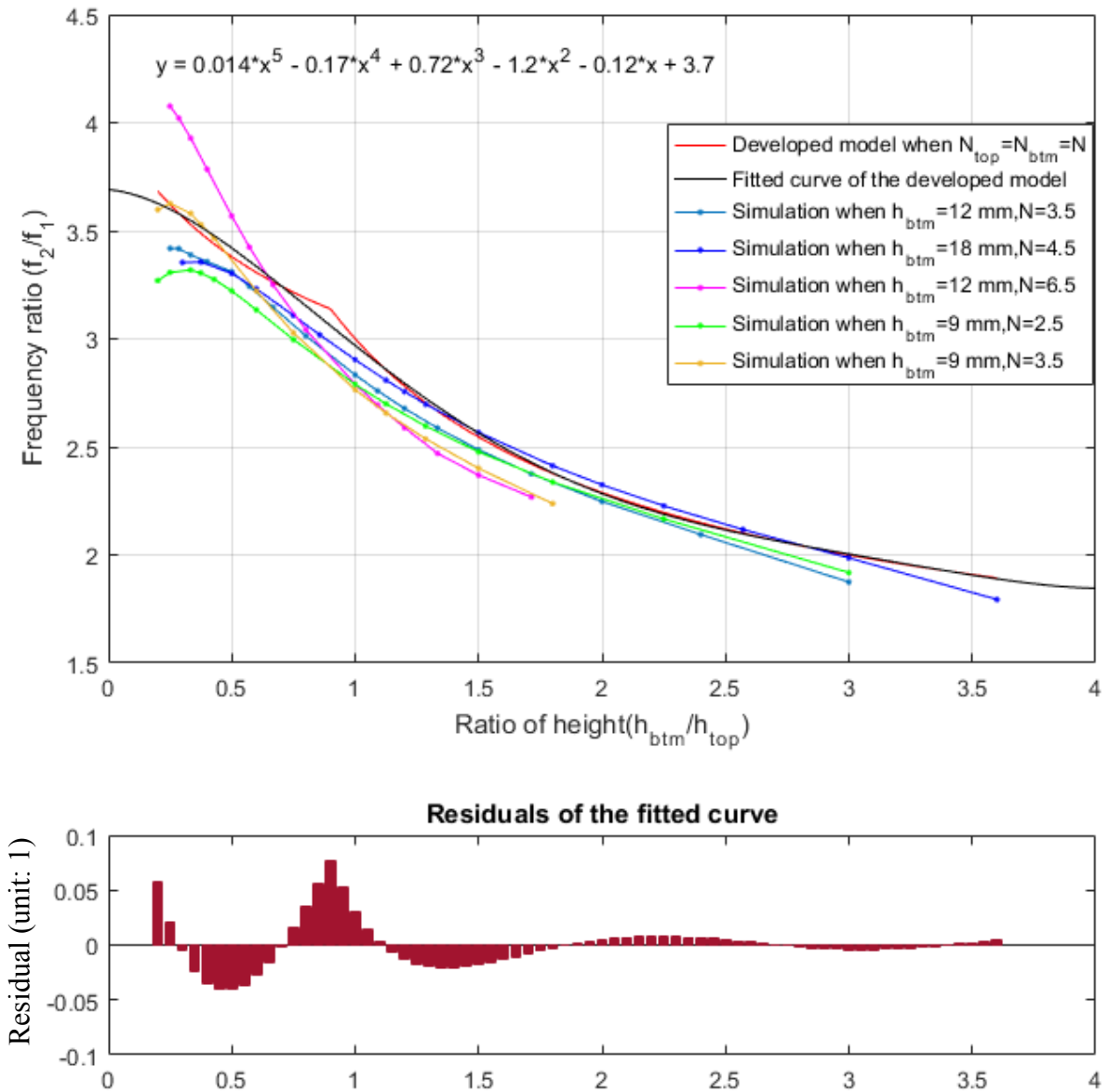


Figure 4.30 Developed model for Category II resonator with curve fitting residuals.

4.3.2 Design procedure

The steps to design a non-uniform pitch helical resonator with characterised resonant frequencies (f_1 and f_2) are generalised and summarised below.

- Step 1.** Select the category of non-uniform pitch helical resonators that could realise the required frequency ratio (f_2/f_1).
- Step 2.** Substitute the required frequency ratio (f_2/f_1) to the analytical equations of the developed models or fitted curves in Section 4.3.1 to obtain the initial approximate

value of the ratio of height ($h_{\text{btm}}/h_{\text{top}}$) or the ratio of the number of turns ($N_{\text{top}}/N_{\text{btm}}$).

- Step 3.** Determine suitable parameters (N_{btm} and h for Category I; h_{btm} and N for Category II) of the non-uniform pitch helical resonator so that the pitches of the top and the bottom part are both reasonable and realisable.
- Step 4.** Select the coil diameter (d), wire diameter (d_0) and support length (l_s) for simulation. It is noted that the design equations in Section 2.3.5 might be helpful for the selection of these parameters.
- Step 5.** Simulate the resonator to obtain the detailed profile of the frequency ratio (f_2/f_1), from which the height (h_{top}) or the number of turns (N_{top}) of the top part is further determined.
- Step 6.** Determine the coil diameter (d) to realise the desired fundamental resonant frequency and the required unloaded Q factor.
- Step 7.** Simulate and optimise the dimensions of the non-uniform pitch helical resonator.
- Step 8.** Fabricate and test the resonator for verification.

Design Example

A design example of a non-uniform pitch helical resonator working at the LTE bands (815 MHz and 1740 MHz) with a minimum unloaded Q factor of 800 is shown here.

Firstly, the frequency ratio (f_2/f_1) is calculated as 2.135. According to the developed model and fitted curves in the previous section, this required frequency ratio is only realisable by a Category II non-uniform pitch helical resonator.

Secondly, the initial approximate ratio of height ($h_{\text{btm}}/h_{\text{top}}$) is obtained by substituting the required frequency ratio into the analytical equations (4.49) - (4.51) or the fitted curve expression (4.52), which is approximately 2.5.

Thirdly, the parameters of the helical are determined considering the structure realisation and required ratio of height. We select $h_{\text{btm}}=18$ mm and $N=3.5$ so that the top part and the bottom part both have reasonable pitches when the ratio of height is about 2.5.

Then, the coil diameter, wire diameter and support length are selected with suitable values to make the helix more resistant to vibration ($d=7.0$ mm, $d_0=1.0$ mm, $l_s=5.0$ mm).

With the determined parameters, the detailed profile of the frequency ratio against the ratio of

height can be obtained by 3D simulation, shown by Figure 4.31. From Figure 4.31, the ratio of height is obtained as 2.82 to realise the required frequency ratio of 2.135. Therefore, the height of the top part is approximate 6.38 mm.

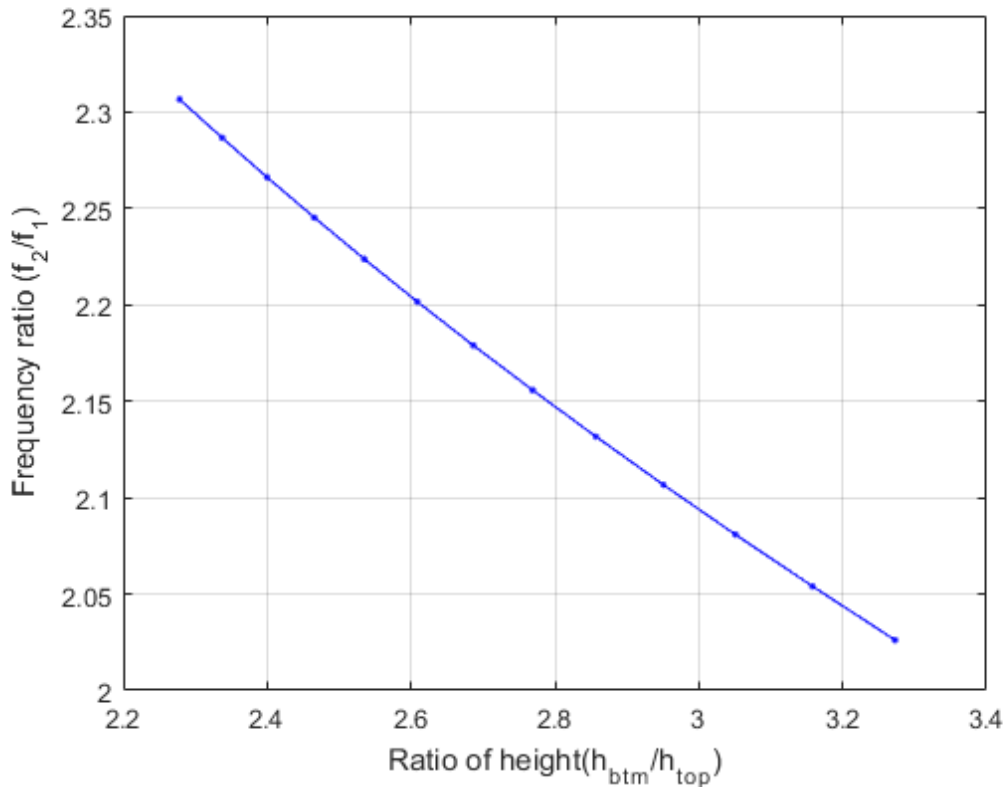


Figure 4.31 Frequency ratio against the ratio of height ($h_{\text{btm}}/h_{\text{top}}$) of the helical resonator when $d=7.0$ mm, $h_{\text{btm}}=18$ mm.

Next, we determine the coil diameter to realise the required fundamental resonant frequency and unloaded Q factor. The required unloaded Q factor roughly suggests a lower limit of the coil diameter. According to the conservative estimation of unloaded Q factor in (2.33), the cavity needs to have a square cross-section length $S \geq 14.3$ mm. If we take $S = 2.4 d$, then the coil diameter needs to satisfy $d \geq 5.93$ mm so that $Q_0 \geq 800$ at both resonant frequencies. Although this lower limit may not be an accurate estimation, it provides a starting point to calculate the cavity size and the coil diameter for the required loaded Q factor. The resonator was then simulated to obtain the fundamental resonant frequency and unloaded Q factor against the coil diameter. Figure 4.32 shows the simulated results that used for determination of the coil diameter. The simulation suggests that $Q_0 \geq 800$ for the coil diameter $d \geq 5$ mm. It also shows that the coil diameter (d) is approximately 6.0 mm to realise the required fundamental resonant frequency of 815 MHz.

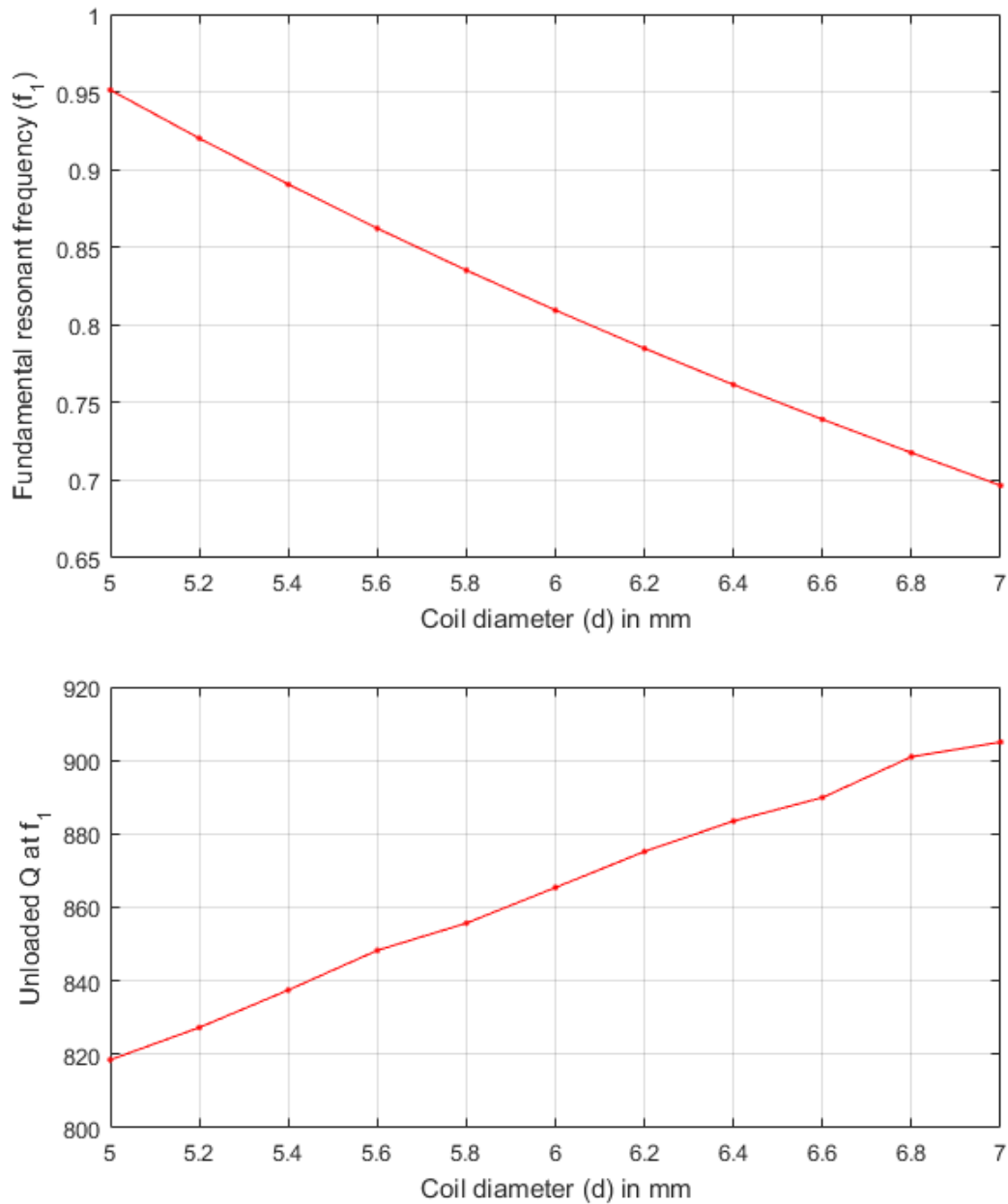


Figure 4.32 Fundamental resonant frequency and the corresponding unloaded Q against the coil diameter when $h_{\text{top}}=6.38$ mm, $h_{\text{btm}}=18$ mm.

The non-uniform pitch helical resonator is then simulated with the above determined dimensions ($d=6.0$ mm, $d_0=1.0$ mm, $l_s=5.0$ mm, $h_{\text{btm}}=18$ mm, $h_{\text{top}} = 6.38$ mm and $N=3.5$). However, it does not provide close enough results. The height of the top part is tuned and optimised to $h_{\text{top}} = 6.0$ mm, in order to realise the required resonant frequencies and unloaded Q factors. The simulated resonant frequencies of the optimised resonator are at 814.6 MHz and 1739.7 MHz, with unloaded Q factor of 868.7 and 1270.9, respectively.

Finally, the non-uniform pitch helical resonator is fabricated and tested to finish the design process. The fabricated resonator and measurement results are shown in Section 4.3.3. Although the measured resonant frequencies and unloaded Q factors are not ideal because of the fabrication process, the measured frequency ratio agrees with the desired value.

4.3.3 Experimented non-uniform pitch helical resonators

This section shows the verification process of the analysis and simulation of non-uniform pitch helical resonators. The coils were made of 1.0 mm diameter insulated copper wires and wound on dual-section formers shown in Figure 4.33.

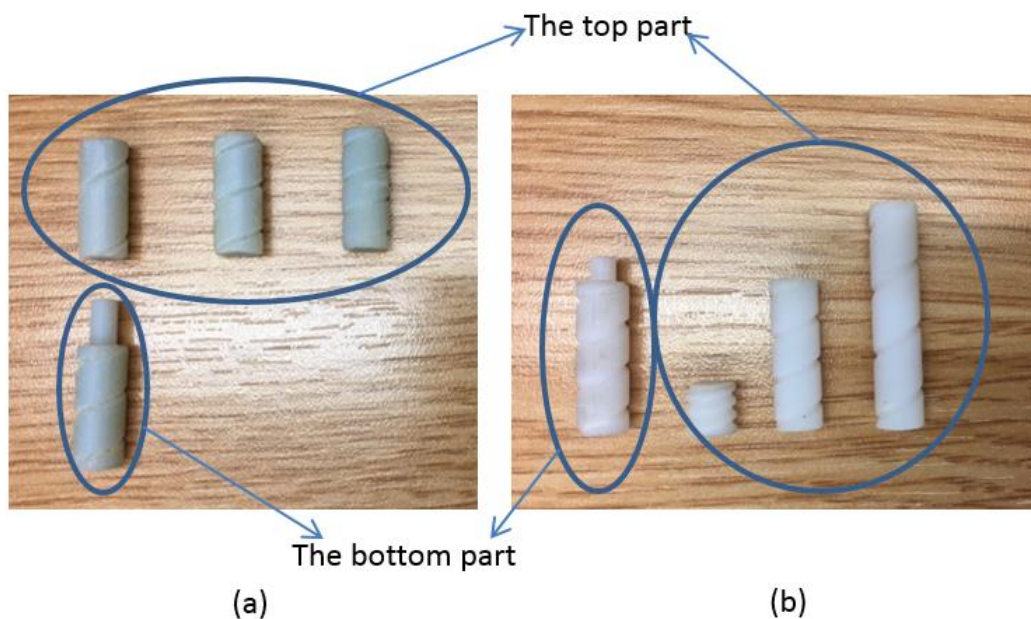


Figure 4.33 3D printed dual-section formers. (a) Category I. (b) Category II.

The formers were made of polymer RGD450 and fabricated using additive manufacturing technology, known as 3D printing. When the winding process finished, the formers were gently twisted out (towards up or down respectively) for removal. However, this twisting process may cause shape change of the coils, resulting in increased coil diameter, increased height, and slight difference in pitches. The increased coil diameter may significantly reduce the resonant frequencies of the resonator, while the slight pitch difference may influence the frequency ratio (f_2/f_1) of the resonator.

The cavities are made of brass sheets. The thickness of brass sheets is 0.3 mm, which is much larger than the skin depth at the frequencies of operation. The brass sheets were cut and soldered together to form the cavity bodies and the lids. In order to see the inner structures of the

resonators, the lids were not soldered onto the cavity bodies because the heat of lid soldering may easily make the coil fall out. Copper tape was used to attach the lids onto the cavity bodies when testing these resonators. However, it will significantly increase the loss and reduce the Q factors. Additionally, the tin used for brass sheets soldering introduces extra losses, which may also further reduce the unloaded Q factor.

These influences on the resonant frequencies, frequency ratio, and unloaded Q factors of the non-uniform pitch helical resonator could be eliminated by improving mechanical design and fabrication process.

The fabricated resonators have SMA connectors soldered onto the cavity and lids sealed by copper tape. They are loosely coupled by external source/load and measured using a Network Analyser to obtain the S_{21} parameters. The resonant frequencies and the unloaded Q factor of the fabricated resonators are obtained employing the measurement method in Section 2.6 and unloaded Q extraction equation (2.82).

Next, the fabricated Category I and Category II non-uniform pitch helical resonators are discussed, respectively.

Category I non-uniform pitch helical resonator: pitch modified by the number of turns

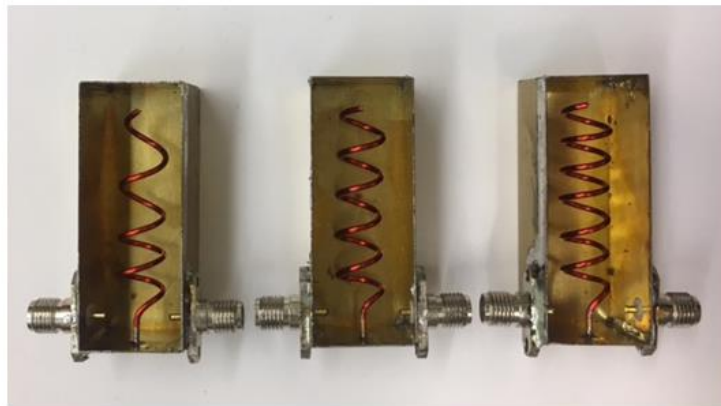
Three Category I non-uniform pitch helical resonators were fabricated and measured to verify the above analysis, simulation and design procedure. All the resonators have the following parameters: $S = 17.5$ mm, $d = 7.3$ mm, $d_0 = 1.0$ mm, $l_s = 5.0$ mm, $h_{top} = h_{btm} = 18.0$ mm and $N_{btm} = 2.5$ turns. These resonators are different in the number of turns of the top part, with $N_{top} = 1.5, 2.5,$ and 3.5 respectively.

Figure 4.34 shows the fabricated Category I non-uniform pitch helical resonators. Table 4-III provides the simulated and measured data of the designed Category I resonators.

The measured frequency ratios have very good agreement with the simulated frequency ratios. They are within 1% different from the simulated values. The measured resonant frequencies are about 10% lower and the measured unloaded Q factors are 1/3 to 1/2 lower than the corresponding simulated values. The fabrication process, including winding process of the coils, twisting process of the formers, soldering loss, and imperfect shield, likely causes the difference in resonant frequencies and unloaded Q factors. Overall, the measured frequency ratios verified the theories, models, and simulation of non-uniform pitch helical resonators in Section 4.3.1.



(a)



(b)

Figure 4.34 Fabricated Category I non-uniform pitch helical resonators. (a) With lids. (b) Without lids.

Table 4-III Data of the fabricated Category I resonators.

	$N_{\text{top}}=1.5$ turns		$N_{\text{top}}=2.5$ turns (Uniform pitch)		$N_{\text{top}}=3.5$ turns	
	Simulated	Measured	Simulated	Measured	Simulated	Measured
f_1 (MHz)	844	785	731	684	665	616
Unloaded Q at f_1	1020	730	930	660	910	690
f_2 (MHz)	2550	2395	2170	2005	1843	1737
Unloaded Q at f_2	1770	850	1550	750	1500	900
Frequency ratio f_2/f_1	3.021	3.052	2.969	2.931	2.771	2.820

There was another resonator fabricated and tested, shown in Figure 4.35. The cavity is made of a one-piece cylindrical copper tube. The dimensions are tube inner diameter $D = 22.0$ mm, coil diameter $d = 7.5$ mm, wire diameter $d_0 = 1.0$ mm, support length $l_s = 5.0$ mm, height of the top part and the bottom part $h_{\text{top}} = h_{\text{btm}} = 18$ mm, the number of turns of the bottom part $N_{\text{btm}} = 2.5$ turns, and the number of turns of the top part $N_{\text{top}} = 1.5$ turns.



Figure 4.35 Fabricated helical resonator in a cylindrical tube [51].

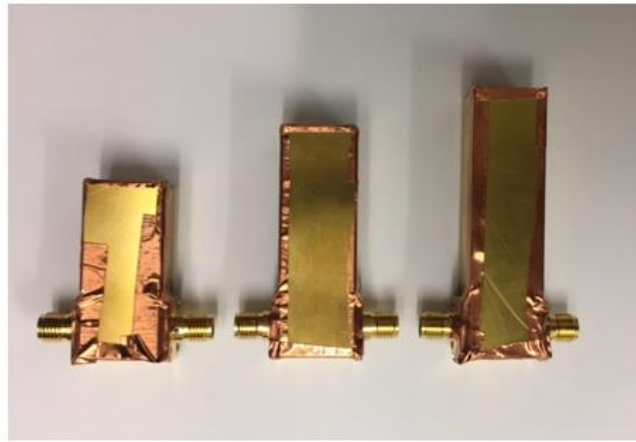
The simulated resonant frequencies are 836 MHz and 2525 MHz, with the unloaded Q factors of 1050 and 1790, respectively. Measured results indicate that the resonant frequencies are 838 MHz and 2548 MHz with the unloaded Q factors of 930 and 1380, respectively. The measured resonant frequencies and frequency ratio have very good agreement (within 1% difference) with the simulated values. The measured unloaded Q factors are about 10% and 25% lower than the simulated unloaded Q factors, respectively. This is mainly because the SMA connectors were not soldered onto the lids of the cavity, in case that the coil falls out when heating the bottom lid of the cavity. The unloaded Q factors could be further improved by using different temperature holders for the soldering process.

This example showed that using a one-piece cavity for shielding significantly improves the unloaded Q factors. It also showed that carefully fabricated helix could realise the expected resonant frequencies.

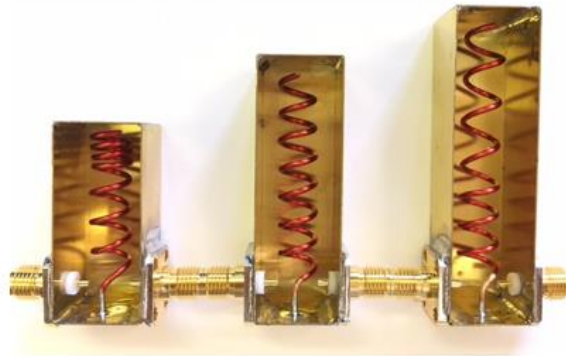
Category II non-uniform pitch helical resonator: pitch modified by the height

The above theoretical models, analysis, simulation and design procedure of Category II non-uniform pitch helical resonator were verified by the measurement of three fabricated resonators. All the resonators have the following parameters: $S = 14.4$ mm, $d = 6$ mm, $d_0 = 1.0$ mm, $l_s = 5.0$ mm, $h_{\text{btm}} = 18.0$ mm, and $N_{\text{top}} = N_{\text{btm}} = 3.5$ turns. However, they are different in the height

of the top part, with $h_{\text{top}} = 6, 18$ and 27 mm respectively, shown in Figure 4.36. Table 4-IV provides the data obtained from simulation and measurement.



(a)



(b)

Figure 4.36 Fabricated Category II non-uniform pitch helical resonators. (a) With lids. (b) Without lids.

Table 4-IV Data of the fabricated Category II resonators.

	$h_{\text{top}}=6$ mm		$h_{\text{top}}=18$ mm (uniform pitch)		$h_{\text{top}}=27$ mm	
	Simulated	Measured	Simulated	Measured	Simulated	Measured
f_1 (MHz)	815	733	687	619	634	567
Unloaded Q at f_1	870	580	780	560	750	530
f_2 (MHz)	1740	1572	2016	1829	1962	1768
Unloaded Q at f_2	1270	860	1320	850	1320	890
Frequency ratio f_2/f_1	2.135	2.144	2.934	2.955	3.095	3.118

Firstly, we can see that the measured frequency ratios have very good agreement with the simulated frequency ratios (within 1% difference). It verifies the theoretical models, analysis and simulation of the frequency characteristics of non-uniform pitch helical resonators in Section 4.3.1. Secondly, the measured resonant frequencies of each resonator are about 10% lower than the simulated resonant frequencies. This is because the winding process of the coils and twisting process of the formers affected the diameters of the coils. In addition, the fabricated coils have shorter air gaps with the cavities at their open-ends, compared to the design and simulation. These air gaps cause stronger capacitive coupling than expected at the open-ends of the resonator, result in lower measured resonant frequencies. Thirdly, the measured unloaded Q factors are about 1/3 smaller than the simulated unloaded Q factors. This is because the cavities are formed by soldered brass sheets and the lids are attached by copper tape, which will introduce losses and energy leakage to which significantly affects the unloaded Q factors.

Overall, the fabricated non-uniform pitch helical resonators have verified the theories, models, and simulation in Section 4.3.1. However, the limited fabrication process influenced some measurements. Advanced mechanical design and fabrication process may eliminate these influences on measurement, such as one-piece cavity, shield without leakage, and improved helices fabrication process.

4.3.4 External coupling and inter-resonator coupling

The structures and topologies of external and inter-resonator couplings are characterised in this section for the filter design using non-uniform pitch helical resonators.

External coupling

The external coupling of a helical resonator can be achieved by direct tap coupling or by parallel plate coupling.

Direct tapping is a type of electric coupling that uses a wire/probe to connect input and the resonator. It is possible to use the probe of SMA connector to connect the input and the resonator directly, instead of using a wire. Ideally, there are five topologies to tap the wire onto the helix, as shown in Figure 4.37. This direction of wiretapping could be an extra degree of freedom to control the external coupling, apart from the tapping location. Considering the ease of soldering and less effect (magnetic coupling) on the resonator, the topologies shown in Figure 4.37 (a) and (c) are preferred for filter design.

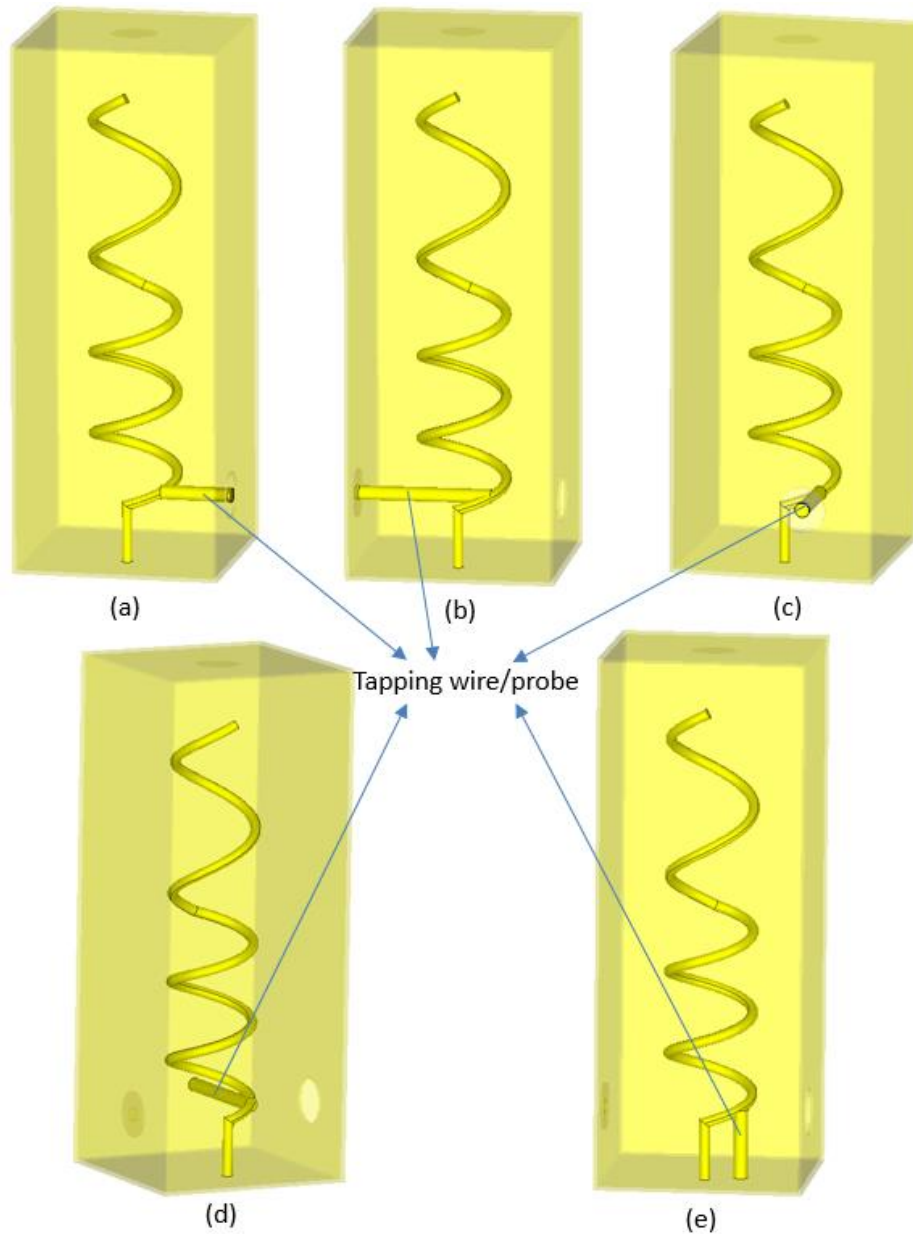


Figure 4.37 Topologies of direct tapping. (a) Right. (b) Left. (c) Front. (d) Back. (e) Bottom.

Parallel plate coupling forms a magnetic type external coupling by a plate that stands next to the helical resonator, as shown in Figure 4.38. Similar to the direct tap coupling, the parallel plate coupling can also be realised in different topologies. The dimensions and location of the disk plate control the coupling hence this structure has more degree of freedom to control the external coupling, compared to direct tapping. It has been used for dual-band helical filter design in [108]. However, we found that the distance between the plate and the coil may be less than 0.5 mm when a strong external coupling is required in filter design. In this case, it is very difficult to realise physically precise short gap between the plate and the coil. Direct tapping to the resonator realises strong and stable external coupling against vibration.

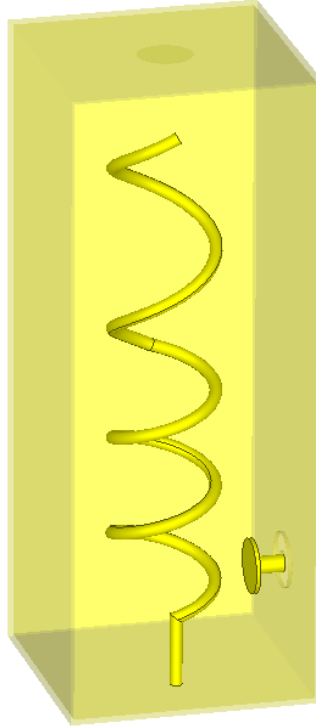


Figure 4.38 Parallel plate coupling.

Additionally, both the first and the second resonant frequencies of the non-uniform pitch helical resonator would be increased when applying strong external coupling to it. This is because of the loading effect of the external source/load, which causes higher resonant frequencies but lower unloaded Q factors of the resonator. However, the loading effect has more impact on the second resonance than the first resonance, which increases the frequency ratio (f_2/f_1) of the external coupled/loaded resonator. The effect on the frequency ratio has been studied to be an increase of approximately 0.05 [51].

Inter-resonator coupling

Apertures are used to realise the inter-resonator couplings for inline cavity filters. A general coupling structure for non-uniform pitch helical resonators by an aperture is illustrated in Figure 4.39 [51]. It realises mixed coupling since the electric coupling and magnetic coupling coexist and cancel each other out. The dimensions of aperture (i.e. dimensions of the wall W and h_{wall}) are the parameters that control the inter-resonator coupling coefficients. A tuning screw is usually used to tune the coupling in practice. However, both W and h_{wall} plays significant role in controlling the coupling coefficient of each frequency band, which may not provide sufficient degree of freedom to realise the required coupling coefficients for the first and the second resonances independently.

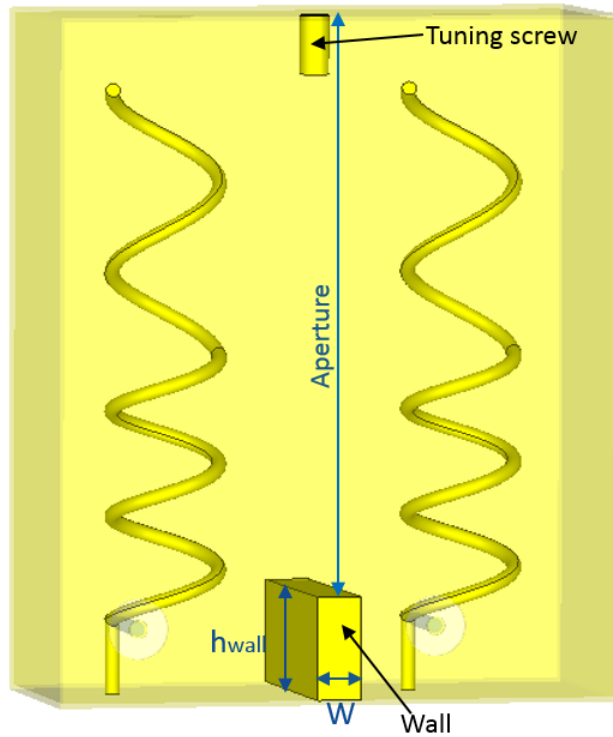


Figure 4.39 General inter-resonator coupling by aperture.

To further study the coupling between non-uniform pitch helical resonators, the field distributions of the non-uniform pitch helical resonator need to be analysed. Figure 4.40 shows the fields of a non-uniform helical resonator.

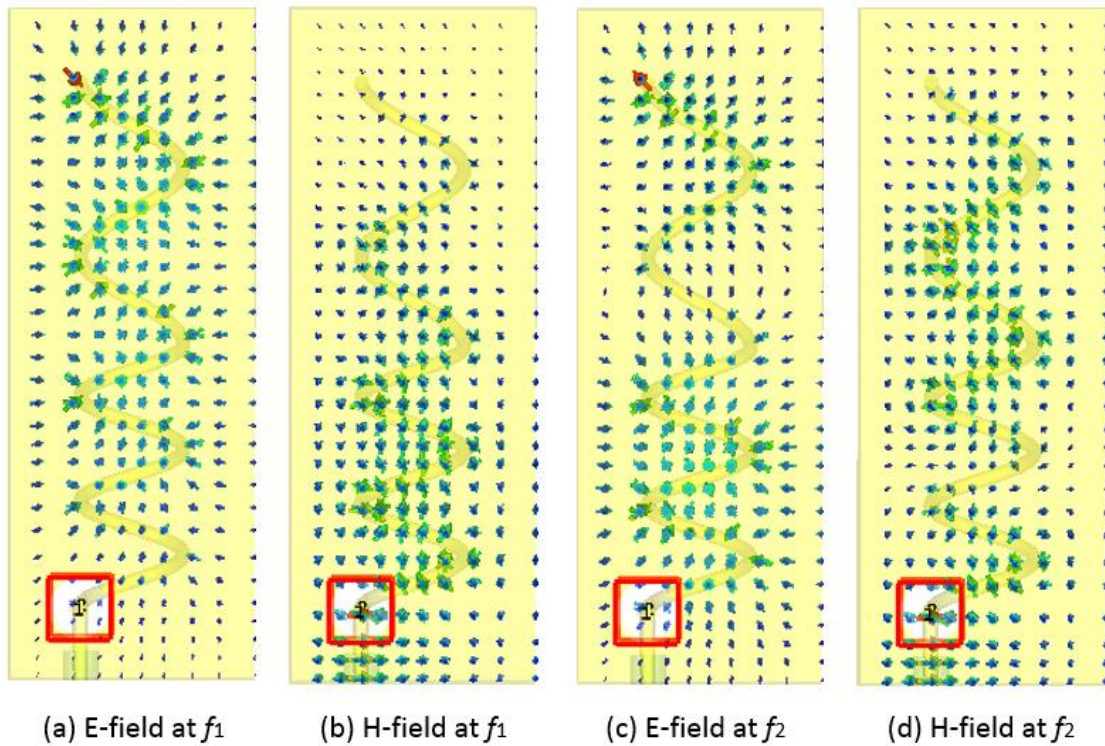


Figure 4.40 Field distributions of a non-uniform pitch helical resonator.

The electric field intensity reaches maximum at the open-end (top) of the resonator while it reaches minimum at the short-circuited end (bottom) for both resonant modes. The magnetic field intensity reaches maximum at the short-circuited end (bottom) of the resonator and reaches minimum at the open-circuited end (top). There is also a peak of magnetic field intensity in the upper part of the helical resonator as well as a peak of electric field intensity in the lower part, close to the break point where the pitch of helical resonator changes, at the second resonant mode. Therefore, at the fundamental resonant mode, the magnetic coupling is dominant in the lower part of the aperture, while the electric coupling is dominant in the upper part of the aperture. However, for the second resonant mode, comparable electric and magnetic coupling coexist in the lower and upper part of the aperture.

Chen et al. proposed step-width aperture to realise the inter-resonator coupling structure of a coaxial SIR filter [106]. The step-width aperture has more degrees of freedom to control the coupling, compared to the traditional uniform-width aperture. In their example [106], the widths of the aperture did not realise the inter-resonator coupling of the resonances independently. Nevertheless, when applying the step-width aperture to the inter-resonator coupling between non-uniform pitch helical resonators, the inter-resonator coupling coefficients of the two resonant modes (f_1 and f_2) can be realised relatively independently.

Figure 4.41 shows a step-width aperture to realise inter-resonator coupling between two Category I non-uniform pitch helical resonators. The lower aperture height (H_1) is set as the sum of support height and lower part height of helical resonator (i.e. $H_1 = h_{\text{btm}} + l_s$). In order to demonstrate the independently controlled couplings, an example of the structure was simulated. The sectional cavity and the non-uniform pitch helical resonator have the following dimensions: $S = 17.5$ mm, $H = 46.0$ mm, $d = 7.3$ mm, $d_0 = 1.0$ mm, $l_s = 5.0$ mm, $h_{\text{top}} = h_{\text{btm}} = 18.0$ mm, $N_{\text{btm}} = 2.5$ turns, $N_{\text{top}} = 1.5$ turns and $H_1 = 23.0$ mm. The thickness of cavity and the coupling wall is 0.3 mm. The coupling coefficients k_1 and k_2 , which represents the coupling coefficient at the fundamental resonant frequency (f_1) and the second resonant frequency (f_2) respectively, were obtained with different values of lower aperture width (W_1) and upper aperture width (W_2). Figure 4.42 shows the coupling profile at the first resonant frequency. The coupling coefficient (k_1) does not change much (only 30%) with the increase of lower aperture width (W_1), when the upper aperture width (W_2) is constant. However, for a constant value of lower aperture width (W_1), the coupling coefficient k_1 increases up to three times the value with the increase of upper aperture width (W_2). In brief, the upper aperture width (W_2) is the dominant parameter that influences the coupling coefficient at the first resonant frequency.

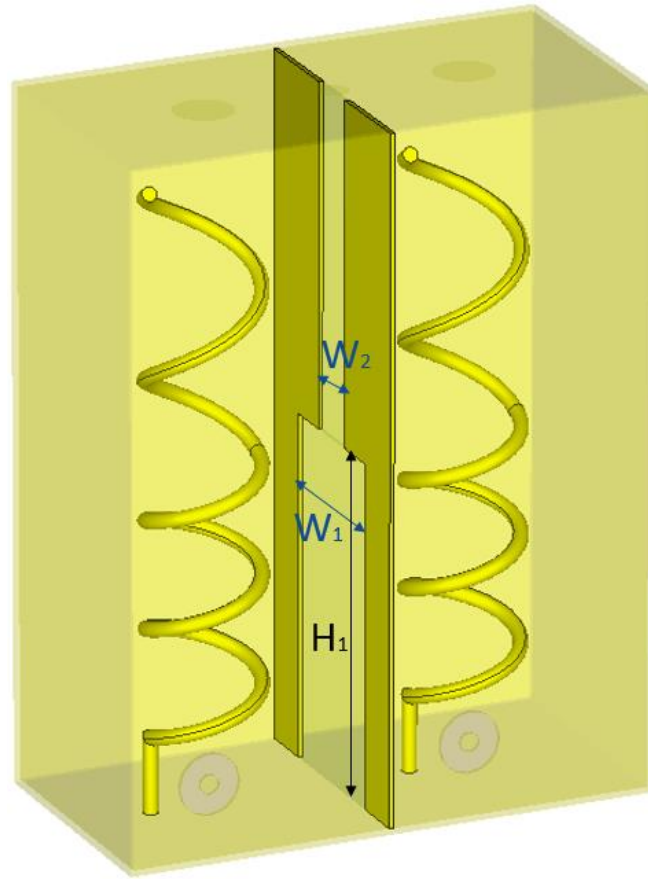


Figure 4.41 Step-width aperture for inter-resonator coupling structure.

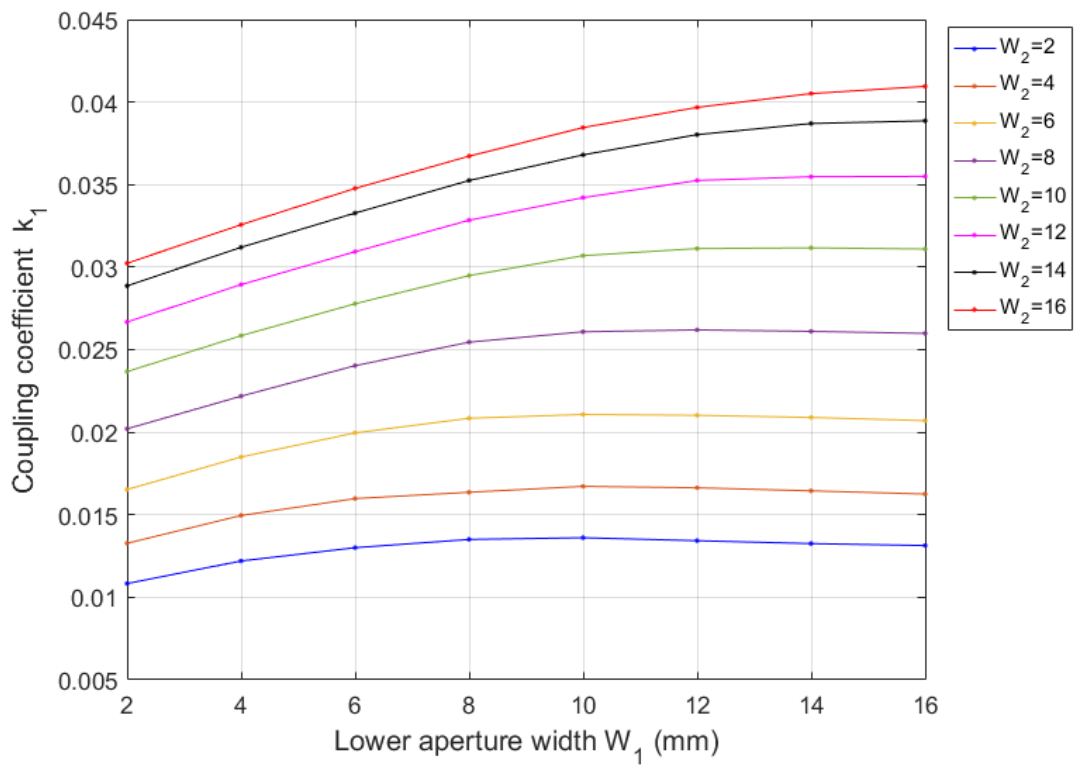


Figure 4.42 Simulation of the coupling coefficients at the first resonant frequency (f_1).

Figure 4.43 shows the coupling profile at the second resonant frequency.

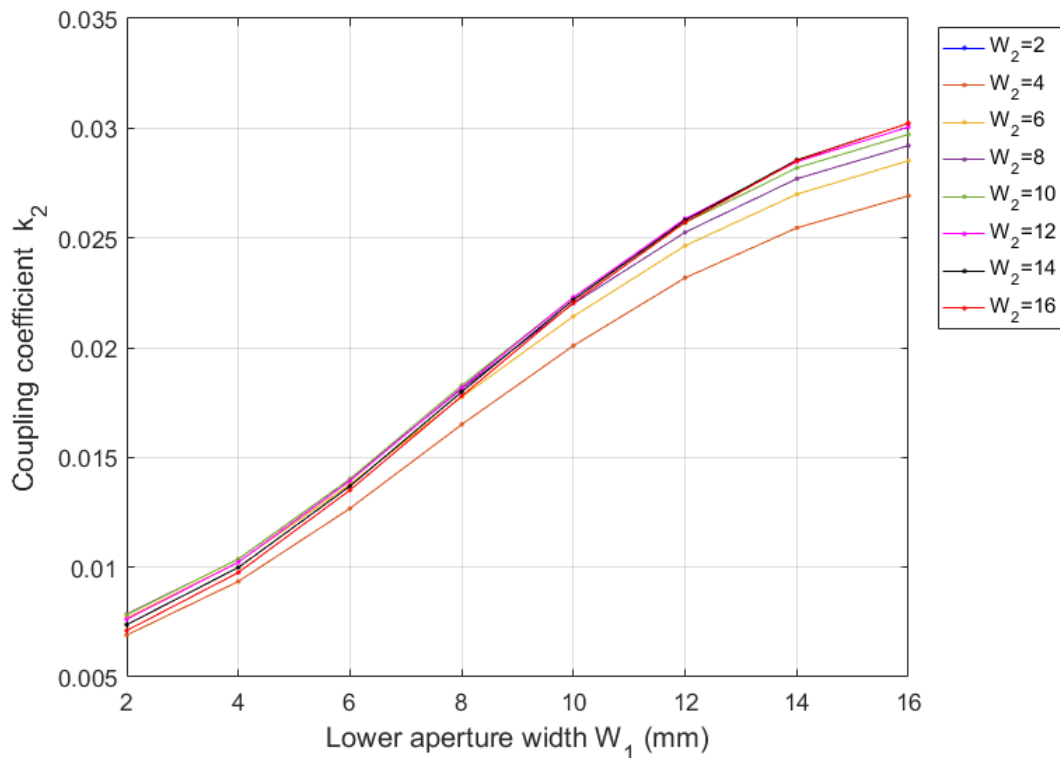


Figure 4.43 Simulation of the coupling coefficients at the second resonant frequency (f_2).

It illustrates that the lower aperture width (W_1) has much more influence on the coupling coefficient of the second resonance (k_2), compared to the upper aperture width (W_2). In other words, the lower aperture width (W_1) is the dominant parameter that controls the coupling coefficient at the second resonant frequency.

Besides the widths of aperture (W_1 and W_2), the lower aperture height (H_1) can also be used as a degree of freedom to control the inter-resonator couplings between non-uniform pitch helical resonators. The influence of the height of width step on coupling coefficients was also analysed.

Figure 4.44 and Figure 4.45 shows the simulated coupling coefficients (k_1 and k_2) for different sets of aperture widths (W_1 and W_2) and lower aperture height (H_1). The simulation results showed that the lower aperture height (H_1) has an influence on the coupling coefficients. However, the ranges of the coupling coefficients were not affected by the lower aperture height. Since the widths of aperture (W_1 and W_2) are sufficient to control the coupling coefficient of each resonance respectively, it may not be necessary to have the lower aperture height (H_1) as an extra degree of freedom to control the couplings.

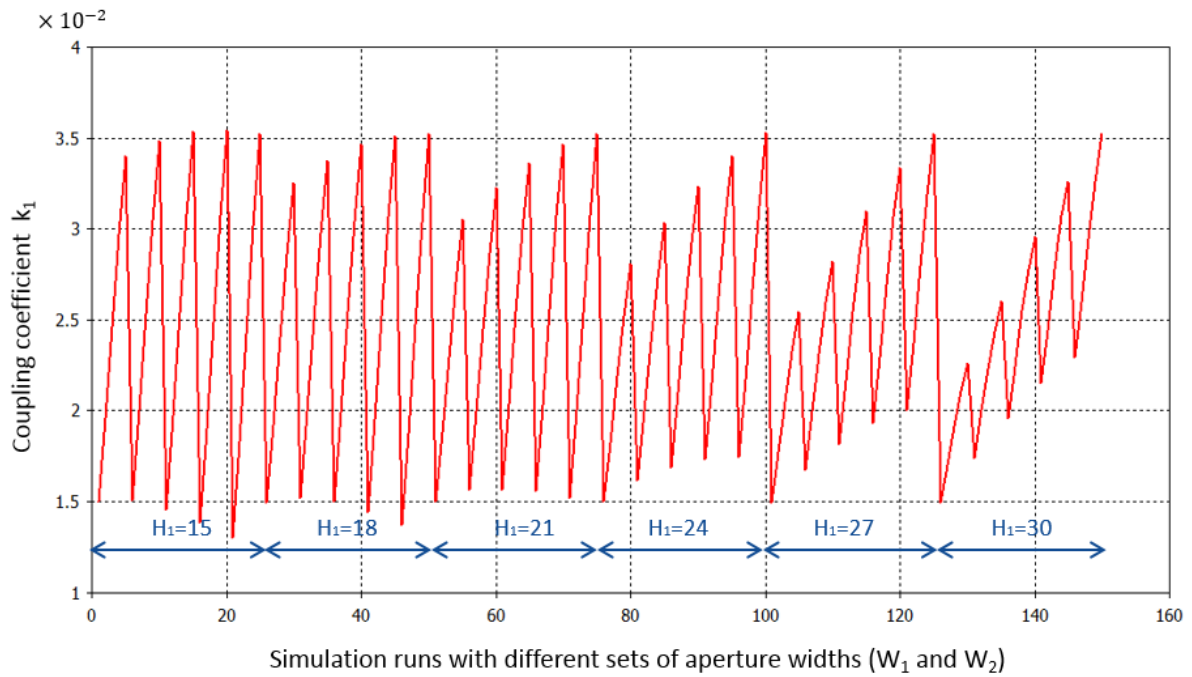


Figure 4.44 Coupling coefficient (k_1) against lower aperture height (H_1).

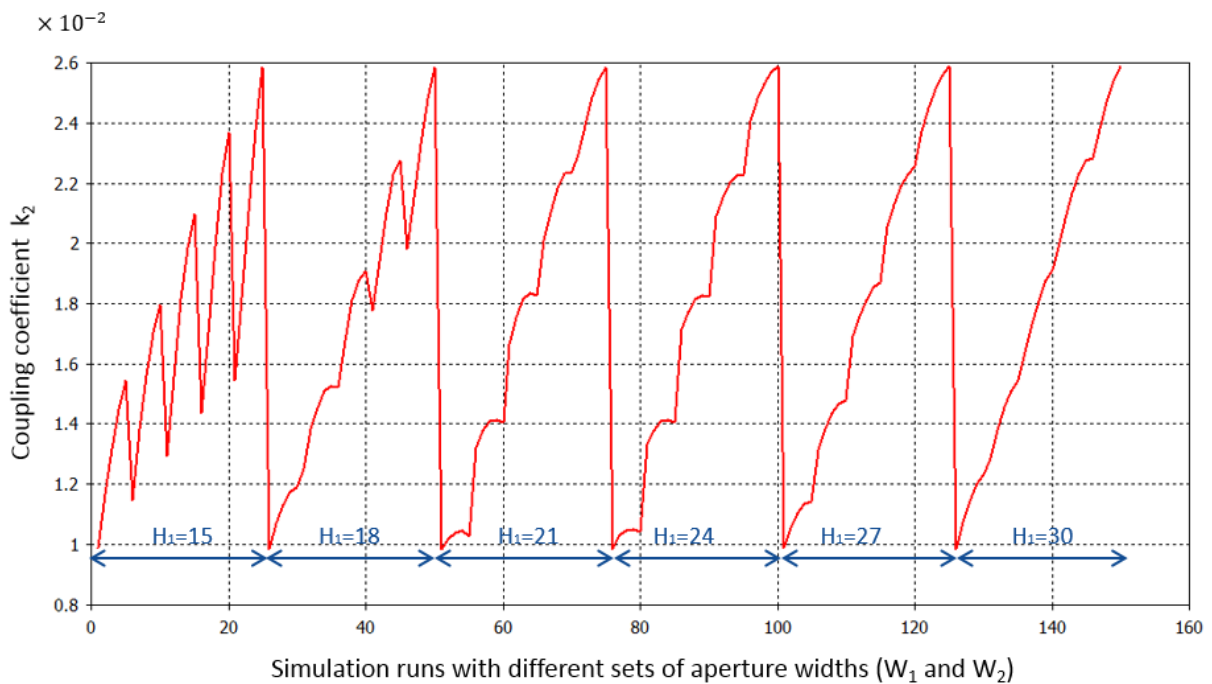


Figure 4.45 Coupling coefficient (k_2) against lower aperture height (H_1).

Because the helices are asymmetrical structures, the inter-resonator couplings can be significantly different with different topologies of the non-uniform pitch helical resonators. For example, the coupled resonators in could be rotated along their vertical axis by an arbitrary angle, respectively. The angle of rotation becomes the extra degree of freedom that control the coupling coefficient.

Figure 4.46 shows an example that the left helical resonator is rotated by 180° while the other one is rotated by 90° .

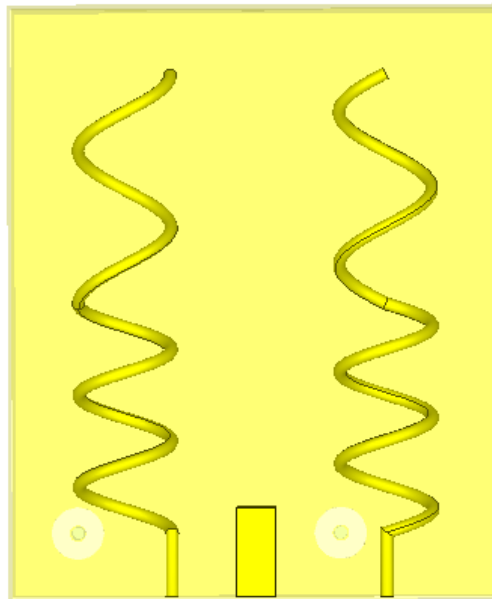


Figure 4.46 Inter-resonator coupling topology for non-uniform pitch helical resonators with rotation of 180° and 90° respectively.

In addition, the helical resonators can be mirrored by a plane, which generates a few more topologies for the inter-resonator coupling structure, shown in Figure 4.47. It is noted that the left resonator in Figure 4.47 has different winding direction compared to the right resonator.

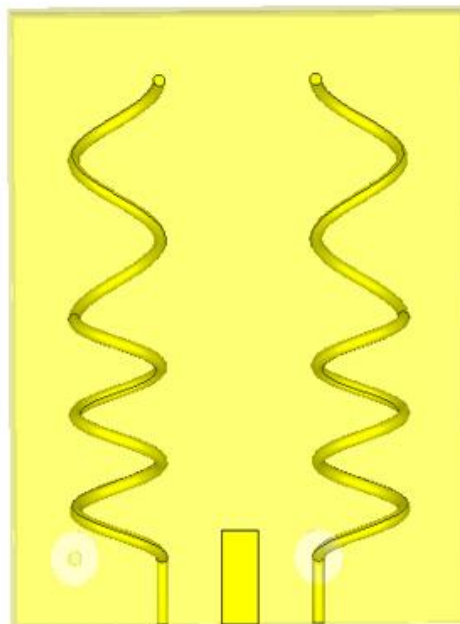


Figure 4.47 Inter-resonator coupling topology with a mirrored helical resonator.

There are other topologies available, such as interdigital types [112] shown in Figure 4.48. The interdigital type may also have extra degrees of freedom, such as the rotated angles and mirrored planes of resonators. Nevertheless, it is noted that creating these extra degrees of freedom does not necessarily extend the tuning range of the coupling coefficients.

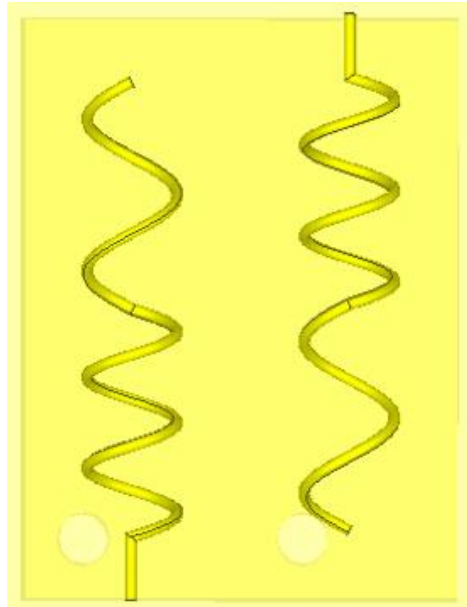


Figure 4.48 Interdigital type topology of inter-resonator coupling.

4.3.5 Filters using non-uniform pitch helical resonators

The above presented non-uniform pitch helical resonators and coupling structures were used to implement dual-band bandpass filters. This section presents three dual-band bandpass filter designs utilising Category I and II non-uniform pitch helical resonators, respectively. The designed dual-band bandpass helical filters have been fabricated and tested. Measured results of the filters are shown as well.

A second order dual-band bandpass filter using Category I resonators

Design specification

A dual-band bandpass filter working in the LTE band with the second order Butterworth response is desired. Two passbands are required at 845 MHz and 2600 MHz, with 3-dB fractional bandwidth (FBW) of 6% and 4.5%, respectively. Passband insertion losses are required to be less than 2 dB.

In order to realise the required FBW, the external Q factor and inter-resonator coupling coefficient of each band are derived as

$$Q_e = \frac{\sqrt{2}}{\text{FBW}} = \begin{bmatrix} 23.6 \\ 31.4 \end{bmatrix} \text{ at } \begin{bmatrix} 845 \\ 2600 \end{bmatrix} \text{ MHz} \quad (4.53)$$

$$k = \frac{\text{FBW}}{\sqrt{2}} = \begin{bmatrix} 0.0424 \\ 0.0318 \end{bmatrix} \text{ at } \begin{bmatrix} 845 \\ 2600 \end{bmatrix} \text{ MHz}$$

Resonator characterisation

Considering the effect of external coupling on frequency ratio (f_2/f_1) and required resonant frequencies, the resonator is characterised as one of the Category I non-uniform pitch resonators in Section 4.3.3. The dimensions of the resonator and the sectional cavity are: $S = 17.5$ mm, $H = 46.0$ mm, $d = 7.3$ mm, $d_0 = 1.0$ mm, $l_s = 5.0$ mm, $h_{\text{top}} = h_{\text{btm}} = 18.0$ mm, $N_{\text{btm}} = 2.5$ turns, and $N_{\text{top}} = 1.5$ turns.

External coupling

The external coupling structure was selected as direct tapping the SMA probe onto the helical resonator, with the topology shown in Figure 4.37 (a). Figure 4.49 shows the external coupling profile obtained from EM simulation by CST MW. Thus, the height of the probe (b) is approximately 4.3 mm to realise the required external Q factors.

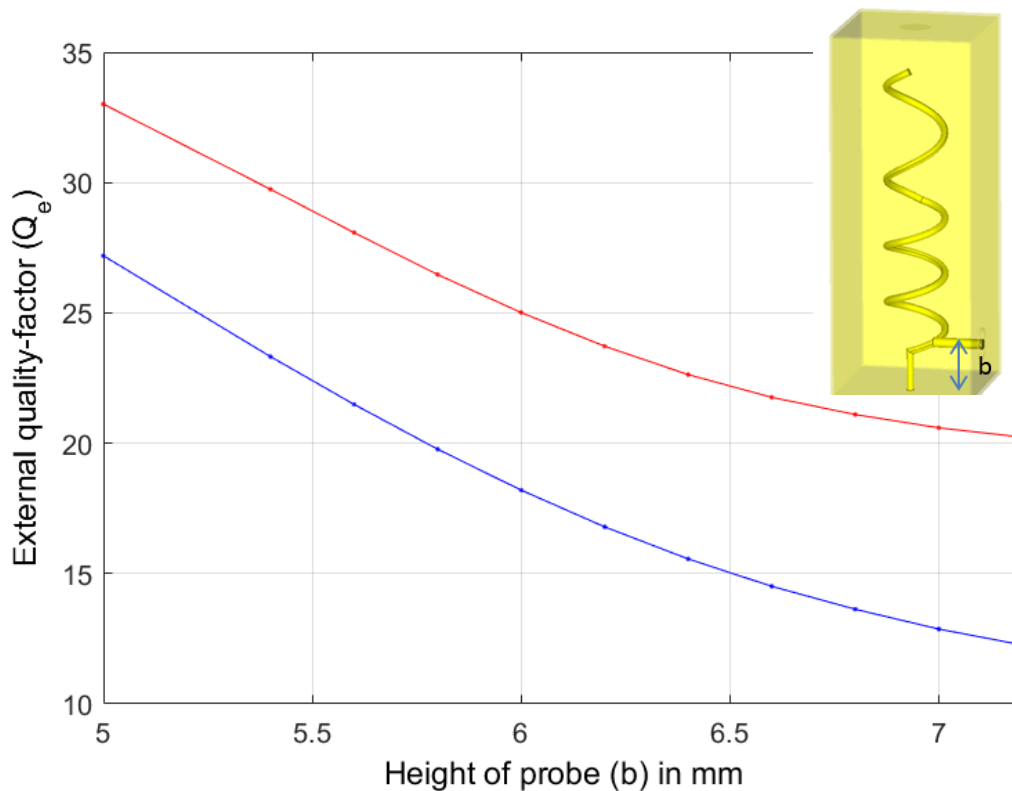


Figure 4.49 External coupling profile of the second order dual-band BPF.

Inter-resonator coupling

The inter-resonator coupling structure is shown in Figure 4.39 in which the coupling coefficients are controlled by wall height (h_{wall}) and wall width (W). The inter-resonator coupling profiles were obtained from CST MW simulation, shown in Figure 4.50 and Figure 4.51, respectively.

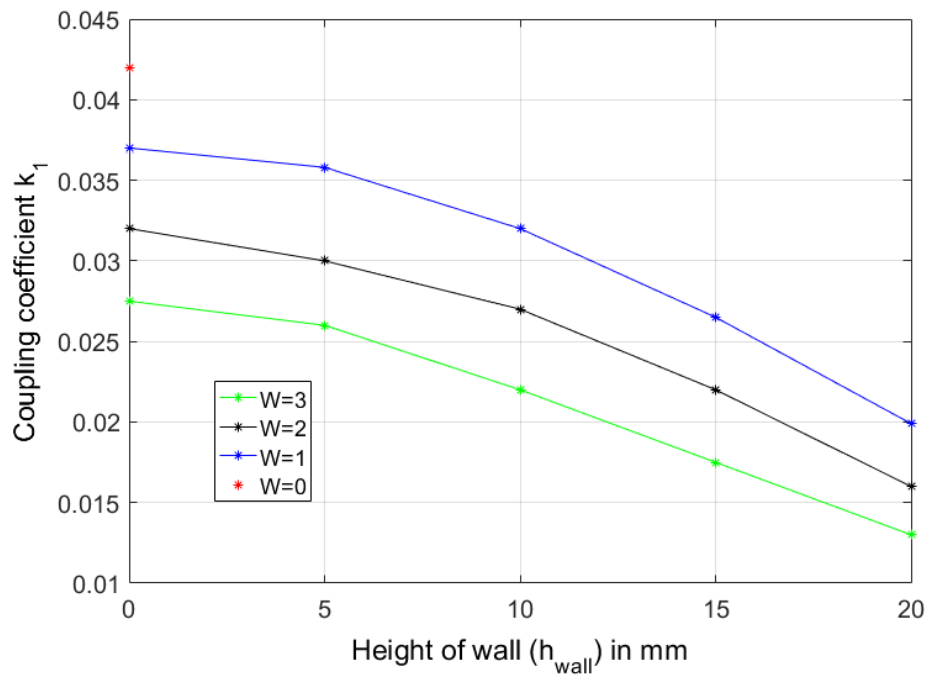


Figure 4.50 Inter-resonator coupling profile at the first band.

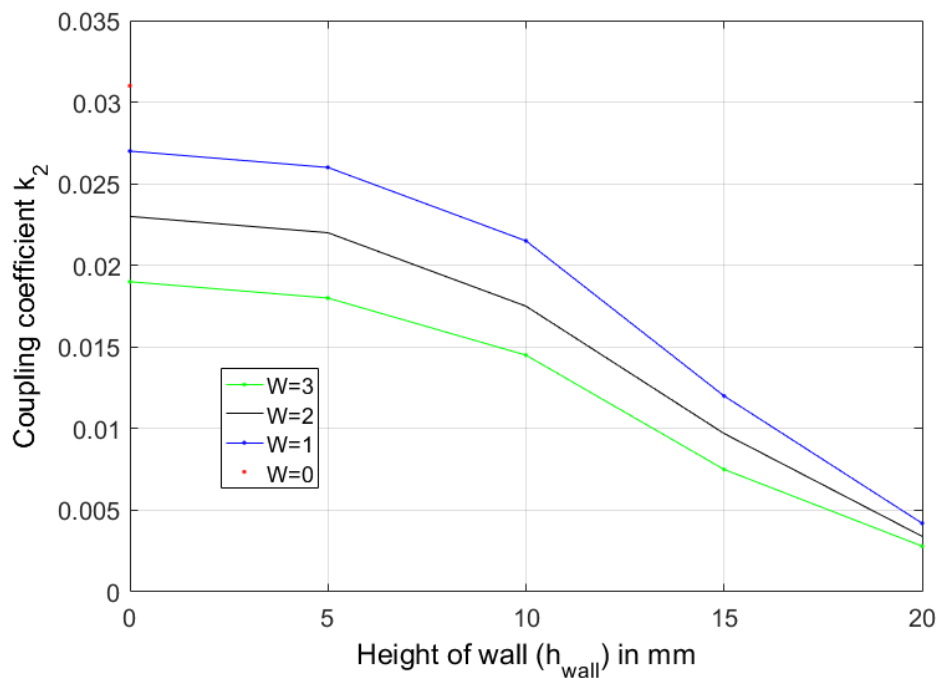


Figure 4.51 Inter-resonator coupling profile at the second band.

The dimensions of the inter-resonator coupling structure were initially obtained by substituting the values in (4.53) into the profiles. Thus, we have $h_{wall}=0$ and $W=0$, implying that the dual-band bandpass filter is realised by two non-uniform pitch helical resonators that are directly coupled in a rectangular cavity.

Filter implementation

Figure 4.52 shows the structure of the designed filter.

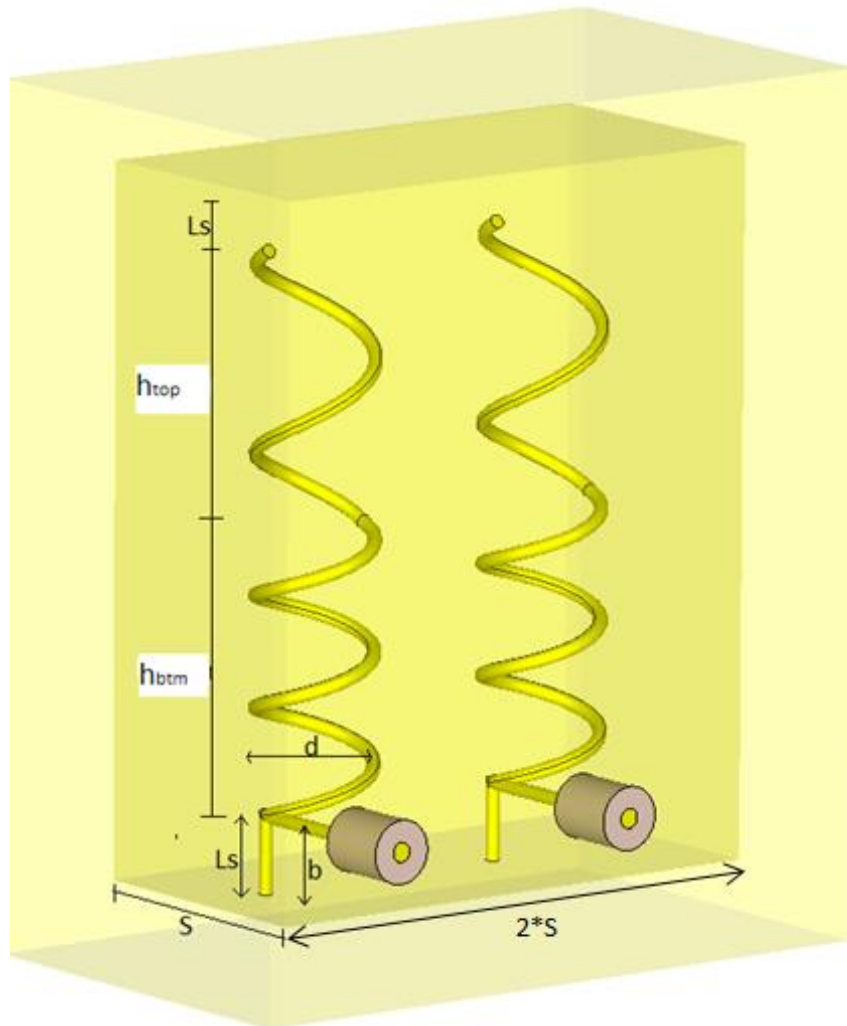


Figure 4.52 Structure of the designed second order dual-band BPF.

The dimensions of the filter were then further tuned and to optimise the frequency response, which are $d=7.5$ mm, $S=18$ mm and $b=5.0$ mm.

The power handling capability of the filter was estimated from the EM simulation using (2.87) in Section 2.7, which is approximately 254.9 Watt. The power handling capability is much higher than the planar structures, and becoming comparable with coaxial and waveguide filters.

Two filters were fabricated using uninsulated copper wire with the same cavity size ($S=18$ mm) but different coil diameters ($d=7.5$ mm and $d=7.3$ mm), considering the possible shape and parameter change during winding process of the coils and the twisting process of the formers. The cavity is made of brass sheets. Figure 4.53 shows one of the fabricated filters.

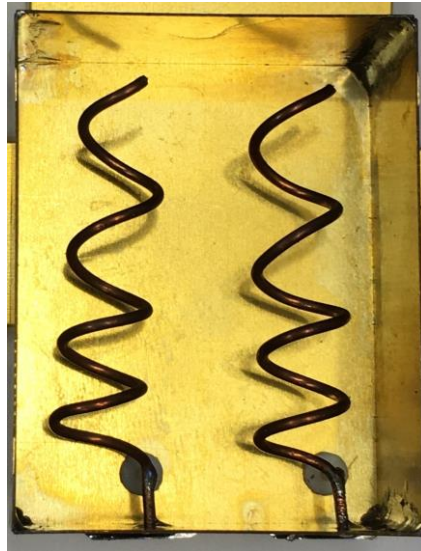


Figure 4.53 The fabricated second order BPF that $d=7.5$ mm.

The simulated and measured S_{11} parameters are shown in Figure 4.54.

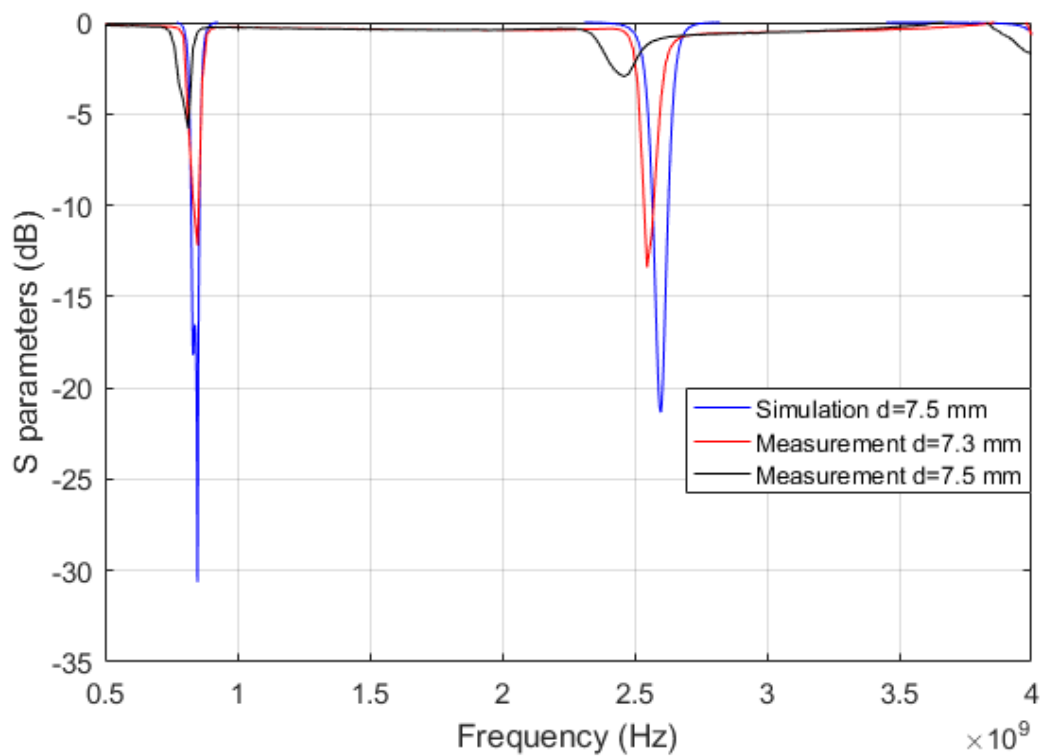


Figure 4.54 S_{11} parameters of the second order dual-band BPFs.

Figure 4.55 and Figure 4.56 shows the simulated and measured frequency responses of a wide frequency range and of passbands, respectively.

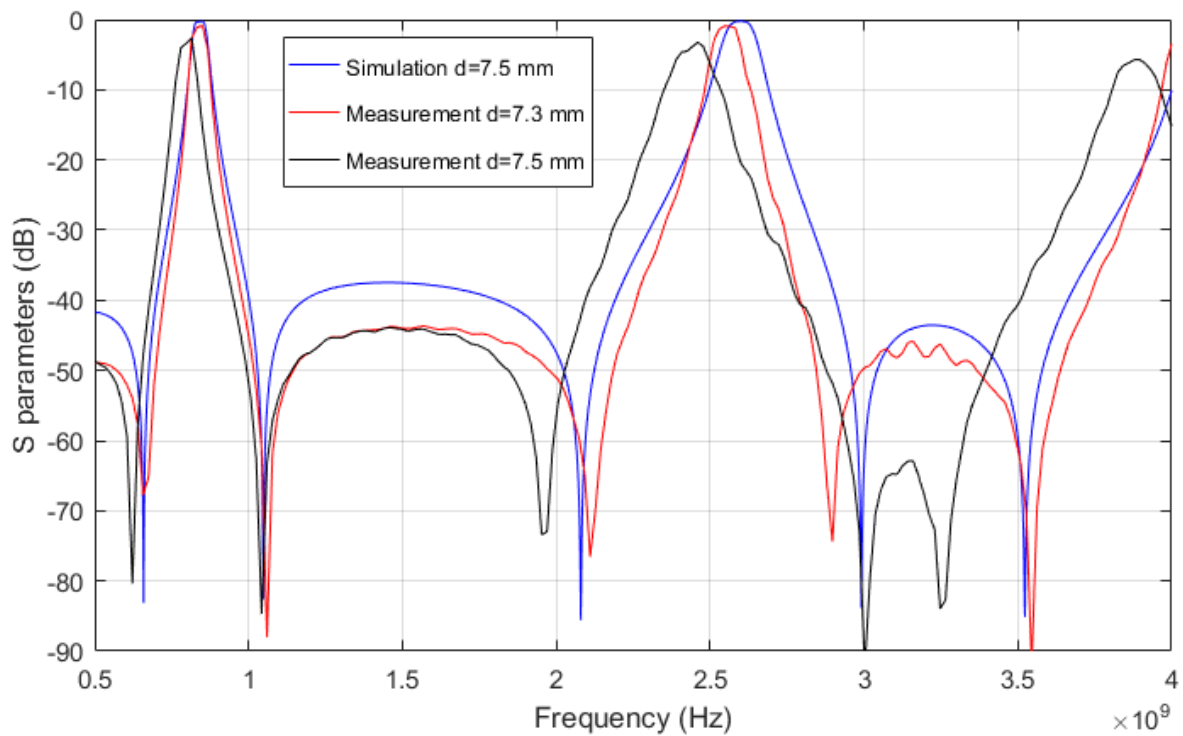


Figure 4.55 Frequency responses of the second order dual-band BPFs over a wide frequency range.

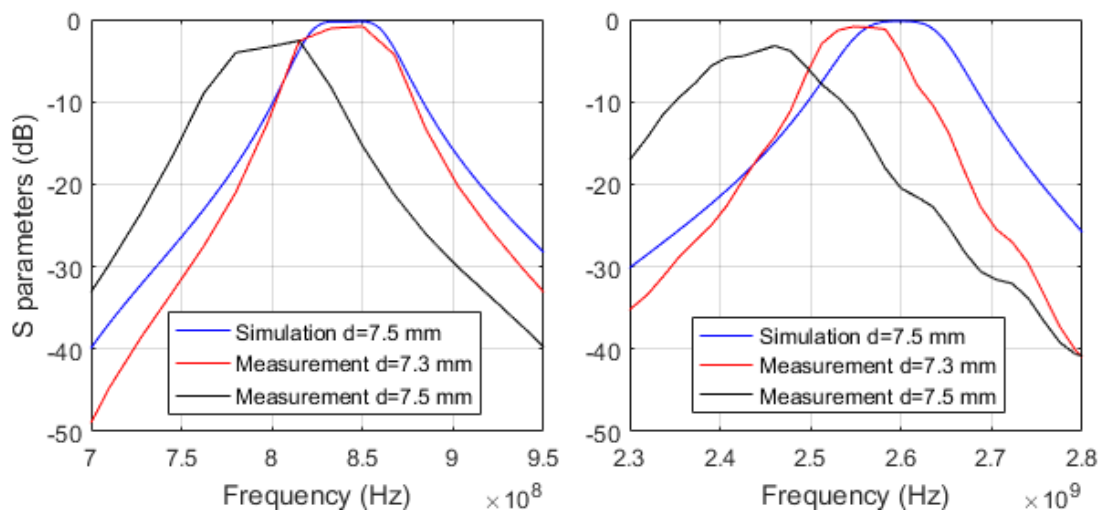


Figure 4.56 Passband S_{21} parameters of the second order dual-band BPFs.

The simulated frequency response shows one transmission zero at the lower stopband and one transmission zero at the higher stopband of each passband, achieving rejection that is 40 dB down of S_{21} parameter at about 15% away from the passband centre frequencies. These transmission zeros significantly improve the selectivity of filter, realising quasi-elliptic like

response. The measured frequency responses have verified the existence of these transmission zeros. These transmission zeros are generated by the cross coupling between input and output [30, 113-115].

Table 4-V shows the filter characteristics from design specification, simulation and measurement for comparison.

Table 4-V Data of the filter characteristics.

	Design specification	Simulation $d=7.5$ mm	Measurement $d=7.5$ mm	Measurement $d=7.3$ mm
Centre frequency of the 1 st passband (MHz)	845	840	799.3	839.6
3-dB fractional bandwidth of the 1 st passband	6.0%	6.0%	6.6%	6.6%
Insertion loss of the 1 st band	< 2 dB	0.26 dB	2.2 dB	0.58 dB
Centre frequency of the 2 nd passband (MHz)	2600	2590	2442.1	2552.1
3-dB fractional bandwidth of the 2 nd passband	4.5%	4.3%	5.0%	3.8%
Insertion loss of the 2 nd band	< 2 dB	0.21 dB	2.8 dB	0.75 dB
Frequency ratio	3.077	3.083	3.055	3.040

As mentioned in Section 4.3.3, the winding process of coils and the twisting process of formers increase the diameter and pitch of coils, which will decrease the resonant frequencies and frequency ratio (f_2/f_1). The filter with smaller coil diameter ($d=7.3$ mm) has better agreements with the design specification and simulation, compared to the other filter ($d=7.5$ mm). It shows that using a smaller diameter former can compensate for the effect of the winding process of coils and the twisting process of formers. Dissolving the formers could also overcome the effect, but results in high cost.

The insulated wire is used in practical applications instead of uninsulated copper wire because the insulation protects the wire from moisture, humidity, and other corrosive elements. The effect of the insulation on copper wire has been investigated. The insulation of copper wire is

usually very thin, less than 0.02 mm. CST MW is not capable to simulate such thin layer due to the limited quantity and resolution of meshes. Therefore, we fabricated another second order filter using insulated copper wire, shown in Figure 4.57. Figure 4.58 compares the frequency responses of the filters ($d=7.5$ mm) using insulated and uninsulated copper wire.

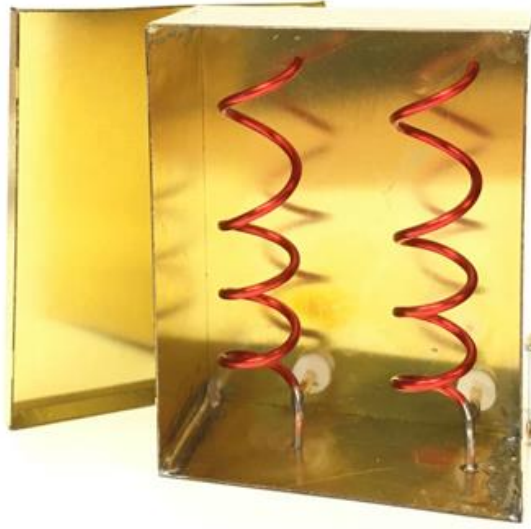


Figure 4.57 The fabricated second order filter using insulated copper wire that $d=7.5$ mm.

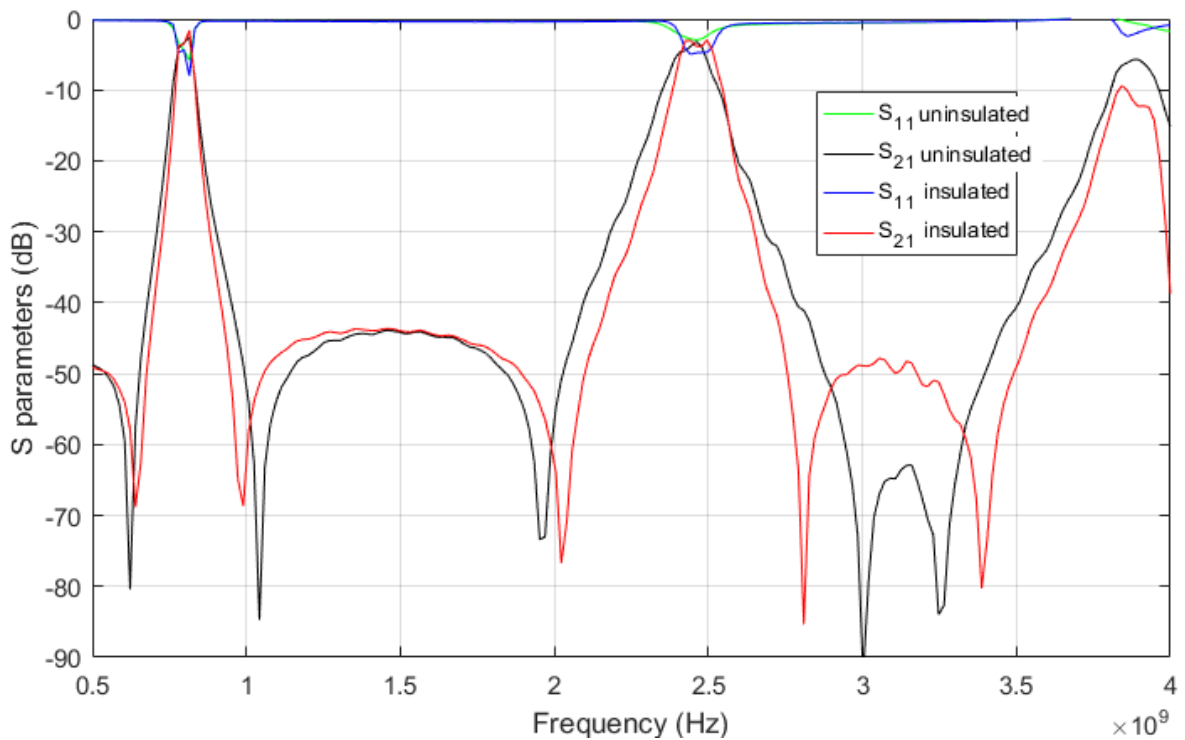


Figure 4.58 Frequency responses of the second order filters using insulated and uninsulated copper wires.

With the insulated copper wire, the filter realises passbands at 800.6 MHz and 2463.1 MHz, with 3-dB FBW of 5.7% and 5.0%, insertion loss of 1.4 dB and 2.6 dB, respectively. These results are very close to those of the filter fabricated using bare copper wire. The discrepancies in passband centre frequencies and fractional bandwidths between these filters are very small. Compared to the fabrication processes (coil winding and former twisting) that may cause significant discrepancies, the effect of insulation is negligible.

A third order dual-band bandpass filter using Category I resonators

Design specification

A dual-band bandpass filter working in the LTE band with the third order Butterworth response is desired. The passbands are required at 845 MHz and 2600 MHz, both with 3-dB fractional bandwidth (FBW) of 2.9%. The insertion losses are expected to be less than 2 dB.

Thus, the external Q factor (Q_e) and inter-resonator coupling coefficients (M_{12} and M_{23}) are obtained as follows.

$$Q_e = \frac{1}{\text{FBW}} = \begin{bmatrix} 34.5 \\ 34.5 \end{bmatrix} \text{ at } \begin{bmatrix} 845 \\ 2600 \end{bmatrix} \text{ MHz} \quad (4.54)$$

$$M_{12} = M_{23} = \frac{\text{FBW}}{\sqrt{2}} = \begin{bmatrix} 0.021 \\ 0.021 \end{bmatrix} \text{ at } \begin{bmatrix} 845 \\ 2600 \end{bmatrix} \text{ MHz}$$

Resonator characterisation

The resonator is characterised as the same of the previous filter example, one of Category I non-uniform pitch resonators designed in Section 4.3.3. The dimensions of the non-uniform pitch helical resonator and the sectional cavity are: $S = 17.5$ mm, $H = 46.0$ mm, $d = 7.3$ mm, $d_0 = 1.0$ mm, $l_s = 5.0$ mm, $h_{\text{top}} = h_{\text{btm}} = 18.0$ mm, $N_{\text{btm}} = 2.5$ turns, and $N_{\text{top}} = 1.5$ turns.

External coupling

The external coupling structure is direct tap coupling, with the same topology of Figure 4.37(a) in Section 4.3.4. However, the structure is slightly different in order to realise higher external Q factors. The input/output probe taps the support of the helix, rather than the helix. Figure 4.59 shows the external coupling structure that uses direct coupling. Figure 4.60 shows the simulated external coupling profile. The initial value of the height of probe (b) was obtained from the profile, which is 4.3 mm, in order to realise the external Q factors in (4.54).

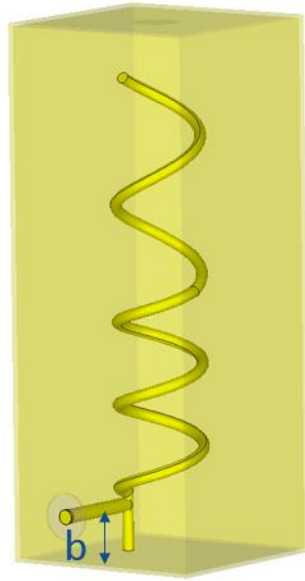


Figure 4.59 Direct coupling by probe on the support of helix.

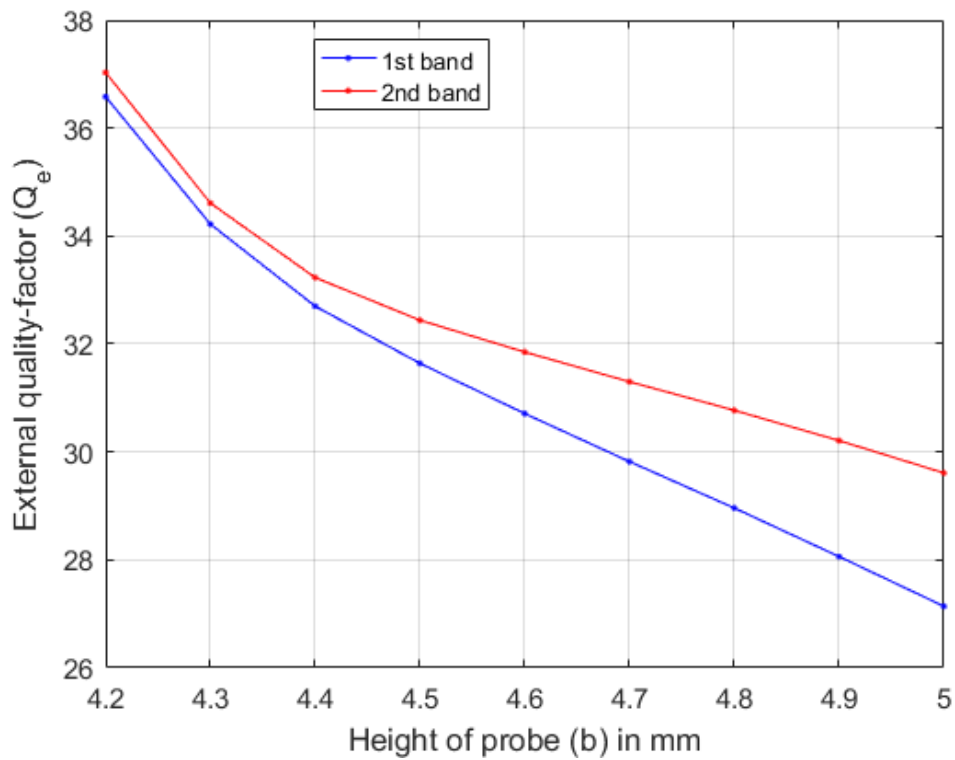


Figure 4.60 External coupling profile when tapping the support of the helical resonator.

Inter-resonator coupling

The inter-resonator coupling of this filter uses the step-width aperture that independently controls the coupling of each band, shown in Figure 4.41, Section 4.3.4. Figure 4.61 and Figure 4.62 shows the detailed coupling profile of the first band and the second band, respectively.

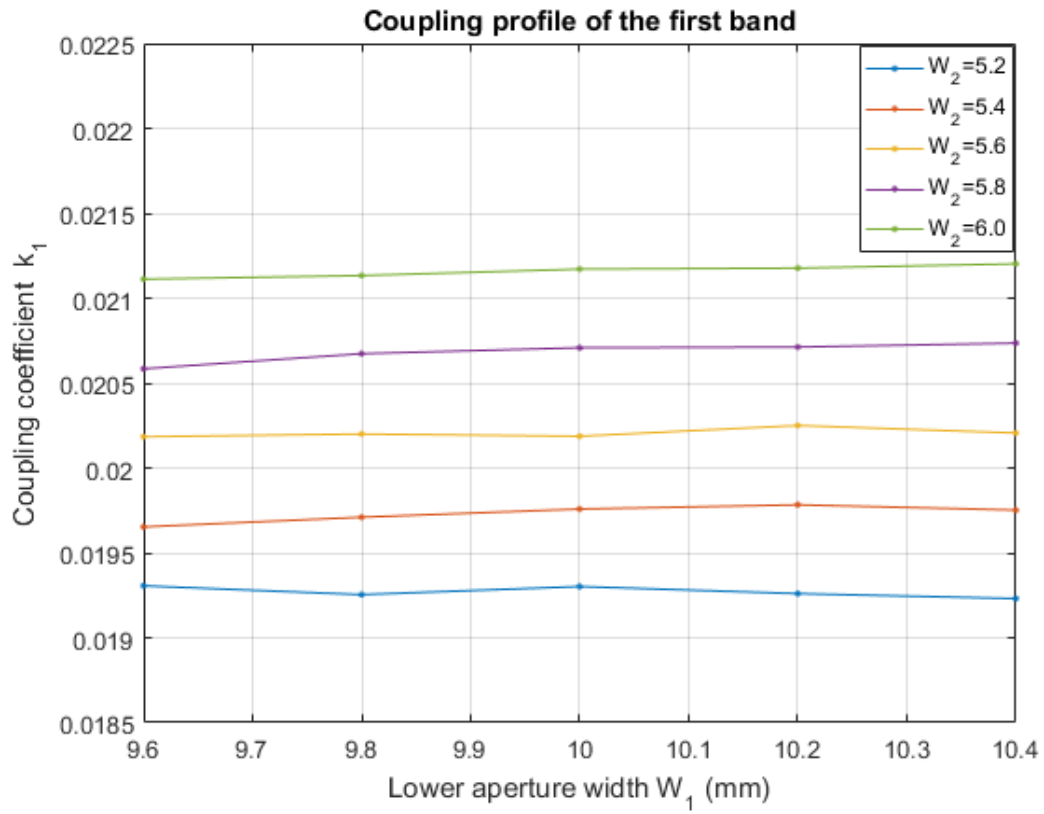


Figure 4.61 Inter-resonator coupling profile of the first band.

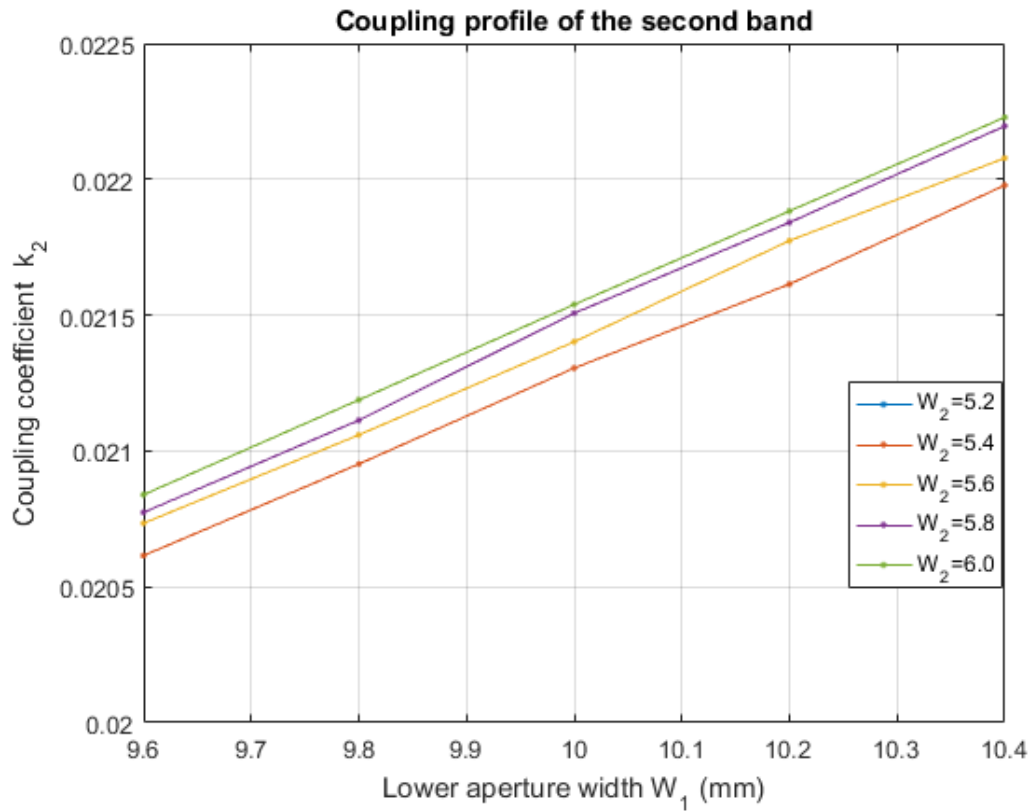


Figure 4.62 Inter-resonator coupling profile of the second band.

Substituting the required coupling coefficients in (4.54) to these profiles, the initial value of the aperture widths (W_1 and W_2) are obtained respectively: $W_1=9.72$ mm and $W_2=5.95$ mm.

Filter implementation

The initial dimensions of the filter were directly applied in CST MW for simulation. The initial simulated S-parameters of the filter are shown in Figure 4.63 and Figure 4.64.

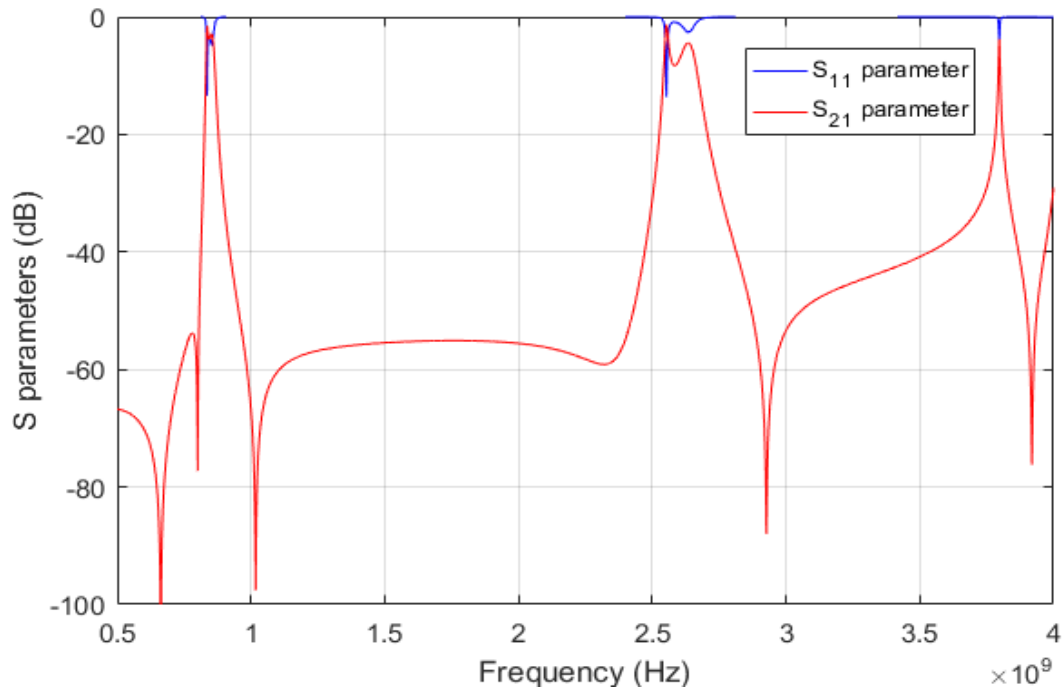


Figure 4.63 Initial simulated S-parameters of the third order BPF.

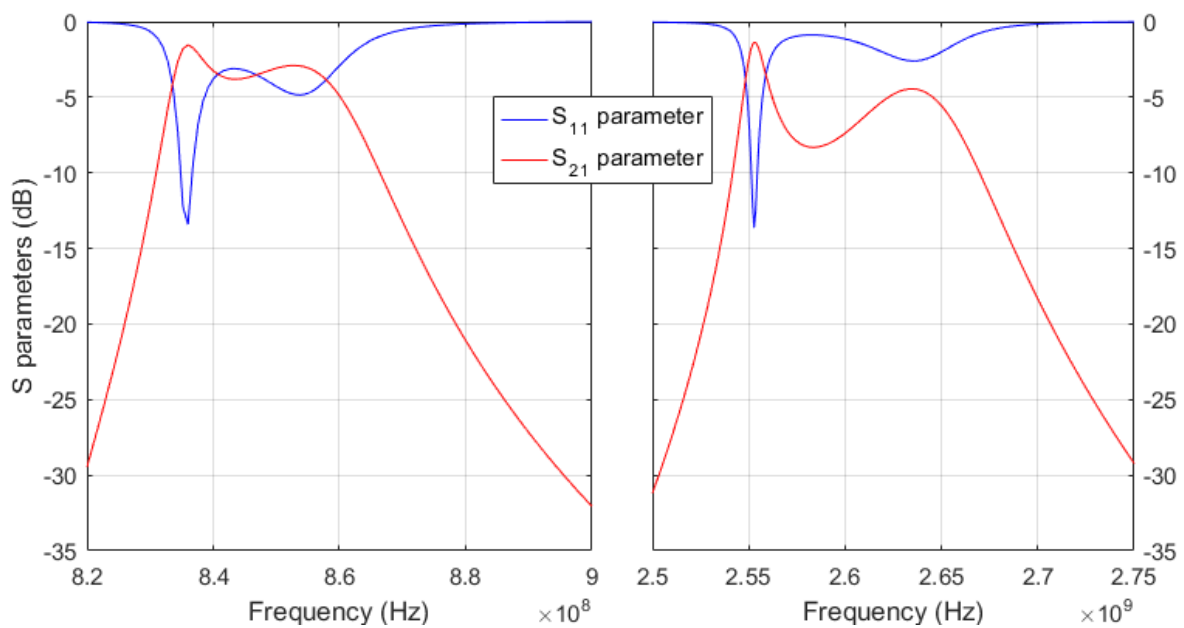


Figure 4.64 Passbands of the initial simulated frequency response of the third order BPF.

The initial simulated S-parameters showed unreasonable frequency response, in both passband ripple and insertion loss. Analysing the field patterns and resonating modes of each resonator by the Eigenmode Solver of CST MW, we found that the first and the third resonators are resonating at higher frequencies than the second resonator. It verifies the statement in Section 4.3.4 that the external coupling increases the resonant frequencies of the external coupled non-uniform pitch helical resonators. It is now necessary to use capacitive tuning screws to mitigate the external loading effect. The model of the filter was updated with capacitive tuning screws. The length of the M3 brass tuning screws for the first and the third resonators is 3.9 and 4.3 mm, respectively.

In addition, the inter-resonator coupling coefficient is smaller than expected at the first band, resulting in narrower bandwidth for the first band. Thus, it requires the tuning of the upper aperture width W_2 . The dimensions of the filter were then optimised, based on the 0.1 mm fabrication tolerance. The structure and dimensions of the optimised third order dual-band bandpass filter are shown in Figure 4.65 and Figure 4.66.

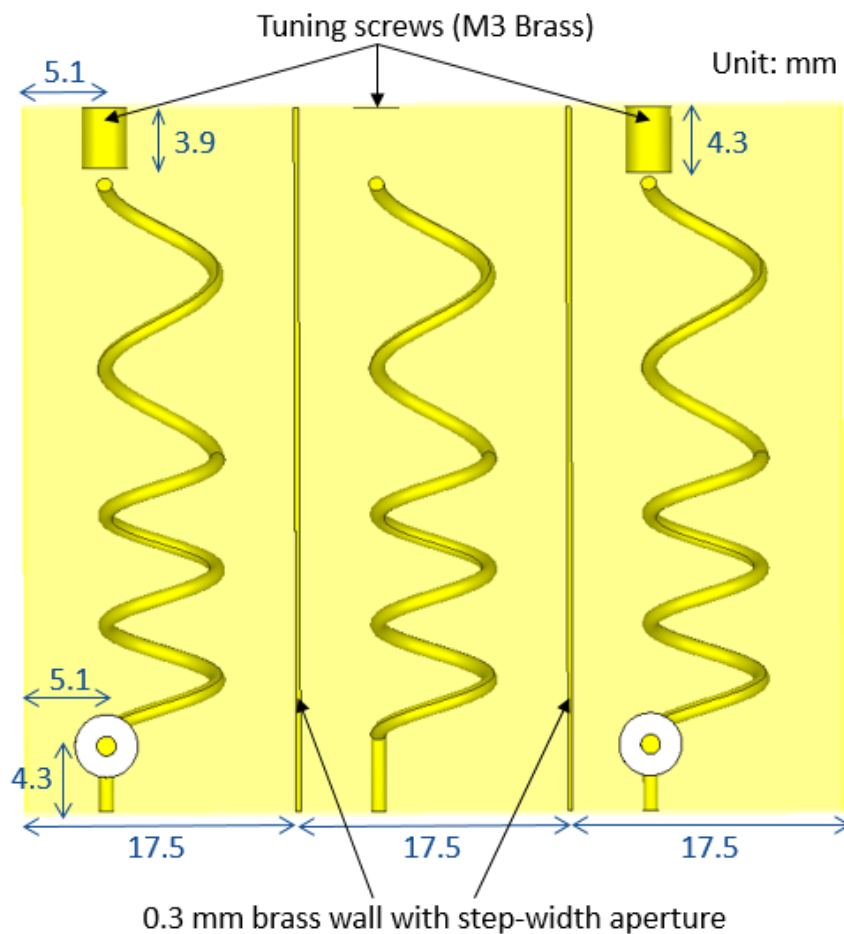


Figure 4.65 Structure and dimensions of the third order filter using Category I resonators (Front view).

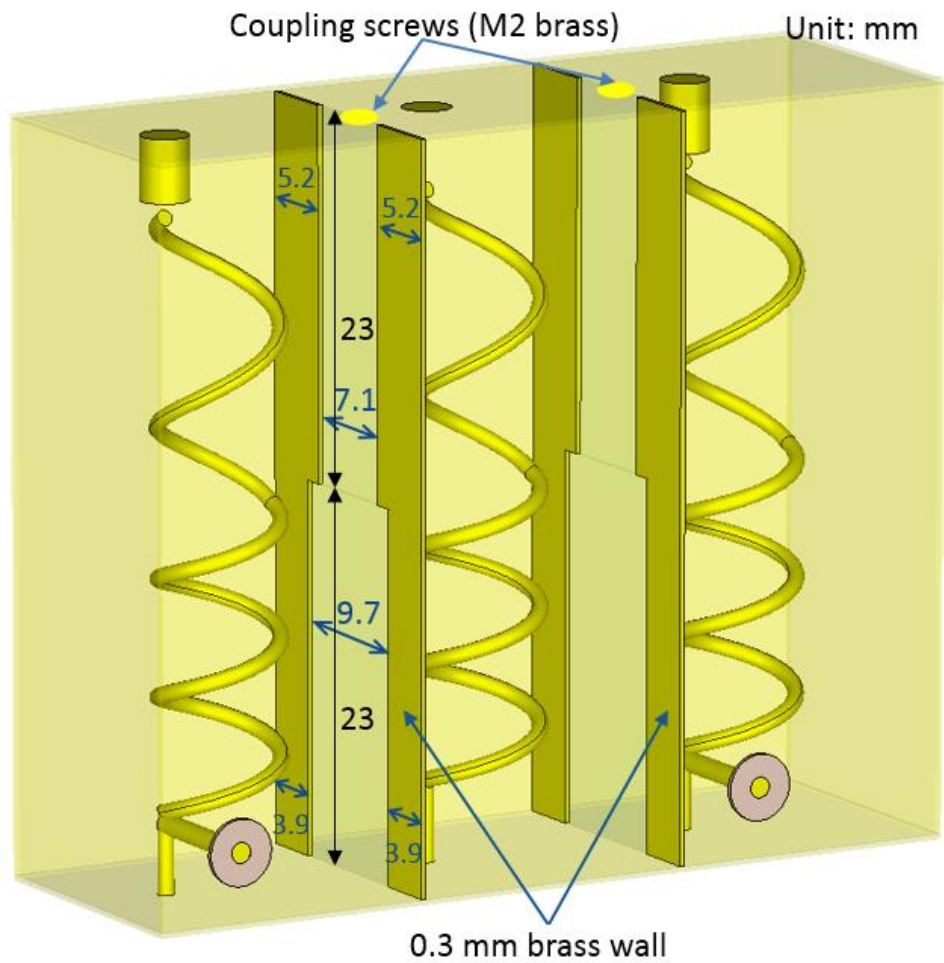


Figure 4.66 Structure and dimensions of the third order filter (Perspective view).

Figure 4.67 shows the photographs of the fabricated filter. The fabricated third order filter consists of a back lid and a cavity body, which were made of 0.3 mm thick brass sheets. The step-width brass walls that realise the step-width aperture were soldered onto the lid and the cavity body, respectively. The lid was fitted onto the main body by copper tape.

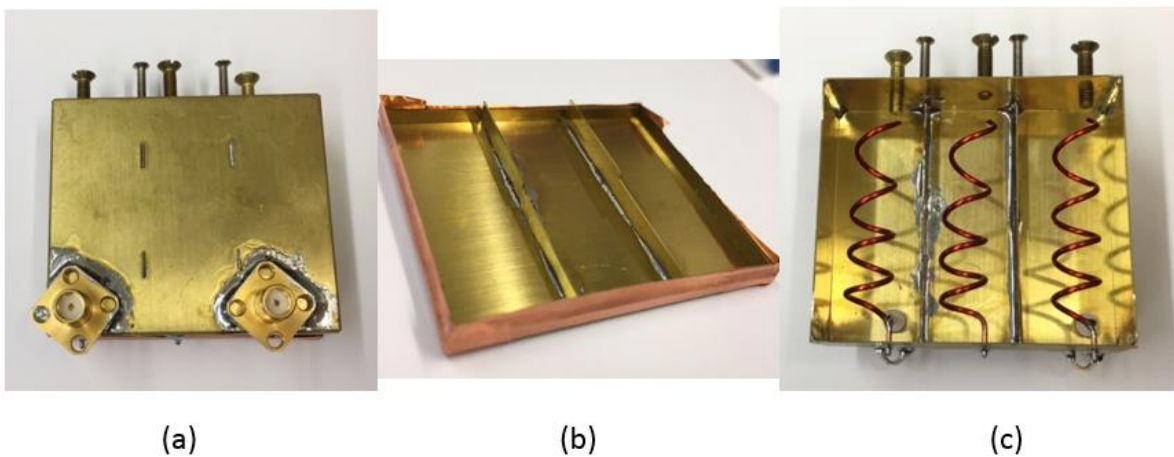


Figure 4.67 Photographs of the fabricated filter. (a) Front view. (b) Back lid. (c) Back view.

Figure 4.68 and Figure 4.69 shows the frequency responses from optimised simulation and measurement.

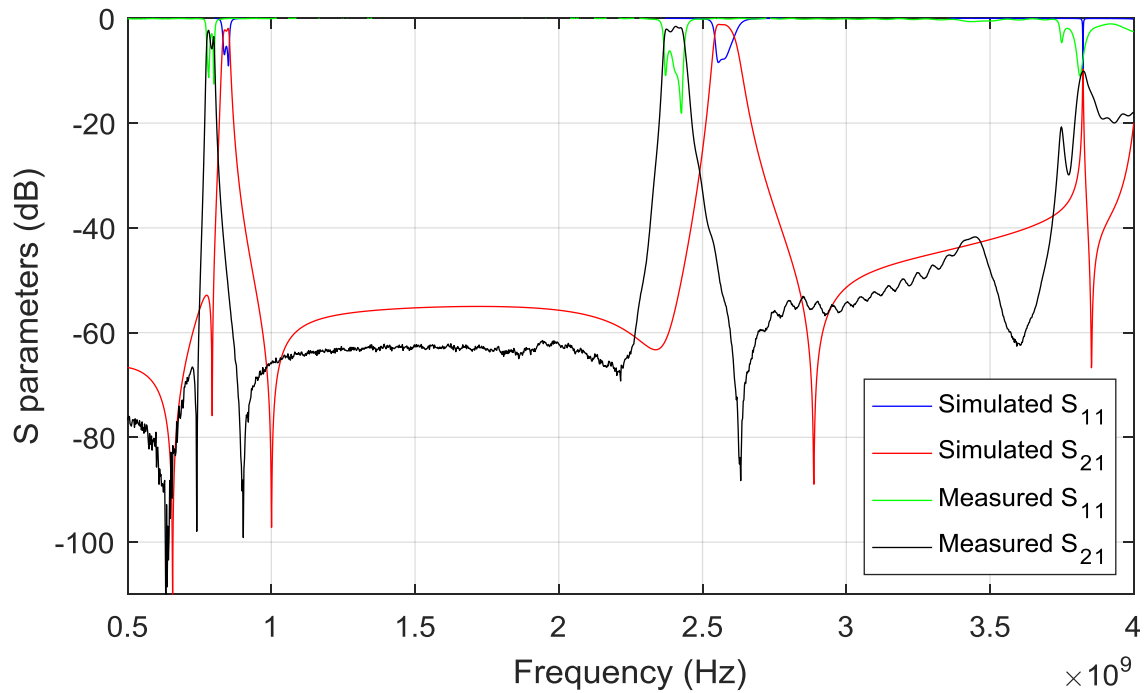


Figure 4.68 Simulated and measured frequency responses of the third order dual-band BPF using Category I non-uniform pitch helical resonators.

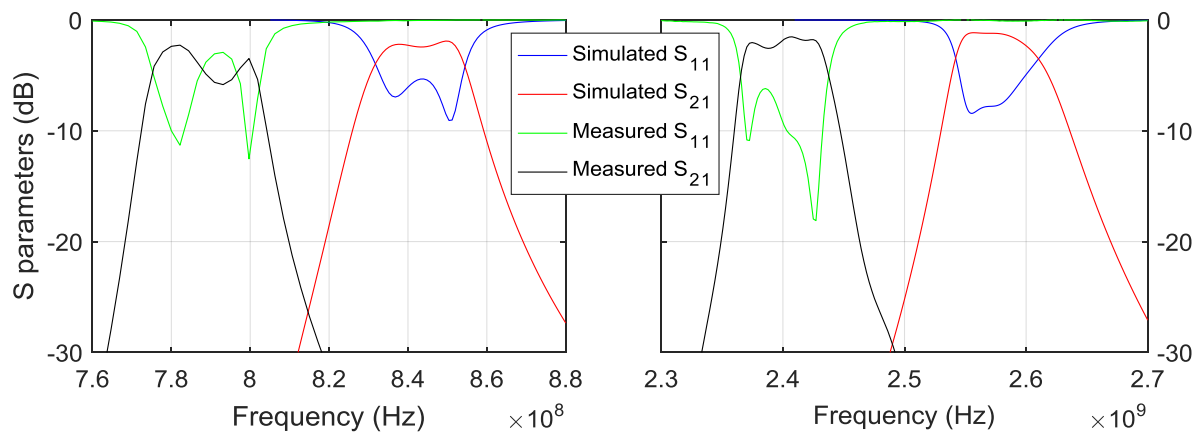


Figure 4.69 Passband frequency responses of the third order dual-band BPF.

Both the simulated and measured frequency responses show two transmission zeros at the lower stopband and one transmission zero at the higher stopband close to the first passband. The first and the third transmission zeros close to the first passband were generated by the cross coupling between input and output [30, 113-115]. The second transmission zero at the lower stopband was generated by the cross coupling between the first and the third resonators [116]. However, the simulated and measured frequency responses both show one transmission zero

at the lower stopband and one at the higher stopband close to the second passband. These two transmission zeros were generated by the input/output cross coupling. The transmission zeros at stopbands significantly improved the selectivity of filter, realising quasi-elliptic like response rather than the expected Butterworth response.

Table 4-VI summarises the filter characteristics of the design specification, optimised simulation, and measurement.

Table 4-VI Data of the third order dual-band BPF using Category I resonators.

	Design specification	Optimised simulation	Measurement
Centre frequency of the 1 st passband (MHz)	845	842.9	788.8
3-dB fractional bandwidth of the 1 st passband	2.9%	2.9%	3.3%
Insertion loss of the 1 st band	< 2 dB	1.9 dB	2.3 dB
Centre frequency of the 2 nd passband (MHz)	2600	2577.6	2401.6
3-dB fractional bandwidth of the 2 nd passband	2.9%	2.9%	3.0%
Insertion loss of the 2 nd band	< 2 dB	1.2 dB	1.5 dB
Frequency ratio	3.077	3.058	3.045

It shows that the simulation results have very good agreement with the design specification. The slight frequency discrepancy was caused by the external loading effect that influences the resonant frequencies and frequency ratio of the external coupled resonators. The measured frequency response agrees reasonably with the simulation and design specification. The winding process of the coils, twisting process of the formers, imperfect resonator tuning process, and fabrication tolerance may cause the significant passband discrepancies in centre frequency and ripple. The measured frequency response can be improved by using a one-piece copper cavity, improved mechanical design and fabrication process.

The power handling capability of the filter is estimated from simulation using (2.87) in Section 2.7, which is approximately 4.1 Watt. The break down power is so low because of the small gap between the tuning screw and the open-end of the third helix. If non-identical helical resonators were used in the filter design, in which case the resonator tuning may not be necessary, the break down power will be significantly improved.

A second order dual-band bandpass filter using Category II resonators

Design specification

A dual-band bandpass filter working in the LTE band with the second order Butterworth response is desired. The passbands are required at 815 MHz and 1740 MHz, with 3-dB fractional bandwidth (FBW) of 2.4% and 2.9%, respectively. The insertion losses of the passbands are required to be less than 2 dB.

The external Q factors (Q_e) and inter-resonator coupling coefficients (k) are obtained as

$$\begin{aligned} Q_e &= \frac{\sqrt{2}}{\text{FBW}} = \begin{bmatrix} 58.9 \\ 48.8 \end{bmatrix} \text{ at } \begin{bmatrix} 815 \\ 1740 \end{bmatrix} \text{ MHz} \\ k &= \frac{\text{FBW}}{\sqrt{2}} = \begin{bmatrix} 0.0170 \\ 0.0205 \end{bmatrix} \text{ at } \begin{bmatrix} 815 \\ 1740 \end{bmatrix} \text{ MHz} \end{aligned} \quad (4.55)$$

Resonator characterisation

The detailed design procedure of the resonator was also shown as an example of the general design procedure of non-uniform pitch helical resonators in Section 4.3.2. The characterised resonator is one of the Category II resonators, with dimensions: $S = 14.4$ mm, $d = 6.0$ mm, $d_0 = 1.0$ mm, $l_s = 5.0$ mm, $h_{\text{btm}} = 18.0$ mm, $h_{\text{top}} = 6.0$ mm, and $N_{\text{top}} = N_{\text{btm}} = 3.5$ turns.

External coupling

The external coupling structure is realised by direct tap coupling the SMA probe onto the helical resonator, with the topology shown in Figure 4.37 (a). The height of the probe (b) is the parameter controlling the external Q factors.

Figure 4.70 shows the simulated external Q factor profile. The initial value of the height of probe was obtained by substituting the required external Q factors in (4.55) to the profile, which is 4.1 mm.

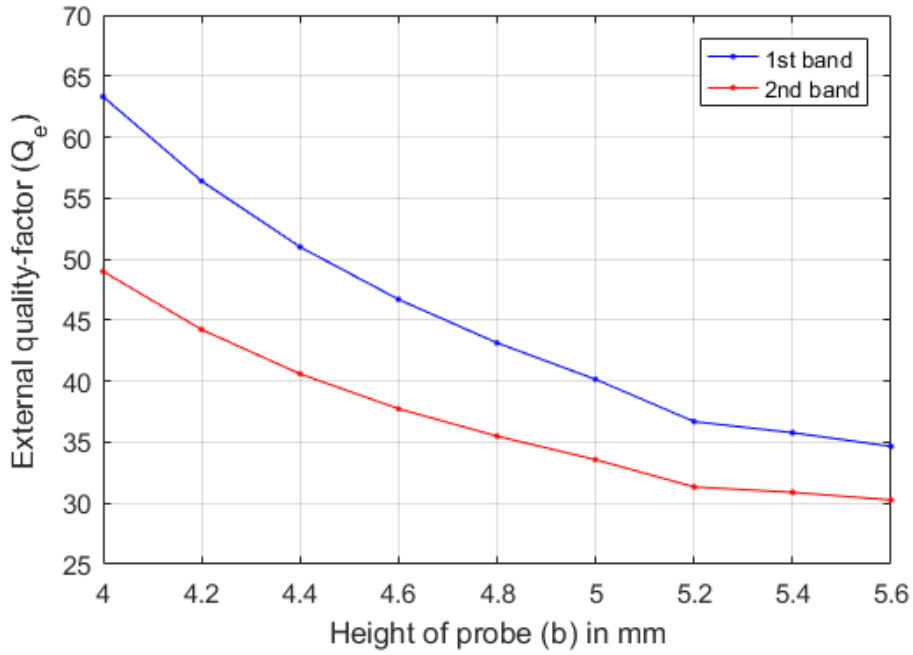


Figure 4.70 External coupling profile of the Category II non-uniform pitch helical resonator.

Inter-resonator coupling

The inter-resonator coupling of this filter uses the step-width aperture to control the coupling of each band independently, shown below.

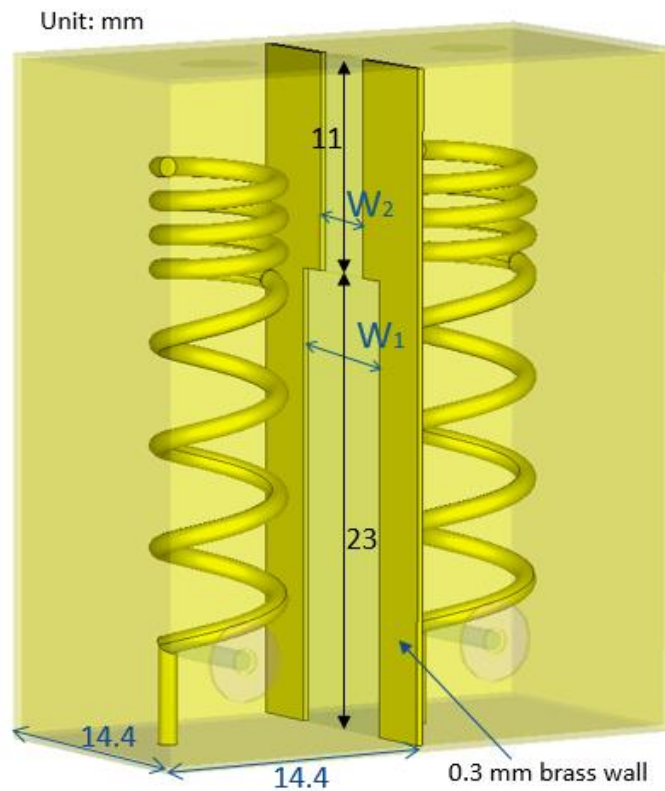


Figure 4.71 Inter-resonator coupling with step-width aperture.

Figure 4.72 and Figure 4.73 shows the simulated coupling profile of the first band and the second band, respectively.

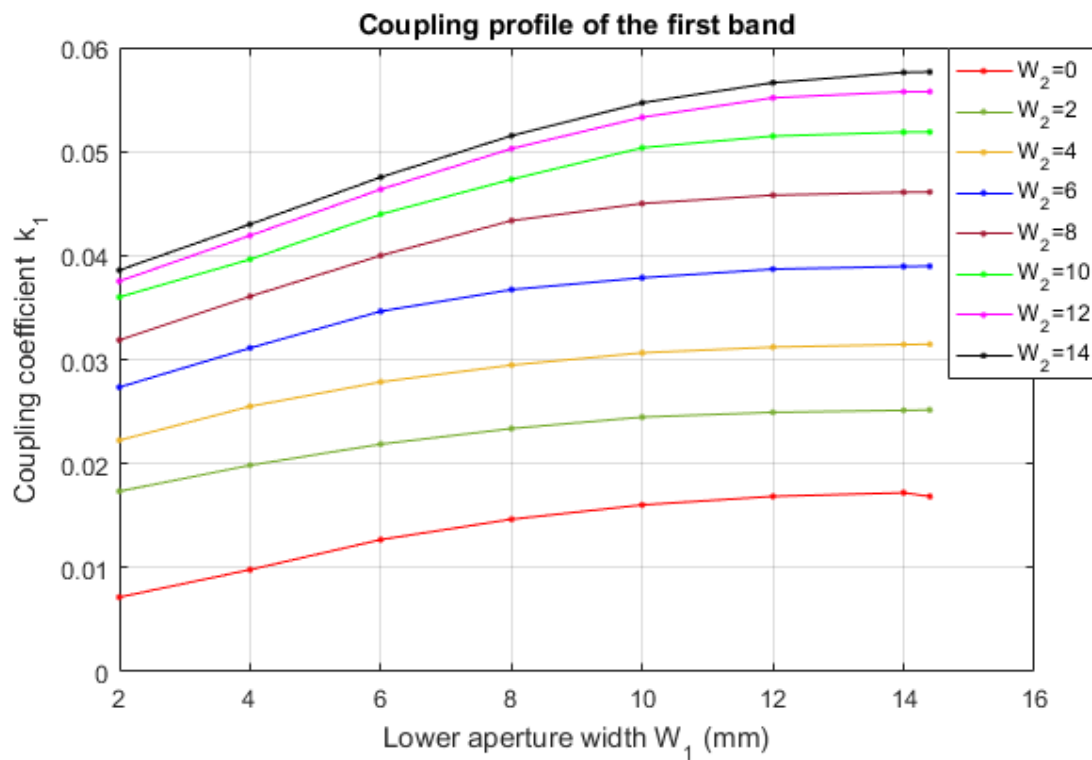


Figure 4.72 Simulated inter-resonator coupling profile of the first band.

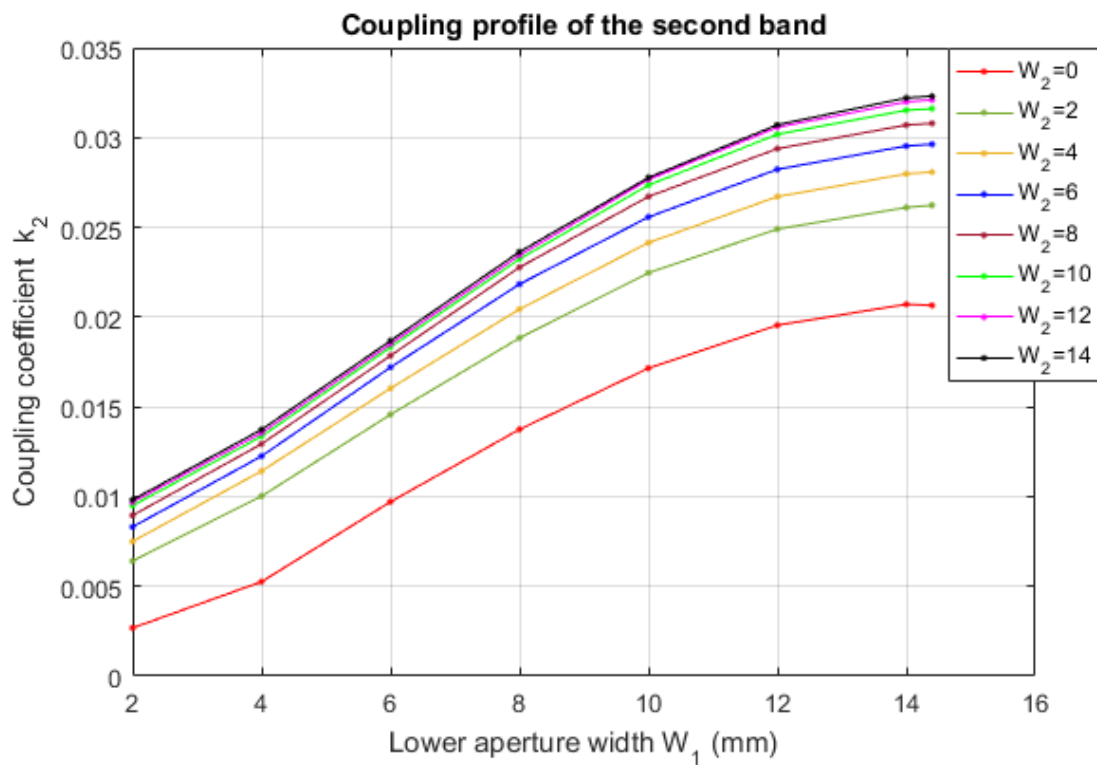


Figure 4.73 Simulated inter-resonator coupling profile of the second band.

The initial values of aperture widths (W_1 and W_2) were obtained from Figure 4.72 and Figure 4.73, which are 14.4 mm and 0 mm, respectively. This means that the upper aperture is entirely blocked by the brass wall whereas the lower aperture is fully open.

Filter implementation

The dimensions of the resonators and the coupling structures were then applied to the model of the filter in CST MW for simulation and optimisation. The height of the SMA probe was tuned to 4.0 mm. Figure 4.74 shows the filter structure and detailed dimensions.

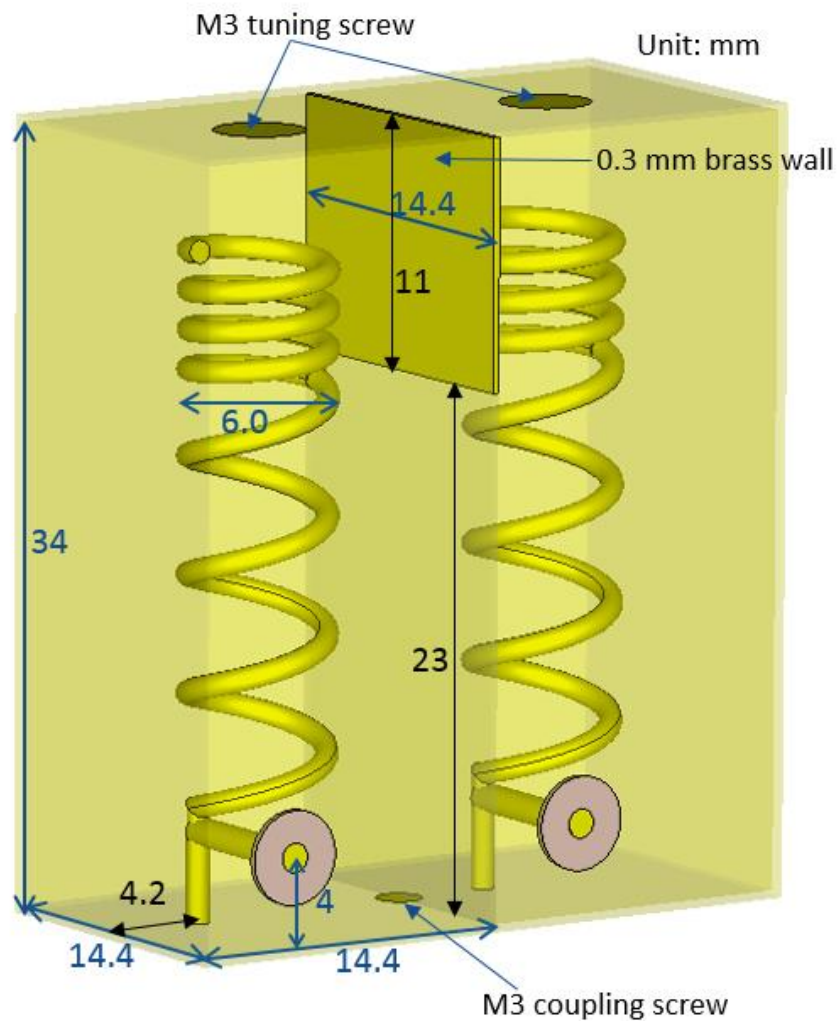


Figure 4.74 Structure and dimensions of the designed second order filter using Category II resonators.

Figure 4.75 shows the fabricated filter. Figure 4.76 shows the simulated and measured frequency response.

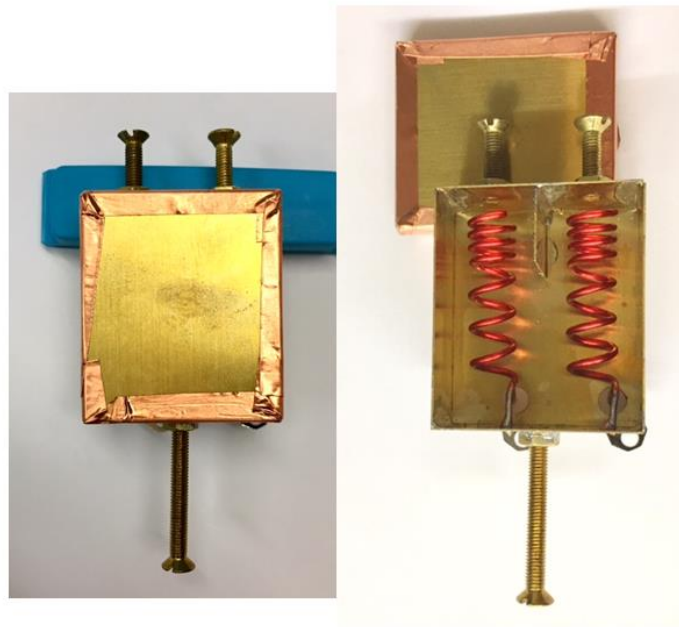


Figure 4.75 Photographs of the fabricated filter.

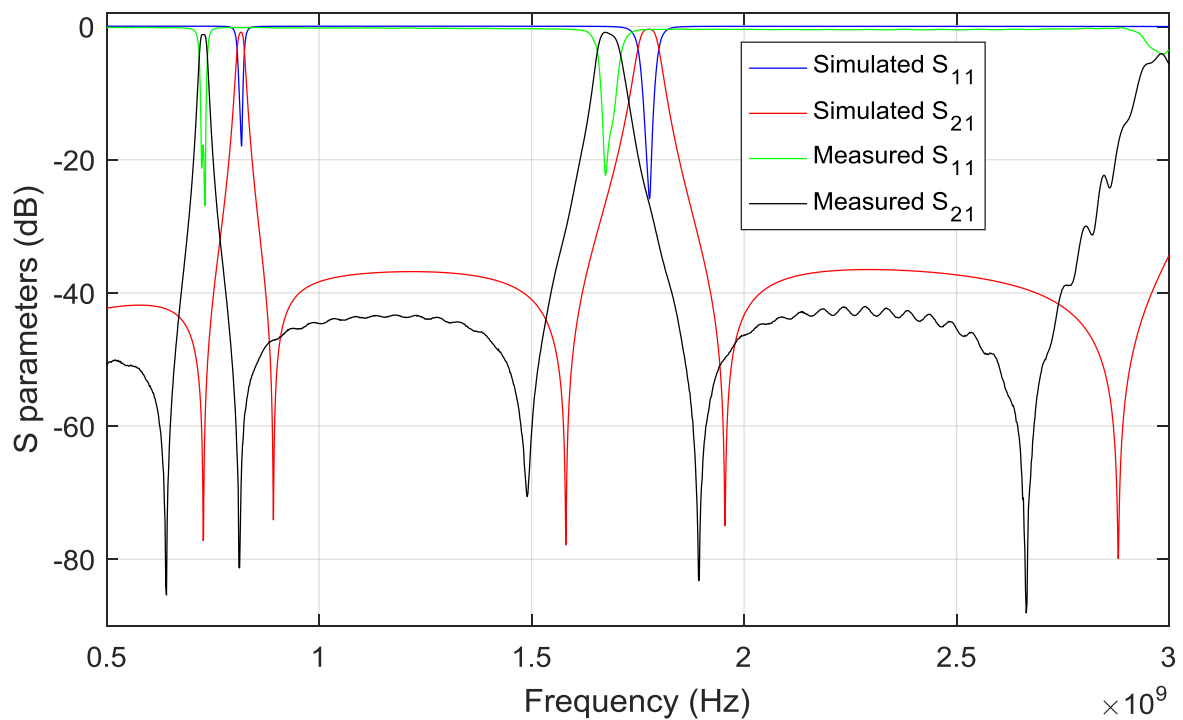


Figure 4.76 Measured and simulated frequency response of the second order dual-band bandpass filter using Category II resonators.

Figure 4.77 shows the passband frequency responses of the second order dual-band BPF. The detailed filter characteristics are shown in Table 4-VII.

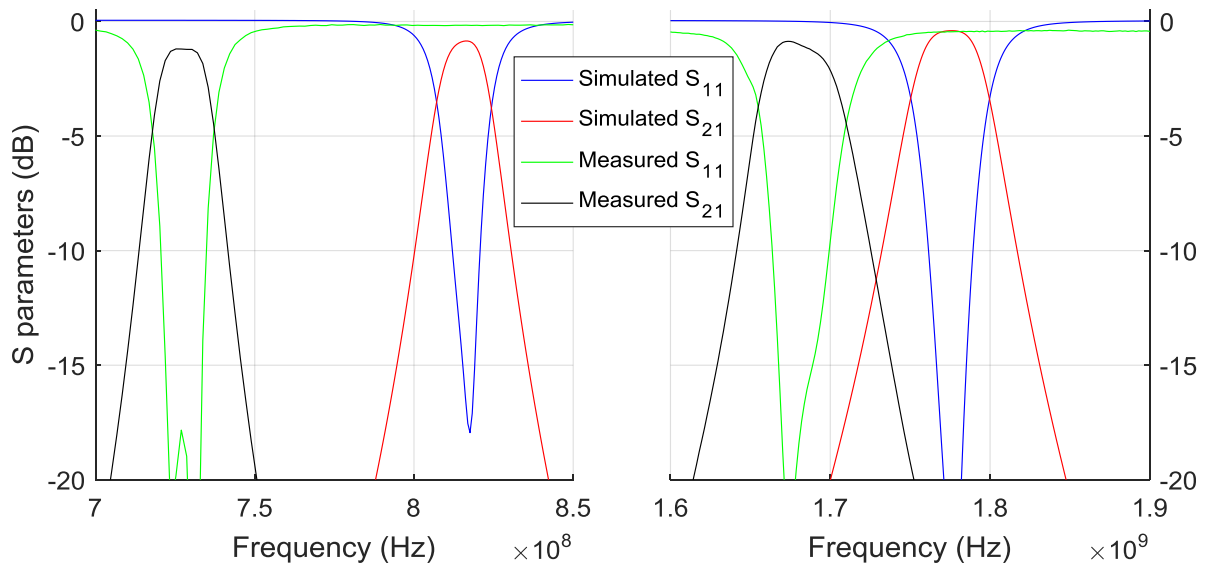


Figure 4.77 Passband frequency responses of the second order dual-band BPF using Category II resonators.

Table 4-VII Data of the second order dual-band BPF using Category II resonators.

	Design specification	Optimised simulation	Measurement
Centre frequency of the 1 st passband (MHz)	815	815.7	727.6
3-dB fractional bandwidth of the 1 st passband	2.4%	2.17%	2.56%
Insertion loss of the 1 st band	< 2 dB	0.9 dB	1.2 dB
Centre frequency of the 2 nd passband (MHz)	1740	1775.4	1680.8
3-dB fractional bandwidth of the 2 nd passband	2.9%	2.79%	3.21%
Insertion loss of the 2 nd band	< 2 dB	0.4 dB	0.9 dB
Frequency ratio	2.135	2.177	2.310

Table 4-VII shows that the simulation results have very good agreement with the design specification. The frequency ratio was increased due to the external loading effect, which also increases the resonant frequencies of the input/output resonators.

The measured frequency response have good agreement with the simulated response, apart from the frequency shift. The frequency discrepancy may be caused by the diameter and pitches change during winding process of the coils, twisting process of the formers, and other fabrication tolerances. The measured insertion losses are slight higher than the simulated losses, mainly because of the soldered brass cavity and the copper tape sealed lid. This can be improved by using a one-piece copper cavity and a soldered lid.

The simulated frequency response in Figure 4.76 has shown one transmission zero at the lower stopband, and one at the higher stopband for each band, respectively. The coupling between input and output probes generate these transmission zeros that improve the selectivity of the filter. The measured frequency response also verified the existence of these transmission zeros.

The breakdown power of the filter is estimated from EM simulation results and (2.87) in Section 2.7, which is approximately 43.8 Watt. Considering the relatively high power handling capability and compact size, this filter could be used for micro/pico base stations.

4.4 Further work and discussion

4.4.1 Coaxial SIR filters

The further work on coaxial SIR filters can be summarised as three aspects: dielectric coaxial SIR filter, tri-band bandpass filters using dual-section coaxial SIRs, and tri-band bandpass filter using tri-section coaxial SIRs.

Dielectric filled coaxial SIR

The dielectric filled coaxial resonator has been introduced in Section 2.3.3 which could further reduce the size of the coaxial SIR. The dielectric coaxial SIR has been proposed in [1], which significantly reduces the size but improves the unloaded Q factor of the resonator. However, dielectric coaxial SIR has not been applied for dual-band applications. Therefore, further research could focus on the implementation of compact dual-band bandpass filters by dielectric coaxial SIRs.

Tri-band bandpass filters using dual-section SIRs

There has not been any research showing independently controllable tri-bands of the dual-section SIR. The analysis in Section 4.2 has shown that the second spurious resonant frequency for quarter-wavelength type dual-section SIR is also related to the impedance ratio of the SIR. The equation expressing the spurious frequency ratios has shown that the dual-section SIR can be directly used to design tri-band bandpass filters that the second and third resonances satisfy the following relationship

$$f_{s2} = f_{s1} + 2f_0 \quad (4.56)$$

where f_0 , f_{s1} , and f_{s2} represents the fundamental, the first and the second spurious resonant frequencies, respectively.

Therefore, the tri-band filter using dual-section SIRs can be further investigated and designed.

Tri-band bandpass filters using tri-section coaxial SIRs

Tri-band bandpass filters have also been designed using tri-section microstrip SIRs [21, 104, 105, 117]. However, there has not any filter implemented employing tri-section coaxial SIRs. This could be another direction for the further research.

4.4.2 Non-uniform pitch helical resonator filters

In this section, the further research on non-uniform pitch helical resonator filters are illustrated. Some early results are also shown and discussed.

Dielectric loaded non-uniform pitch helical resonator

The dielectric loaded helical resonators have been studied in [118, 119] to further reduce the size of the helical resonators. The dielectric load also provides a holder for the coil, realising an anti-vibration structure. Additionally, the dielectric improves the temperature stability of the helical resonator and the filter [118]. However, the dielectric loaded helical resonator has lower unloaded Q factors due to the extra loss introduced by the dielectric load [118]. This effect can be mitigated by using low loss dielectric material.

The dielectric load could also be applied to the proposed non-uniform pitch helical resonators to further reduce resonator size, enhance the resistance to vibration, improve the temperature stability and thermal transfer, and avoid the dimension changes during the fabrication process

of helices.

The effect of the dielectric load on the resonant frequencies and frequency ratio has been studied by simulating non-uniform pitch helical resonators with air-load and dielectric load, respectively. The employed dielectric materials are PTFE and Preperm L900HF, which has dielectric constant (ϵ_r) of 2.1 and 9, respectively. The loss constants ($\tan\delta$) of PTFE and Preperm L900HF are 0.0002 and 0.0004, respectively.

Firstly, the Category I non-uniform pitch helical resonator was simulated with an air-load, a PTFE load, and a Preperm L900HF load, respectively. The dimensions of the resonator and cavity are listed: $S = 17.5$ mm, $H = 46.0$ mm, $d_{load} = d = 7.3$ mm, $d_0 = 1.0$ mm, $l_s = 5.0$ mm, $h_{top} = h_{btm} = 18.0$ mm, and $N_{btm} = 2.5$ turns, where d_{load} represents the diameter of the dielectric load.

Secondly, the air-loaded, PTFE loaded and Preperm L900HF loaded Category II non-uniform pitch helical resonators were simulated to investigate the effect of dielectric load, respectively. The dimensions are: $S = 17.5$ mm, $H = 46.0$ mm, $d_{load} = d = 7.3$ mm, $d_0 = 1.0$ mm, $l_s = 5.0$ mm, $h_{btm} = 18.0$ mm, and $N_{top} = N_{btm} = 4.5$ turns.

Figure 4.78 shows the simulated resonant frequencies (f_1 and f_2) of the Category I non-uniform pitch helical resonator with load.

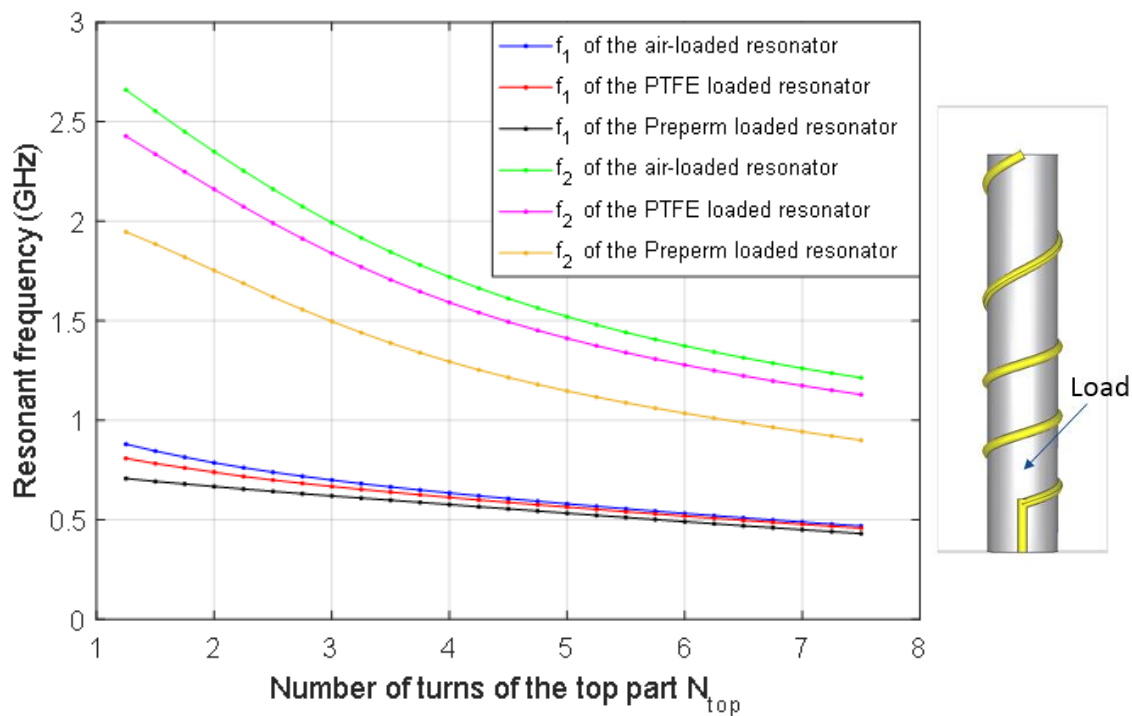


Figure 4.78 Resonant frequencies of the Category I non-uniform pitch helical resonator with load.

Figure 4.79 shows the simulated frequency ratio (f_2/f_1) of the air-loaded and dielectric loaded Category I non-uniform pitch helical resonators, respectively.

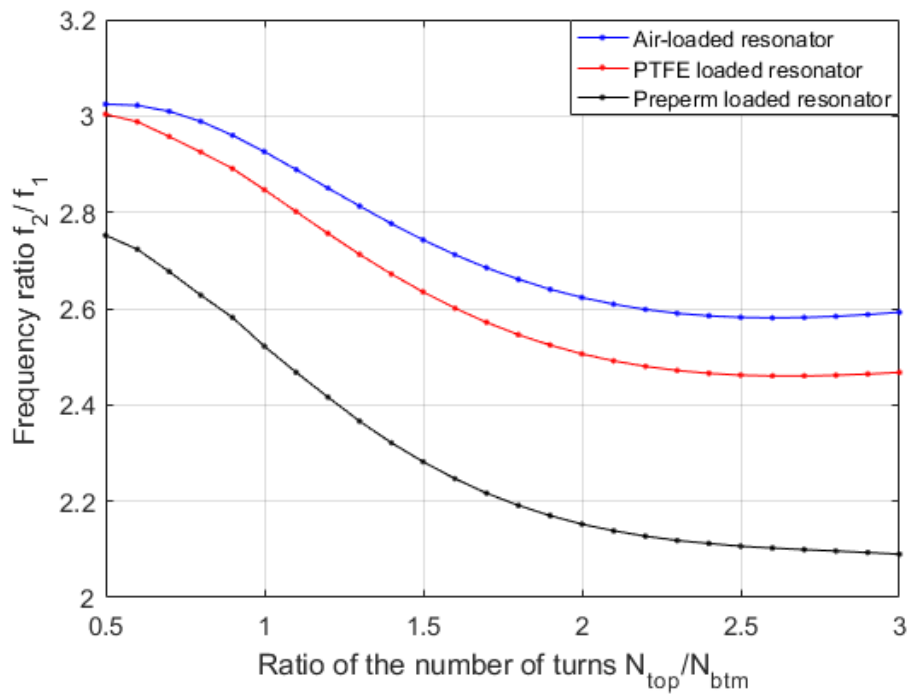


Figure 4.79 Frequency ratio of the Category I non-uniform pitch helical resonator with load.

Figure 4.80 shows the first and the second resonant frequencies (f_1 and f_2) of the Category II non-uniform pitch helical resonator with load.

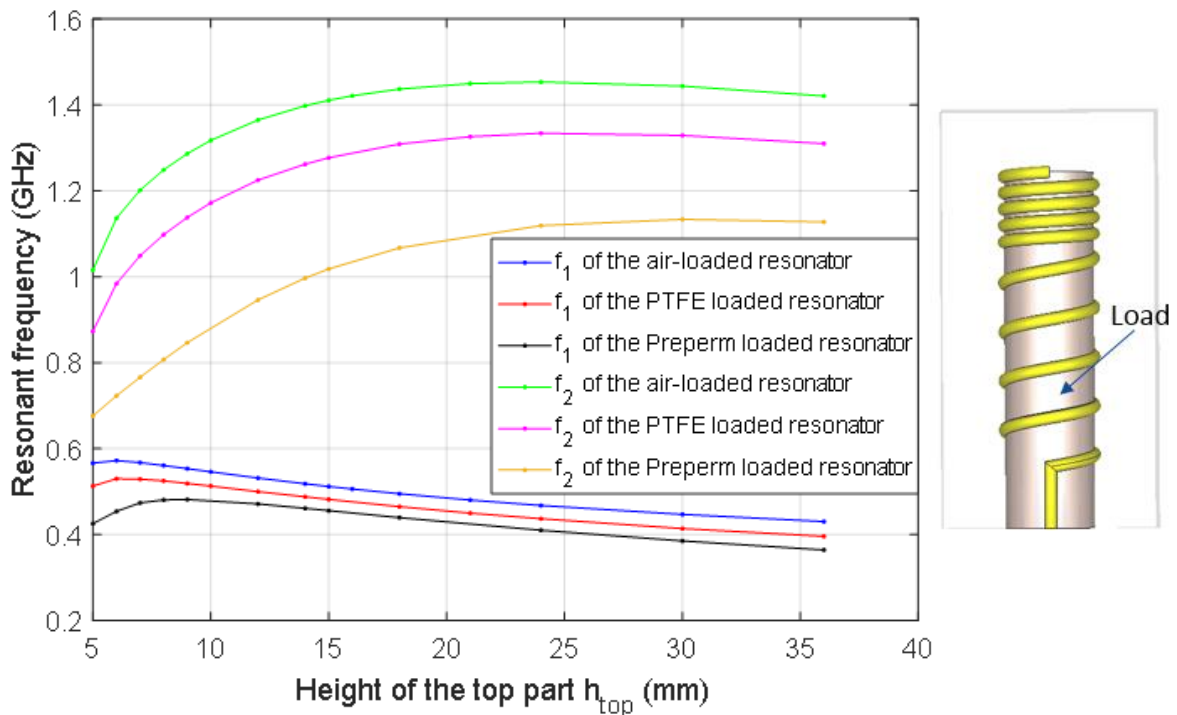


Figure 4.80 Resonant frequencies of the Category II resonator with load.

Figure 4.81 shows the frequency ratio (f_2/f_1) of the Category II non-uniform pitch helical resonator with load.

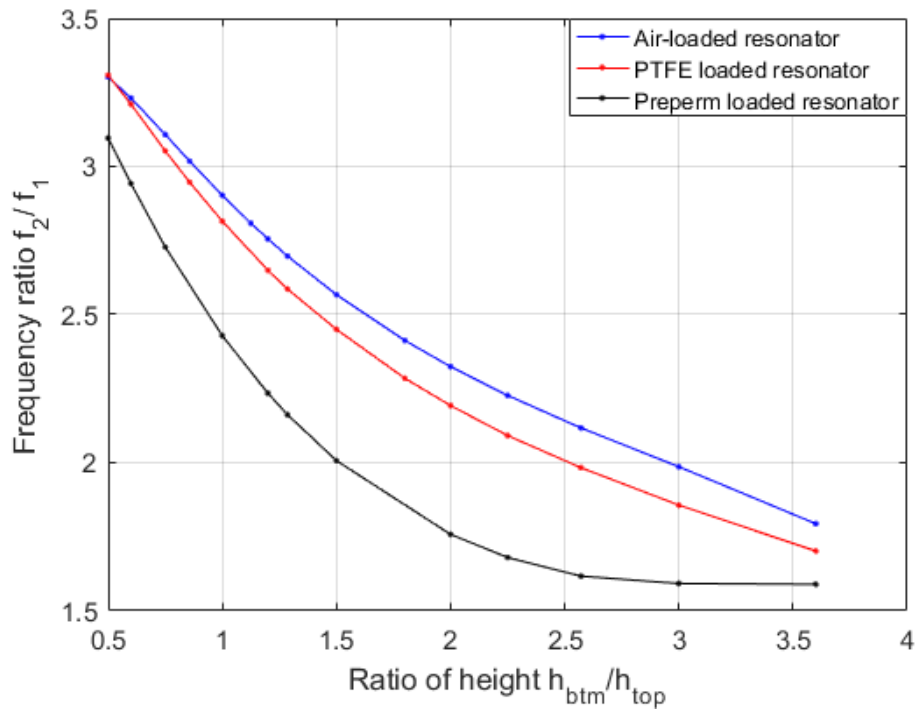


Figure 4.81 Frequency ratio of the Category II resonator with load.

It can be observed that the dielectric load lowers the first and the second resonant frequencies (f_1 and f_2) of both the Category I and Category II non-uniform pitch helical resonators, agreeing with the effect of dielectric load on uniform pitch helical resonator in [118, 119]. In order to realise the same fundamental resonant frequency with the air-loaded resonator, the diameter of the dielectric loaded non-uniform pitch helical resonator must be reduced. This implies that the dielectric load would reduce the size of non-uniform pitch helical resonator.

The dielectric load also reduces the frequency ratio (f_2/f_1) of non-uniform pitch helical resonator because the loading effect of dielectric load has more impact on the second resonant frequency than the first one. However, the frequency ratio (f_2/f_1) can still be altered in a wide range, showing that the dielectric load does not have significant influence on the dual-band characteristic of non-uniform pitch helical resonators.

The above simulation also shows that high ϵ_r material Preperm L900HF has more impact on the resonant frequencies and frequency ratio, compared to the low ϵ_r material PTFE. Thus, the resonator size could be further reduced by a high ϵ_r load.

Experimented results are required in the future. The effect of the loss constant on the unloaded

Q factors could also be studied. Moreover, the dual-band filter examples could be implemented using the dielectric loaded non-uniform pitch helical resonators.

Advanced fabrication techniques

The dielectric load with helical patterns was used to be achieved by chemical or laser etching [119]. The recent additive and differentiated manufacturing technique, known as 3D printing, has been developed and is capable of printing the dielectric support with non-uniform helical pattern. The suppliers of 3D printers have developed and expanded the available material for 3D printing, including fluoropolymer PTFE [120]. Additionally, the helix can be fabricated as metallic strip line, instead of wire [119]. A helical model made of metallic printed strip lines is shown in Figure 4.82.

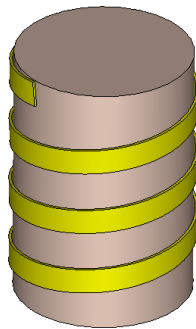


Figure 4.82 A helical resonator made of metallic printed strip lines on a dielectric load.

The helical resonator can also be fabricated as multi-layer striplines via holes on a multi-layer substrate. Figure 4.83 shows the helical resonators realised by multi-layer rectangular or circular striplines via holes. The structure is very compact, but via holes may be lossy to the resonator and thus lower the unloaded Q factors.

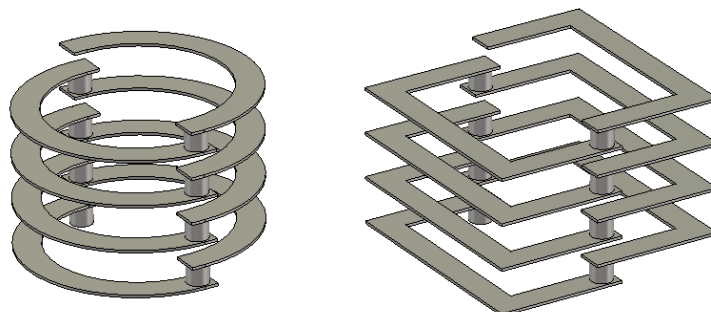


Figure 4.83 Helical resonator realised by multi-layer strip lines via hole.

The pitch length corresponds to the height of layers, thus this structure is theoretically applicable to the non-uniform pitch helical resonators. Alternatively, the using layers with equal

height but different dielectric materials can modify the pitch. Printed helical resonators has been designed and fabricated in [121] but have not been designed as a non-uniform pitch helical resonator for dual-band bandpass filters.

However, there has not been any research on the effect of these advanced fabrication techniques on the dual-band characteristics of non-uniform pitch helical resonator. The further research could focus on this subject to develop the structure and realisation of non-uniform pitch resonators for implementation of multi-band bandpass filters.

4.5 Conclusions

In conclusion, this chapter has presented two types of quarter-wavelength dual-band resonator for the implementation of dual-band bandpass filters: stepped impedance resonator and non-uniform pitch helical resonator.

Firstly, the dual-section SIR was analysed in quarter- and half-wavelength stripline models. It has shown that the fundamental and the first spurious resonant frequencies (f_0 and f_{s1}) of a SIR are independently controllable. Therefore, the SIR can be used as a dual-band resonator to realise dual-band bandpass filters. The coaxial line configuration of dual-section quarter-wavelength SIR has also been introduced. The frequency characteristics of the coaxial SIR were investigated. A quarter-wavelength coaxial SIR has been characterised and employed to design a second order dual-band BPF. A tuneable external coupling structure was proposed and utilised. The inter-resonator coupling structure was realised by an aperture with a coupling screw. This designed second order dual-band BPF has been simulated, fabricated and tested. The estimated breakdown power of the filter is 1077.9 Watt, showing capability of high power applications. The measured frequency response showed that the filter realises 3-dB FBW of 1.23% and 1.07% at 906.5 MHz and 1772.5 MHz respectively, which has a good agreement with the simulated frequency response. The discrepancies in frequency may be compensated by tuning screws of the coaxial SIRs. The mechanical design and fabrication process can be improved to reduce insertion losses, such as using a one-piece aluminium cavity and using a silver plated cavity. The frequency discrepancies could be reduced by using tuning screws or reducing the length of coaxial lines.

Secondly, this chapter showed non-uniform pitch helical resonator for the realisation of dual-band bandpass filters. Two non-uniform pitch helical resonator structures were proposed and categorised as Category I and Category II, in terms of their pitch modification method.

Category I non-uniform pitch helical resonator has equal number of turns for the top and the bottom sections, therefore, the pitch is modified by the height of each section. Category II non-uniform pitch helical resonator has equal height for the top and the bottom sections, but different number of turns for the top and the bottom sections to modify its pitch. The SIR model and the circuit model have been used to analyse the dual-band characteristics of the proposed non-uniform pitch helical resonator structures. However, the accuracy of the SIR model and circuit model is limited by the assumptions and valid range of applied equations. A new model has then been developed based on these theoretical models and simulation studies. The developed model allows more accurately predictions about the frequency ratio of the proposed non-uniform pitch helical resonator structure. It can be directly used in the general design procedure to extract the geometry non-uniform pitch helical resonator structure. The general design procedure of non-uniform pitch helical resonator was summarised and shown with a design example.

There were three resonators fabricated for each category of non-uniform pitch helical resonator. The measured frequency ratios have very good agreement with the simulated values, verifying the theoretical analysis and simulation studies on the dual-band characteristics of non-uniform pitch helical resonator. However, the measured resonant frequencies and the unloaded Q factors were smaller than the simulated values. It may be caused by the fabrication processes, including the winding process of coils, twisting process of formers, soldering loss, and imperfect shield. There was also a non-uniform pitch helical resonator fabricated in a one-piece cylindrical copper tube. The experimented results showed that using a one-piece copper cavity could significantly improve the unloaded Q factors.

The structures and topologies of external and inter-resonator couplings were characterised for the design of dual-band bandpass filters employing non-uniform pitch helical resonators. The external coupling can be realised by direct tapping or parallel plate coupling. The parallel plate coupling provides more degrees of freedom to control the external coupling of each band, compared to the direct tapping. Direct tapping to the resonator realises the strong external coupling required for the bandpass filter designs considered in the research. Furthermore, it is convenient to realise with the helical resonator, providing stable external coupling against vibration. The external coupling also causes loading effect to the non-uniform pitch helical resonator, resulting in slight higher resonant frequencies and frequency ratio. The inter-resonator coupling can be realised by uniform-width aperture or step-width aperture. Compared to the uniform-width aperture, the step-width aperture has an extra degree of freedom on

aperture width to control the inter-resonator coupling of each frequency band independently.

A second order dual-band bandpass filter with Butterworth response has been implemented using Category I non-uniform pitch helical resonators. The resonators were excited by direct tapping and coupled by a uniform-width aperture. The measured results reasonably agree with the simulation and design specifications. The insertion losses were observed low (< 3 dB) for each passband of the simulated and measured frequency responses. The power handling capability of the designed filter was estimated as 254.9 Watt, showing comparable power handling capability with coaxial and waveguide filters. Transmission zeros on either sides of the two passbands have been observed in both simulated and measured frequency responses though these were not expected in a Butterworth response. The transmission zeros are generated by the coupling between the input and output probes as the probes are closely placed in the filter structure. The presence of the transmission zeros improves the selectivity of the filter.

Another filter with a smaller resonator diameter was also fabricated and tested, showing that the frequency shift could be compensated by using smaller diameter resonators, with negligible influence on the frequency ratio. The effect of coil insulation on the frequency response was also investigated by measurement and has been found negligible.

A third order dual-band BPF with Butterworth response was further implemented using Category I non-uniform pitch helical resonators. Direct tapping structure was used for external coupling. The inter-resonator coupling structure used step-width aperture to control the couplings of each band independently. Tuning screws were necessary for the filter to compensate for the loading effect of external source/load on the input/output resonators, which has significant influence on the filter response. The breakdown power of the filter was estimated as 4.1 Watt, which is so low due to the use of tuning screws. The power handling capability can be improved by using resonators with different diameters to compensate for the external loading effect. The measured fractional bandwidth is 3.3% and 3.0% at 788.8 MHz and 2401.6 MHz, with insertion loss of 2.3 dB and 1.5 dB, respectively. The measured frequency response has reasonable agreement with the simulated frequency response. The frequency discrepancies between the measured response and simulated response were mainly caused by the increased coil diameter during the winding process of coils and the twisting process of formers. This can be eliminated by advanced fabrication process of non-uniform pitch helical resonators. The insertion loss was increased due to the soldering loss and the energy leakage of the imperfect shielding. It can be reduced by using a one-piece copper cavity

and a soldered lid. The coupling between the input and output probes, and the cross coupling between the first and the third resonators, have generated transmission zeros at the lower and higher stopbands of each passband, respectively.

Category II non-uniform pitch helical resonators were also utilised to implement a second order dual-band BPF with Butterworth response. The measured fractional bandwidth of the filter is 2.56% with the centre frequency of 727.6 MHz and 3.21% with the centre frequency of 1680.8 MHz, respectively. The measured insertion losses are 1.2 dB and 0.9 dB, respectively. The measured frequency response of the fabricated filter had a good agreement with the simulated response, apart from the frequency shift caused by the winding process of coils and twisting process of formers. The insertion losses were slightly increased because of the soldering loss and the energy leakage of the shielding. The selectivity of filters have been improved by stopband transmission zeros that were generated by the coupling between input and output probes. This filter can be further improved by using advanced resonator fabrication process, a one-piece copper cavity and a soldered lid. The breakdown power of this filter was estimated as 43.8 Watt, showing a relatively high power handling capability with such a compact size.

Finally, this chapter discussed and suggested some possible further research. The size of coaxial SIR could be further reduced by dielectric filling. The tri-band characteristics of dual-section SIR could be further studied for tri-band BPF design. In addition, the tri-section coaxial SIR could be developed and applied for tri-band bandpass filter design. The dielectric loaded non-uniform pitch helical resonator were studied. Early simulation has shown that the dielectric load could reduce the size of a non-uniform pitch helical resonator, enhance the resistance to vibration, improve the temperature stability and thermal transfer, and avoid the dimension change during helices fabrication process. The simulation results also showed that dual-band characteristic of a non-uniform pitch helical resonator would not significantly influenced by the dielectric load. Further work may also include verification of these early simulation results, investigation of the dielectric load on the unloaded Q factors of resonator, and filter implementation employing dielectric loaded non-uniform pitch helical resonators. The advanced fabrication techniques and modified structures could also be developed and applied as alternative implementation methods of non-uniform pitch helical resonators in further work, such as metallic printed helical stripline with 3D printed dielectric load, and multi-layer circular or square strip lines via holes.

Chapter 5: Conclusions

Modern wireless communication systems require dual-band bandpass filters to support communication standards that operate in multiple frequency bands. The use of dual-band bandpass filter reduces the required number of components, miniaturising the overall wireless communication system. The purpose of the research presented in the thesis is to develop synthesis procedures, and to characterise resonator and coupling structures for the realisation of dual-band bandpass filters working at microwave frequencies. This chapter summarises the achievements of the presented research, followed by the conclusions of the thesis.

5.1 Achievements

The objectives set for the research have been successfully completed. The achievements of the research are described below, in terms of importance.

The most significant achievement of the presented research is the investigation on non-uniform pitch helical resonator. This is a very compact resonator first proposed by the author for dual-band bandpass filter design. Two non-uniform pitch helical resonator structures were proposed for dual-band bandpass filter design. They were categorised in terms of the pitch modification. Category I non-uniform pitch helical resonator has equal number of turns for the top and the bottom sections, therefore, the pitch is modified by the height of each section. Category II non-uniform pitch helical resonator has equal height for the top and the bottom sections, but different number of turns for the top and the bottom sections to modify its pitch. Their resonant frequencies were analysed using the SIR model and the circuit model.

A new model has been developed to describe the dual-band characteristics of non-uniform pitch helical resonator structure, based on the above theoretical models and simulation studies. The developed model allows more accurately predictions about the frequency ratio of the proposed non-uniform pitch helical resonator structure. It can be used to extract the geometry of non-uniform pitch helical resonator structure from the design specifications. Several non-uniform pitch helical resonators were fabricated to verify the dual-band characteristics of the proposed helical resonator structure. The experimented results of the fabricated helical resonators have verified the above models, simulation and design procedures of non-uniform pitch helical resonators.

Suitable coupling structures and topologies for the realisation of external and inter-resonator

couplings for non-uniform pitch helical resonators have been investigated and characterised. For the external coupling, two well-known structures have been investigated: direct tapping and parallel plate coupling. Direct tapping to the resonator realises the strong external coupling required for the bandpass filter designs considered in the research. Furthermore, it is convenient to realise with the helical resonator, providing stable external coupling against vibration. Thus, direct tapping has been selected for the filters implemented in this research work. For the inter-resonator coupling, the uniform-width aperture and the step-width aperture have been investigated. Between them, the step-width aperture can independently control the coupling of each band, with the extra degree of freedom on aperture width. Both these structures have been applied for the filters realised in the research.

Three dual-band bandpass filters with Butterworth frequency characteristics have been designed, implemented and tested, based on the resonators and coupling structures described above. Different non-uniform pitch helical resonator structures and inter-resonator coupling structures were used in the filter designs. Direct tapping was used for all the external couplings of the filter designs. The measured frequency responses of the filters reasonably agree with the simulation and design specifications. Transmission zeros have been observed in the simulated and measured frequency responses of these filters.

A second order dual-band bandpass filter has been designed utilising two Category I non-uniform pitch helical resonators. The resonators were excited by direct tapping and coupled by a uniform-width aperture. The measured results reasonably agree with the simulation and design specifications. The insertion losses were observed low (< 3 dB) for each passband of the simulated and measured frequency responses. The power handling capability of the designed filter was estimated as 254.9 Watt, showing the capability of high power. Transmission zeros on either sides of the two passbands have been observed in both simulated and measured frequency responses though these were not expected in a Butterworth response. The transmission zeros are generated by the coupling between the input and output probes as the probes are closely placed in the filter structure. The presence of the transmission zeros improves the selectivity of the filter. The measured results also showed that the frequency discrepancies with simulation could be reduced by decreasing the diameter of the employed resonators. The effect of coil insulation has also been found negligible according to the measured results.

A third order dual-band bandpass filter has also been designed and implemented using Category I non-uniform pitch helical resonators. The resonators were excited by direct tapping, and

coupled by step-width apertures to control the couplings of each band independently. The measured frequency response agrees reasonably with the simulated frequency response. The simulated and measured insertion losses are observed low (< 3 dB) for each passband. The estimated breakdown power of the filter was as low as 4.1 Watt, due to the use of tuning screws that compensate for the external loading effect. Nevertheless, the power handling capability could be improved by a different method that compensate for the loading effect using resonators with different diameters. The coupling between input and output, and the cross coupling between the first and the third resonators, generated transmission zeros for both the simulated and measured responses at lower and higher stopbands of each passband. These transmission zeros have significantly improved the selectivity of the filter.

A second order dual-band bandpass filter was designed using Category II non-uniform pitch helical resonators. The resonators were excited by direct tapping and coupled by a step-width aperture. The filter was simulated, fabricated and tested. The measured frequency response has good agreement with the simulation, apart from the frequency discrepancies. The simulated and measured insertion losses are observed low (< 2 dB). The estimated breakdown power of the filter was 43.8 Watt, showing relatively high power handling capability compared to planar filters. Transmission zeros were observed at lower and higher stopbands for both the simulated and measured frequency responses. The transmission zeros were generated due to the coupling between the input and output probes. Although they were not expected in a Butterworth frequency response, they improved the selectivity of the filter.

These filter designs showed that non-uniform pitch helical resonators can be used to realise compact microwave dual-band bandpass filters with low insertion losses and relatively high power handling capabilities.

The next achievement is the development on coaxial SIRs for the realisation of dual-band bandpass filters. The dual-band characteristics of coaxial SIR has been analysed. In addition, the external and inter-resonator coupling structures for coaxial SIR have been characterised. A tuneable external coupling structure was proposed, providing the ability of tuning for practical design. The inter-resonator coupling structure was realised by an aperture with a coupling screw, to control the coupling of each band simultaneously. A second order dual-band bandpass filter with Butterworth frequency response has been designed, simulated, fabricated and tested, based on the resonators and coupling structures described above. The measurement showed a Butterworth frequency response with low insertion loss, which is very close to the simulation. The estimated breakdown power of the filter is 1077.9 Watt, showing that the filter is capable

of high power operation.

The other achievement is the design and implementation of dual-band bandpass filters based on the synthesis procedure. An eighth order and a sixth order dual-band bandpass filters were designed based on coupling matrices that were synthesised using Newton-Raphson method.

The eighth order filter was realised by microstrip square open-loop resonators. The microstrip square open-loop resonator, external and inter-resonator coupling structures were characterised for the filter design. However, neither the simulation and measurement of the designed filter showed a reasonable frequency response, due to the low unloaded Q factor of the employed microstrip resonators. The passbands are narrow and high selective due to the assumptions made in the synthesis procedures, thus the desired filter requires high Q resonators. The effect of finite Q on resonators for the realisation of narrow dual-band bandpass filters has been investigated. The simulation studies and measured results revealed that unloaded quality factor of the resonator is required to be ten times greater than the quality factor of each passband in order to realise the narrow passbands.

Therefore, high Q resonators were used for the design of a sixth order dual-band bandpass filter. This filter was realised by $TE_{01\delta}$ mode quarter cylindrical dielectric resonators that provide unloaded Q of 2120 with a very compact size. The resonator structure, suitable external and inter-resonator coupling structures have been investigated and characterised for the filter design. A curved probe was proposed for the realisation of magnetic type external coupling structure. Two types of aperture were utilised to realise the magnetic inter-resonator couplings. The designed filter is very compact and the simulation showed that it has relatively high power handling capability of 95 Watt. The simulated frequency response showed two narrow passbands agreeing with the design specifications. However, there were significant discrepancies between the simulated and measured frequency responses. The investigation based on simulation studies showed that the discrepancies might be caused by the epoxy used for resonator fixture. The epoxy influenced the $TE_{01\delta}$ resonant mode as well as introduces losses, results in measured frequency discrepancies and increased insertion losses.

The results of these two filters were not to a satisfactory level, as the filters were designed at the early stages of the research. The author has analysed and explained the effects that might cause the discrepancies from design specifications. The solid understanding of Q factors, characterisation of resonators, external and inter-resonator couplings, external loading effect, and filter design process have also been acknowledged.

5.2 Conclusions and further work

Chapter 2 reviewed some basic concepts, elements, theories and tools for microwave filter design. The general design process of a microwave filter was reviewed, starting from the specifications to the realisation of a microwave filter. Secondly, the definition of Q factor of a resonator was introduced, as a narrowband filter has specific requirements for the unloaded Q factor of the employed resonators. Since resonator is a key component of filters, various types of resonator were presented in Chapter 2. The lumped element circuit was used as the equivalent circuit of the distributed element resonator for analysis and simulation of microwave filters. The basic structures and characteristics of coaxial, microstrip, dielectric and helical resonators were also introduced. These types of resonator were modified and then used in the subsequent chapters for the implementation of dual-band bandpass filters.

The frequency response of a filter is not only characterised by the resonator, but also the external and inter-resonator couplings. Chapter 2 reviewed the coupled resonator circuits, including the external coupling between resonator and input/output, and the coupling between resonators. The external quality factor and the inter-resonator coupling coefficients can be extracted from the simulated or measured frequency responses of the corresponding circuit.

Simulation plays a significant role in filter design. The commercial software utilised in this research program includes MATLAB, Keysight ADS, and CST MW. MATLAB was used for the computation, data processing and result visualisation. Keysight ADS was used to simulate the equivalent circuit of filter for analysis. CST MW was used for the full-wave EM simulation in the presented research. Two solvers of CST MW used in the research are: the Eigenmode Solver and the Frequency Domain Solver. The Eigenmode Solver in CST MW provides fields distribution and resonant modes of the resonator or filter. The Frequency Domain Solver in CST MW shows the simulated S-parameters of the resonator or filter. In Chapter 2, these tools were introduced and discussed about their general functions and solvers that involved in the design of bandpass filter.

The main measurements of resonator, coupling, and filter is measuring the S-parameters. S-parameters give the frequency characteristics of resonator or filter, and allow extracting the unloaded Q factor of resonator, external Q factor, and inter-resonator coupling coefficient. The extractions of the above parameters have been reviewed in this chapter. Since it is difficult and destructive to measure the power handling capability, Chapter 2 reviewed a method to estimate the peak breakdown power of a microwave filter by analysing the simulated electric fields and

group delays of the filter. This method was used to estimate the breakdown powers of the designed filters in the research.

The research on the development of dual-passband filters in the thesis can be categorised as two design approaches.

One of the design approaches focuses on the synthesis procedures of filter design, as presented in Chapter 3. This approach utilises the fundamental resonant frequency of the resonators to form the dual-passband of the filter. The dual-passband response is synthesised by placing finite frequency transmission zeros within the single-passband of a filter to split into dual passbands. It produces narrow passbands close to each other but with high selectivity due to the transmission zeros in the stopband between the desirable passbands.

Chapter 3 has reviewed a frequency transformation technique that generates a symmetrical dual-passband response from a normalised low pass prototype response. A coupling matrix can be synthesised from the transformed dual-passband response and then used for the realisation of the dual-band bandpass filter. The synthesis procedures of coupling matrix have been described, starting from the frequency response to reduction of coupling matrix. They are briefly summarised in the following paragraph.

The coupling matrix can be derived from an orthogonal matrix and a diagonal matrix. The first and the last rows of the orthogonal matrix and the elements of the diagonal matrix can be generated from the admittance matrix of the circuit, which are derived from the given frequency responses of the network. The other rows of the orthogonal matrix can be constructed by Gram-Schmidt or Newton-Raphson procedure.

The design procedure of dual-passband response synthesis for filter realisation has also been shown. An eighth order dual-band bandpass filter has been designed. The frequency transformation technique was applied to a four-pole generalised Chebyshev response to generate the dual-passband frequency response. The coupling matrix of the eighth order filter was synthesised using the Newton-Raphson method. Microstrip square open-loop resonators were characterised for the filter design, as well as the external and inter-resonator coupling structures. However, neither the EM simulation nor the measurement showed reasonable frequency responses because of the low unloaded Q factor of employed resonators. The passbands are narrow and high selective due to the assumptions made in the synthesis procedures, thus the desired filter requires high Q resonators. The simulation studies on finite Q suggested that the resonator for implementation of narrow dual-band bandpass filters must

have an unloaded Q factor at least ten times the loaded Q from the filter response. As this was one of the first filters designed by the author, the key effect of finite Q on resonator was not fully considered. Therefore, high Q resonators were used for the design of a sixth order dual-band bandpass filter.

The sixth order dual-band bandpass filter was designed and implemented using TE_{018} mode quarter cylindrical dielectric resonators that have an unloaded Q of 2120. The dual-passband frequency response was obtained by applying the frequency transformation to a three-pole generalised Chebyshev response. The coupling matrix of this filter was also synthesised from the transformed frequency response using the Newton-Raphson method. The resonator structure, suitable external and inter-resonator coupling structures have been investigated and characterised for the filter design. A curved probe was proposed for the realisation of magnetic type external coupling structure. Two types of aperture were utilised to realise the magnetic inter-resonator couplings. The EM simulation showed two passbands at 2.565 GHz and 2.630 GHz, with 3-dB bandwidth of 28 MHz and 35 MHz, respectively. The EM simulation agrees closely with the simulation of equivalent circuit, the synthesised response, and the design specifications. This designed filter is very compact, saving more than 75% volume when compared with a filter using coaxial resonators or traditional cylindrical dielectric resonators. Moreover, it has good thermal resistance since the heat of the DRs can be directly transferred to the Aluminium cavity. The breakdown power of the filter was estimated from EM simulation, approximately 95 Watt. It showed a relatively high power handling capability in comparison with planar filters. However, the measured frequency response of the filter was hardly a reasonable bandpass filter response. The study on EM simulation showed that the epoxy losses and the imperfect TE_{018} resonant mode might cause the discrepancies between simulation and measurement. The filter could be further improved by using silver-plated DRs, DRs fabricated in appropriate moulds, one-piece external coupling probes, tuning screws for resonators and inter-resonator couplings, and smaller fabrication tolerance.

The limitations of the synthesis method for the realisation of dual-band bandpass filters have been discussed. This synthesis method is only applicable for the passbands spread across a narrow frequency band since the couplings are assumed frequency invariant. Additionally, it has a requirement for the unloaded Q factor of resonators. High Q resonators are suggested when designing narrow dual-band bandpass filters. The loading effect of external coupling on the resonator is also neglected in the synthesis procedures, thus the tuning and optimisation process are required in filter implementation. Since only the fundamental resonant frequency

of resonators is employed to realise the dual-passband response, the resonator must be designed carefully to avoid any possible interference or overlap with its spurious resonance.

The further work includes developing this synthesis method with the consideration of the above limitation and requirement, and improving the designed sixth order dual-band bandpass filter with silver plated dielectric resonators.

The second design approach of dual-band bandpass filter is based on the resonators with two resonant modes operating at different frequencies to form the dual passbands. Chapter 4 presented two types of dual-band resonator with quarter-wavelength implementations for dual-band bandpass filters: stepped impedance resonator and non-uniform pitch helical resonator.

Chapter 4 reviewed the microstrip line configuration of dual-section SIR and analysed its dual-band characteristics, showing that the second resonant frequency of a stepped impedance resonator varies against the impedance ratio of the non-uniform microstrip line while the overall length of the microstrip line determines the fundamental resonant frequency. This chapter also analysed the dual-band characteristics of the dual-section SIR in coaxial line configuration.

A second order dual-band bandpass filter was designed, simulated, fabricated using the characterised coaxial SIRs. An external coupling structure was proposed with the flexibility of tuning. The inter-resonator coupling structure was realised by an aperture with a coupling screw to control the coupling of each band simultaneously. The measured response showed 3-dB fractional bandwidth of 1.23 % and 1.07 % at 906.5 MHz and 1772.5 MHz respectively, agreeing closely with the simulated response and the design specifications. The measured insertion losses are 2.7 dB and 2.8 dB for the passbands, respectively. There was a spurious band generated by the coupling screw at 2.1 GHz. The measured filter response could be further improved by using a one-piece Aluminium cavity, silver plated cavity, and resonator tuning screws. The estimated breakdown power of this filter is 1077.9 Watt, showing the capability of high power applications.

The coaxial SIR could be further studied with dielectric filling to further reduce its size. The tri-band characteristics of dual-section SIR could be further studied for tri-band BPF design. In addition, the tri-section coaxial SIR could be developed and applied for tri-band bandpass filter design.

Chapter 4 then presented non-uniform pitch helical resonators for the realisation of dual-band bandpass filters. Two non-uniform pitch helical resonator structures were proposed and

categorised as Category I and Category II, in terms of their pitch modification method. The pitches of Category I and Category II non-uniform pitch helical resonators are modified by the number of turns and the height, respectively. The resonant frequencies of these resonator structures were then analysed by the SIR model and the circuit model. A new model has been developed based on these theoretical models and simulation studies. It provides more accurate predictions on the frequency ratios of Category I and II non-uniform pitch helical resonators. The developed model can be used to extract the geometry of non-uniform pitch helical resonator structures from the design specifications. The general design procedure of non-uniform pitch helical resonator was then presented with a resonator design example.

The dual-band characteristics of non-uniform pitch helical resonator were verified by experimented results of fabricated resonators. The measured frequency ratios of the fabricated resonators are very close to the simulated frequency ratios. However, the fabrication processes, including the winding process of coils, twisting process of the formers, soldering loss, and imperfect shield, caused small offsets for the measured resonant frequencies and unloaded Q factors. The experimented results of a non-uniform pitch helical resonator fabricated in a one-piece cylindrical copper cavity have shown that using a one-piece cavity could improve the unloaded Q factors.

The structures and topologies of the external and inter-resonator couplings for non-uniform pitch helical resonators have then been characterised for filter design. The external coupling can be realised by direct tapping or parallel plate coupling. The parallel plate coupling provides more degrees of freedom to control the external coupling of each band, compared to the direct tapping. However, it is difficult to realise the short air-gap between the coil and the parallel plate, when strong external coupling is required. On the contrary, direct tapping could provide strong external coupling with ease of realisation. Additionally, it provides a stable external coupling structure against the coil vibration. It is also found that there is loading effect on the external coupled non-uniform pitch helical resonator, resulting in increased resonant frequencies and frequency ratio. The inter-resonator coupling structure can be realised by a uniform-width aperture or a step-width aperture. The step-width aperture has an extra degree of freedom on the width, independently realising the inter-resonator coupling coefficient of each frequency band.

A second order dual-band BPF with Butterworth response was designed using Category I non-uniform pitch helical resonators. The external and inter-resonator coupling structures were realised by direct tapping and a uniform-width aperture, respectively. The filter was simulated,

fabricated, and tested. The measured frequency response showed reasonable agreement but with a frequency shift, compared to the simulated response. The insertion losses were observed low (< 3 dB) for each passband of the simulated and measured frequency responses. The estimated breakdown power of this filter is 254.9 Watt, showing a comparable power with coaxial and waveguide filters. Transmission zeros on either sides of the two passbands have been observed in both simulated and measured frequency responses though these were not expected in Butterworth response. They are generated by the coupling between the input and output probes as the probes are closely placed in the filter structure, improving the selectivity of the filter. Another filter with a smaller resonator diameter was also fabricated and tested, showing that the frequency shift could be compensated by using smaller diameter resonators, with negligible influence on the frequency ratio. The effect of coil insulation on the frequency response was also investigated by measurement and it turned out negligible.

A third order dual-band bandpass filter with Butterworth response was also designed and implemented using Category I non-uniform pitch helical resonators. Direct tapping structure was used for external coupling. Step-width apertures were used for the inter-resonator couplings of the filter. Tuning screws were necessary for the filter to reduce the loading effect on the filter response. The measured fractional bandwidth is 3.3% and 3.0% at 788.8 MHz and 2401.6 MHz, with insertion loss of 2.3 dB and 1.5 dB, respectively. The measured frequency response reasonably agrees with the simulated response and the design specifications, but has increased insertion loss and frequency discrepancies. The frequency discrepancies between the measured response and simulated response were mainly caused by the increased coil diameter during the winding process of coils and the twisting process of formers. This can be eliminated by advanced fabrication process of non-uniform pitch helical resonators. The insertion loss was increased due to the soldering loss and the energy leakage of the imperfect shielding. It can be reduced by using a one-piece copper cavity. The coupling between the input and output probes, and the cross coupling between the first and the third resonators, have generated transmission zeros at the lower and higher stopbands of each passband, respectively. Due to the utilisation of tuning screws, the estimated breakdown power of this filter is just 4.1 Watt. The power handling capability can be improved by using resonators with different diameters to compensate for the external loading effect, instead of using tuning screws.

Additionally, Category II non-uniform pitch helical resonators were utilised for design and implementation of a second order dual-band bandpass filter with Butterworth response. The measured fractional bandwidth of the filter is 2.56% with the centre frequency of 727.6 MHz

and 3.21% with the centre frequency of 1680.8 MHz, respectively. The measured insertion losses are 1.2 dB and 0.9 dB, respectively. The measured frequency response of the fabricated filter had a good agreement with the simulated response, apart from the frequency shift caused by the winding process of coils and twisting process of formers. The insertion losses were slightly increased because of the soldering loss and the energy leakage of the shielding. The selectivity of filters have been improved by stopband transmission zeros that were generated by the coupling between input and output probes. This filter can be further improved by using advanced resonator fabrication process, a one-piece copper cavity and a soldered lid. The breakdown power of this filter was estimated as 43.8 Watt, showing a relatively high power handling capability with such a compact size.

The dielectric loaded non-uniform pitch helical resonator were further studied as a part of future work. The early simulation results have shown that the dielectric load could reduce the size of a non-uniform pitch helical resonator, with slight influence on its dual-band characteristics. In addition, the dielectric load enhances the resistance to vibration, improves the temperature stability and thermal transfer, and avoids the dimension change during helical resonator fabrication. Further work also includes investigating the dielectric load on the unloaded Q factors, fabricating and testing dielectric loaded non-uniform pitch helical resonators, and filter implementation utilising dielectric loaded non-uniform pitch helical resonators. The advanced fabrication techniques and modified structures could also be developed and applied as alternative implementation methods of non-uniform pitch helical resonators in further work, such as metallic printed helical stripline with 3D printed dielectric load, and multi-layer circular or square strip lines via holes.

Abbreviations

ADS	Advanced Design System
BPF	Bandpass Filter
BSF	Band-stop Filter
CST MW	Computational Software Technology Microwave Studio
CPW	Coplanar Waveguide
DR	Dielectric Resonator
EM	Electromagnetic
EMC	Electromagnetic Compatibility
FBW	Fractional Bandwidth
FEM	Finite Element Method
GPS	Global Positioning System
GSM	Global System for Mobile Communication
HEM	Hybrid Electromagnetic
IEEE	Institute of Electrical and Electronics Engineers
LTE	Long Term Evolution
MATLAB	Matrix Laboratory
MMIC	Monolithic Microwave Integrated Circuit
MoM	Method of Moments
PEC	Perfect Electric Conductor
RF	Radio Frequency
SAW	Surface Acoustic Wave
SIR	Stepped Impedance Resonator
TEM	Transverse Electromagnetic
TE	Transverse Electric

TM	Transverse Magnetic
UHF	Ultra High Frequency
VHF	Very High Frequency
WLAN	Wireless Local Area Network

References

- [1] M. Makimoto and S. Yamashita, *Microwave resonators and filters for wireless communication: theory, design and application* vol. 4: Springer, 2001.
- [2] J. S. Hong and M. J. Lancaster, *Microstrip filters for RF/microwave applications* vol. 167: John Wiley & Sons, 2004.
- [3] I. C. Hunter and Institution of Engineering and Technology., *Theory and design of microwave filters*. London: Institution of Engineering and Technology, 2001.
- [4] A comparison of Passive Filters and Active Filters. (2014, 17/06/2017). Available: http://www.schematica.com/active_filter_resources/comparison_of_active_and_passive_filters.html
- [5] *Spectrum*. (2017). Available: <https://www.ofcom.org.uk/spectrum/information>
- [6] IEEE Standards Association, "IEEE 802.11n: Wireless LAN Medium Access Control and Physical Layer Specifications," 2012.
- [7] C. Chu-Yu and H. Cheng-Ying, "A simple and effective method for microstrip dual-band filters design," *IEEE Microwave and Wireless Components Letters*, vol. 16, pp. 246-248, 2006.
- [8] T. Lin-Chuan and H. Ching-Wen, "Dual-band bandpass filters using equal-length coupled-serial-shunted lines and Z-transform technique," *IEEE Transactions on Microwave Theory and Techniques*, vol. 52, pp. 1111-1117, 2004.
- [9] J. Lee and K. Sarabandi, "Synthesizing microwave resonator filters," *IEEE Microwave Magazine*, vol. 10, pp. 57-65, 2009.
- [10] J. Lee and K. Sarabandi, "A Synthesis Method for Dual-Passband Microwave Filters," *Microwave Theory and Techniques, IEEE Transactions on*, vol. 55, pp. 1163-1170, 2007.
- [11] J. Lee and K. Sarabandi, "Design of Triple-Passband Microwave Filters Using Frequency Transformations," *IEEE Transactions on Microwave Theory and Techniques*, vol. 56, pp. 187-193, 2008.
- [12] A. E. Atia and A. E. Williams, "Narrow-Bandpass Waveguide Filters," *IEEE Transactions on Microwave Theory and Techniques*, vol. 20, pp. 258-265, 1972.

- [13] A. E. Atia, A. E. Williams, and R. W. Newcomb, "Narrow-band multiple-coupled cavity synthesis," *Circuits and Systems, IEEE Transactions on*, vol. 21, pp. 649-655, 1974.
- [14] R. J. Cameron, "General coupling matrix synthesis methods for Chebyshev filtering functions," *Microwave Theory and Techniques, IEEE Transactions on*, vol. 47, pp. 433-442, 1999.
- [15] K. Yi-Ting, L. Jhe-Ching, L. Ching-Ku, and C. Chi-Yang, "New Multiband Coupling Matrix Synthesis Technique and Its Microstrip Implementation," *Microwave Theory and Techniques, IEEE Transactions on*, vol. 58, pp. 1840-1850, 2010.
- [16] X. Shang, Y. Wang, G. L. Nicholson, and M. J. Lancaster, "Design of multiple-passband filters using coupling matrix optimisation," *IET Microwaves, Antennas & Propagation*, vol. 6, pp. 24-30, 2012.
- [17] J. Chen, B. Wu, L. W. Jiang, and C. H. Liang, "Design of dual-band substrate integrated waveguide filter using frequency transformation method," in *2010 International Conference on Microwave and Millimeter Wave Technology*, 2010, pp. 1286-1289.
- [18] G. Xuehui, M. Zhewang, C. Peng, L. Guohui, Y. Kobayashi, T. Anada, "A dual-band bandpass filter synthesized by using frequency transformation and circuit conversion technique," in *2005 Asia-Pacific Microwave Conference Proceedings*, 2005, pp. 4-8.
- [19] R. N. Gajaweera, "Coupling Matrix Generation for Narrowband Dual- and Triple-passband Filters," unpublished, 2012.
- [20] M. Makimoto and S. Yamashita, "Bandpass Filters Using Parallel Coupled Stripline Stepped Impedance Resonators," *IEEE Transactions on Microwave Theory and Techniques*, vol. 28, pp. 1413-1417, 1980.
- [21] C. Yu-Cheng, H. Yi-Huan, L. Ching-Her, and I. G. H. Chung, "Tri-band microstrip BPF design using tri-section SIRs," in *2007 IEEE Antennas and Propagation Society International Symposium*, 2007, pp. 3113-3116.
- [22] Q. X. Chu and F. C. Chen, "A Compact Dual-Band Bandpass Filter Using Meandering Stepped Impedance Resonators," *IEEE Microwave and Wireless Components Letters*, vol. 18, pp. 320-322, 2008.
- [23] S. Zhang and L. Zhu, "Compact microstrip dual-band bandpass filter with quarter-wavelength stepped impedance resonators," in *2013 IEEE International Wireless Symposium (IWS)*, 2013, pp. 1-4.

- [24] R. Zhang and R. R. Mansour, "Dual-Band Dielectric-Resonator Filters," *IEEE Transactions on Microwave Theory and Techniques*, vol. 57, pp. 1760-1766, 2009.
- [25] M. Memarian and R. R. Mansour, "Dual-band half-cut dielectric resonator filters," in *Microwave Conference, 2009. EuMC 2009. European*, 2009, pp. 555-558.
- [26] G. Zhou, "A non-uniform pitch dual band helix antenna," in *Antennas and Propagation Society International Symposium, 2000. IEEE*, 2000, pp. 274-277 vol.1.
- [27] I. Egorov and Y. Zhinong, "A non-uniform helical antenna for dual-band cellular phones," in *IEEE Antennas and Propagation Society International Symposium. Transmitting Waves of Progress to the Next Millennium. 2000 Digest. Held in conjunction with: USNC National Radio Science Meeting (C, 2000*, pp. 652-655 vol.2.)
- [28] W.-K. Chen, *Passive, active, and digital filters*. Boca Raton, FL: CRC Press, 2009.
- [29] G. Macchiarella, "Accurate synthesis of inline prototype filters using cascaded triplet and quadruplet sections," *IEEE Transactions on Microwave Theory and Techniques*, vol. 50, pp. 1779-1783, 2002.
- [30] R. N. Gajaweera and L. F. Lind, "Coupling Matrix Synthesis for Asymmetric Filter Topologies," in *2008 IEEE MTT-S International Microwave Workshop Series on Art of Miniaturizing RF and Microwave Passive Components*, 2008, pp. 79-82.
- [31] R. N. Gajaweera and L. F. Lind, "Coupling matrix extraction for cascaded-triplet (CT) topology," *IEEE Transactions on Microwave Theory and Techniques*, vol. 52, pp. 768-772, 2004.
- [32] D. Kajfez and P. Guillon, *Dielectric resonators*. Dedham, MA: Artech House, 1986.
- [33] J. M. Golio, *The RF and microwave handbook*. Boca Raton, Fla.: CRC Press, 2001.
- [34] D. Kajfez. (1999, 16/01/2014). Q factor measurements, analog and digital. Available: <http://www.engineering.olemiss.edu/~eedarko/experience/rfqmeas2b.pdf>
- [35] R. R. Mansour, "Filter technologies for wireless base stations," *IEEE Microwave Magazine*, vol. 5, pp. 68-74, Mar 2004.
- [36] E. J. Denlinger, "Losses of microstrip lines," *IEEE Transactions on Microwave Theory Techniques*, vol. 28, pp. 513-522, 1980.
- [37] E. O. Hammerstad, "Equations for Microstrip Circuit Design," in *Microwave Conference, 1975. 5th European*, 1975, pp. 268-272.

- [38] T. C. Edwards and M. B. Steer, *Foundations of interconnect and microstrip design* vol. 3: John Wiley, 2000.
- [39] R. Garg, I. J. Bahl, and M. Bozzi, *Microstrip lines and slotlines*: Artech House, 2013.
- [40] Y. Wu, R. Gajaweera, and J. Everard, "Dual-band bandpass filter using TE₀₁ mode quarter cylindrical dielectric resonators," in *2016 Asia-Pacific Microwave Conference (APMC)*, 2016, pp. 1-4.
- [41] P. Guillon, J. P. Balabaud, and Y. Garault, "TM/sub 01p/ Tubular and Cylindrical Dielectric Resonator Mode," in *1981 IEEE MTT-S International Microwave Symposium Digest*, 1981, pp. 163-166.
- [42] J. X. Chen, J. Li, Y. Zhan, W. Qin, J. Shi, and Z. H. Bao, "Design of Balanced and Balun Filters Using Dual-Mode Cross-Shaped Dielectric Resonators," *IEEE Transactions on Microwave Theory and Techniques*, vol. 65, pp. 1226-1234, 2017.
- [43] M. Hoft, "Y-Shape Dielectric Dual-Mode Resonator," *IEEE Transactions on Microwave Theory and Techniques*, vol. 56, pp. 3066-3071, 2008.
- [44] W. Chi and K. A. Zaki, "Analysis of power handling capacity of band pass filters," in *2001 IEEE MTT-S International Microwave Symposium Digest (Cat. No.01CH37157)*, 2001, pp. 1611-1614 vol.3.
- [45] S. B. Cohn, "Microwave Bandpass Filters Containing High-Q Dielectric Resonators," *IEEE Transactions on Microwave Theory and Techniques*, vol. 16, pp. 218-227, 1968.
- [46] S. W. Chen and K. A. Zaki, "Dielectric ring resonators loaded in waveguide and on substrate," *IEEE Transactions on Microwave Theory and Techniques*, vol. 39, pp. 2069-2076, 1991.
- [47] M. Memarian and R. R. Mansour, "Dual-mode half-cut dielectric resonator filters," in *2009 IEEE MTT-S International Microwave Symposium Digest*, 2009, pp. 1465-1468.
- [48] M. O. Moraes, F. R. Borges, and H. E. Hernández-Figueroa, "Efficient technique for suppression of undesirable modes in dielectric resonator filters," in *2009 SBMO/IEEE MTT-S International Microwave and Optoelectronics Conference (IMOC)*, 2009, pp. 775-777.
- [49] M. Memarian and R. R. Mansour, "Quad-mode and dual-mode dielectric resonator filters," *IEEE Transactions on Microwave Theory and Techniques*, vol. 57, pp. 3418-

3426, 2009.

- [50] Y. Zhan, J. X. Chen, W. Qin, J. Li, and Z. H. Bao, "Spurious-Free Differential Bandpass Filter Using Hybrid Dielectric and Coaxial Resonators," *IEEE Microwave and Wireless Components Letters*, vol. 26, pp. 574-576, 2016.
- [51] Y. Wu, R. Gajaweera, and J. Everard, "Dual-band bandpass filter using helical resonators," in *2016 46th European Microwave Conference (EuMC)*, 2016, pp. 237-240.
- [52] A. Zverev and H. Blinchikoff, "Realization of a Filter with Helical Components," *IRE Transactions on Component Parts*, vol. 8, pp. 99-110, 1961.
- [53] N. P. Spencer, "A Review of the Design of Helical Resonator Filters," *Journal of the Institution of Electronic and Radio Engineers*, vol. 57, pp. 213-220, Sep-Oct 1987.
- [54] S. Sensiper, "Electromagnetic Wave Propagation on Helical Structures (A Review and Survey of Recent Progress)," *Proceedings of the IRE*, vol. 43, pp. 149-161, 1955.
- [55] D. Miley and J. Beyer, "Field Analysis of Helical Resonators with Constant-Bandwidth Filter Application," *IEEE Transactions on Parts, Materials and Packaging*, vol. 5, pp. 127-132, 1969.
- [56] S. Sensiper and Massachusetts Institute of Technology. Research Laboratory of Electronics., *Electromagnetic wave propagation on helical conductors*. Cambridge, Mass.: Massachusetts Institute of Technology, Research Laboratory of Electronics, 1951.
- [57] L. Stark, *The lower modes of a concentric line having a helical inner conductor*. Cambridge, Mass., M.I.T. Lincoln Laboratory, 1953.
- [58] J. M. Miller, "Electrical Oscillations in Antennas and Inductance Coils," *Proceedings of the Institute of Radio Engineers*, vol. 7, pp. 299-326, 1919.
- [59] J. S. Stone, *Theory of Wireless Telegraphy* vol. 3. St Louis: Transaction of International Electrical Congress, 1904.
- [60] W. W. Macalpine and R. O. Schildknecht, "Coaxial Resonators with Helical Inner Conductor," *Proceedings of the IRE*, vol. 47, pp. 2099-2105, 1959.
- [61] C. Wang, H. W. Yao, K. A. Zajum, and R. Mansour, "Mixed modes cylindrical planar dielectric resonator filters with rectangular enclosure," in *Proceedings of 1995 IEEE MTT-S International Microwave Symposium*, 1995, pp. 501-504 vol.2.

- [62] H. W. Yao, C. Wang, and A. K. Zaki, "Quarter wavelength ceramic combline filters," *IEEE Transactions on Microwave Theory and Techniques*, vol. 44, pp. 2673-2679, 1996.
- [63] J. S. Hong and M. J. Lancaster, "Couplings of microstrip square open-loop resonators for cross-coupled planar microwave filters," *Microwave Theory and Techniques, IEEE Transactions on*, vol. 44, pp. 2099-2109, 1996.
- [64] H. Jia-Sheng and M. J. Lancaster, "Cross-coupled microstrip hairpin-resonator filters," *IEEE Transactions on Microwave Theory and Techniques*, vol. 46, pp. 118-122, 1998.
- [65] H. Jia-Sheng, M. J. Lancaster, D. Jedamzik, and R. B. Greed, "On the development of superconducting microstrip filters for mobile communications applications," *IEEE Transactions on Microwave Theory and Techniques*, vol. 47, pp. 1656-1663, 1999.
- [66] J. S. Hong, "Couplings of asynchronously tuned coupled microwave resonators," *Microwaves, Antennas and Propagation, IEE Proceedings*, vol. 147, pp. 354-358, 2000.
- [67] C. G. Montgomery, R. H. Dicke, and E. M. Purcell, *Principle of Microwave Circuits*. New York: McGraw-Hill, 1948.
- [68] S. Sheng and Z. Lei, "Compact dual-band microstrip bandpass filter without external feeds," *IEEE Microwave and Wireless Components Letters*, vol. 15, pp. 644-646, 2005.
- [69] Keysight Technologies, 2016. *Advanced Design System - Brochure*. Available: <http://literature.cdn.keysight.com/litweb/pdf/5988-3326EN.pdf?id=921864>
- [70] Agilent Technology, *Circuit Design Cookbook 2.0*. (2012, 20/05/2017).
- [71] Computer Simulation Technology, *Eigenmode Solver*. (2017). Available: <https://www.cst.com/products/cstmws/Solvers/EigenmodeSolver>
- [72] Keysight Technologies, "W2341EP Momentum G2 Element," in *ADS Simulation Elements*, 2016.
- [73] Keysight Technologies, "W2342EP Keysight FEM Simulator Element," in *ADS Simulation Elements*, 2016.
- [74] V. K. Aatre, *Network theory and filter design*. New York: Wiley, 1981.
- [75] A. Woode and J. Petit, "Diagnostic investigations into the multipactor effect, Susceptibility zone measurements and parameters affecting a discharge," Noordwijk, Netherlands., 1989.

- [76] Computer Simulation Technology, Five-Section Microstrip Hairpin-Filter, 2014.
- [77] Computer Simulation Technology, "MultiPhysics-Analysis: Power Handling, Multipaction and Corona-Analysis applied to MW-Filters," in *MW & RF Filter Workshop*, 2014.
- [78] G. L. Matthaei, E. M. T. Jones, and L. Young, *Microwave filters, impedance-matching networks, and coupling structures*. Dedham, Artech House, 1980.
- [79] J. Everard, *Fundamentals of RF circuit design with low noise oscillators*. New York: John Wiley., 2001.
- [80] M. Yu, "Power-handling capability for RF filters," *IEEE Microwave Magazine*, vol. 8, pp. 88-97, 2007.
- [81] *MATLAB: The Language of Technical Computing*. (2017). Available: <https://uk.mathworks.com/products/matlab.html>
- [82] R. Woo, "Final report on RF voltage breakdown in coaxial transmission lines," Jet Propulsion Lab, CA, U.S.A.1970.
- [83] A. R. Harish and R. J. Cameron, "Peak voltage analysis in high power microwave filters," in *IEE Colloquium on Microwave Filters and Multiplexers (Ref. No. 2000/117)*, 2000, pp. 10/1-10/5.
- [84] C. Ernst, V. Postoyalko, and N. G. Khan, "Relationship between group delay and stored energy in microwave filters," *IEEE Transactions on Microwave Theory and Techniques*, vol. 49, pp. 192-196, 2001.
- [85] G. Macchiarella and S. Tamiazzo, "A design technique for symmetric dualband filters," in *Microwave Symposium Digest, 2005 IEEE MTT-S International*, 2005, pp. 4-8.
- [86] G. Macchiarella and S. Tamiazzo, "Design techniques for dual-passband filters," *IEEE Transactions on Microwave Theory and Techniques*, vol. 53, pp. 3265-3271, 2005.
- [87] A. I. Zverev, *Handbook of filter synthesis*. New York: John Wiley and Sons Inc., 1967.
- [88] G. Pfitzenmaier, "Synthesis and Realization of Narrow-Band Canonical Microwave Bandpass Filters Exhibiting Linear Phase and Transmission Zeros," *Microwave Theory and Techniques, IEEE Transactions on*, vol. 30, pp. 1300-1311, 1982.
- [89] J. Helszajn, *Synthesis of Lumped Elements, Distributed and Planar Filters*. London: McGraw-Hill., 1990.

- [90] J. Rhodes and M. Ismail, "Cascade Synthesis of Selective Linear-Phase Filters," *IEEE Transactions on Circuit Theory*, vol. 19, pp. 183-189, 1972.
- [91] H. C. Bell, "Canonical Asymmetric Coupled-Resonator Filters," *IEEE Transactions on Microwave Theory and Techniques*, vol. 30, pp. 1335-1340, 1982.
- [92] J. S. Hong and M. J. Lancaster, "Design of highly selective microstrip bandpass filters with a single pair of attenuation poles at finite frequencies," *Microwave Theory and Techniques, IEEE Transactions on*, vol. 48, pp. 1098-1107, 2000.
- [93] Q. X. Chu and H. Wang, "A Compact Open-Loop Filter With Mixed Electric and Magnetic Coupling," *IEEE Transactions on Microwave Theory and Techniques*, vol. 56, pp. 431-439, 2008.
- [94] C. Karpuz and A. Gorur, "Dual-mode dual-band microstrip filters," in *Microwave Conference, 2009. EuMC 2009. European*, 2009, pp. 105-108.
- [95] J. S. Hong and M. J. Lancaster, "Development of new microstrip pseudo-interdigital bandpass filters," *IEEE Microwave and Guided Wave Letters*, vol. 5, pp. 261-263, 1995.
- [96] M. Zhou, X. Tang, and F. Xiao, "Compact Dual Band Bandpass Filter Using Novel E-Type Resonators With Controllable Bandwidths," *IEEE Microwave and Wireless Components Letters*, vol. 18, pp. 779-781, 2008.
- [97] F. Wei, P. Y. Qin, Y. J. Guo, and X. W. Shi, "Design of multi-band bandpass filters based on stub loaded stepped-impedance resonator with defected microstrip structure," *IET Microwaves, Antennas & Propagation*, vol. 10, pp. 230-236, 2016.
- [98] J. D. Rhodes and I. H. Zabalawi, "Synthesis of Symmetrical Dual Mode in-Line Prototype Networks," *International Journal of Circuit Theory and Applications*, vol. 8, pp. 145-160, 1980.
- [99] T. Nishikawa, K. Wakino, K. Tsunoda, and T. Nishikawa, "Dielectric High-Power Bandpass Filter Using Quarter-Cut TE₀₁₈/ Image Resonator for Cellular Base Stations," *Microwave Theory and Techniques, IEEE Transactions on*, vol. 35, pp. 1150-1155, 1987.
- [100] A. A. Kishk and H. Wei, "Size-Reduction Method for Dielectric-Resonator Antennas," *Antennas and Propagation Magazine, IEEE*, vol. 53, pp. 26-38, 2011.
- [101] M. J. Akhtar, L. Feher, and M. Thumm, "Measurement of dielectric constant and loss

- tangent of epoxy resins using a waveguide approach," in *2006 IEEE Antennas and Propagation Society International Symposium*, 2006, pp. 3179-3182.
- [102] H. Heng-Tung, Y. Hui-Wen, K. A. Zaki, and A. E. Atia, "Computer-aided diagnosis and tuning of cascaded coupled resonators filters," *IEEE Transactions on Microwave Theory and Techniques*, vol. 50, pp. 1137-1145, 2002.
- [103] S. Chang, Y. Jeng, and J. Chen, "Dual-band step-impedance bandpass filter for multimode wireless LANs," *Electronics Letters*, vol. 40, pp. 38-39, 2004.
- [104] C. I. G. Hsu, C. H. Lee, and Y. H. Hsieh, "Tri-Band Bandpass Filter With Sharp Passband Skirts Designed Using Tri-Section SIRs," *IEEE Microwave and Wireless Components Letters*, vol. 18, pp. 19-21, 2008.
- [105] Q. X. Chu and X. M. Lin, "Advanced triple-band bandpass filter using tri-section SIR," *Electronics Letters*, vol. 44, pp. 295-296, 2008.
- [106] F.-C. Chen, J.-M. Qiu, S.-W. Wong, and Q.-X. Chu, "Dual-Band Coaxial Cavity Bandpass Filter With Helical Feeding Structure and Mixed Coupling," *IEEE Microwave and Wireless Components Letters*, vol. 25, pp. 31-33, 2015.
- [107] Y. Wu, R. Gajaweera, and J. Everard, "Dual-band bandpass filter using coaxial Stepped Impedance Resonators," in *2016 International Conference for Students on Applied Engineering (ICSAE)*, 2016, pp. 181-185.
- [108] Q. X. Chu and Z. C. Zhang, "Dual-Band Helical Filters Based on Nonuniform Pitch Helical Resonators," *IEEE Transactions on Microwave Theory and Techniques*, vol. 65, pp. 2886-2892, 2017.
- [109] M. Sagawa, M. Makimoto, and S. Yamashita, "Geometrical structures and fundamental characteristics of microwave stepped-impedance resonators," *IEEE Transactions on Microwave Theory and Techniques*, vol. 45, pp. 1078-1085, 1997.
- [110] M. Sagawa, M. Makimoto, and S. Yamashita, "A Design Method of Bandpass Filters Using Dielectric-Filled Coaxial Resonators (Short Papers)," *IEEE Transactions on Microwave Theory and Techniques*, vol. 33, pp. 152-157, 1985.
- [111] K. D. Xu and J. Ai, "Compact microstrip quad-band bandpass filter using stub-loaded SIRs," in *2015 Asia-Pacific Microwave Conference (APMC)*, 2015, pp. 1-3.
- [112] E. Doumanis, G. Goussetis, and S. A. Kosmopoulos, "Inline Interdigital Pseudo-Elliptic

- Helical Resonator Filters," *IEEE Microwave and Wireless Components Letters*, vol. 21, pp. 400-402, Aug 2011.
- [113] W. Feng, L. Gu, W. Che, and H. Chen, "Tri-band microstrip bandpass filter using input/output cross coupling," *International Journal of Electronics*, vol. 101, pp. 405-409, 2014/03/04 2014.
- [114] H. Shaman and J. S. Hong, "Input and Output Cross-Coupled Wideband Bandpass Filter," *IEEE Transactions on Microwave Theory and Techniques*, vol. 55, pp. 2562-2568, 2007.
- [115] M. Ohira and Z. Ma, "A Parameter-Extraction Method for Microwave Transversal Resonator Array Bandpass Filters With Direct Source/Load Coupling," *IEEE Transactions on Microwave Theory and Techniques*, vol. 61, pp. 1801-1811, 2013.
- [116] J. T. Kuo, C. L. Hsu, and E. Shih, "Compact Planar Quasi-Elliptic Function Filter With Inline Stepped-Impedance Resonators," *IEEE Transactions on Microwave Theory and Techniques*, vol. 55, pp. 1747-1755, 2007.
- [117] X. B. Wei, P. Wang, P. Gao, Z. Q. Xu, J. X. Liao, L. Jin, "Compact Tri-Band Bandpass Filter Using Open Stub Loaded Tri-Section Stepped Impedance Resonator," *IEEE Microwave and Wireless Components Letters*, vol. 24, pp. 512-514, 2014.
- [118] S. J. Fiedziuszko and R. S. Kwok, "Novel helical resonator filter structures," in *1998 IEEE MTT-S International Microwave Symposium Digest (Cat. No.98CH36192)*, 1998, pp. 1323-1326 vol.3.
- [119] R. S. Kwok and S. J. Fiedziuszko, "Dual-mode helical resonators," *IEEE Transactions on Microwave Theory and Techniques*, vol. 48, pp. 474-477, 2000.
- [120] 3M, 3M pioneers 3D printing with PTFE. (2017). Available: <http://solutions.3m.com/>
- [121] J. K. A. Everard and C. D. Broomfield, "High Q Printed Helical Resonators for Oscillators and Filters," *IEEE Transactions on Ultrasonics, Ferroelectrics, and Frequency Control*, vol. 54, pp. 1741-1750, 2007.